



THE HONG KONG
POLYTECHNIC UNIVERSITY

香港理工大學

Pao Yue-kong Library

包玉剛圖書館

Copyright Undertaking

This thesis is protected by copyright, with all rights reserved.

By reading and using the thesis, the reader understands and agrees to the following terms:

1. The reader will abide by the rules and legal ordinances governing copyright regarding the use of the thesis.
2. The reader will use the thesis for the purpose of research or private study only and not for distribution or further reproduction or any other purpose.
3. The reader agrees to indemnify and hold the University harmless from and against any loss, damage, cost, liability or expenses arising from copyright infringement or unauthorized usage.

IMPORTANT

If you have reasons to believe that any materials in this thesis are deemed not suitable to be distributed in this form, or a copyright owner having difficulty with the material being included in our database, please contact lbsys@polyu.edu.hk providing details. The Library will look into your claim and consider taking remedial action upon receipt of the written requests.

**MEASUREMENT OF NITRYL CHLORIDE WITH
A CHEMICAL IONIZATION MASS
SPECTROMETER IN POLLUTED CHINA
ENVIRONMENT: INVESTIGATION OF ITS
ABUNDANCE, ORIGIN, AND IMPACT ON
OXIDATIVE CHEMISTRY**

THAM YEE JUN

Ph.D

The Hong Kong Polytechnic University

2017

The Hong Kong Polytechnic University
Department of Civil and Environmental Engineering

**Measurement of Nitryl Chloride with a Chemical
Ionization Mass Spectrometer in Polluted China
Environment: Investigation of Its Abundance,
Origin, and Impact on Oxidative Chemistry**

Tham Yee Jun

**A thesis submitted in partial fulfillment of the
requirements for the Degree of Doctor of Philosophy**

August 2016

CERTIFICATE OF ORIGINALITY

I hereby declare that this thesis is my own work and that, to the best of my knowledge and belief, it reproduces no material previously published or written, nor material that has been accepted for the award of any other degree or diploma, except where due acknowledgement has been made in the text.

Sign:

Name: Tham Yee Jun

ABSTRACT

Nitryl chloride (ClNO_2) is an important source of highly reactive chlorine radical that may affect the atmospheric oxidative chemistry in the daytime. However, the abundance of ClNO_2 and its roles are not fully understood under different environmental conditions. This thesis presents the first detailed investigation of ClNO_2 and its impact in polluted China environments based upon field measurements of ClNO_2 and its precursor, N_2O_5 , using chemical ionization mass spectrometry (CIMS).

Preliminary studies of ClNO_2 were conducted in Tung Chung and Hok Tsui (both in Hong Kong) with a thermal decomposition (TD) CIMS between 2011 and 2012. ClNO_2 shows a clear diurnal pattern with significant concentrations being observed during the night-time. Formation of ClNO_2 was persistent throughout the year with the highest level of ClNO_2 observed during the autumn season followed by spring, winter, and summer, which is consistent with the seasonal variation of NO_x , O_3 , and particle chloride. The variations of the ClNO_2 were found to be influenced by the air masses origin with elevated ClNO_2 mixing ratios observed in plumes from Hong Kong and the Pearl River Delta region and lower concentrations in marine air. Calculations suggest that photolysis of ClNO_2 contributed up to 0.02 pptv/s of Cl atom production rate in the early morning and exceeded the OH production rate via O_3 photolysis by a factor of 3. These results provide an initial understanding of ClNO_2 and its potential importance in Asian coastal regions.

To improve the quality of measurement, we then reconfigured and optimized the TD-CIMS to an unheated version of CIMS. A series of testing were performed, including calibrations, background zeroing and inlet transmission efficiency. The

optimized CIMS demonstrates high sensitivity (~ 1 Hz/pptv) with a low detection limit of 5 pptv for both N_2O_5 and ClNO_2 measurement. The sampling line was also optimized and was suggested to be replaced and washed daily to reduce the artifacts from aerosol deposition on the inlet surface. Field verification of the in-situ CIMS N_2O_5 measurements with observations by a cavity ring-down spectroscopy (CRDS) showed excellent agreement (slope = 0.99; $R^2 = 0.93$). These testing results indicate that the optimized CIMS is capable of accurately detecting both N_2O_5 and ClNO_2 under polluted China environment.

In keeping the works above, the optimized CIMS was deployed to the peak of Tai Mo Shan (957 m above sea level) in late autumn of 2013. The measurement found significant levels of ClNO_2 (>400 pptv) and its precursor, N_2O_5 (>1000 pptv) on 6 out of the 12 consecutive nights with full CIMS data. The highest ever reported levels of ClNO_2 (4.7 ppbv, 1 min average) and N_2O_5 (7.7 ppbv, 1 min average) were observed in one night. High-resolution meteorological simulations revealed that this ClNO_2 and N_2O_5 -laden air originated from the surface of urban/industrial areas north of the site with enriched anthropogenic chloride as well as NO_x and aerosol. We demonstrated that the fast production of NO_3 and moderate N_2O_5 uptake and ClNO_2 yield initiated the very high concentration of ClNO_2 , which led to a large production rate of Cl atom (up to 0.59 pptv/s) in the next morning. Daytime ClNO_2 and N_2O_5 were also observed in this measurement. The heterogeneous uptake of daytime N_2O_5 on fog/cloud droplets was shown to be a potentially important production mechanism for soluble nitrate and additional source of VOC oxidants during the daytime.

Elevated ClNO₂ mixing ratios (>350 pptv) were measured in an inland site of northern China during the summer CAREBEIJING 2014 campaign. The ClNO₂ mixing ratio of up to 2070 pptv (1-min average) was observed on 20-21 June 2014 and was characterized with a larger N₂O₅ heterogeneous loss rate and ClNO₂ production rate compared to the campaign average condition. A salient feature of this observation is that the abundant ClNO₂ concentration kept increasing even after sunrise and reached a peak 4 hours later. Such highly sustained ClNO₂ peaks in the morning are discrepant from the typical diurnal pattern previously observed in other places. As evidenced by the meteorological and chemical analysis, the sustained ClNO₂ morning peaks were caused by the significant ClNO₂ production in the residual layer at night followed by downward mixing after the break-up of the nocturnal boundary layer at sunrise. Calculations showed that ~1.7-4.0 ppbv of ClNO₂ would exist in the residual layer in order to sustain the observed morning ClNO₂ peaks at the surface site. Photolysis of the ClNO₂ was shown to be a dominant radical source and contributed up to 46%, 37%, 10%, 7% and 13% of the integrated oxidation of alkane, alkyne, alkene, aromatic and OVOC, respectively, throughout the morning. Overall, the findings of this thesis reveal that ClNO₂ is ubiquitous over the polluted regions of China and is a crucial pollutant to be considered when assessing photochemical and haze pollutions in China.

PUBLICATIONS

1. **Tham Y. J.**, Wang Z., Li Q., Yun H., Wang W., Wang X., Xue L., Lu K., Ma N., Bohn B., Li X., Kecorius S. and Größ J., Shao M., Wiedensohler A., Zhang Y., and Wang T.*. Significant concentrations of nitryl chloride sustained in the morning: Investigations of the causes and impacts on ozone production in a polluted region of northern China. *Atmospheric Chemistry and Physics* 16, 2016, doi:10.5194/acp-16-14959-2016.
2. Li Q., Zhang L., Wang T.*, **Tham Y. J.**, Ahmadov R., Xue L., Zhang Q., and Zheng J.. Impacts of heterogeneous uptake of dinitrogen pentoxide and chlorine activation on ozone and reactive nitrogen partitioning: Improvement and application of WRF-Chem model in southern China. *Atmospheric Chemistry and Physics* 16, 2016, doi:10.5194/acp-16-14875-2016.
3. Wang T.*, **Tham Y. J.**, Xue L., Li Q., Zha Q., Wang Z., Poon S. C. N., Dubé W. P., Blake D. R., Louie P. K. K., Luk C. W. Y., Tsui W., and Brown S. S.. Observations of nitryl chloride and modeling its source and effect on ozone in the planetary boundary layer of southern China. *Journal of Geophysical Research: Atmospheres*, 121, 2016, doi:10.1002/2015JD024556.
4. Brown S. S.*, Dubé W. P., **Tham Y. J.**, Zha Q., Xue L., Poon S., Wang Z., Blake D. R., Tsui W., Parrish D. D., and Wang T.. Nighttime chemistry at a high altitude site above Hong Kong. *Journal of Geophysical Research: Atmospheres*, 121, 2016, doi:10.1002/2015JD024566.
5. **Tham Y. J.**, Yan C., Xue L., Zha Q., Wang X., and Wang T.*. Presence of high nitryl chloride in Asian coastal environment and its impact on atmospheric photochemistry. *Chinese Science Bulletin* 59(4), 2014, 356–359
6. Wang X., Wang T.*, Yan C., **Tham Y. J.**, Xue L., Xu Z., and Zha Q.. High concentrations of N₂O₅ and NO₃ observed in daytime with a TD-CIMS: chemical interference or a real atmospheric phenomenon? *Atmospheric Measurement Techniques* 7, 2014, 1-12.

CONFERENCE PRESENTATIONS

1. **Tham Y. J. et al.**, Observation of nitryl chloride and its effect on ozone in the planetary boundary layer of southern China. *The 4th GIGCAS-HKPOLYU Joint Workshop on Environmental Science and Engineering, 2015, Shenzhen.*
2. **Tham Y. J. et al.**, N₂O₅ measurement in Hong Kong by a chemical ionization mass spectrometry: Presence of high N₂O₅ and implications. *Geophysical Research Abstracts, Vol. 16, European Geoscience Union General Assembly 2014, Vienna.*
3. **Tham Y. J. et al.**, Development and application of chemical ionization mass-spectrometry (CIMS) for measurement of N₂O₅ in Hong Kong. *The 4th International Workshop on Regional Air Quality Management in Rapidly Developing Economic Regions, Hong Kong University of Science and Technology, 2013, Hong Kong.*

ACKNOWLEDGEMENTS

I am deeply indebted to my advisor, Professor Wang Tao, who guided and supported me throughout my Ph.D. study. I would not have completed my graduate research work without his insightful comments, assistance, and patience. Although he was always very busy, he always made himself available to me whenever I had research problems or questions to discuss with him.

Special thanks go to Steven Poon, Professor Xue Likun, Dr. Wang Zhe, and Dr. Wang Xinfeng for their help and guidance. Without them, my research works will not go on smoothly. I would like to express my gratitude to all my group members: Dr Nie Wei, Dr Guo Jia, Dr Xu Zheng, Dr Zhou Shengzhen, Zha Qiaozhi, Yan Chao, Zhang Li, Li Qinyi, Wang Weihao, Yun Hui, Much Yeung, James Chan, Wu Jueqi, and other group members who have helped me to adapt life in Hong Kong and cooperated in completing my research works.

I am grateful to David Tanner for his technical support and advice on the CIMS, to Dr. Steven Brown and Bill Dubé for their N₂O₅ data and discussion on the data analysis. I am also thankful to the organizer and science team of CAREBEIJING-14 campaign, especially Professor Zhang Yuanhang and Dr. Lu Keding, for inviting us to participate in the study and providing us with all the auxiliary data.

I would like to thank my parents, family members, Gao Yuan, and all my friends who are supporting and encouraging me all the time with their care and love.

Finally, I would like to acknowledge the studentship from Hong Kong Polytechnic University in supporting my study. The field projects were funded by Environment and Conservation Fund of Hong Kong (project no. 7/2009), Hong Kong Research Grants Council (PolyU 153026/14P & PolyU5015/12P), National Natural Science Foundation of China (41275123) and PolyU Project of Strategic Importance (1-ZE13).

TABLE OF CONTENTS

Certificate of Originality	I
Abstract	II
Publications	V
Conference Presentations	VI
Acknowledgements	VII
Table of Contents	IX
List of Tables	XIII
List of Figures	XIV
List of Abbreviations	XIX

Chapter 1: Introduction

1.1 Background	1
1.2 Research objectives	5
1.3 Structure of the thesis	5

Chapter 2: Literature review

2.1 Formation of ClNO ₂	7
2.1.1 The availability of N ₂ O ₅	7
2.1.2 Heterogeneous uptake coefficient of N ₂ O ₅	12
2.1.3 ClNO ₂ production yield	16
2.2 Sink processes of ClNO ₂	18
2.3 Field observations of ClNO ₂	19
2.3.1 Marine coastal environment.....	20
2.3.2 Inland environment	22
2.3.3 Vertical distributions of ClNO ₂	24
2.3.4 Daytime ClNO ₂ and N ₂ O ₅	25
2.4 Potential impacts of ClNO ₂ in the troposphere.....	26
2.4.1 Impacts on radical chemistry	26
2.4.2 Impacts on VOCs oxidation and ozone production	29
2.4.3 Impacts on NO _x loss.....	31
2.5 Measurement techniques for ClNO ₂	32
2.5.1 Chemical ionization mass spectrometry technique.....	33

2.5.2 Cavity ring-down spectroscopy technique.....	37
Chapter 3: Methodology	
3.1 Study locations	39
3.1.1 Tung Chung	39
3.1.2 Hok Tsui.....	40
3.1.3 Tai Mo Shan.....	40
3.1.4 Wangdu	43
3.2 Instrumentation	46
3.2.1 Chemical ionization mass spectrometer	46
3.2.1 Inlet setup in the field	48
3.3 Preparation of calibration standards for CIMS	50
3.3.1 Synthesis of N ₂ O ₅	50
3.3.2 Production of ClNO ₂ standard	52
3.4 Background zeroing system.....	53
3.5 Auxiliary measurements	54
3.6 Estimation of the unmeasured photolysis frequencies	59
3.7 Time-dependent chlorine chemistry box model	59
Chapter 4: Preliminary field observations of ClNO₂ in Asian coastal environment	
4.1 First attempt of ClNO ₂ measurement	63
4.2 Preliminary observation of ClNO ₂ at Tung Chung	64
4.3 Second attempt of ClNO ₂ measurement.....	67
4.4 Preliminary observation of ClNO ₂ at Hok Tsui.....	69
4.5 Potential impacts of ClNO ₂	71
4.6 Summary.....	75
Chapter 5: Optimization of CIMS for N₂O₅ and ClNO₂ measurement in polluted China environment	
5.1 Instrument sensitivity towards N ₂ O ₅ and ClNO ₂	77
5.1.1 Calibration.....	77
5.1.2 Effect of humidity on the sensitivities of N ₂ O ₅ and ClNO ₂	79
5.2 Determinations of instrument zero and detection limits.....	82
5.3 Inlet transmission efficiency	84
5.3.1 Conversion of N ₂ O ₅ to ClNO ₂ on the inlet	84
5.3.2 Conversion of N ₂ O ₅ to ClNO ₂ on Teflon filter.....	86
5.4 Ambient trial run.....	89

5.5 Verification of ambient measurement.....	92
5.6 Testing on corona discharge as ionization source	94
5.6.1 Setup of corona discharge ion source	95
5.6.2 Sensitivity	96
5.6.3 Mass spectra of $I(N_2O_5)^-$ and $I(ClNO_2)^-$	98
5.6.4 Background and detection limits	99
5.6.5 Ambient performance and signal stability	101
5.7 Summary.....	103

Chapter 6: Observation of $ClNO_2$ at a high altitude site in southern China

6.1 Meteorological overview at TMS	107
6.2 General observations at TMS	108
6.3 Variations of $ClNO_2$	111
6.3.1 Diurnal average.....	111
6.3.2 Night of 30 November-1 December: Early $ClNO_2$ peak	112
6.3.3 Night of 3-4 December: Extremely high $ClNO_2$ and N_2O_5 plume ...	115
6.4 N_2O_5 heterogeneous uptake and production of $ClNO_2$	120
6.5 Impact of the $ClNO_2$ on the production rate of Cl atom and O_3	123
6.6 Presence of daytime N_2O_5 and $ClNO_2$ at TMS.....	125
6.6.1 Daytime N_2O_5 chemistry.....	125
6.6.2 Daytime N_2O_5 chemistry as an HNO_3 source	127
6.6.3 Daytime N_2O_5 chemistry as an NO_3 source and impact on VOC oxidation	128
6.7 Summary	131

Chapter 7: Observation of $ClNO_2$ and its impact on VOC oxidation in polluted environment of northern China

7.1 Overview results	134
7.2 Diurnal variations	137
7.3 Factors affecting the variation of $ClNO_2/N_2O_5$ ratios	140
7.3.1 Production rate of NO_3	140
7.3.2 N_2O_5 reactivity	141
7.3.3 Yield of $ClNO_2$	144
7.3.4 $ClNO_2$ production rate	146
7.4 Sustained $ClNO_2$ morning peak.....	147
7.4.1 Factors contributing to the sustained $ClNO_2$ morning peak	148

7.4.2 Prediction of the ClNO ₂ concentrations in the residual layer	153
7.5 Chloride availability and its potential sources.....	155
7.6 Impacts of ClNO ₂ on the oxidative chemistry	159
7.6.1 Primary radical production	159
7.6.2 VOCs oxidation	161
7.7 Summary.....	164
Chapter 8: Conclusions	
8.1 Key findings and conclusions	166
8.2 Future work.....	168
References	170

LIST OF TABLES

Table 2.1. The lifetimes of selected VOCs with NO₃ predicted at a fixed NO₃ mixing ratio of 20 ppt (from Atkinson and Arey, 2003; Brown and Stutz, 2012).

Table 2.2. Currently available measurement techniques for ambient N₂O₅ and ClNO₂ in the literature.

Table 3.1. Measurement techniques and time resolution of the supporting data used in Tung Chung, Hok Tsui, and Tai Mo Shan.

Table 3.2. Measurement method for trace gasses and aerosols at Wangdu.

Table 3.3. Reactions included in the chlorine chemistry time-dependent model.

Table 4.1. The mean values of ClNO₂, NO_x, O₃, aerosols, temperature and RH in the four seasons.

Table 4.2. Mean mixing ratio of nighttime NO₂, O₃, N₂O₅, and ClNO₂ in three different types of air masses categories.

Table 6.1. Particulate chloride and sodium for night of 3-4 December and daytime of 4 December 2013.

Table 6.2. ClNO₂ production parameters in the 'young' ClNO₂-laden plume and 'aged' ClNO₂ plumes (three plumes).

Table 6.3. The VOCs mixing ratios sampled at 12:22 (LT) on 27th November 2013

Table 7.1. Correlations and slopes of chloride with power plant (SO₂) and biomass burning (CH₃CN) indicators from 20:00-09:30.

Table 7.2. Mean concentrations and standard deviations (σ) of each species and meteorological conditions used as input in the box model simulations. Concentrations are in ppbv unless mentioned.

Table 7.3. The relative importance of Cl on oxidation rates of different VOCs groups for average condition and the 21 June case.

LIST OF FIGURES

Figure 1.1. Schematic of ClNO₂ heterogeneous production from N₂O₅ and its potential impact in the troposphere. Emission from the natural and anthropogenic sources are believed to play important roles in the formation of ClNO₂.

Figure 2.1. The ratio of N₂O₅/NO₃ as a function of temperature by using the K_{eq} determined in the literature (from Chang et al., 2010).

Figure 2.2. Plots of the efficiency of conversion of N₂O₅ to ClNO₂ versus the substrate chloride concentration obtained from different studies (Roberts et al., 2009 and references therein).

Figure 2.3. The observations of ClNO₂ available around the world. The mixing ratios here (in red color wording) are the maximum level of ClNO₂ of that campaign.

Figure 2.4. a) Vertical distributions of ClNO₂ in the nocturnal PBL for average of 21 profiles from flight measurements within Los Angeles basin (Young et al., 2010). Vertical profiles of ClNO₂ in b) urban diffused plume and c) coal-fired power plant plume measured on a tower in Boulder (Riedel et al., 2013).

Figure 2.5. Schematic diagram of radical chemistry, illustrating the key chemical pathways in the troposphere. The radical chemistry is initiated by primary radical production from the ‘conventional’ sources (in light blue) and ‘new’ radical source of Cl atom (in purple). Radical chain reactions cause cycling between OH, HO₂, and RO₂, leading to the formation of O₃ and SOA.

Figure 2.6. An example of the schematic design of an iodide TD-CIMS instrument used by University of Calgary for ClNO₂ measurement (figure adapted from Mielke et al., 2011).

Figure 2.7. The schematic drawing of TD-CRDS applied for ClNO₂ measurement (figure adapted from Thaler et al., 2011).

Figure 3.1. Google map shows the locations of the measurement site at a) Tung Chung, b) Hok Tsui, and c) Tai Mo Shan in relation to the surrounding of Hong Kong and Pearl River Delta of China.

Figure 3.2. a) Location of northern China (blue dash-box) and Wangdu site (red box); b) an expanded view of NCP with the topography, major cities and the locations of major coal-fired power plants (yellow circles); c) nearby environment of Wangdu site. The photos on the right corner are the trailers at the sampling site and surrounding view of the site.

Figure 3.3. Active fire hotspots (red dots) in the region covering the study period of 20 June – 9 July 2014 (data from FIRMS, <https://earthdata.nasa.gov/firms>).

Figure 3.4. Schematic diagram of the unheated iodide-CIMS (not to scale).

Figure 3.5. Comparison of the calculated and measured concentrations of the produced N_2O_5 after dilutions (in 5.0 SLPM). The shaded area (in gray) show the standard deviation (1σ) of the calculation. The error bar represents the standard deviation (1σ) of measured N_2O_5 .

Figure 3.6. Schematic diagram of the N_2O_5 exposure to slurry NaCl to produce ClNO_2 .

Figure 3.7. The design of the background zeroing system for ClNO_2 and N_2O_5 .

Figure 4.1. Overview of ClNO_2 mixing ratios measured in the four non-consecutive months (different seasons).

Figure 4.2. Seasonal diurnal variations of ClNO_2 concentrations at Tung Chung.

Figure 4.3. Time series of ClNO_2 and N_2O_5 together with related parameters measured at Hok Tsui from 23 August to 1 September 2012.

Figure 4.4. Twenty-four hour back trajectories from HYSPLIT covering the period of 23 August 2012 to 1 September 2012.

Figure 4.5. Cl atom production rate in four different seasons at Tung Chung.

Figure 4.6. The Cl production rate on 24 August 2012. Pie charts represent the ratio of Cl production from ClNO_2 and OH production via photolysis of ozone.

Figure 5.1. Schematic diagram of the off-line calibration system for N_2O_5 . The black line represents $\frac{1}{4}$ " O.D. PFA tubing and blue line is $\frac{1}{8}$ " O.D. PFA tubing.

Figure 5.2. The CIMS N_2O_5 and ClNO_2 signal at $I(\text{N}_2\text{O}_5)^-$ and $I(\text{ClNO}_2)^-$ versus the concentrations of N_2O_5 and ClNO_2 . The calibrations were conducted in a humidified zero air stream maintained at $\text{RH} = \sim 55\%$.

Figure 5.3. The CIMS a) $I(\text{H}_2\text{O})^-$ ion signal; b) sensitivity of ClNO_2 ; and c) sensitivity of N_2O_5 versus humidity (RH) in the range of 0-90% at room temperature. The color circle dots represent the experiment data and the break-line is the trend-line of curve fittings.

Figure 5.4. An example of raw background signal versus ambient signal for N_2O_5 (upper panel) and ClNO_2 (lower panel) taken at 8-s time resolution. During ambient measurement, background measurements were performed for a duration of 3 min in every hour.

Figure 5.5. Percentage of the N_2O_5 signal loss and relatively increase in ClNO_2 signal in different types of inlet condition. The testing was performed by adding 4.1 ppbv of N_2O_5 into a stream of humidified zero air ($\text{RH}=60\%$) at room temperature. Error bars represent the standard deviation of the tests ($n=3$).

Figure 5.6. Percentage of N_2O_5 loss and relative ClNO_2 signal on Teflon filter for a) empty filter housing and intervals between 2 hours of ambient sampling b) the aged-filter (2-hour ambient sampling) in different RH conditions.

Figure 5.7. An example of the $I(\text{N}_2\text{O}_5)^-$ signal in standard addition of N_2O_5 (yellow zone) during ambient measurement.

Figure 5.8. a) The concentration of N_2O_5 and ClNO_2 measured at Hong Kong Polytechnic University for 3 continuous nights. The yellow-shaded zone represents the daytime. b) A subset of measured N_2O_5 versus steady-state calculated N_2O_5 on the night on 20-21 October 2013.

Figure 5.9. Scatterplot between 1 min averaged N_2O_5 mixing ratios from the NOAA-CRDS (x-axis) and from the CIMS (y-axis) for 12 days ($N = 9148$). a) Solid line (red) represents an RMA linear fit and b) an example of N_2O_5 mixing ratios from CIMS and CRDS during night-time and daytime.

Figure 5.10. Scatter plots of 1 min averaged raw ambient signal of 208 *a.m.u.* with 210 *a.m.u.* measured at a) Hong Kong Polytechnic University b) TMS and c) Wangdu.

Figure 5.11. Schematic drawing of corona discharge ion source built by THS Instrument.

Figure 5.12. Sensitivity of N_2O_5 and ClNO_2 as a function of relative humidity. The blue and red solid lines are the curve fits for the data. Ratio of the sensitivity from corona to radioactive source is shown on the right y-axis.

Figure 5.13. Examples of mass spectrum for a) $I(\text{ClNO}_2)^-$ (208 *a.m.u.*) and b) N_2O_5 (235 *a.m.u.*) measured with corona discharge and radioactive ion source. The upper panel shows the mass scans of $I(\text{N}_2\text{O}_5)^-$ and $I(\text{ClNO}_2)^-$ during calibration with a radioactive ion source.

Figure 5.14. Distributions of ambient background signals for (a) ClNO_2 (in purple) and (b) N_2O_5 (in gray) from CIMS operated with corona discharge source and ^{210}Po radioactive source ($N = 902$).

Figure 5.15. Time series of the raw ambient signal measured CIMS operated with a corona ion source. Dots represent the 8-s signal data and the solid lines are the 1-min average signal data.

Figure 5.16. Comparison of a new gold-coated needle (right) with a corroded or 'darkened' one (left) after more than 36 hours of sampling.

Figure 6.1. a) Wind rose plot, b) diurnal average of wind and c) diurnal average of temperature and humidity at the TMS site.

Figure 6.2. Time series of ClNO_2 , N_2O_5 and related chemical and meteorological parameters for period of a) 15-17 November 2013, b) 23-29 November 2013, c) 30 November – 6 December 2013. The data gap is due to calibrations, inlet maintenance, and instrument problems.

Figure 6.3. The diurnal average of N_2O_5 (red) and ClNO_2 (purple) for the campaign. Dots represent the 10th and 90th percentile of the N_2O_5 (pink) and ClNO_2 (grey) data set.

Figure 6.4. An expanded view of ClNO₂ and related chemical and meteorological parameters for 30 November-1 December 2013, as the example of the typical diurnal pattern at TMS.

Figure 6.5. a) The concentration of N₂O₅ and ClNO₂ in relation to the NO_z and NO_y. N₂O₅ has been multiplied by two-fold (as it contains two nitrogen atoms) and is stacked on the ClNO₂. b) The ratio of NO_x/NO_y in relation to ClNO₂/N₂O₅ ratios on the night of 30 November 2013.

Figure 6.6. Twelve-hour backward particle dispersion for 17:00, 20:00 on 30 November and 03:00 of 1 December. Contours represent the number of particles in each 0.02 degree latitude × 0.02 degree longitude grid.

Figure 6.7. Expanded time series of ClNO₂, N₂O₅ and related chemical and meteorological parameters for 3-4 December 2013. The arrows indicate Plumes I, II, and III (as identified in the text).

Figure 6.8. a) The concentration of N₂O₅ and ClNO₂ in relation to the NO_z and NO_y in the three different plumes (I, II, and III) on the night of 4 December 2013. N₂O₅ has been multiplied by two-fold and is stacked on the ClNO₂. b) The ratios of NO_x/NO_y in relation to ClNO₂/N₂O₅ ratios.

Figure 6.9. Examples of 12-h backward particle dispersion for 00:00 and 04:00 on 4 December. Contours represent the number of particles in each 0.02 degree latitude × 0.02 degree longitude grid.

Figure 6.10. Cl production rate (black circle) from photolysis of ClNO₂ in Plume II and III of the extreme case. The lower panel shows the O₃ increases caused by constraining the ClNO₂ in Plume II and III into an MCM box model (The MCM result was provided by L. Xue, refer to Wang et al., 2016 for more details).

Figure 6.11. Observed and calculated daytime N₂O₅ (from equation 6.4) and observed ClNO₂ (for the period when these data were available), production rate of the nitrate radical, and relative humidity for (a) 27 November and (b) 30 November 2013.

Figure 6.12. The VOC oxidation rate by NO₃ in the daytime of 27 and 30 November 2013 in comparison with the VOC oxidation rate by OH (assumed at a mixing ratio of 2×10⁶ molecule/cm³).

Figure 7.1. Time series of ClNO₂, N₂O₅, related species and meteorological parameters observed at Wangdu. Data are at 1 min time resolution, except for the NO_x data (5 min average).

Figure 7.2. History of air masses arriving at the measurement site at 08:00 (12 h backward). Yellow cross represents the major coal-fired power plant in the region.

Figure 7.3. Diurnal variation of ClNO₂, N₂O₅, NO_x, NO_y, O₃ and particle surface area for a) campaign average (from 20 June to 9 July 2014 when ClNO₂ data is available); b) 20-21 June; c) 28-29 June.

Figure 7.4. The production rate of NO_3 for the nighttime of campaign average, 20-21 June, and 28-29 June.

Figure 7.5. The fractions of N_2O_5 loss rate coefficient through NO_3+NO , NO_3+VOC , and heterogeneous reaction for campaign average, 20-21 June, and 28-29 June.

Figure 7.6. Comparison of ClNO_2 yield determined in the observation with the calculated ClNO_2 yield from the laboratory derived parameterization.

Figure 7.7. The production rates of ClNO_2 for 20-21 June, 28-29 June, and campaign average.

Figure 7.8. An expanded view of the sustained morning ClNO_2 peaks together with some relevant chemical information including SO_2/NO_y , $\text{Cl}^- (\times 3)$, NO_3^- , and $\text{P}(\text{NO}_3)$ for a) campaign average; b) 21 June; and c) 29 June.

Figure 7.9. The observed enhancement of ClNO_2 and the calculated in-situ production of ClNO_2 for a) campaign average; b) 21 June case; and c) 29 June case.

Figure 7.10. Fractions of air masses arriving at the Wangdu site at different time of the day (average condition). These fractions are derived from the simulation results of 1 h backward-in-time HYSPLIT.

Figure 7.11. a) Conceptual diagram of the simplified 1D model used to demonstrate the entrainment; b) the WRF-simulated boundary layer heights (above ground level) for the average condition and 21 June case.

Figure 7.12. Concentrations of fine Cl^- , SO_2 (a coal-fired power plant indicator) and CH_3CN (a biomass burning indicator) from 20 June to 9 July 2014. The black dash line represents the mass ratio of $[\text{Cl}^-]$ to $[\text{Na}^+]$ in seawater (1.8).

Figure 7.13. An example of biomass burning event from the active fire hotspots data (red dots) on 27-29 June.

Figure 7.14. The relative importance of production rate of Cl atom from photolysis of ClNO_2 and reaction of $\text{OH}+\text{HCl}$ for a) the campaign average and b) the 21 June case, in comparison with the production rates of primary OH radical ($\text{P}(\text{OH})$). The $\text{P}(\text{OH})$ from photolysis of O_3 is stacked on the $\text{P}(\text{OH})$ from HONO.

LIST OF ABBREVIATIONS

a.g.l.	Above Ground Level
a.m.u.	Atomic Mass Unit
a.s.l.	Above Sea Level
BB-CEAS	Broadband Cavity-Enhanced Absorption Spectroscopy
CalNex	California Research at the Nexus of Air Quality and Climate Change
CARE-Beijing	Campaigns of Air Quality Research in Beijing and Surrounding Regions
CDC	Collisional Dissociation Chamber
CIMS	Chemical Ionization Mass Spectrometer
ClearfLo	Clean Air for London
CRDS	Cavity Ring-Down Spectroscopy
DOAS	Differential Optical Absorption Spectroscopy
FEP	Fluorinated Ethylene Propylene
FIRMS	Fire Information for Resource Management System
HYSPLIT	HYbrid Single-Particle Lagrangian Integrated Trajectory
I.D.	Internal Diameter
ICEALOT	International Chemistry in the Arctic Lower Troposphere
IR	Infra-red
IUPAC	International Union of Pure and Applied Chemistry
LIF	Laser-Induced Fluorescence
LOPAP	Long-Path Absorption Photometer
LPM	Litre per Minute
MBL	Marine Boundary Layer
MCM	Master Chemical Mechanism
NACHTT	Nitrogen, Aerosol Composition, and Halogens on a Tall Tower
NBL	Nocturnal Boundary Layer
NCP	North China Plain

NOAA	National Oceanic and Atmospheric Administration
O.D.	Outer Diameter
OVOCs	Oxygenated Hydrocarbons
PBL	Planetary Boundary Layer
PFA	Perfluoroalkoxy
pop.	Populations
ppbv	Parts Per Billion by Volume
pptv	Parts Per Trillion by Volume
PRD	Pearl River Delta
PTR-MS	Proton-Transfer-Reaction-Mass Spectrometer
RH	Relative Humidity
RL	Residual Layer
RMA	Reduced Major Axis
SLPM	Standard Litre per Minute
STP	Standard Temperature and Pressure
TD-CIMS	Thermal Dissociation-Chemical Ionization Mass Spectrometer
TEOM	Tapered Element Oscillating Microbalance
TUV	Tropospheric Ultraviolet and Visible
UBWOS	Uintah Basin Winter Ozone Studies
UV	Ultra-violet
VOC	Volatile Organic Compounds
WRF	Weather Research and Forecasting

Chapter 1 Introduction

1.1 Background

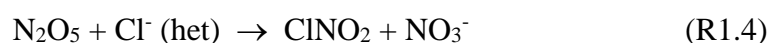
Emissions of nitrogen oxides ($\text{NO}_x = \text{NO} + \text{NO}_2$) via anthropogenic activities degrade the air quality and negatively affect human health (Ramanathan et al., 2001, Zipprich et al., 2002). During the daytime, NO_x participates in a series of photochemical reactions to produce ozone (O_3) and nitric acid (HNO_3). These daytime NO_x reactions have been extensively studied since the 1980s (Parrish et al., 1993). NO_x involves in a different set of reactions after sunset. Oxidation of nitrogen dioxide (NO_2) by O_3 yields the nitrate radical, NO_3 (R1.1), which is extremely susceptible to sunlight.



Thus, NO_3 only accumulates at nightfall and can further react with another NO_2 to produce dinitrogen pentoxide (N_2O_5). N_2O_5 always co-exists in thermal equilibrium with NO_3 and NO_2 .



N_2O_5 can undergo irreversible hydrolysis (reaction with liquid water in the aerosol) to produce two water-soluble HNO_3 (R1.3). If chloride (Cl^-) is available in the aerosol, N_2O_5 undergoes chlorine activation, leading to the production of nitryl chloride (ClNO_2) and nitrate (NO_3^-) (R1.4) (Finlayson-Pitts et al., 1989).



The ClNO_2 serves as a stable reservoir of radical and NO_x during the night, but it is subjected to photolysis at sunrise, liberating a reactive chlorine (Cl) atom and NO_2 to the ambient atmosphere (see Figure 1.1). Cl atom is reactive towards VOCs and can enhance ozone production in the polluted regions (Osthoff et al., 2008; Simon et al., 2010; Riedel et al., 2014; Sarwar et al., 2014). The presence of Cl atom also increases the production of secondary aerosol (Jimenez et al., 2009; Cai et al., 2008) and affects the lifetime of greenhouse gasses like methane (Liao et al., 2014).

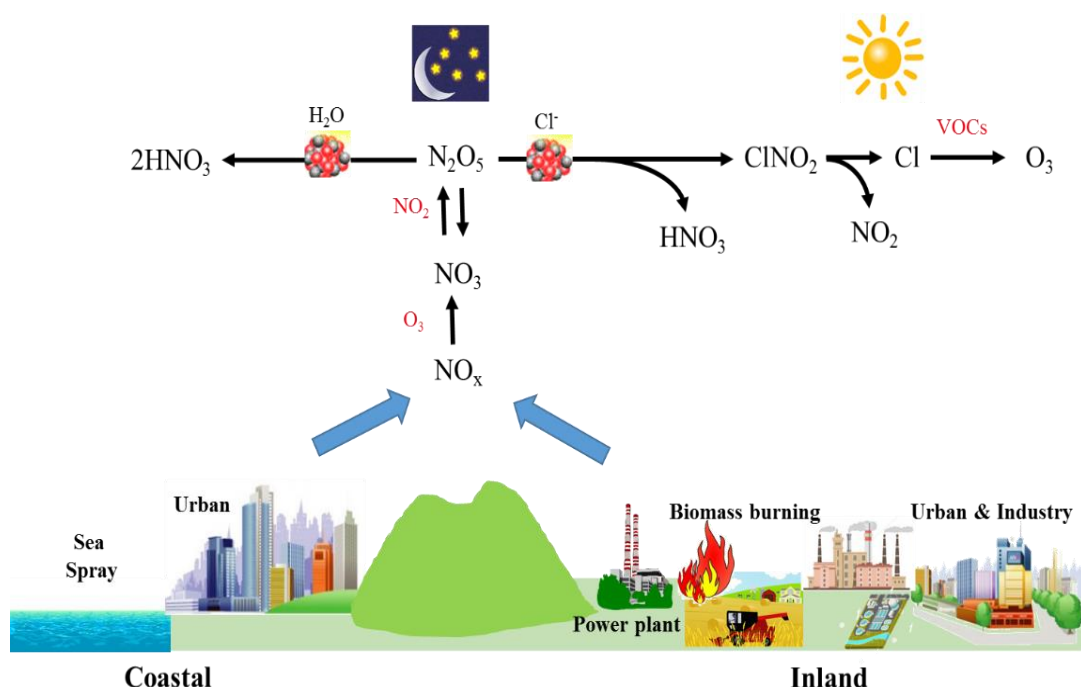


Figure 1.1. Schematic of ClNO_2 heterogeneous production from N_2O_5 and its potential impact in the troposphere. Emission from the natural and anthropogenic sources are believed to play important roles in the formation of ClNO_2 .

The above nocturnal chemistry is unknown in the real atmosphere until a decade ago. The first ambient measurement of ClNO_2 took place in 2006 along the coast of Texas (Osthoff et al., 2008). They observed high levels of ClNO_2 with mixing ratios >1 ppbv, indicating the importance of ClNO_2 production in the coastal

environment. Later studies in other polluted marine regions also reported large ClNO₂ mixing ratios of up to 3.6 ppbv (Riedel et al., 2012; Wagner et al., 2012; Mielke et al., 2013; Bannan et al., 2015a). Production of ClNO₂ in the inland environment has been thought to be slow, but Thornton and co-workers found significant ClNO₂ mixing ratios of up to 0.45 ppbv in Boulder (Thornton et al., 2010). They suggested that non-marine Cl⁻ emitting sources like coal-fired power plants, industries, biomass burning, road salts and soil dust may support the ClNO₂ production in that region. ClNO₂ mixing ratios ranging from tenths of pptv to 1.3 ppbv were later observed at other inland sites (Mielke et al., 2011; Phillips et al., 2012; Riedel et al., 2013; Faxon et al., 2015).

To date, the research on heterogeneous production of ClNO₂ was only conducted in the United States (US) (e.g. Osthoff et al., 2008; Thornton et al., 2010; Riedel et al., 2012; Riedel et al., 2013; Mielke et al., 2013; Faxon et al., 2015), Canada (Mielke et al. 2011, 2015), and a few in Europe (Phillips et al., 2012; Bannan et al., 2015a). The lack of measurement data in other parts of the world limits our ability to evaluate the global impact of ClNO₂ on tropospheric chemistry and air quality.

China has been suffering from severe air pollution problems due to the rapid economic development and excessive consumption of energy. Emission of NO_x was found to increase steadily in Asia until recently, a phenomenon that is different with those in North America and Europe which showed a declining trend of NO_x (Russell et al., 2012; Hilboll et al., 2013). Satellite NO₂ column data showed a maximum NO₂ emission of 127 Gg N yr⁻¹ in 2011 and an increase of 5–10% per annum over megacities of China (Mijling et al., 2013; Hilboll et al., 2013). A recent study indicated

decreasing (but still high) NO₂ column concentrations since 2011 over China (Duncan et al., 2016). High levels of surface O₃ were frequently reported in China. For example, a maximum hourly concentration of 286 ppbv was observed in a rural site downwind of Beijing (Wang et al., 2006). Tropospheric ozone over the last two decades has increased in both northern and southern China at a rate of 2.6 - 3.0 ppbv yr⁻¹ and 0.6 - 0.9 ppbv yr⁻¹, respectively (Ding et al., 2008; Wang et al., 2009; Xue et al., 2014; Zhang et al., 2014). The abundant of NO_x and O₃ coupled with significant of chloride aerosol (e.g. Lai et al., 2007; Tan et al., 2009; Huang et al., 2014; Sun et al., 2015) may make the heterogeneous production of ClNO₂ particularly important in China.

Previous studies indicated that the nocturnal N₂O₅ heterogeneous processes are potentially important in China. Wang et al. (2013) observed significant level of NO₃ in the urban area of Shanghai by using a differential optical absorption spectroscopy (DOAS) and showed evidence of the efficient heterogeneous reaction of N₂O₅ at that urban site. A more recent study with a global model (incorporated with heterogeneous ClNO₂ formation chemistry) suggested the summertime production of ClNO₂ up to 0.4 ppbv in the inland region of China, where the heterogeneous conversion of N₂O₅ to ClNO₂ could be enhanced by the chloride presence in biomass burning plumes (Sarwar et al., 2014). These studies, however, lack of direct measurements of key chemicals involved in the N₂O₅ heterogeneous uptake. Field measurements of ClNO₂ (and N₂O₅) are clearly needed in China to understand the production mechanisms and impact of ClNO₂ in China's environment.

1.2 Research objectives

The objectives of this study are to:

- Develop and optimize CIMS method for accurate measurements of ClNO_2 and N_2O_5 under polluted condition of China.
- Characterize the abundance of ClNO_2 and its formation chemistry in polluted regions of southern and northern China.
- Assess the impacts of ClNO_2 on the primary radical production and VOCs oxidation rate.

1.3 Structure of the thesis

The thesis is composed of eight chapters as the followings:

- 1) Chapter 1 introduces the research background, rationale, main research objectives, and the outline of this study.
- 2) Chapter 2 reviews the current understanding of ClNO_2 including its formation and loss chemistry, distributions, potential impacts and measurement techniques.
- 3) Chapter 3 describes the sampling locations, instrumentation, experimental procedures and model techniques.
- 4) Chapter 4 reports preliminary observational data of ClNO_2 at two coastal sites in Hong Kong.

- 5) Chapter 5 presents the testing results of CIMS optimization and method improvement for measurements of N_2O_5 and ClNO_2 in polluted China condition.
- 6) Chapter 6 assesses the production of ClNO_2 (and N_2O_5) in the planetary boundary layer of southern China and their potential importance in the next day photochemistry.
- 7) Chapter 7 investigates the abundance of ClNO_2 and impacts on the primary radical production and VOCs oxidation in a polluted region of northern China.
- 8) Chapter 8 underlines the key findings, implications of the study and future works.

Chapter 2 Literature Review

2.1 Formation of ClNO₂

ClNO₂ is produced from the heterogeneous reaction of N₂O₅ on chloride particles (see R1.4). The production rate of ClNO₂ (P(ClNO₂)) is given as a function of N₂O₅ heterogeneous loss rate coefficient ($k(\text{N}_2\text{O}_5)_{\text{het}}$), N₂O₅ concentration and production yield of ClNO₂ (ϕ), as shown in equation (2.1).

$$P(\text{ClNO}_2) = k(\text{N}_2\text{O}_5)_{\text{het}}[\text{N}_2\text{O}_5]\phi \quad (2.1)$$

In other word, factors like the N₂O₅ availability, N₂O₅ heterogeneous uptake coefficient on aerosol, and yield of ClNO₂ determine the concentration of ClNO₂ in the ambient atmosphere. Each of these factors is reviewed in the following sub-sections.

2.1.1 The availability of N₂O₅

N₂O₅ is a key precursor of heterogeneous ClNO₂ production. It is produced from the gas-phase oxidation of NO₂ by O₃, followed by the reaction of NO₂ and NO₃ (see R1.1 and 1.2). N₂O₅ always exists in thermal equilibrium with NO₂ and NO₃. If the reaction tends toward the right, more N₂O₅ is produced, while N₂O₅ will be dissociated into NO₂ and NO₃ if it shifts toward the left. The thermal equilibrium between [N₂O₅] and [NO₂][NO₃] is given by equation (2.2), where, K_{eq} is a temperature-dependent equilibrium constant (e.g. $K_{\text{eq}} = 2.93 \times 10^{-11} \text{ cm}^3 \text{ molecule}^{-1}$ at 298 K as recommended by the IUPAC Kinetics database).

$$[\text{N}_2\text{O}_5] = K_{\text{eq}}[\text{NO}_2][\text{NO}_3] \quad (2.2)$$

This equilibrium is, therefore, influenced by the temperature and NO_2 concentrations as well as the NO_3 sinks (i.e. reaction with NO , VOCs, and heterogeneous uptake of NO_3) leading to indirect N_2O_5 loss (shifting the equilibrium to the left).

2.1.1.1 Thermal equilibrium and NO_2 concentrations

Ambient temperature and $[\text{NO}_2]$ are two important parameters in determining the equilibrium of equation 2.2. N_2O_5 is thermally unstable, so the formation of N_2O_5 is preferable at a lower temperature, whereas higher $[\text{NO}_2]$ in the ambient can increase the reaction rate of NO_3 and NO_2 and shift the equilibrium of R1.2 towards N_2O_5 . Figure 2.1 shows the example of N_2O_5 to NO_3 ratio as a function of temperature at different NO_2 mixing ratios (Chang et al., 2011). It shows that at 1 ppbv of NO_2 and 295 K, the N_2O_5 and NO_3 are roughly equal to each other (~1:1). The $[\text{N}_2\text{O}_5]$ is about 10 times of $[\text{NO}_3]$ at temperature of 278 K. The graph also shows that the $[\text{N}_2\text{O}_5]$ to $[\text{NO}_3]$ ratio at 10 ppbv of NO_2 is much larger than the ratio at 1 ppbv of NO_2 . It means that N_2O_5 is normally more abundant than NO_3 in NO_2 rich regions.

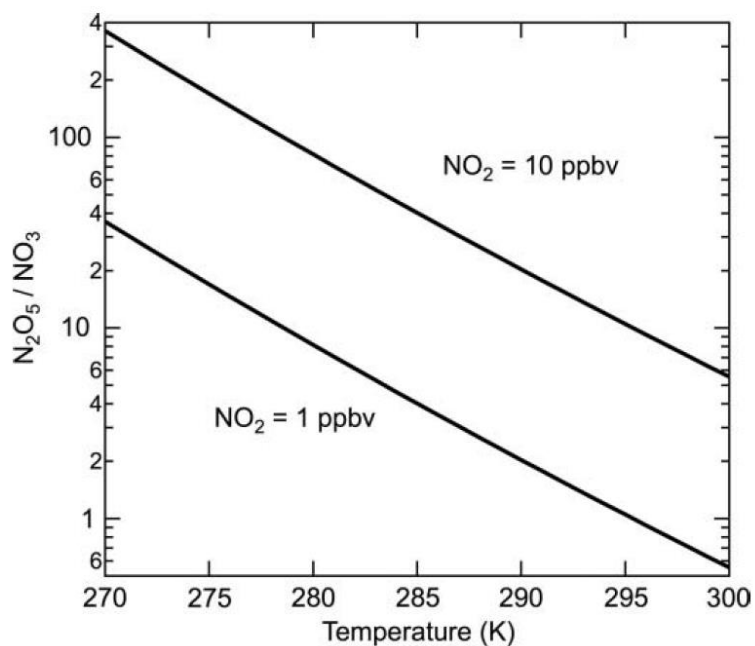


Figure 2.1. The ratio of N₂O₅/NO₃ as a function of temperature by using the K_{eq} determined in the literature (from Chang et al., 2010).

2.1.1.2 Indirect loss of N₂O₅ via reaction of NO₃ with NO

Reaction of NO₃ with NO is an important loss of NO₃ (R2.1). According to the IUPAC Kinetic database, the reaction rate coefficient of NO+NO₃ is $2.6 \times 10^{-11} \text{cm}^3 \text{molecule}^{-1} \text{s}^{-1}$ at 298 K.



This reaction is important during the daytime or near the anthropogenic NO sources during the night. For example, the lifetime of NO₃ in the presence of ~0.1 ppbv at standard temperature and pressure (STP) is about 15 seconds. Wayne et al., (1991) suggested that the lifetime of NO₃ with respect to R2.1 is shorter than photolysis of NO₃ at noon-time for NO concentrations ≥ 0.3 ppbv. The rapid loss of NO₃ would shift the equilibrium of R1.2 towards NO₃ + NO₂, resulting in indirect loss of N₂O₅ via its dissociation. Field measurements always found a sharp decrease of N₂O₅

mixing ratios to near zero level when high NO plumes were intercepted at night (e.g. Brown et al. 2012). Thus, the presence of NO in the air mass is a limiting factor of N₂O₅ production which in turn restricts the production of ClNO₂.

2.1.1.3 Indirect loss of N₂O₅ via reaction with VOCs

The reaction of NO₃ with VOCs (R2.2) can be another major indirect loss of N₂O₅.



Reaction of NO₃ + VOCs mainly proceeds by abstraction of H-atom and addition of NO₃ to the carbon double bond, producing variable products like OVOC, multifunctional organic nitrates, HNO₃ and NO₂. NO₃ can react rapidly with several groups of VOCs. Table 2.1 shows the lifetime of selected VOCs for NO₃ of 20 pptv. The lifetimes of alkenes, phenols, reduced sulfur compounds (e.g. dimethyl sulfide (DMS)), isoprene and terpenes are short, ranging from 14 s to 55 h, while the reaction of NO₃ with alkanes, aromatics (except styrene), ethane, and some oxygenated hydrocarbons are slow enough to have significant impacts in the ambient atmosphere (Atkinson and Arey, 2003; Brown and Stutz, 2012).

The indirect loss of N₂O₅ through NO₃ + VOCs was shown to be considerably important in various environments due to the different VOCs sources, especially in regions with low NO. A study in the polluted marine region along the Gulf of Maine showed that the loss of N₂O₅ was dominated by the NO₃ + VOCs on several nights (Aldener et al., 2006). They illustrated an example night with fast NO₃ loss rate coefficient up to $\sim 3 \times 10^{-2} \text{ s}^{-1}$, and the interaction of terrestrial biogenic VOC (isoprene

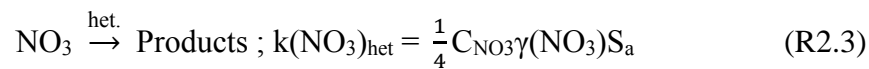
and monoterpenes) and DMS contributed to 71% and 10% of the total NO₃ sink, respectively. Brown et al. (2011) conducted extensive flight measurements to look into the NO₃ and N₂O₅ reactivity aloft of Texas regions which have influences from petrochemical facilities. They summarized that the reactivity of NO₃ and N₂O₅ was dominated by the reaction of NO₃ with VOCs in different types of air masses. Anthropogenic VOCs (i.e. alkenes and aromatics) was found to contribute to 54%, 46%, and 30% of the NO₃ loss in the fresh urban emissions, petrochemical emissions, and rural air masses, respectively. While biogenic VOCs (i.e. isoprene) were determined to be the dominant loss of NO₃, contributing 35-49% of the NO₃ loss in the rural area and aged urban plumes.

Table 2.1. The lifetimes of selected VOCs with NO₃ predicted at a fixed NO₃ mixing ratio of 20 ppt (from Atkinson and Arey, 2003; Brown and Stutz, 2012).

VOC	Lifetime for NO ₃ = 20 pptv
<i>Anthropogenic</i>	
Alkanes	>46 days
Aromatics	>11 days
Ethene	>116 days
Linear alkenes	22–55 h
Internal, branches alkenes	0.5 min–1.9 h
<i>Oxygenates</i>	
Formaldehyde	39 days
Acetaldehyde	7.7 days
Higher aldehydes	18 h – 3.3 days
Alcohols	11–230 days
Ketones	>38 days
Phenol, cresols	3–17 min
<i>Biogenic</i>	
Isoprene	0.8 h
Monoterpenes	3–15 min
Sesquiterpenes	14 s–0.8 h
Dimethyl sulfide	0.6 h

2.1.1.4 Indirect loss of N₂O₅ via NO₃ heterogeneous reaction

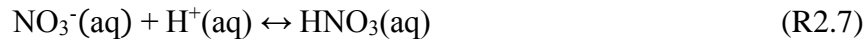
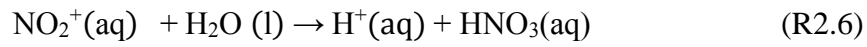
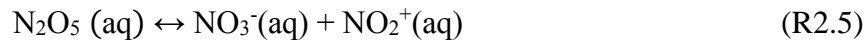
Heterogeneous reaction of NO₃ with aerosols is another indirect sink for the N₂O₅. Its reaction rate, $k(\text{NO}_3)_{\text{het}}$, can be determined by the uptake coefficient of NO₃ ($\gamma(\text{NO}_3)$), molecular speed of NO₃ (C_{NO_3}) and S_a , the surface area density, as shown in R2.3.



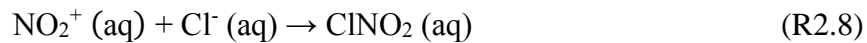
Heterogeneous reaction of NO₃ is usually regarded to be of insignificance in the atmosphere (Brown and Stutz, 2012 and references therein). For example, Aldener et al (2006) reported that only 2% of the NO₃ loss in a polluted marine region was caused by the NO₃ heterogeneous reaction. Tang et al. (2010) conducted an assessment of the uptake rate of NO₃ and N₂O₅ on mineral dust and indicated that the mineral dust is probably not a significant contributor to the loss of NO₃ in the boundary atmosphere, but suggested the needs of more future works at different environment. Crowley et al. (2011) later also found that the NO₃ loss on aerosols was insignificant in Spain for most of the time.

2.1.2 Heterogeneous uptake coefficient of N₂O₅

The second factor that can directly affect the ClNO₂ production is the direct loss of N₂O₅ via heterogeneous uptake. Before proceeding with the description of N₂O₅ heterogeneous uptake rate, it is useful to precede with the mechanisms of N₂O₅ heterogeneous uptake. The heterogeneous reactions of N₂O₅ on aerosol surfaces were demonstrated to be efficient under atmospheric conditions in late 1980s (Mozurkewich and Calvert, 1988). The mechanisms were proposed as in the reactions below.



It starts with the net accommodation of N_2O_5 onto the aqueous surface of the aerosol (R2.4). N_2O_5 will undergo solvation and ionization in the water, dissociating into NO_2^+ and NO_3^- ions, and NO_3^- (R2.5) as proposed by Thornton et al., (2003). The NO_2^+ ion will ultimately react with a water molecule (H_2O) to produce $\text{HNO}_3/\text{NO}_3^-$ (R2.6-2.7). Halides ions such as Cl^- could compete with water molecules to react with NO_2^+ to form nitryl halides like ClNO_2 (see R2.8) (Finlayson-Pitts et al., 1989; George et al., 1994; Behnke et al, 1997; Frenzel et al., 1998).



Later, Thornton et al., (2005) proposed another mechanism similar to the above, with the formation of the hydrated intermediate, H_2ONO_2^+ , instead of NO_2^+ , before reacting with another H_2O or halides ions.

As shown above, the ClNO_2 production depends on the heterogeneous loss rate coefficient of N_2O_5 ($k(\text{N}_2\text{O}_5)_{\text{het}}$) which is governed by the molecular speed of N_2O_5 ($C_{\text{N}_2\text{O}_5}$), particle surface area and $\gamma(\text{N}_2\text{O}_5)$, the uptake coefficient of N_2O_5 , defined as the probability of collisions of N_2O_5 with the aerosol surface that lead to reaction.

$$k(\text{N}_2\text{O}_5)_{\text{het}} = \frac{1}{4} C_{\text{N}_2\text{O}_5} \gamma(\text{N}_2\text{O}_5) S_a \quad (2.3)$$

In other words, N_2O_5 uptake coefficient is an important parameter for the N_2O_5 heterogeneous loss. A fixed value of $\gamma(\text{N}_2\text{O}_5) = 0.1$ was first proposed by Dentener and Crutzen (1993) for determining the tropospheric N_2O_5 heterogeneous loss. Later

studies, however, have found that the $\gamma(\text{N}_2\text{O}_5)$ was somewhat smaller and more variable.

Laboratory studies of the N_2O_5 heterogeneous uptake on sea-salts, sulfates, nitrates, chlorides, acids, organics, pure water, mineral dusts, and soots have reported $\gamma(\text{N}_2\text{O}_5)$ ranging between $10^{-4} - 10^{-2}$ (e.g. Thornton et al., 2003; Bertram and Thornton, 2009; Tang et al., 2012; Brown and Stutz, 2012 and references therein; Gaston et al., 2014; Gaston and Thornton, 2016). The $\gamma(\text{N}_2\text{O}_5)$ is highly affected by the changes of temperatures and RH. For example, Mozurkewich and Calvert (1988) found that the $\gamma(\text{N}_2\text{O}_5)$ on ammonium bisulphate aerosols increased from 0.05 at the temperature of 298 K to 0.09 at 274 K. Hu and Abbatt (1997) demonstrated a decreasing trend of N_2O_5 uptake onto ammonium sulfate aerosols towards higher RH at room temperature. They found $\gamma(\text{N}_2\text{O}_5) = 0.04-0.05$ for RH = 50-69% while decreased to 0.02 at high RH (83-94%). The $\gamma(\text{N}_2\text{O}_5)$ also depends on the magnitude of chemical compositions mix in the aerosol. Mentel et al., (1999) showed that the $\gamma(\text{N}_2\text{O}_5)$ on NO_3^- containing aerosol was an order of magnitude smaller than on sodium bisulfate and sulfate aerosols, illustrating that the presence of high NO_3^- loading effectively reverses the ionization process of N_2O_5 in the aqueous phase (see R2.5), which is known as the ‘nitrate effect’. This effect was also confirmed by other studies that found the reaction rate of NO_2^+ with NO_3^- to be 30-40 times faster than the reaction of NO_3^- with H_2O (Bertram and Thornton, 2009; Griffiths et al., 2009). However, if Cl^- is present in the aerosol, the ‘nitrate effect’ could be effectively negated (Bertram and Thornton, 2009).

Organics coating on the aerosol could also modify its surfactant properties and was shown to have strong suppression of the N_2O_5 uptakes. Folkers et al. (2003)

investigated the N_2O_5 uptakes on aqueous NH_4HSO_4 particles coated with α -pinene products (from ozonolysis) and showed a reduction of $\gamma(\text{N}_2\text{O}_5)$ by more than an order of magnitude. Thornton and Abbatt, (2005) later demonstrated that the presence of hexanoic acid as a monolayer of the aerosol decreases the $\gamma(\text{N}_2\text{O}_5)$ on NaCl from 0.025 to 0.008. Different effects of organics coating were observed in the ambient measurement with aerosol flow tube, where the $\gamma(\text{N}_2\text{O}_5)$ showed a clear dependence on particulate organic to sulfate ratios in Seattle, whereas no dependence of $\gamma(\text{N}_2\text{O}_5)$ was observed in Boulder (Bertram et al., 2009). Ryder et al., (2014) suggested the chemical composition and physical phase state of particulate organics likely controlled the $\gamma(\text{N}_2\text{O}_5)$ in the air masses from polluted coastal regions of San Diego. A more recent study also pointed out that the degree of oxidation of the organic aerosol (indicated by the atomic O:C ratios) and molecular weight, and the particle phase, morphology, and RH, can explain the different effects of organic aerosol on $\gamma(\text{N}_2\text{O}_5)$ (Gaston et al., 2014).

In the ambient atmosphere, variable values of $\gamma(\text{N}_2\text{O}_5)$ have been reported: 0.001-0.0017 at high altitude in New England region (Brown et al., 2006), 0.0004-0.006 in upper air in Texas (Brown et al., 2009), 0.001-0.029 at Los Angeles basin (Riedel et al., 2012), 0.002-0.1 at a downwind site of urban city in Colorado (Wagner et al., 2013), 0.012-0.037 in polluted and less polluted air masses in San Diego (Ryder et al., 2014), and 0.0076-0.03 at a high altitude in north-western Europe (Morgan et al., 2015).

2.1.3 ClNO₂ production yield

The final factor affecting the ClNO₂ production is the influence of ClNO₂ yield from the N₂O₅ heterogeneous reactions, which is defined as the branching ratio of R1.3 and R1.4. Laboratory studies (e.g. Benhke et al., 1997; Roberts et al., 2009; Bertram and Thornton, 2009) have shown that the ClNO₂ yield is solely dependent on the relative amount of chloride and water content, and can be expressed as the following equation.

$$\phi = \frac{1}{\frac{k_{2.6}[\text{H}_2\text{O}]}{k_{2.8}[\text{Cl}^-]} + 1} \quad (2.4)$$

The rate coefficients of $k_{2.6}$ and $k_{2.8}$ are the reactions of NO₂⁺ with H₂O (see R2.6) and Cl⁻ (see R2.8), respectively. Roberts et al. (2009) reported that the coefficient rate of $k_{2.8}$ is about 450 times faster than $k_{2.6}$ and suggested that even at a small amount of Cl⁻, the N₂O₅ uptake is more favor to undergo reaction R2.8. Figure 2.2 illustrates the yield of ClNO₂ from N₂O₅ heterogeneous uptake as a function of substrate chloride concentration determined by several laboratory studies, which generally agreed with each other (Roberts et al., 2009 and references therein). It can be seen that small amount of Cl⁻, for example at 0.05 molar (M), the yield of ClNO₂ is about 1/3 and reaches almost unity when the chloride concentration is larger than 1 M. However, presence of other bulk chemical composition in the aerosol can reduce the N₂O₅ conversion efficiency to ClNO₂. Species like bromide (Schweitzer et al., 1998) and organic molecules such as phenol and humic acid (Ryder et al., 2015) can efficiently compete with the Cl⁻ to react with NO₂⁺ in R2.8. A laboratory study also suggest that aerosol with high acidity (low pH<2) can lead to a direct conversion of N₂O₅ to Cl₂ instead of producing ClNO₂ (Roberts et al., 2008).

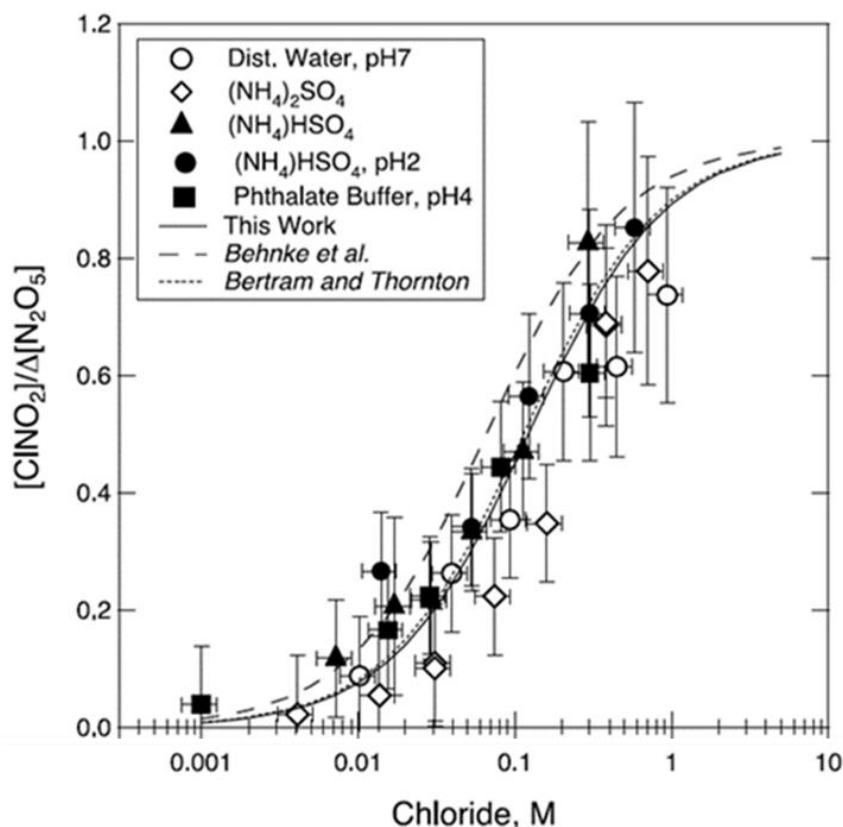


Figure 2.2. Plots of the efficiency of conversion of N_2O_5 to $ClNO_2$ versus the substrate chloride concentration obtained from different studies (Roberts et al., 2009 and references therein).

Field studies indicate that the yields of $ClNO_2$ from the N_2O_5 heterogeneous reactions are varying between environment, ranging from 0.07 to 0.98 (Mielke et al., 2011; Osthoff et al., 2008; Riedel et al., 2013; Thornton et al., 2010; Wagner et al., 2013). For instance, Osthoff et al., (2008), reported ϕ of 0.1–0.65 in the polluted marine boundary layer of Texas while Thornton et al. (2010) predicted smaller ϕ of 0.07–0.36 in a continental setting of Boulder, but both studies suggest the needs of a gas phase chloride reservoir (i.e. HCl) to justify chlorine mass balance for these observations. Enhanced $ClNO_2$ yields of 0.72–0.98 were also observed in the coal-fired power plant plumes relative to the ϕ of 0.26–0.45 in diffused urban plumes in Colorado (Riedel et al., 2013).

2.2 Sink processes of ClNO₂

The major removal pathway of ClNO₂ in the troposphere is through photolysis. At sunrise, the ClNO₂ undergoes photolysis at wavelengths greater than 290 nm in the UV/vis region (Ghosh et al., 2011). The photodissociation of ClNO₂ can have several possible dissociation channels, but the dissociation into a Cl atom and NO₂ (R2.9) was shown to be the dominant photodissociation pathway of ClNO₂ at 350 and 308 nm (Plenge et al., 2001).



The lifetime of ClNO₂ due to photolysis in the morning (a few hours after sunrise) is about 2-3 hours, while the photolysis frequency can be $>3.0 \times 10^{-4} \text{ s}^{-1}$ to at noon, decreasing the ClNO₂ lifetime to less than 50 minutes (e.g. Phillips et al., 2012; Riedel et al., 2014; Bannan et al., 2015a).

ClNO₂ is typically unreactive in the night-time despite it may involve in several sink processes. The reaction of ClNO₂ with gas-phase species like NO and OH was shown to be sufficiently slow or unimportant in the ambient condition (e.g. Wilkins et al., 1974; Ganske et al., 1991). Heterogeneous uptake of ClNO₂ also occurs at a very slow rate. Behnke et al. (1997) reported the uptake of ClNO₂ on neutral pure water or sea-salt (NaCl) with uptake coefficients of $\gamma = 0.3 \times 10^{-6}$ to 5×10^{-6} , but was determined to have much faster uptake ($\gamma = 6 \times 10^{-3}$ to 2×10^{-3}) on acidic (pH<2) chloride containing aerosols (Robert et al., 2008). These slow ClNO₂ losses lead to the accumulation of ClNO₂ at sunset and the nocturnal lifetime of ClNO₂ could be >8 h.

2.3 Field observations of ClNO₂

Despite the importance of ClNO₂, the distribution of ClNO₂ in the troposphere is unclear. There were no direct field measurements of ClNO₂ available a decade ago. The reported production of ClNO₂ was modelled from the measured N₂O₅ concentrations and its reactivity in some earlier field measurements. For instance, Aldener et al. (2006) calculated the ClNO₂ from the measured N₂O₅ with the assumption that N₂O₅ would exclusively undergo hydrolysis on submicron aerosol, but would uptake onto the supermicron aerosol (presumed to be sea-salt) to produce ClNO₂ with unity yield. They showed at most 50 pptv of total ClNO₂ can be produced overnight along the United States east coast. Another field measurement in 2005 predicted the ClNO₂ production based on their observed N₂O₅, NO₂, and O₃, and found ClNO₂ of 0.061 - 1.6 ppbv were produced over the night at the MBL of Canada (McLaren et al., 2010).

The first direct ambient measurement of ClNO₂ was only available in 2006 along the coast of Houston, Texas (Osthoff et al., 2008). After that, a number of studies have been conducted in other places. Figure 2.3 summarizes the field measurements of ClNO₂ around the world. It is clear that majority of the ClNO₂ field studies were conducted in North America (U.S and Canada), while a few campaigns were in Europe and near Arctic regime. These limited field studies, nevertheless, provided useful information on the distributions of ClNO₂ with mixing ratios which varied in the range of tenths of pptv to ppbv under different environment. The following sections review these field observations of ClNO₂.

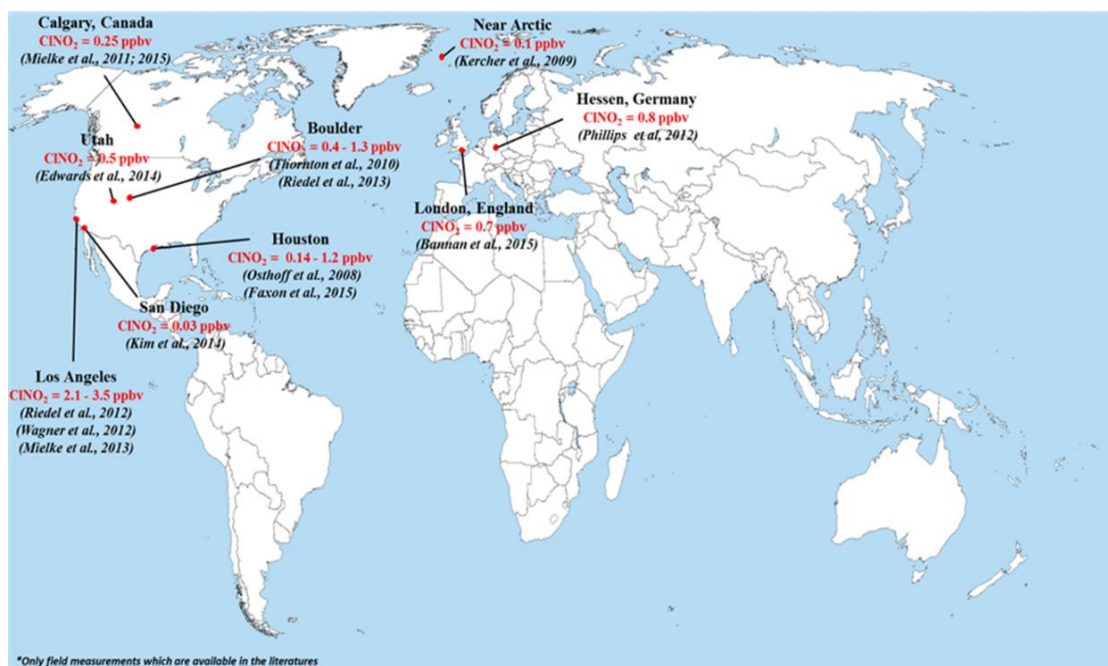


Figure 2.3. The observations of CINO₂ available around the world. The mixing ratios here (in red color wording) are the maximum level of CINO₂ of that campaign.

2.3.1 Marine coastal environment

Chloride aerosol is abundant in the coastal environment since it can be derived from the acid displacement of sea-spray (Graedel and Keene, 1996; Keene et al., 1999). As a result, efficient production of CINO₂ was frequently found in the polluted coastal regions, where NO_x is abundant as well. The landmark field measurement of CINO₂ by Osthoff et al. (2008) was conducted on board of a research vessel (Ronald H. Brown) along the Gulf of Mexico, Houston. They found high levels of CINO₂ with mixing ratio > 1 ppbv in the urban outflow of Houston, confirming the efficient production of CINO₂ in the field. Through the estimated N₂O₅ heterogeneous loss rate and good correlation with CINO₂ concentrations, they concluded that N₂O₅ is the source of CINO₂ and suggested that substantial fraction of the heterogeneous reaction would take place on submicron Cl⁻ containing aerosol, which could be continuously replenished by the gas-phase chloride (HCl) from acid displacement of sea spray.

Therefore, the strong emissions of NO_x from urban/ships sources on the coast and of chloride aerosol from the sea sprays were presumed as the causes of the high ClNO_2 production in Houston.

ClNO_2 was later measured during the California Research at the Nexus of Air Quality and Climate Change (CalNex) 2010 summertime campaign on the ship, ground-site, and airplane covering the Los Angeles basin (Ryerson et al., 2013). Reidel et al. (2012) observed ClNO_2 mixing ratios up to 2.15 ppbv in the Los Angeles urban out-flow plume when sampling near the Santa Monica Bay on board of a research vessel. Wagner and co-workers estimated the amount of ClNO_2 being produced over the water of Santa Monica Bay with a box model and found that the ClNO_2 production with a unity yield (100%) cannot reproduce the observed mixing ratio of ClNO_2 (Wagner et al., 2012). Their results indicated that the ClNO_2 production took place over the land of Los Angeles and then transported to Santa Monica Bay (the sampling points of the ship) by the night-time land breeze, rather than being produced over the water of Los Angeles. The ground-based measurement at Pasadena, about 35 km from the coastal of Los Angeles, observed high ClNO_2 mixing ratios during the nights with a maximum of 3.6 ppbv (Mielke et al., 2013).

Another field measurement of ClNO_2 was conducted at an urban background site in London during the ClearfLo (Clean Air for London) campaign in the summer of 2012. A maximum concentration of 724 pptv of ClNO_2 was detected in the marine influenced air masses (Bannan et al., 2015a). The higher ClNO_2 to N_2O_5 production ratios during periods when Na and Cl concentrations are high indicated that the major source of chloride for the production of ClNO_2 in London is from the marine origin.

They employed a box-model to show that the different concentrations of Cl^- containing aerosol could change the ClNO_2 to N_2O_5 production ratios in the study.

Kim et al., (2014) assessed the role of the ocean surface on N_2O_5 deposition and ClNO_2 production during the field measurement at La Jolla, San Diego in late winter of 2013. They measured the vertical fluxes and observed small concentrations of ClNO_2 up to 30 pptv and N_2O_5 (up to 50 pptv) in the marine air masses with influence from Los Angeles emissions. The study showed the N_2O_5 are efficiently deposited into the ocean during the night. Surprisingly, no ClNO_2 was produced via the N_2O_5 deposition as the observation of the vertical fluxes of ClNO_2 also display net deposition, instead of emission from the ocean. This result led to a conclusion that the ClNO_2 mixing ratios observed in the marine boundary layer are primarily caused by the reactions of chloride containing aerosol with N_2O_5 .

2.3.2 Inland environment

A major breakthrough result of ClNO_2 is that Thornton et al. (2010) surprisingly found ClNO_2 mixing ratios of up to 0.45 ppbv in urban plumes of Boulder, Colorado, which is 1400 km away from the nearest coastal area. The study implied the existence of non-oceanic chloride sources from coal-fired power plants, industries, biomass burning, and soil-dust for which supports the widespread production of ClNO_2 in the inland regions. The presence of significant ClNO_2 within the urban plume in mid-continental setting was confirmed in a short field study at Calgary, Canada (Mielke et al., 2011). ClNO_2 was observed in the three nights, with maxima value ranging between 80 and 250 pptv. The chloride that involves in the ClNO_2

production was inferred to be from the anthropogenic activities within the city of Calgary such as the suspension of road dust (e.g. road salt used during wintertime).

In keeping with the works of ClNO₂ production in inland environment, Phillips et al., (2012) conducted a ClNO₂ and N₂O₅ measurement at a mountain site (825 m above sea level, (a.s.l.)) in Hessen, southwestern Germany, which is located at ~400 km from the nearest coastline. At this inland site, significant concentrations of ClNO₂ were always observed in the air masses originated from UK marine regions, with the largest mixing ratio of 800 pptv. Their measurements also showed high levels of N₂O₅ with little or no ClNO₂ when sampling continental air masses. Therefore, they suggested that the ClNO₂ production at this site was attributed to the Cl⁻ which originated from long-range transport of marine aerosol rather than from anthropogenic sources.

More recent field campaigns have observed variations of ClNO₂ mixing ratios in other polluted inland regions. For example, the Nitrogen, Aerosol Composition, and Halogens on a Tall Tower (NACHTT) 2011 winter campaign measured ClNO₂ mixing ratios ranging from tenths of pptv to 1.3 ppbv at Boulder, Colorado (Brown et al., 2013; Riedel et al., 2013). Faxon et al., (2015) reported ClNO₂ mixing ratios of up to 150 pptv at an inland site of Houston. Measurement at a remote location within the oil and gas basin of northeastern Utah during the Uintah Basin Winter Ozone Studies (UBWOS) observed ClNO₂ exceeding 200 pptv (Edward et al., 2014).

2.3.3 Vertical distributions of ClNO₂

Most of the ClNO₂ field studies were made at the ground level, with only two field measurements of ClNO₂ were conducted in the planetary boundary layer (PBL). In the CalNex 2010 summer campaign, ClNO₂ vertical profiles were measured on a research aircraft (NOAA P-3) within the Los Angeles basin (Young et al., 2012). Average of the 21 vertical profiles showed no significant dependence on height where concentrations of ClNO₂ were relatively constant within the nocturnal boundary layer (NBL) and residual layer (RL) (see Figure 2.4a). They suggested that such results underscore the importance of heterogeneous reaction of N₂O₅ on chloride aerosol as the key source of ClNO₂ in the PBL of Los Angeles.

The NACHTT 2011 winter campaign at an inland site of Boulder provided another ClNO₂ vertical measurement on a 300 m height tower (Brown et al., 2013; Riedel et al., 2013). They found that the ClNO₂ vertical distributions were variable, with some cases in which ClNO₂ enhanced at <50 m in depth while the majority of cases showed enhanced-ClNO₂ from tens of meters above ground level to the highest point of the tower, which appeared to be influenced by different type of air masses in the region. They focused on two examples of vertical profiles: one from a diffuse urban plume and the other from a local coal-fired power plant plume. As shown in Figure 2.4b, the ClNO₂ mixing ratios in the diffuse urban plume reached maximum at 60 m of height (up to 600 pptv) and then remained relatively constant up to 200 m above the ground. The ClNO₂ enhancements were narrower in the plume of coal-fired power plant, confining to heights between 80 and 120 m (Figure 2.4c). A maximum ClNO₂ mixing ratio of 1300 pptv was observed in this plume. This observation raised the

possibility that coal combustion contribute to the widespread of ClNO_2 production in polluted region of Boulder.

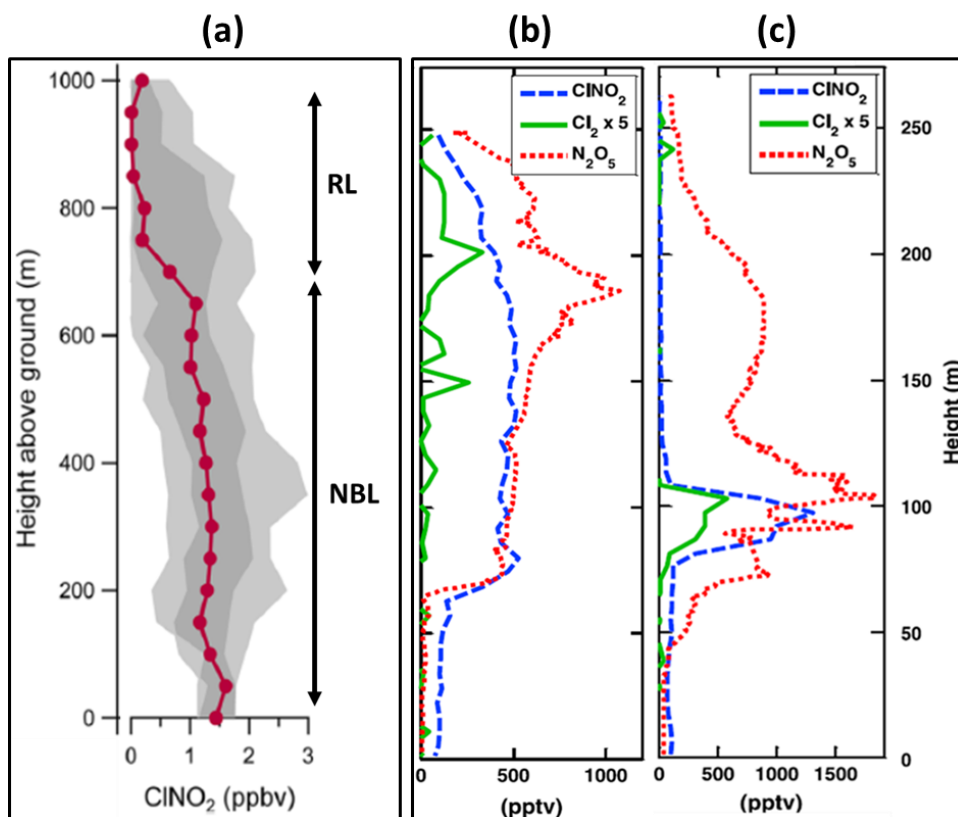


Figure 2.4. a) Vertical distributions of ClNO_2 in the nocturnal PBL for average of 21 profiles from flight measurements within Los Angeles basin (Young et al., 2010). Vertical profiles of ClNO_2 in b) urban diffused plume and c) coal-fired power plant plume measured on a tower in Boulder (Riedel et al., 2013).

2.3.4 Daytime ClNO_2 and N_2O_5

According to their chemistry, ClNO_2 and its precursor, N_2O_5 , occur primarily during the night-time due to the fast photolysis of $\text{NO}_3/\text{N}_2\text{O}_5$ and ClNO_2 , but they can present at non-zero levels during the daytime. A few previous studies have reported the presence of daytime NO_3 and N_2O_5 peak of several pptv at surface sites (Geyer et al., 2003), coast (Osthoff et al., 2006) as well as from aircraft measurements (Brown

et al., 2005) in the US. These studies indicated that the presence of daytime NO_3 and N_2O_5 could increase the daytime heterogeneous production rate of HNO_3 and/or initiate the oxidation of biogenic VOCs.

As for the ClNO_2 , it is unusual to measure at daytime but under certain conditions like during the time when the sun-light intensity is relatively low, small ClNO_2 concentrations may persist during the daytime. For instance, during heavy cloud and aerosol cover or fog, a median ClNO_2 mixing ratios of 100 pptv was observed at Pasadena even 4 hours after sunrise (Mielke et al., 2013). Recently, measurements at surface sites at London and Texas found an increase of ClNO_2 soon after sunrise on several occasions with concentration of 40-150 pptv. They suggested that this could be due to transport of ClNO_2 from region with higher ClNO_2 concentrations (Bannan et al., 2015a; Faxon et al., 2015).

2.4 Potential impacts of ClNO_2 in the troposphere

Daytime photolysis of ClNO_2 is a source of Cl radical and NO_x (see R2.9). Hence, the efficient ClNO_2 production in polluted regions has potential impact on the radical chemistry, VOCs oxidative capacity and O_3 production, and the NO_x nocturnal lifetime.

2.4.1 Impacts on radical chemistry

Figure 2.5 depicts the role of ClNO_2 in tropospheric radical chemistry. Hydroxyl radical is long known as the ‘conventional’ radical in the troposphere. It

plays a critical role in the removal of trace gasses through the RO_x ($OH+HO_2+RO_2$) cycle, leading to the formation of O_3 and secondary aerosols (e.g. Rohrer et al., 2014). Sources of OH in the troposphere include the photolysis of O_3 and $HONO$, reaction of VOCs with O_3 , and recycling processes involving the odd hydrogen radicals ($HO_x = OH + HO_2$), oxygenated-VOCs and NO_x .

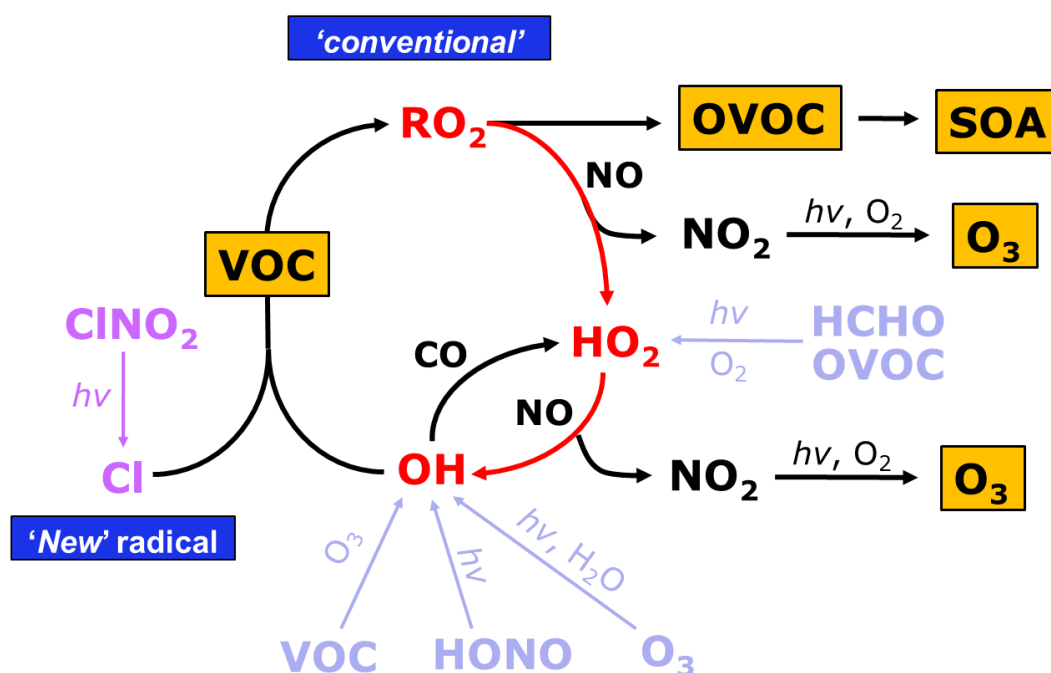


Figure 2.5. Schematic diagram of radical chemistry, illustrating the key chemical pathways in the troposphere. The radical chemistry is initiated by primary radical production from the ‘conventional’ sources (in light blue) and ‘new’ radical source of Cl atom (in purple). Radical chain reactions cause cycling between OH , HO_2 , and RO_2 , leading to the formation of O_3 and SOA .

The $ClNO_2$ could be a ‘new’ source of radical in the polluted regions of the troposphere. Photolysis of $ClNO_2$ was shown to produce reactive chlorine atom rapidly, with the maximum production rate in the range of 2.0×10^5 to 3.4×10^6 molecule $cm^{-3} s^{-1}$ (Osthoff et al., 2008; Riedel et al., 2012; Young et al., 2012; Phillips et al., 2012; Riedel et al., 2014; Faxon et al., 2015; Mielke et al., 2015). Riedel et al., (2012) showed that $ClNO_2$ was the predominant source of Cl atom as the production

of Cl atom via photolysis of ClNO₂ in the morning was faster than the reaction through HCl + OH by a factor of 5 in Los Angeles. They later determined that photolysis of ClNO₂ could contribute up to 56% of daily Cl atom production (Riedel et al., 2014).

Although OH is generally the dominant oxidant in the atmosphere, Phillips et al. (2012) reported that the Cl atom production rate exceeded the production of hydroxyl radical via photolysis of O₃ by up to a factor of 10 for several hours after sunrise. Likewise, integrating the morning time production of radicals within the boundary and residual layers in Los Angeles revealed that the production of Cl atom via ClNO₂ surpassed the production rate of OH through HONO by nine times (Young et al., 2012). Mielke et al. (2015) also reported that the production rate of Cl atom via ClNO₂ is more important during the morning hours of the winter season in Canada. Hence, photolysis of ClNO₂ is a crucial radical source in the atmosphere, and it could contribute up to 9-13% of the total daily primary radical production (Edwards et al., 2013, Young et al., 2014).

The impacts of Cl atom could be further enhanced by its efficient recycling process during the daytime. Self-reaction of Cl atom and reaction of Cl atom with OH produce Cl₂ and HOCl, respectively (R2.10 and 2.11). The Cl₂ and HOCl can undergo photolysis or heterogeneous reaction to regenerate Cl atoms (Simpson et al., 2015).



The dominant reaction of Cl atom during the mid-day is with O₃ (Riedel et al., 2014), forming a ClO (R2.12). Subsequent reactions of ClO with NO and HO₂ (R2.13-2.14) can produce Cl atom directly or via heterogeneous reaction of HOCl.



In a VOCs rich environment, the Cl atom can attack the VOCs, leading to the formation of HCl (R2.15) which later reacts with OH to give a Cl atom back to the atmosphere.



Young et al., (2014) showed that the recycling of Cl atom, especially via R2.12, was more efficient in initiating the radical propagation chains compared to OH since ~70% of the primary OH lost to a chain termination reaction with NO₂ (but not for the case of Cl atom).

There is also an important interplay between the reactive chlorine atom and HO_x as the reaction of Cl atom with VOCs can produce RO₂ and recycled HO_x by reacting with NO. Constraining ClNO₂ into a chemical box model increased the OH by 1.9 times and up to 2.2 times for HO₂ and RO₂ in Los Angeles (Riedel et al., 2014). Bannan et al., (2015b) demonstrated that the ClNO₂ resulted in a maximum of 9% increase of RO_x during the morning in the UK. On a global scale, the ClNO₂ chemistry could increase the averaged OH concentration over the entire Northern Hemisphere by 3.5% and 0.3% during winter and summer, respectively (Sarwar et al., 2014).

2.4.2 Impacts on VOCs oxidation and ozone production

Cl atom is highly reactive towards many classes of VOCs and has reaction rate constant of one to two orders of magnitude faster than the OH-driven reactions

(Atkinson et al., 1999). Chemical box model analysis showed the reactivity of Cl atom with VOCs was dominated by alkane which is relatively unreactive with OH (Riedel et al., 2014; Young et al., 2014). About 25% of the daily alkane oxidations in Los Angeles basin was found to be caused by the Cl atom via photolysis of ClNO₂ (Riedel et al., 2012). Bannan and colleagues later estimated the impacts of ClNO₂ on the oxidation rates of alkane, alkene, and alkyne in London and showed that on average, 4% of alkane, 1% of alkene and 8% of alkyne removal were driven by reactions with Cl atom. In their highest ClNO₂ case, the removal of alkane, alkene and alkyne by Cl atom reached 15%, 3% and 26%, respectively (Bannan et al., 2015a).

Subsequent reaction of Cl atom and VOC produces RO₂, leading to the formation of ozone via a similar gas-phase mechanism as that for OH (see Figure 2.5). Chemical box models and chemical transport models studies indicated that the ClNO₂ chemistry initiated notable enhancement of ozone. Osthoff et al. (2008) constrained 0.65 and 1.5 ppbv of ClNO₂ into a box model and reported additional 6 to 9 ppbv of ozone production in the polluted air from Houston. Later, an emission-driven chemical transport model demonstrated only a modest increases in ozone concentrations up to 1.0 - 1.5 ppbv in Texas (Simon et al., 2009). However, more recent model studies revealed slightly larger impact of ClNO₂ on the O₃ photochemistry. Sarwar and co-workers examined the air quality impacts due to ClNO₂ across the Northern Hemisphere. Up to 2 ppbv increase on 8 hour ozone was found on the U.S. east coast (Sarwar et al., 2012) and up to 7 ppbv of daily 8-hour average ozone increment was predicted in polluted inland of China and Western Europe (Sarwar et al., 2014). Another box model study with inclusion of 1.5 ppbv of ClNO₂ as the input indicated

an increase of ~12 ppbv of ozone production in Los Angeles if neglecting the contribution of HONO (Riedel et al., 2014).

2.4.3 Impacts on NO_x loss

Another impact of the ClNO₂ is the effect on the NO_x lifetime. Traditionally, the night-time loss of NO_x was assumed only to proceed via N₂O₅ hydrolysis, forming two moieties of HNO₃ (Morris and Niki 1973) which can permanently lose through depositions. Later, heterogeneous uptake of N₂O₅ onto chloride containing aerosol was shown to produce ClNO₂ (Finlayson-Pitts et al., 1989) and also recycled an NO_x into the ambient air at sunrise. This process revealed that non-negligible fractions of NO_x could recycle through ClNO₂ as the night ends. Thornton et al. (2010) demonstrated that 8–22% of the emitted NO_x in the US was recycled through ClNO₂ production. The effects of ClNO₂ on NO_x lifetime was also reported during the CalNex study, where the total nocturnal NO₂ loss rates decreased by 0.13 ppbv h⁻¹ on the night with high ClNO₂ production (Tsai et al., 2014). The inclusion of ClNO₂ chemistry in a global model decreased the total nitrates up to 25% during the winter and 7% during the summer (Sarwar et al., 2014). However, a recent study in the marine boundary layer of California reported a different result of the impact of ClNO₂. Kim and co-workers found that the air-sea exchange processes could serve to decrease ClNO₂ by over 20% at sunrise. Thus, it limited the NO_x recycling rates and caused up to 15% of the nocturnal NO_x removal.

2.5 Measurement techniques for ClNO₂

Measurement of trace gasses like ClNO₂ and its precursors (N₂O₅) has always been challenging, due to their trace concentrations in the atmosphere (e.g. Kercher et al., 2009; Aufmhoff et al., 2012). Therefore, specific techniques with fast response, good selectivity and sensitivity, and high precision are required. Several techniques have been reported to have the capability to measure real-time N₂O₅ and ClNO₂. Table 2.2 summarizes the currently available techniques for N₂O₅ and ClNO₂ measurement. Some techniques have been applied to measure N₂O₅ directly in the ambient air, namely the Broadband Cavity-Enhanced Absorption Spectroscopy (BB-CEAS), Laser-Induced Fluorescence (LIF), Differential Optical Absorption Spectroscopy (DOAS), Cavity Ring-Down Spectroscopy (CRDS), and Chemical Ionization Mass Spectrometry (CIMS). With the recent improvement on the instrumentation, ClNO₂ can be measured by both CIMS and CRDS techniques. The reader is directed to the review papers by Chang et al. (2010) and Brown and Stutz (2012) for the in-depth descriptions of these N₂O₅ measurement approaches. The following sections only focus on the techniques for ClNO₂ measurement.

Table 2.2. Currently available measurement techniques for ambient N₂O₅ and ClNO₂ in the literature.

Target species	Techniques	<i>e.g.</i> References
N ₂ O ₅	Broadband Cavity-Enhanced Absorption Spectroscopy	Langridge et al., 2008 Kennedy et al., 2011
	Laser-Induced Fluorescence	Wood et al., 2003 Matsumoto et al., 2005
	Differential Optical Absorption Spectroscopy	Stutz et al., 2004 Platt et al., 2009

	Cavity Ring-Down Spectroscopy	Dube et al., 2006 Wagner et al., 2011
	Chemical Ionization Mass Spectrometry	Slusher et al., 2004 Kercher et al., 2009
ClNO ₂	Cavity Ring-Down Spectroscopy	Thaler et al., 2011
	Chemical Ionization Mass Spectrometry	Kercher et al., 2009 Mielke et al., 2011

2.5.1 Chemical ionization mass spectrometry technique

Chemical ionization mass spectrometry is a state-of-the-art technique that combines ion–molecule chemistry and mass spectrometry detection. The principle of this technique is based on soft ionization by using a reagent ion to selectively ionize the target compounds in the matrix of ambient air, forming an ion-molecule which is later guided into a vacuum chamber for detection by a mass spectrometer. Its major advantage is high sensitivity and selectivity, since the soft ionization produces relatively little fragmentation, while the selected choice of reagent ion determines the specific compounds being detected. This method has been shown to be capable of measuring several other atmospheric trace species in the field, for examples, HNO₃, pernitric acid (HO₂NO₂), peroxyacyl nitrates (PANs) and N₂O₅ (Huey, 2007).

2.5.1.1 Iodide CIMS for ClNO₂ measurement

One of the commonly used reagent ions for CIMS measurements is the iodide (I⁻). It was found to react fast and selectively with N₂O₅ and halogen species (e.g. Huey et al., 1995). The iodide-based CIMS method with heated-inlet has been demonstrated in a field study by Osthoff and co-workers for the first ClNO₂ measurement (Osthoff

et al. 2008), followed by the later field studies in Canada and Los Angeles (Mielke et al., 2011 and 2013). Their heated-inlet (TD-CIMS) instruments setup is an identical apparatus that has also been previously reported to detect the PANs and N₂O₅ (e.g. Slusher et al., 2004). Figure 2.6 displays an example of the schematic of the TD-CIMS instrument used in Mielke et al., (2011) study. The sampling inlet was heated at 150-190°C which was suggested to be too low for dissociating the ambient ClNO₂. The iodide ions were generated by passing a mixture of methyl iodide (CH₃I) in N₂ through a ²¹⁰Po radioactive source. The soft ionization process took place in the reaction chamber (flow tube) maintained at ~20 Torr. The reaction of iodide ions with ClNO₂ can dissociate into I(Cl⁻) or form cluster of I(ClNO₂)⁻ (R2.16-2.17). Since the former may subject to potential interferences from other chlorine species, they have chosen the latter ion cluster, which has less possibility of interference, for the ClNO₂ measurements.



Their CIMS instruments also equipped with a collisional dissociation chamber (CDC) and octopole ion guide which consists of an electric field to break up weakly bound clusters (e.g. water molecules in the hydrated clusters) to obtain more simple and clean mass spectra. This setup showed low detection limits of 5 pptv (25s data) for ClNO₂ (Mielke et al., 2011).

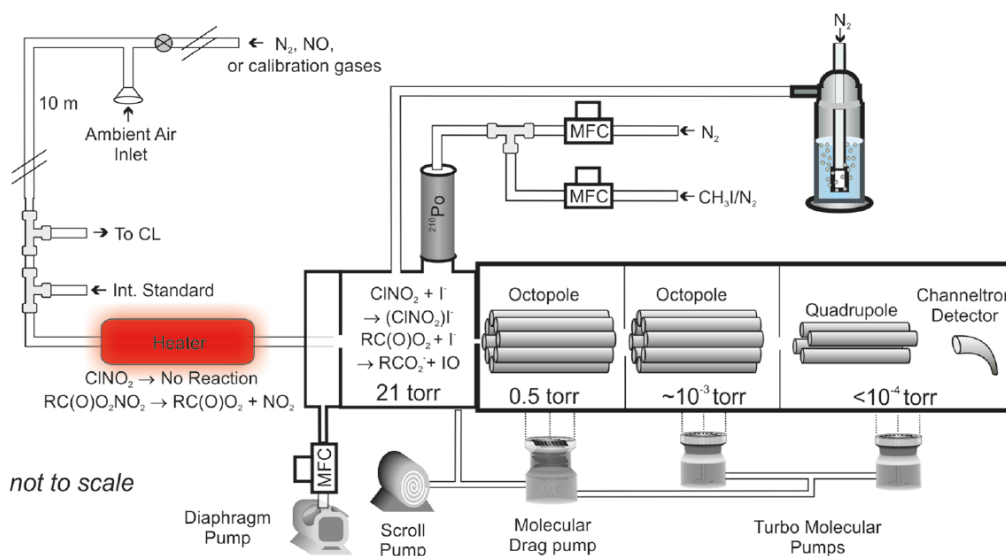


Figure 2.6. An example of the schematic design of an iodide TD-CIMS instrument used by University of Calgary for CINO₂ measurement (figure adapted from Mielke et al., 2011).

In the work of Kercher et al. (2009), they modified their CIMS by removing the heater in the inlet, aiming to detect iodide-containing clusters of N₂O₅ and CINO₂, which have less possible interferences. Formation of these ion clusters is optimized in the unheated CIMS by tuning the flow-tube pressures to about 60 Torr and adjusting the CDC voltages to create an electric field <70 V/cm. They also correlated the raw signal of I(³⁵CINO₂)⁻ and its isotope I(³⁷CINO₂)⁻ signal and found slope similar to the theoretical isotopic value, 0.3199, suggesting the absence of interference in the CINO₂ signal. This instrument was deployed on a research vessel during the International Chemistry in the Arctic Lower Troposphere (ICEALOT) campaign for CINO₂ measurement and demonstrated a detection limit of 3 ± 2 pptv (1 min average). Similar applications of unheated iodide CIMS method have been reported in both field (e.g. Betram et al., 2009; Thornton et al., 2010) and laboratory studies (e.g. Betram and Thornton et al., 2009; Gaston et al., 2014).

2.5.1.2 Disadvantages of iodide CIMS for ClNO₂ measurement

A major drawback of the iodide CIMS technique for ClNO₂ measurement is that the ClNO₂ detection is water dependable. During the chemical ionization process, iodide ions could form hydrated-clusters with one or more H₂O molecules. This I(H₂O)⁻ cluster likely becomes an important additional reagent ion for the formation of both ClNO₂ and N₂O₅ ion clusters (Kercher et al., 2009). They also showed that the signals at both the I(ClNO₂)⁻ and I(N₂O₅)⁻ increase promptly with water vapor up to ~0.3 torr of water vapor pressure in the flow tube and become constant after that concentration. Mielke et al., (2011) reported similar responses of I(ClNO₂)⁻ with water vapor in their CIMS setup and found a 27% lower in the response factor if the CIMS was calibrated with dry zero gasses. In other word, measurements of ClNO₂ (and/or N₂O₅) with iodide CIMS technique in regions with high or low ambient humidity would be challenging.

Another disadvantage of the CIMS technique application is the needs of external calibration of the ClNO₂ (and N₂O₅) from time to time. There is no commercial calibration source of ClNO₂ (and N₂O₅) available in the market. Therefore, generation of a well-quantified ClNO₂ standard which is suitable for field measurement is a major challenge. The production of ClNO₂ standard gas from its condensed phase (commonly used in laboratory studies, e.g. Hoffman et al., 2003) is inconvenient to be applied during the field since it needs to be cooled at dry ice temperature. This ClNO₂ source is also hygroscopic and readily hydrolyzes, making the quantification of the concentration difficult. A more direct method to synthesis ClNO₂ gas standard for field calibration is by passing N₂O₅ over a bed of wet sodium

(NaCl) (e.g. Kercher et al. 2009). This method, however, requires the accurate measurement of N_2O_5 concentrations. An alternative approach for generating ClNO_2 is by passing Cl_2 over an aqueous slurries mixture of NaCl and sodium nitrite (NaNO_2) but was found to produce impurities gasses like NO_2 and HONO (Thaler et al., 2011, Mielke et al., 2013).

2.5.2 Cavity ring-down spectroscopy technique

Cavity ring-down spectroscopy (CRDS) is a direct absorption technique which is based on the quantification of the time constant for single exponential decay of light intensity from an optical cavity (O'Keefe and Deacon, 1988). This method is highly sensitive and does not require external calibration like the CIMS method. It has been widely used for measuring NO_3 and N_2O_5 in the field (e.g. Brown et al., 2001; Dubé et al., 2006, Wagner et al., 2011). More recently, Thaler and co-workers applied a thermal dissociation (TD)-CRDS to quantify ClNO_2 in the laboratory (Thaler et al. 2011). As illustrated in Figure 2.7, the TD-CRDS consists of two sample cells, where a cell was equipped with a quartz tube heated at $450\text{ }^\circ\text{C}$, aiming to dissociate ClNO_2 to NO_2 , while another cell acted as the reference cell that quantified the background NO_2 concentrations at room temperature. The instrument used a pulsed blue diode laser and the NO_2 from dissociation of ClNO_2 was detected by optical absorption at 405 nm. The difference of NO_2 concentration between the two cells was used to determine the ClNO_2 mixing ratios. Despite its capability in measuring ClNO_2 , this instrument has yet to be deployed in field campaigns since it has high detection limits of 120 pptv (3σ , 10s data) and may be potentially interfered by the NO_x -containing species (e.g. alkyl nitrates, PANs) or aerosol in the ambient atmosphere.

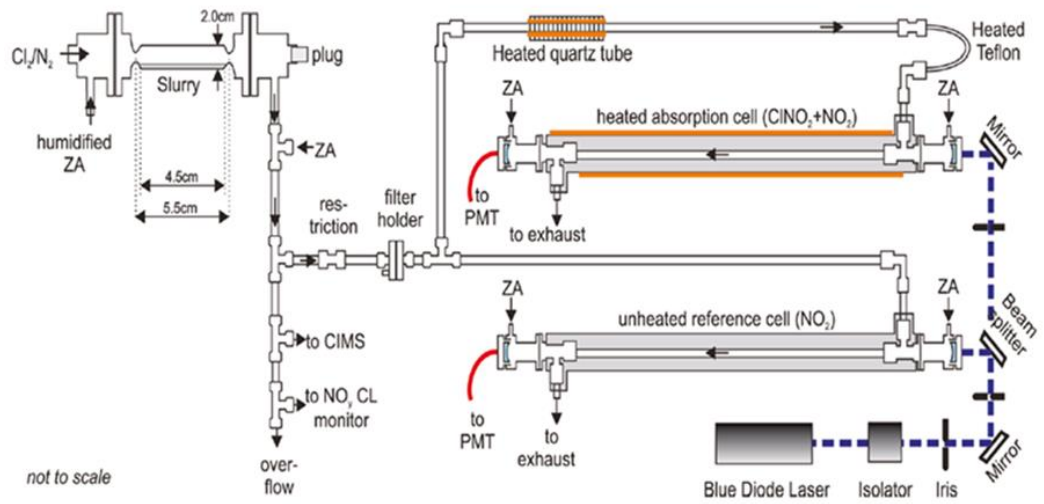


Figure 2.7. The schematic drawing of TD-CRDS applied for ClNO_2 measurement (figure adapted from Thaler et al., 2011).

Chapter 3 Methodology

3.1 Study locations

From 2011 to 2014, field measurements of CINO₂ had been carried out at Tung Chung, Hok Tsui and Tai Mo Shan in Hong Kong followed by Wangdu in northern China. Below are the detail descriptions of each sampling sites.

3.1.1 Tung Chung

Tung Chung (22.29° N, 113.94° E), a newly developed suburban residential area, is located in the northern part of Lantau Island, Hong Kong. The measurements were conducted at an air-quality monitoring station operated by the Hong Kong Environmental Protection Department (Figure 3.1a). The CIMS was placed on the roof-top of an eight-storey primary school building which is about 200 m away from the main monitoring station.

The sampling site is close to the Hong Kong International Airport (Chek Lap Kok) which is situated at ~3 km on the north. Another nearby major emission source is the Tung Chung Expressway (~80 m away). This highway usually has a high volume of vehicles as it is the major link between Lantau Island (and the airport) to other parts of Hong Kong (Xu et al., 2015). Other than the local emissions, transportation of pollutants from the urban areas of Kowloon or Hong Kong (in the east direction) and the Pearl River Delta (PRD) region (in the northwest direction) can affect the air

quality of Tung Chung (e.g. Wang et al., 2003). The Lantau Mountain (peak = 700-950 m a.s.l.) is lying on the south, and several high-rise commercial/residential buildings of ~100 m height are situated in the northeast and southwest of the site.

3.1.2 Hok Tsui

Figure 3.1b shows the location of Hok Tsui atmospheric research station at the south-eastern tip of Hong Kong Island (22.22° N, 114.25° E). The site is located on a 60 m a.s.l. high cliff, facing the South China Sea from northeast to the west (~270° view). There are no strong emission sources within the surrounding area since it is approximately 15 km away from the nearest Hong Kong's urban center. For most of the time, Hok Tsui is in the upwind of the urban cores of Hong Kong and PRD. Therefore, measurements at Hok Tsui station are expected to have background characteristics. Nevertheless, the site may occasionally impact by the ship emissions from the international shipping lane (~6 km south of the site) and pollutants transported from the continental of mainland China. The combination of these geographical and meteorological features makes Hok Tsui a suitable place to study the impact of the long-range transportation of pollutants on Hong Kong air quality. Indeed, this site has been used for the long term study of photochemical pollution in this region (e.g. Wang et al., 2009).

3.1.3 Tai Mo Shan

Tai Mo Shan (TMS; 22.41° N, 114.13° E) is the highest point of Hong Kong with a peak of 957 m a.s.l.. The measurement site is situated on the peak of the

mountain and lies within a natural reserve with restricted access to vehicles. Figure 3.1c shows that the site is located in the southeast part of the PRD region which is surrounded by the dense urban areas of Hong Kong (nearest is Tsuen Wan), Shenzhen and other cities of the Guangdong Province in the north. According to Yang et al. (2013), the average daytime mixing layer height in Hong Kong during the autumn and winter is 1.2 km and 1.0 km, respectively. Therefore, during the TMS campaign study period (November–December), the site would lie near the top of the mixing layer in the daytime and within the residual layer during the night.

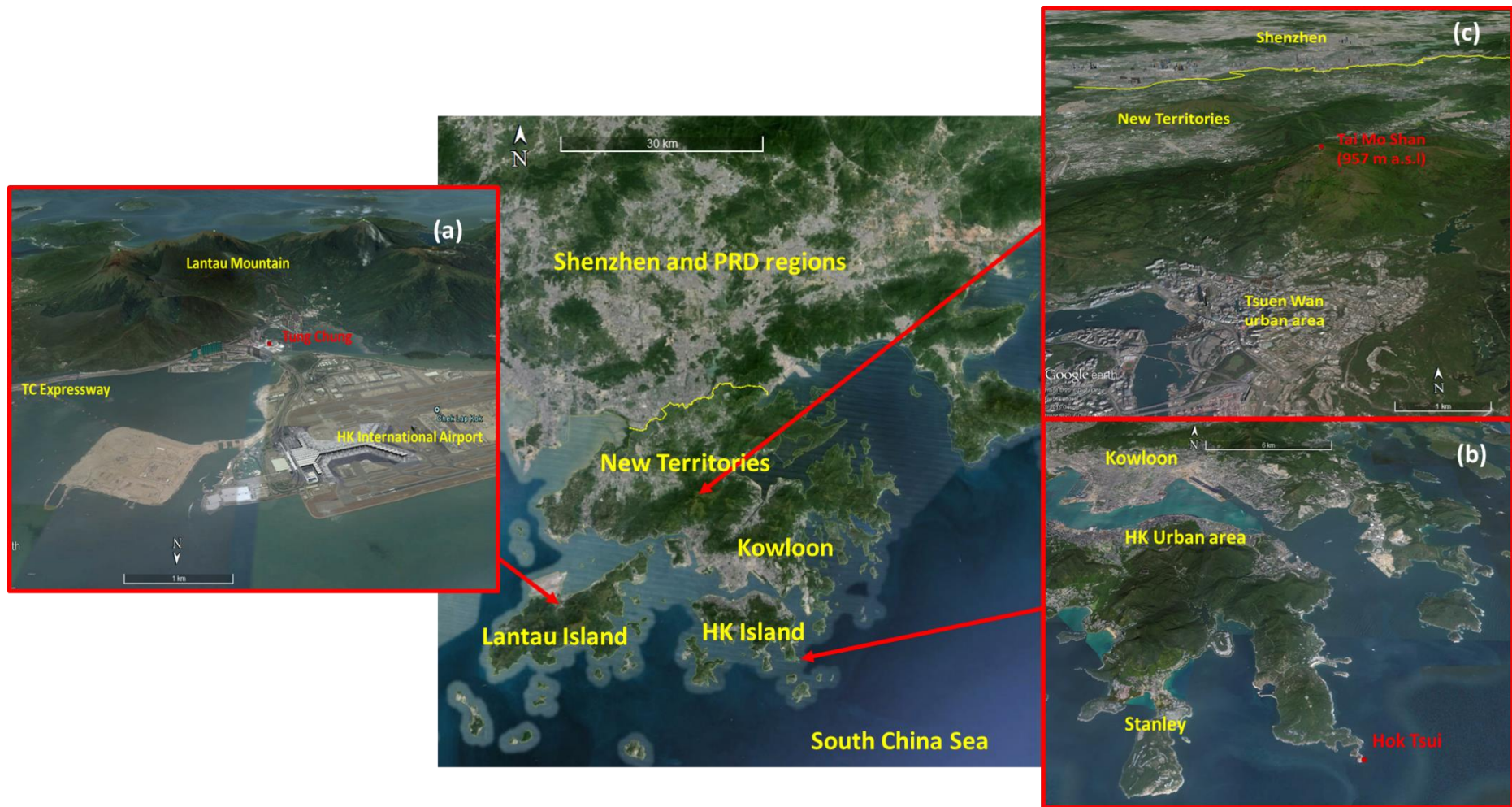


Figure 3.1. Google map shows the locations of the measurement site at a) Tung Chung, b) Hok Tsui, and c) Tai Mo Shan in relation to the surrounding of Hong Kong and Pearl River Delta of China.

3.1.4 Wangdu

The campaign in the northern China took place at a semi-rural site (38.67° N, 115.20° E) at Wangdu County of Hebei province. Wangdu is situated within the North China Plain (NCP). Figure 3.2 shows the location of the study site in relation to the topography and emission sources in the NCP.

The national capital, Beijing (pop. > 21 million) is located ~170 km in the northeast, and another megacity, Tianjin (pop. >15 million), is situated about 180 km to the east, while Shijiazhuang which is the capital and largest city of Hebei province (pop. >12 million) is 90 km in the southwest. In addition, two prefecture-level cities are located within a radius of 120 km including megacity of Baoding (pop. ~11 million), which is 33 km in the northeast, and Hengshui city (pop. ~4 million) which is 110 km in the south. There are some county-level cities in the surrounding areas which can be the additional sources of pollutants.

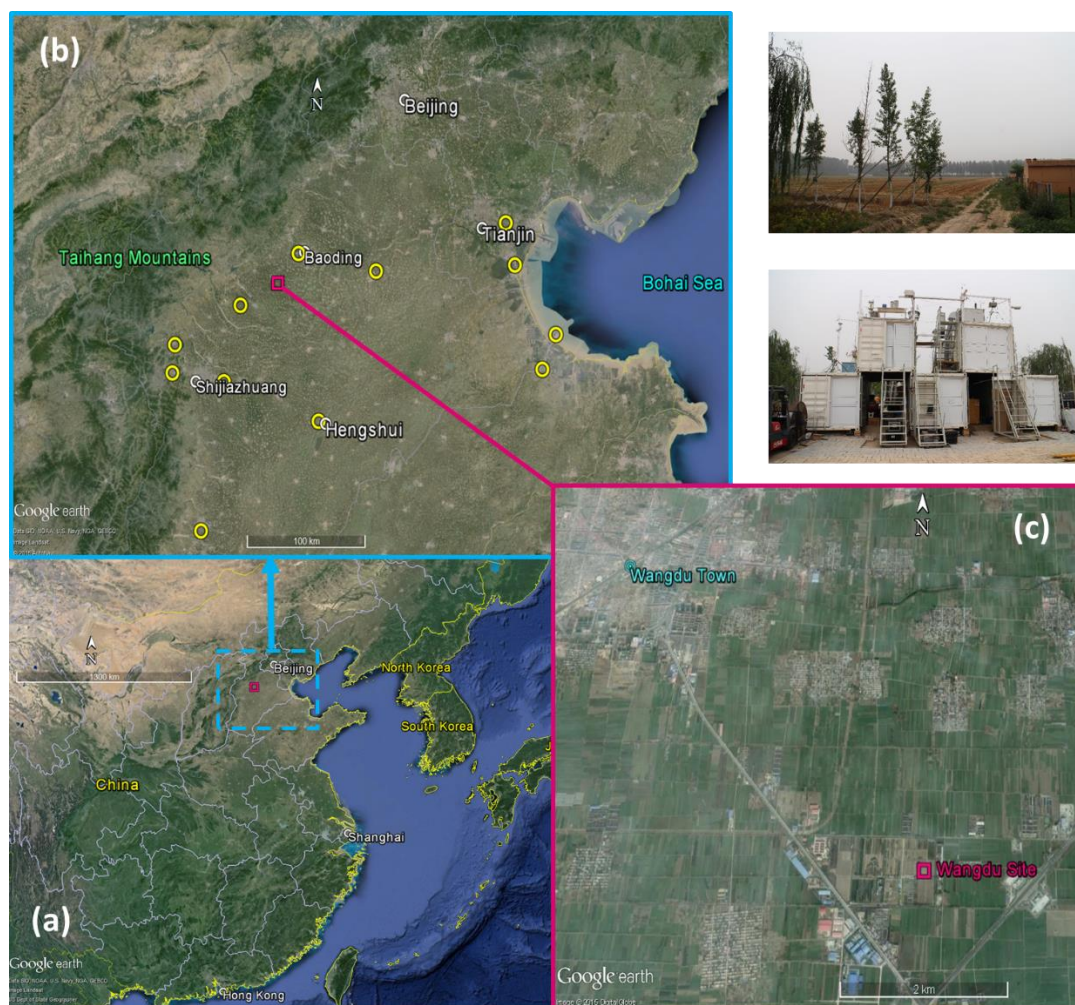


Figure 3.2. a) Location of northern China (blue dash-box) and Wangdu site (red box); b) an expanded view of NCP with the topography, major cities and the locations of major coal-fired power plants (yellow circles); c) nearby environment of Wangdu site. The photos on the right corner are the trailers at the sampling site and surrounding view of the site.

Dozens of coal-fired power stations are situated within the radius of 200 km. Among the nearest are Datang power plant (capacity 650 MW) which is 27 km away in the northeast and Dingzhou power station (capacity 2520 MW) which is 35 km away in the southwest. Emissions from the agriculture activities also have impacts on the site. The time of the study was the harvesting season of winter wheat (Sun et al., 2007) and burning activities were frequently observed in the region, as displayed by the active fire hotspots obtained from FIRMS (MODIS C5, data available at

<https://earthdata.nasa.gov/firms>) (see Figure 3.3). The less developed area of Taihang Mountains ranges (peak = 2882 m a.s.l) is located at 50-100 km in the northern to the western sector of the site. The nearest coastline of Bohai Sea is ~200 km in the eastern sector.

The immediate surrounding area (i.e. within 5 km) of the sampling site is mostly covered by agricultural lands and some villages. The closest large local emission sources include a national highway and a provincial road (~1 km away). The major town area of Wangdu County is located ~5 km to the northwest while many small villages are sporadically spread around the area (see Figure 1c).

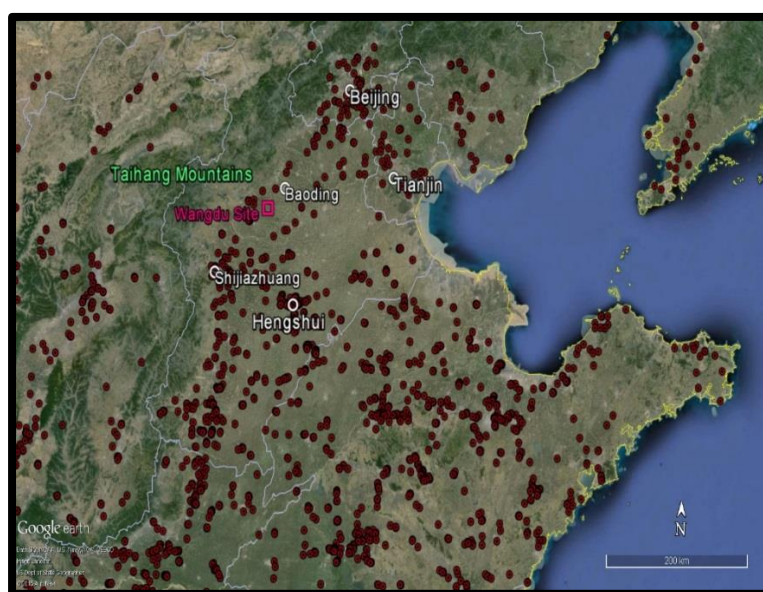


Figure 3.3. Active fire hotspots (red dots) in the region covering the study period of 20 June – 9 July 2014 (data from FIRMS, <https://earthdata.nasa.gov/firms>).

3.2 Instrumentation

3.2.1 Chemical ionization mass spectrometer

The ClNO_2 and N_2O_5 were quantified by a chemical ionization mass spectrometer (CIMS). It was acquired from THS Instrument (Atlanta, USA). The default setup is a thermal desorption (TD)-CIMS similar to Slusher et al., (2004) and it was used for measurements in both Tung Chung and Hok Tsui campaign. This setup was shown to cause substantial interferences (up to 50%) in the N_2O_5 signal measured at 62 *a.m.u.* when sampling under high NO_x condition. Due to the interferences in TD-CIMS, the instrument was modified by removing the thermal desorption (heating) inlet and operated according to the recommendations from Kercher et al., (2009). This unheated setup of CIMS was deployed for the later field measurements at Tai Mo Shan and Wangdu. Only the setup of the unheated version of CIMS is described here while the details on the TD-CIMS setup, detections, and potential interferences can be found in our previous publications (X.Wang et al., 2014; Tham et al., 2014).

Figure 3.4 shows the schematic diagram of the unheated iodide CIMS setup. The instrument consists of four separate main components include: the reaction chamber (flow-tube), collisional dissociation chamber (CDC), octopole ion guide, quadrupole mass filter, and detector. In order to maintain the system under low-pressure conditions, the chamber of octopole and quadrupole were each pumped by a turbo-molecular pump (model V81, Agilent Technologies). The CDC was directly pumped by a drag pump (Adixen MDP 5011, Alcatel Vacuum Technology Ltd.), which also serves as the backup to the two turbo-molecular pumps. The reaction

chamber was connected to a vacuum pump (Model TriScroll 300, Agilent Technologies). It backed both the drag and turbo-molecular pumps at the same time.

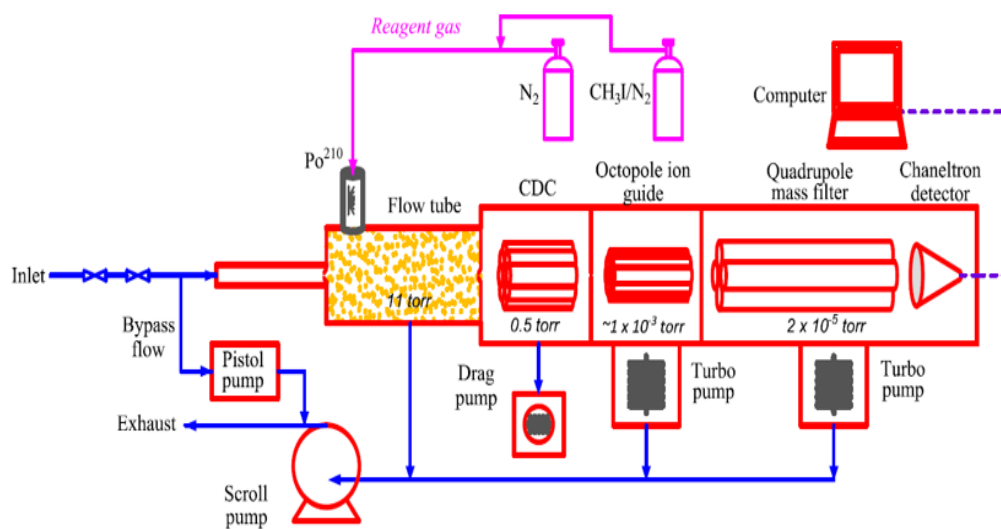


Figure 3.4. Schematic diagram of the unheated iodide-CIMS (not to scale).

About 1.8 standard liters per minute (SLPM) of ambient air were drawn through an orifice (pin-hole diameter = 0.45 mm) into the reaction chamber. The reaction chamber is made of a stainless steel flow tube and was maintained at ~11 Torr. The reaction chamber is the place where the sampled neutral molecules in the air (i.e. the N_2O_5 and ClNO_2) were ionized by an excess of primary reagent ions, iodide (I^-). The iodide was generated by passing a mixture of 1.0 SLPM of ultra-high purity N_2 (99.998%) with methyl iodide, CH_3I (0.03% in N_2 , Arkonic, USA) through a commercial ^{210}Po alpha ion source (10 mCi, NRD, P-2031-2000). The ionization schemes for N_2O_5 and ClNO_2 in this chamber are as below:



The I⁻ initially reacts with a water molecule (H₂O) and a third body (M) to form iodide-water cluster ion (R3.1). Then, the iodide-water cluster, I(H₂O)⁻, ionizes the N₂O₅ and ClNO₂ to produce cluster ions of I(N₂O₅)⁻ and I(ClNO₂)⁻ (R3.2-R3.3).

A fraction of the ion-molecule reaction mixture was sampled via an aperture (hole diameter = 0.635 mm) which was biased to -11 V (relative to the ground) for allowing the transmission of the ions into a lower pressure region of CDC (maintained at ~0.5 Torr). The CDC is comprised of eight stainless steel rods (octopole), serving as a site for dissociating weakly bound cluster ions through energetic collisions. The CDC were optimized to remove water molecules of the hydrated clusters but were weak enough to avoid significant fragmentation of I(ClNO₂)⁻ and I(N₂O₅)⁻ ion clusters.

The ions were focused in a narrow beam at a vacuum chamber (maintained at ~1 x 10⁻³ Torr) and were transmitted through an octopole ion guide into the next high vacuum chamber that housed a quadrupole mass filter (held at 2 x 10⁻⁵ Torr). The ions were mass selected by the quadrupole mass filter (Extrel Inc., mass range: 0 - 300 *a.m.u.*) and then detected by a detector. In the case of ClNO₂ and N₂O₅, both species were detected at the mass of 208 *a.m.u.* (I(ClNO₂)⁻) and 235 *a.m.u.* (I(N₂O₅)⁻), respectively.

3.2.2 Inlet setup in the field

The inlet setup in field measurement was as the following:

1) *Tung Chung*:

Ambient air was sampled through a 3 m length of perfluoroalkoxy (PFA) tube (with 1/2" outer diameter (O.D.)). It was set at the roof top of the primary school building and was about 16 m above the ground. A 7.7 SLPM of bypass flow was added to the sampling line to reduce the sampling residence time. Prior to the inlet of the CIMS instrument, the last 14.8 cm of the inlet was heated to 180 °C.

2) *Hok Tsui:*

The sampling inlet was set on the roof of the trailer and was 4 m above ground level. Ambient air was drawn down through a 3-m PFA tubing (1/2" O.D.) at a total sampling flow of 6 SLPM, resulting in sampling residence time of less than 1 second. Immediately before entering CIMS instrument, 14.8 cm of the inlet was heated with a heater set at 180 °C. The temperature of the air on the axis of the heated inlet was estimated to be ~117 °C, and this temperature is sufficient to thermal-dissociate the N₂O₅ but unable to thermal-dissociate the ClNO₂ (Slusher et al., 2004, Thaler et al., 2011).

3) *Tai Mo Shan:*

Ambient air was drawn through a 6-m long fluorinated ethylene propylene (FEP) tubing (1/4" O.D.) at a total flow rate of 10 SLPM. The aim of using a smaller tubing diameter in this campaign was to reduce the residence time in the inlet. The sampling inlet was affixed to a scaffold which was 2 m above the trailer roof and was about 6 m above the ground level. A standard addition port (a 1/4" PFA union tee) was added at the front of the inlet for adding N₂O₅ standard during the measurement. The sampling line was maintained and replaced daily to reduce the possibility of inlet conversion of N₂O₅ to ClNO₂.

4) Wangdu:

The sampling line used in this campaign was a 7.5-m long PFA tubing ($\frac{1}{4}$ " O.D.). The inlet was set at ~ 2 m above the roof and ~ 10 m from ground level with a total sampling flow rate of 10 \sim 11 SLPM. The inlet configuration was similar to a virtual impactor which intends to remove large particles (e.g. Kercher et al., 2009; Kulkarni et al., 2011). Only ~ 4 SLPM from the total flow was diverted to the CIMS, ozone, and NO_x analyzer, while the rest was dumped as exhaust. A port (a $\frac{1}{4}$ " PFA union tee) was fixed at the front of the inlet for the standard addition of N_2O_5 during the measurement. The sampling line and the orifice of the CIMS were replaced and washed daily to reduce the formation of artifacts in the inlet.

3.3 Preparation of calibration standards for CIMS

3.3.1 Synthesis of N_2O_5

N_2O_5 standard was produced in-situ by reacting O_3 in excess of NO_2 at room temperature (Bertram et al., 2009). Ozone was generated via photolysis of O_2 (from the compressed zero gas supplied by Linde) with a mercury lamp equipped inside an ozone generator of a commercial calibrator (Model 4010, Sabio Instrument Inc.). About 100 standard cubic centimetres per minute (sccm) of the produced O_3 was mixed with 49 sccm of NO_2 (10 ppmv balanced in N_2 ; Arkonic, USA). The mixture was then allowed to react in a Teflon reaction chamber (volume = 68 cm^3) for about 28 s prior to dilution by a stream of 5.0 SLPM zero air. Under excess NO_2 condition, the system is expected to shift the equilibrium in R1.2 towards N_2O_5 . Prior to the generation of N_2O_5 , the calibration system was purged with dry zero gas for at least

~2 h to make sure that the water content is at a minimal level (to prevent hydrolysis of the N_2O_5).

Concentrations of the synthesized N_2O_5 were calculated by the observed changes in NO_2 (before and after addition of O_3). This system was shown to be capable of producing N_2O_5 concentrations up to 5.0 ppbv (after dilution). Testing results from measuring the total reactive nitrogen (NO_y) of the N_2O_5 generated by this source with and without a Nylon filter (pore size = 2 μm ; Pall) did not indicate production of HNO_3 from N_2O_5 . The N_2O_5 concentrations were also quantified and confirmed by a CRDS (Dubé et al., 2006; Wagner et al., 2011). Figure 3.5 shows that the two quantification approaches (calculation from the changes of NO_2 and the measured N_2O_5 by CRDS) gave similar N_2O_5 concentrations with an average difference of $\pm 3\%$.

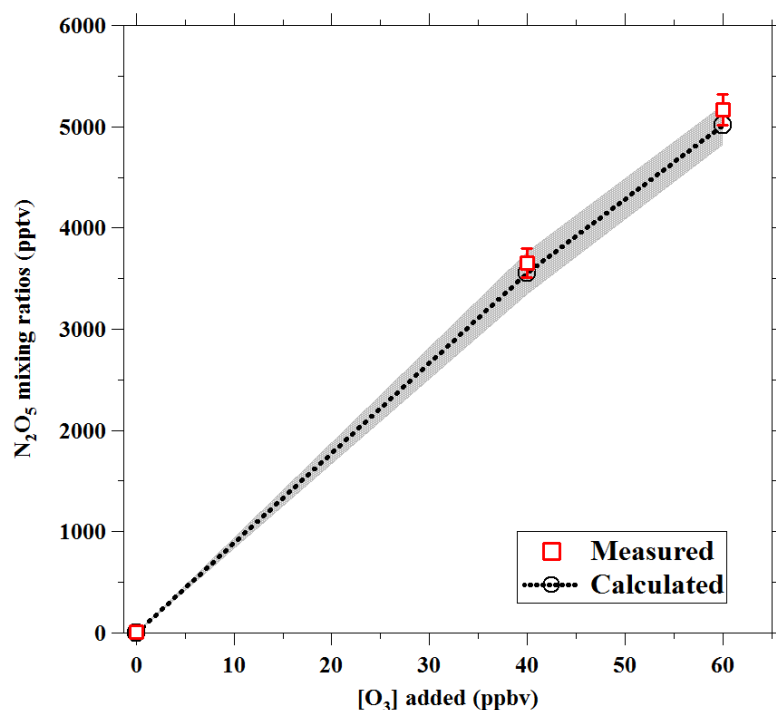


Figure 3.5. Comparison of the calculated and measured concentrations of the produced N_2O_5 after dilutions (in 5.0 SLPM). The shaded area (in gray) show the standard deviation (1σ) of the calculation. The error bar represents the standard deviation (1σ) of measured N_2O_5 .

3.3.2 Production of ClNO₂ standard

ClNO₂ was produced by passing 150 sccm of known concentration of N₂O₅ through a 25 cm length and ½” O.D. PFA reactor which has been quarter-filled with sodium chloride (NaCl) slurry. The NaCl slurry was prepared by adding ~3 mL of ultrapure deionized water into 1 g of solid NaCl (Sigma-Aldrich, ≥99.8%) producing saturated mixtures. The concentration of the ClNO₂ was determined via the amount of N₂O₅ loss through the NaCl-filled reactor compared to an empty reactor (see Figure 3.6) with the assumption of 100% conversion efficiency. The conversion efficiency of N₂O₅ to ClNO₂ on the deliquesced NaCl slurry was shown to be in unity (Finlayson-Pitts et al., 1989; Roberts et al., 2009). The loss of the produced ClNO₂ in the system are negligible since its uptake on the water or neutral NaCl slurry (pH = 7, measured by litmus paper) was inefficient (Rossi, 2003; Roberts et al., 2008). An in-line Teflon filter (diameter 47 mm; pore size 2 μm; Pall) was connected at the rear of the reactor to avoid NaCl particles from entering/contaminating the CIMS. Testing showed that the differences of ClNO₂ and N₂O₅ signals for with and without the filter were less than 3%.

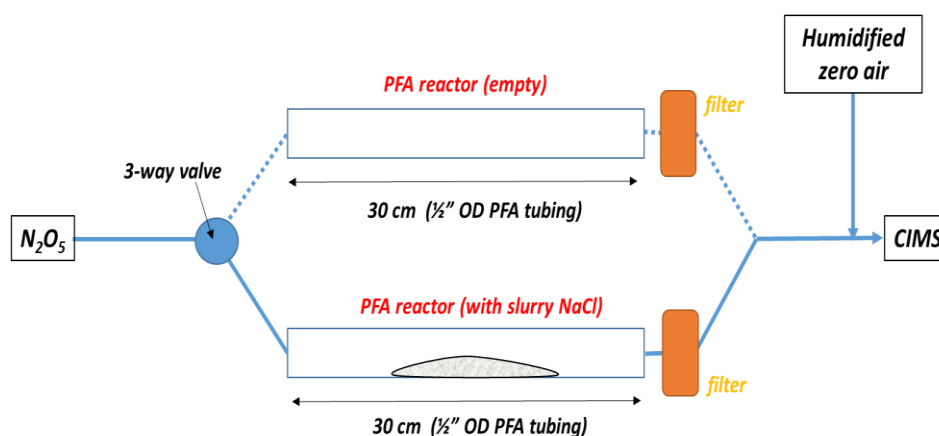


Figure 3.6. Schematic diagram of the N₂O₅ exposure to slurry NaCl to produce ClNO₂.

3.4 Background zeroing system

A background zeroing system for N_2O_5 and ClNO_2 was constructed as shown in Figure 3.7. The instrument background zeroing was performed by scrubbing the sampled ambient air through a 25 cm length of $\frac{1}{2}$ " OD stainless steel tubing packed with stainless steel wool. The packed-tubing was heated and maintained at $200 \pm 5^\circ\text{C}$, creating a large hot surface area for breaking down the N_2O_5 and ClNO_2 to NO_3 and Cl atom, which were efficiently scrubbed by the hot stainless steel wool (Behnke et al., 1997; Kercher et al., 2009; Phillips et al., 2012). The zeroing system is connected in series with a 40 cm length of $\frac{1}{2}$ " OD PFA tubing reaching the CIMS inlet. Therefore the air was expected to cool back to ambient temperature before entering the CIMS. Laboratory study showed that this zeroing system has a removal efficiency of more than 98% for 5 ppbv of N_2O_5 and ClNO_2 .

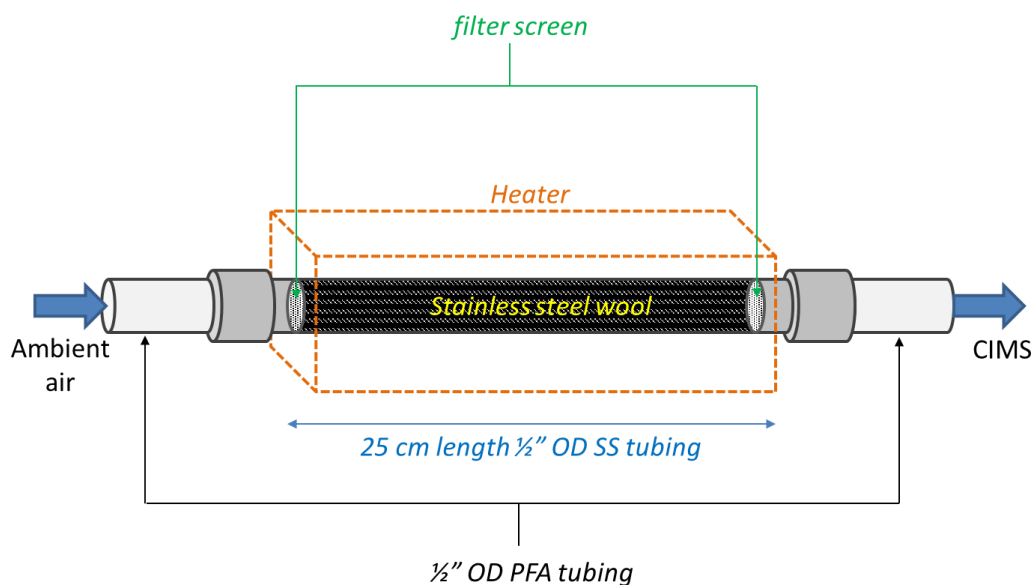


Figure 3.7. The design of the background zeroing system for ClNO_2 and N_2O_5 .

3.5 Auxiliary measurements

Auxiliary measurements of trace gasses, aerosols, and meteorological parameters were conducted in the field to support the data analysis. Table 3.1 shows the instruments used for the supporting measurements in Hong Kong, including the field measurement at Tung Chung, Hok Tsui, and Tai Mo Shan. NO, and NO₂ were measured by a chemiluminescence NO_x analyzer (Thermo, Model 42i) equipped with a blue light photolytic converter (BLC), and total reactive nitrogen (NO_y) was determined by another chemiluminescence NO_x analyzer (Thermo, Model 42i) with an externally attached molybdenum oxide (MoO) catalytic converter (Xu et al., 2013). Ozone was measured by a UV photometric analyzer (Thermo, Model 49i). Carbon monoxide (CO) was measured with a nondispersive analyzer (API, model 300) while sulfur dioxide (SO₂) was quantified by UV fluorescence (Thermo, Model 43A). VOCs were collected hourly on selected days with evacuated electro-polished stainless steel canisters. The canisters were later shipped to the University of California, Irvine (UCI) laboratory for chemical analysis of methane and non-methane hydrocarbons (Blake et al., 1994; Simpson et al., 2010).

As for aerosol measurement, an ambient ion monitor (AIM, Model URG-9000B, USA) was used to measure the concentrations of water-soluble inorganic ions, including SO₄²⁻, NO₃⁻, Cl⁻, NH₄⁺, Na⁺, K⁺, Mg²⁺ and Ca²⁺ (Gao et al., 2012). The mass concentration of PM_{2.5} was measured using a tapered element oscillating microbalance (TEOM 1405-DF, Thermo Scientific) with a Filter Dynamic Measurement System (FDMS). Particle size distribution and numbers were also measured in real-time by an Ultrafine Particle Monitor (TSI Model 3031). It was measured at a 10 min interval the

count of particles in six size bins (i.e., 20–30, 30–50, 50–70, 70–100, 100–200, and 200–1000 nm) with $RH \leq 50\%$ controlled by a nafion dryer. The aerosol surface areas were calculated based on the particle number and geometric mean diameter in each size bin. For the largest size bin of 200–1000 nm, the geometric mean diameter (GMD) of 447 nm may lead to an overestimation in surface area. Our previous measurement of the particle size distribution with more size bins at a suburban site in Hong Kong (Guo et al., 2014; Xu et al., 2015) showed that the surface area-weighted mean diameter for 200–1000 nm particles was around 290 nm and the surface area contributed by particles larger than 400 nm accounted for less than 15% of the total surface area for majority of the time. Therefore, a mean diameter of 282 nm (GMD for 200–400 nm) was used to determine the aerosol surface area of 200–1000 nm particles for the data analysis in Tai Mo Shan. Furthermore, the particle diameters were corrected for particle hygroscopicity by growth factors under high relative humidity condition ($RH > 50\%$). The wet diameters of particles were calculated with kappa-Köhler function, with mean kappa values of 0.3 adopted from ambient measurement at a suburban coastal site in Hong Kong (Yeung et al., 2014).

Ambient temperature, relative humidity (RH), wind speed and direction were monitored using an RH/temperature probe and a wind monitor (*Gill, UK*). Photolysis frequency of NO_2 (j_{NO_2}) was obtained using a filter radiometer (*Meteorologie consult gmbh*).

Table 3.1. Measurement techniques and time resolution of the supporting data used in Tung Chung, Hok Tsui, and Tai Mo Shan.

	Parameter	Technique	Time resolution
Gas	NO, and NO ₂	blue light photolytic converter and chemiluminescence	1 min
	NO _y	MoO and chemiluminescence	1 min
	O ₃	UV photometric	1 min
	CO	IR absorption	1 min
	SO ₂	Pulsed UV fluorescence	1 min
	VOCs	Canisters; GC-MS	Specific time
Aerosol	PM _{2.5}	TEOM	1 min
	PM _{2.5} ionic composition	Ambient Ion Monitor	1 h
	Particle size distribution and number	Ultrafine Particle Monitor	10min
Meteorological	Wind	Wind monitor	1 min
	RH and Temperature	Probe	1 min
	J_{NO_2}	Filter radiometer	1 min

As the field study at Wangdu is an international collaborative campaign, another set of instruments/techniques was used to measure the gasses and aerosol species. Table 3.2 summarizes the techniques used for the supporting measurements at Wangdu. During the study, many of the trace gasses were simultaneously measured by different instruments/techniques. The agreement between these instruments or techniques and the justification on the data set selections have been discussed elsewhere (refer to Tan et al., 2016). Briefly, NO and NO₂ were measured by the chemiluminescence/photolytical conversion techniques, while NO_y was determined by the chemiluminescence method with a molybdenum oxide (MoO) catalytic

converter. O₃ was quantified by a UV absorption analyzer. Sulfur dioxide (SO₂) was measured by a pulsed UV fluorescence analyzer and carbon monoxide (CO) with an infrared photometer. C₂-C₁₀ hydrocarbons (NMHCs), formaldehyde (HCHO), and other oxygenated hydrocarbons (OVOCs) were measured with an online gas chromatograph (GC) equipped with a mass spectrometer and a flame ionization detector (FID), a Hantzsch fluorimetric monitor, and proton-transfer-reaction mass spectrometer (PTR-MS), respectively (Yuan et al., 2010, 2012; M. Wang et al., 2014). Methane was measured by cavity ring down spectroscopy technique (CRDs). Measurement of nitrous acid (HONO) was performed by a long-path absorption photometer (LOPAP) instrument (Li et al., 2014; Liu et al., 2016). Hydroxyl (OH) and hydroperoxyl (HO₂) radical were measured in parallel by using a compact laser-induced fluorescence (LIF) system (Hofzumahaus et al., 2009; Lu et al., 2012).

Particle mass concentrations (PM_{2.5}) were measured using a TEOM. The ionic compositions of PM_{2.5} were determined by a gas aerosol collector (GAC) -ion chromatography system (Dong et al., 2012). The dry-state particle number size distribution was determined by combining the data (Pfeifer et al., 2014) from a Mobility Particle Size Spectrometer (Dual TROPOS-type SMPS; Birmili et al., 1999; Wiedensohler et al., 2012) and an Aerodynamic Particle Size Spectrometer (TSI-type APS model 3321; Pfeifer et al., 2016) covering the size ranges from 4-800 nm (mobility particle diameter) and 0.8-10 μm (aerodynamic particle diameter), respectively. The ambient particle number size distributions as a function of the relative humidity were calculated from a size-resolved kappa-Köhler function determined from real time measurement of a High Humidity Tandem Differential Mobility Analyzer (HHTDMA) (Hennig et al., 2005; Liu et al., 2014). Ambient

particle surface area concentrations (S_a) were calculated based on the ambient particle number size distribution assuming spherical particles.

Meteorological parameters including wind direction, wind speed, relative humidity (RH), pressure and temperature were measured with an ultrasonic anemometer and a weather station on a 20-m height tower which was situated 30 m from the trailers. Photolysis frequency of NO_2 , O_3 (j_{O_3}) and HONO (j_{HONO}) and ClNO_2 (j_{ClNO_2}) was determined from actinic flux densities measured by a spectroradiometer (Meteorologie Consult) (Bohn et al., 2008).

Table 3.2. Measurement method for trace gasses and aerosols at Wangdu.

	Species	Measurement Techniques	Time resolution
Gas	O_3	UV photometry	1 min
	NO	Chemiluminescence	3 min
	NO_2	Photolytical converter & Chemiluminescence	1 min
	NO_y	MoO catalytic converter & Chemiluminescence	1 min
	CH_4	CRDs	1 min
	SO_2	Pulsed-UV fluorescence	1 min
	CO	IR photometry	1 min
	HONO	LOPAP	30 s
	OH, HO ₂	LIF	30 s
	HCl	GAC-IC	30 min
	Methane	cavity ring down	1 min
	VOCs	GC-FID/MS	1 h
OVOCs	PTR-MS	5 min	

	Formaldehyde	Hantzsch (wet chemical fluorimetric)	1 min
Aerosol	PM _{2.5}	TEOM	1 min
	Aerosol ionic compositions	GAC-IC	30 min
	Particle surface area	Mobility Particle Size Spectrometer + HHTDMA	30 min
Meteorological	RH and Temperature	weather station	1 min
	photolysis frequency	spectrum radiometer	20 s

3.6 Estimation of the unmeasured photolysis frequencies

Direct observation of photolysis frequency constants (j) for NO₂ was available in all the field measurements, but not for other species such as ClNO₂, O₃, HONO, NO₃, formaldehyde and other chlorine containing species, which were the critical parameters used in the data analysis or calculations. These photolysis rates were predicted from the Tropospheric Ultraviolet and Visible model (TUV) version 5.2, (the model is available for download at <https://www2.acom.ucar.edu/modeling/tuv-download>). Since the TUV output of the photolysis frequencies was based on a clear sky scenario, the predicted photolysis frequencies were then scaled with the observed j_{NO_2} to account for the variations of ambient conditions.

3.7 Time-dependent chlorine chemistry box model

Time-dependent models are widely used in the study of atmospheric chemistry to investigate the processes and/or species that cannot be directly measured (e.g. Kim et al., 2014; Liao et al., 2014; Reidel et al., 2015). Here, a time-dependent chlorine

chemistry box model was employed to predict the mixing ratios of Cl atom. It was constructed by utilizing the Kinetic Preprocessor software (KPP, version 2.2.3, available at <http://people.cs.vt.edu/~asandu/Software/Kpp>) (Damian et al., 2002; Sandu et al., 2003; Daescu et al., 2003; Sandu and Sander, 2006). KPP is a freely available software tool under the terms of GNU public license (<http://www.gnu.org/copyleft/gpl.html>). Similar to other software like Fascimile (Curtis and Sweetenham, 1987) and AutoChem (<http://gest.umbc.edu/AutoChem>), KPP was designed to solve stiff ordinary differential equations (ODEs) in the chemical kinetic system (Sandu and Sander, 2006). Due to its simplicity in adding and modifying of the chemical kinetic system, KPP has been widely used for setting up box models like MCM (<http://mcm.leeds.ac.uk/MCM/>) and Module Efficiently Calculating the Chemistry of the Atmosphere (MECCA) (e.g. Sander et al., 2011).

The time-dependent chlorine chemistry box model was designed and built together with a colleague (Qinyi Li who help in writing the source codes) based on the work of Liao et al. (2014). Since the work of Liao and co-workers focuses in the clean environment of Artic, several modifications were made on the model for the conditions of polluted China environment. First, more reactions of Cl atom with VOCs were added into the model. Second, all of the reaction rates were updated with the recommendation from IUPAC Kinetics database (available at <http://iupac.pole-ether.fr/index.html>). The reactions and rate coefficients included in the model were summarized in Table 3.3.

The model was constrained with observational data measured at the site. All of the observation data with hourly, 10 min or 5 min resolutions were linearly

$\text{Cl} + \text{benzene} \rightarrow \text{HCl} + \text{C}_6\text{H}_5$	1.3×10^{-15}
$\text{Cl} + \text{toluene} \rightarrow \text{HCl} + \text{C}_6\text{H}_5\text{CH}_2$	6.2×10^{-11}
$\text{Cl} + \text{isoprene} \rightarrow 0.15\text{HCl} + \text{C}_5\text{H}_7$	4.3×10^{-10}
$\text{Cl} + \text{HO}_2 \rightarrow \text{HCl} + \text{O}_2$	$1.8 \times 10^{-11} \exp(170/T)$
$\text{Cl} + \text{HO}_2 \rightarrow \text{ClO} + \text{OH}$	$4.1 \times 10^{-11} \exp(-450/T)$
$\text{Cl} + \text{CH}_3\text{CN} \rightarrow \text{HCl} + \text{CH}_2\text{CN}$	$1.6 \times 10^{-11} \exp(-2140/T)$
$\text{ClO} + \text{HO}_2 \rightarrow \text{HOCl} + \text{O}_2$	$2.7 \times 10^{-12} \exp(220/T)$
$\text{ClO} + \text{ClO} \rightarrow \text{Cl}_2 + \text{O}_2$	$1.0 \times 10^{-12} \exp(-1590/T)$
$\quad \rightarrow \text{ClOO} + \text{Cl}$	$3.0 \times 10^{-11} \exp(-2450/T)$
$\quad \rightarrow \text{OCIO} + \text{Cl}$	$3.5 \times 10^{-13} \exp(-1370/T)$
$\quad \rightarrow \text{Cl}_2\text{O}_2$	$k_0 = 1.6 \times 10^{-32} (T/300)^{-4.5}$ $k_\infty = 2.0 \times 10^{-12} (T/300)^{-2.4}$
$\text{ClO} + \text{NO} \rightarrow \text{Cl} + \text{NO}_2$	$6.4 \times 10^{-12} \exp(220/T)$
$\text{ClO} + \text{NO}_2 \rightarrow \text{ClONO}_2$	$k_0 = 1.8 \times 10^{-31} (T/300)^{-3.4}$ $k_\infty = 2.0 \times 10^{-12} (T/300)^{-1.9}$
$\text{ClO} + \text{OH} \rightarrow \text{Cl} + \text{HO}_2$	$7.4 \times 10^{-12} \exp(270/T)$
$\text{ClO} + \text{OH} \rightarrow \text{HCl} + \text{O}_2$	$6.0 \times 10^{-13} \exp(230/T)$
$\text{Cl}_2 + \text{OH} \rightarrow \text{HOCl} + \text{Cl}$	$1.4 \times 10^{-12} \exp(-900/T)$
$\text{HOCl} + \text{OH} \rightarrow \text{ClO} + \text{H}_2\text{O}$	$3.0 \times 10^{-12} \exp(-500/T)$
$\text{HCl} + \text{OH} \rightarrow \text{Cl} + \text{H}_2\text{O}$	$2.6 \times 10^{-12} \exp(-350/T)$
$\text{OH} + \text{ClNO}_2 \rightarrow \text{HOCl} + \text{NO}_2$	$2.4 \times 10^{-12} \exp(-1250/T)$
$\text{Cl} + \text{OCIO} \rightarrow \text{ClO} + \text{ClO}$	$3.2 \times 10^{-11} \exp(170/T)$
$\text{OCIO} + \text{NO} = \text{ClO} + \text{NO}_2$	$1.1 \times 10^{-13} \exp(350/T)$
$\text{Cl} + \text{ClONO}_2 \rightarrow \text{Cl}_2 + \text{NO}_3$	$6.2 \times 10^{-12} \exp(145/T)$
$\text{Cl} + \text{Cl}_2\text{O}_2 \rightarrow \text{Cl}_2 + \text{ClOO}$	$7.6 \times 10^{-11} \exp(65/T)$
$\text{HOCl} + \text{het} \rightarrow \text{Cl}_2$	$0.25 \times 315 (\text{C}_{\text{HOCl}}) \times 0.1 (\gamma) \times \text{S}_a$
$\text{Cl}_2 + h\nu \rightarrow 2\text{Cl}$	j_{Cl_2}
$\text{ClO} + h\nu \rightarrow \text{Cl} + \text{O}$	j_{ClO}
$\text{HOCl} + h\nu \rightarrow \text{Cl} + \text{OH}$	j_{HOCl}
$\text{ClNO}_2 + h\nu \rightarrow \text{Cl} + \text{NO}_2$	j_{ClNO_2}

het = heterogeneous reaction ($0.25 \times \text{C} \times \gamma \times \text{S}_a$)

Chapter 4 Preliminary field observations of ClNO₂ in Asian coastal environment

Prior to this study, the presence of ClNO₂ and its impacts were unknown in the Asian region although the ‘ingredients’ for the production of ClNO₂ such as NO_x, O₃, and particulate chloride were abundant in this region (e.g. Lai et al., 2007; Wang et al., 2009; Hilboll et al., 2013). This chapter reports the preliminary attempts to measure ClNO₂ and its precursor, N₂O₅, with a TD-CIMS at two coastal sites in Hong Kong. The concentrations of ClNO₂ at the two locations were presented, and their potential impact was discussed.

4.1 First attempt of ClNO₂ measurement

A TD-CIMS was deployed to Tung Chung for an intensive field campaign during 2011-2012. The TD-CIMS was configured and optimized for measurement of N₂O₅ and PANs with a heated inlet (X. Wang et al., 2014). The calibrations and zeroing determinations were only performed for N₂O₅ and PANs during the field measurements. Nonetheless, the signal at 208 *a.m.u.* (of ClNO₂) was also recorded by the TD-CIMS during the campaign. This study was conducted in four non-consecutive months: 5 August to 4 September 2011 (late summer); 1 November to 2 December 2011 (late autumn); 6 February to 2 March 2012 (late winter) and 16 May to 5 June 2012 (late spring).

Although there was no direct calibration of ClNO₂ in the field, the ClNO₂ signals were corrected based on the correction factor predicted by multiplying the N₂O₅ sensitivity determined in the field with 0.16 (the ratio of ClNO₂ sensitivity to N₂O₅ sensitivity that was derived in the later field study at Hok Tsui), with assumption that this ratio was similar in both campaigns. The mean sensitivity of ClNO₂ for the entire campaign at Tung Chung was 0.40 ± 0.09 Hz/pptv. The detection limit of ClNO₂ determined by flooding the TD-CIMS with zero air was 7 pptv (3σ , 1 min average). Potential interference from the inlet chemistry is likely trivial at this site due to the high NO condition (>5 ppbv on majority of the nights), which would limit the presence of N₂O₅ in the sampled air.

As for the measurement of N₂O₅ at 62 *a.m.u.*, the signal was subjected to large interferences from the high concentration of NO_x and PAN at this site. These interferences have been described in the works of a colleague (refer to the publication of X.Wang et al., (2014) for more details). Hence, the N₂O₅ data set was omitted from this analysis.

4.2 Preliminary observation of ClNO₂ at Tung Chung

An overview of the ClNO₂ concentrations deducted from 208 *a.m.u.* signal is presented in Figure 4.1. Significant ClNO₂ concentrations were observed on majority of the nights at Tung Chung. It indicates that there was a persistent production of ClNO₂ in this region. The ClNO₂ accumulated after sunset and decreased rapidly at sunrise as a result of photolysis of ClNO₂ and its precursors NO₃/N₂O₅.

Figure 4.2 illustrates the diurnal variations of ClNO₂ in 4 different seasons. It can be seen that the ClNO₂ was season dependent. Highest diurnal ClNO₂ mixing ratios were observed during the autumn season with the maximum value of 530 pptv. It was followed by the spring (maximum 470 pptv), winter (maximum 210 pptv) with the lowest levels during the summer season (maximum 150 pptv). By comparing with a recent study in Calgary, Canada (Mielke et al., 2015), their observed seasonal variations of ClNO₂ was slightly different with the trend at Tung Chung. They reported that ClNO₂ was most abundant during the winter, followed by the spring, autumn, and summer, which apparently influenced by the local weather conditions and human activities (e.g. applying road salts) in Calgary.

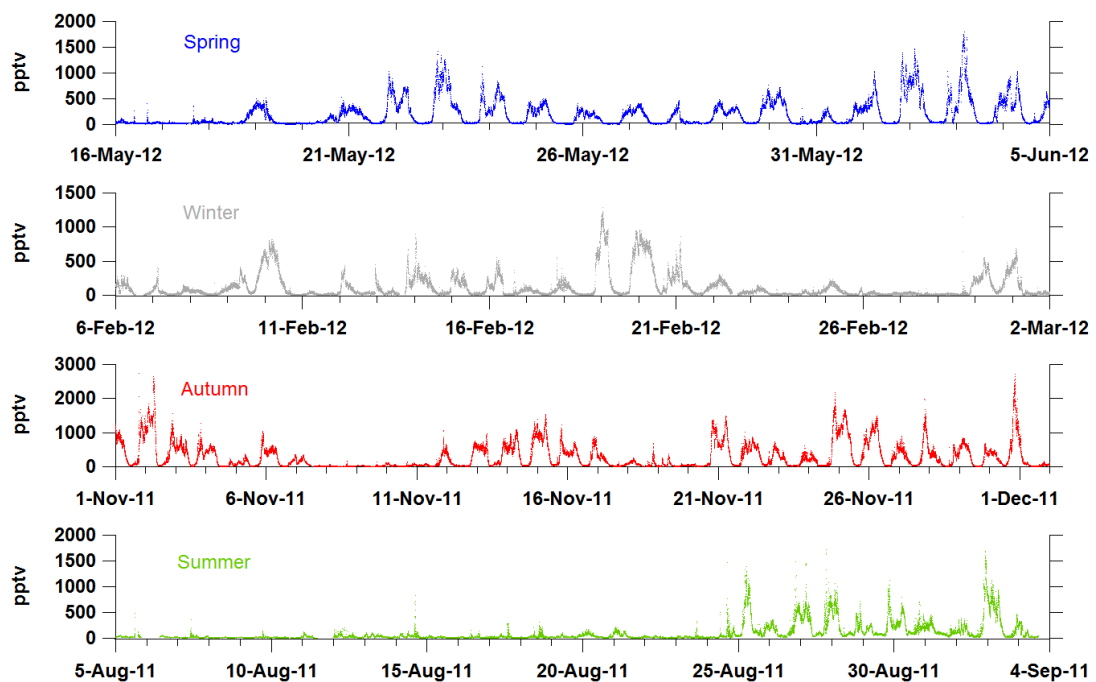


Figure 4.1. Overview of ClNO₂ mixing ratios measured in the four non-consecutive months (different seasons).

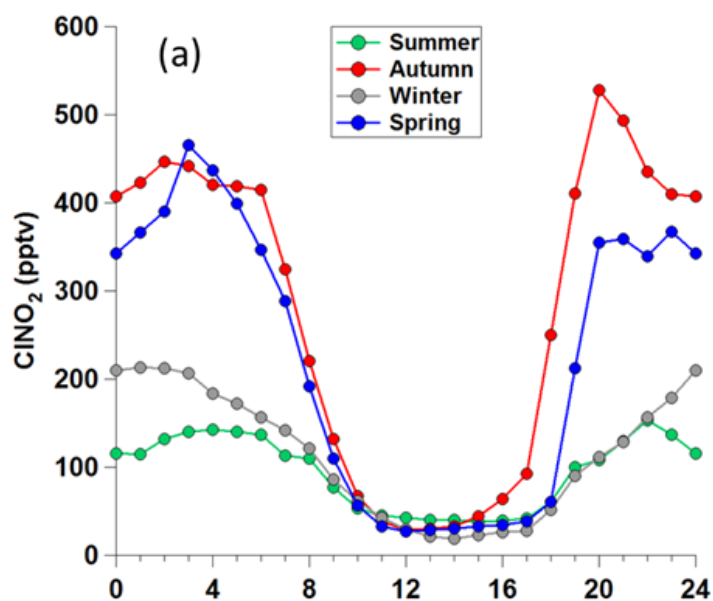


Figure 4.2. Seasonal diurnal variations of ClNO₂ concentrations at Tung Chung.

The seasonal variations of ClNO₂ can be explained by related chemical data and meteorological parameters. Table 4.1 shows the mean concentrations of ClNO₂, NO_x, O₃, PM_{2.5}, together with RH and temperature in the 4 different seasons. The high levels of ClNO₂ during the autumn were corresponding to the highest mixing ratios of odd oxygen (O_x = O₃ + NO₂), aerosol loading of PM_{2.5} and fine chloride aerosols. The average mixing ratio/concentration of O_x, PM_{2.5}, and chloride during the autumn was 51.2 ppbv, 32 μg/m³ and 1.11 μg/m³, respectively. High levels of O_x and aerosols were common during the autumn season as Hong Kong is often influenced by the long-range transportation of pollutants from the continental outflow of PRD and East China (Zhang et al., 2007; Wang et al., 2009; Guo et al., 2009). With abundant ClNO₂ precursors and moderate temperature and humidity conditions, heterogeneous production of ClNO₂ during autumn was expected to be fast. On the other hand, the summertime production of ClNO₂ was probably restricted by the lower level of production precursors and hot weather conditions. The O_x was observed to be at low levels during the summer, with a mean concentration of 41.9 ppbv. The average

temperature of 32°C in the summertime could lead to faster thermal dissociation of N₂O₅ into NO₃ + NO₂ (Eq. 2.2), reducing the N₂O₅ heterogeneous uptake, and together with the lower availability of chloride aerosol (0.11 µg/m³), the ClNO₂ production may be less efficient during the summer season in Hong Kong.

Table 4.1. The mean values of ClNO₂, NO_x, O₃, aerosols, temperature and RH in the four seasons.

	ClNO ₂ (pptv)	NO (ppbv)	NO ₂ (ppbv)	O ₃ (ppbv)	PM _{2.5} (µg/m ³)	Cl ⁻ (µg/m ³)	Temp (°C)	RH (%)
Summer (Aug)	94	9.3	20.0	21.9	20	0.11	32	71
Autumn (Nov)	274	10.8	28.2	23.0	32	1.11	24	67
Winter (Feb)	111	19.4	24.4	13.9	28	0.82	17	79
Spring (May)	221	5.4	14.8	25.5	16	0.47	28	75

4.3 Second attempt of ClNO₂ measurement

After the Tung Chung campaign, the TD-CIMS was deployed to a rural/background coastal site located at Hok Tsui with the primary objective to measure N₂O₅. N₂O₅ was detected as the NO₃⁻ at 62 *a.m.u.* Similarly, it was found to have high interferences when the PAN and NO_x were at maximum level in the noon-time. The concentrations of PAN and NO_x were relatively low during the night and the correction of the 62 *a.m.u.* data for the interference initiated by PAN and NO_x was estimated to be less than 15%. Therefore, only the night-time N₂O₅ data were used in this study.

Detection of ClNO₂ was initially not the major target of this campaign. However, due to the observation of high ambient ClNO₂ signal at the beginning of the campaign, improvement on the ClNO₂ measurement was made after that. It included the development of an on-site ClNO₂ calibration system (see section 3.3.2). Offline calibrations of ClNO₂ were performed twice a week. The average sensitivity of ClNO₂ for this campaign was 0.44 ± 0.05 Hz/pptv. The determined sensitivities of ClNO₂ were normalized with I⁻ signal and then used for correcting the ambient ClNO₂ signal (at 208 *a.m.u.*). The limit of detection for ClNO₂ was determined to be 2 pptv (3σ). ClNO₂ measurements were available from 23 August to 19 December 2012.

The major uncertainty of the ClNO₂ measurement is the potential conversion of N₂O₅ to ClNO₂ on the inlet surface as the same sampling line was used for the entire campaign. Post-campaign testing on this used-inlet (after sampling for 4 months) showed significant N₂O₅ loss up to 69% when adding 4 ppbv of N₂O₅ and 19% of the added N₂O₅ was converted to the ClNO₂. Hence, only the data in the first 10 days of the campaign (23 Aug - 1 Sept 2012) were used for the further analysis to avoid the large uncertainty of the measurement due to inlet chemistry. Later laboratory testing suggested that the potential ClNO₂ formation on the surface of the inlet which had sampled ambient air for a week was less than 10% of the added N₂O₅ (refer to section 5.3.1 in Chapter 5). Upon checking on the ambient data during this period, no significant reduction of the ambient ClNO₂ signal was observed when flooding the inlet with very high NO concentration (for the N₂O₅ zeroing purpose), while the ambient N₂O₅ signals immediately dropped to zero level. It suggests insignificant N₂O₅ conversion to ClNO₂ in the inlet.

4.4 Preliminary observation of ClNO₂ at Hok Tsui

The time series of ClNO₂, N₂O₅, NO₂ and O₃ at Hok Tsui are presented in Figure 4.3. ClNO₂ was detected throughout the campaign, with a distinct diurnal variation, showing night-time peaks and daytime levels close to the detection limit. This pattern is similar to those measured in other marine environments (Osthoff et al., 2008, Kercher et al., 2009; Wagner et al., 2012). The mean mixing ratio of ClNO₂ was 148 pptv with a large standard deviation of 253 pptv. Maximum ClNO₂ of 1997 pptv (1-min average) was observed on the night of 23-24 August, which is comparable to the reported maximum concentrations (2.1-3.5 ppbv) in the Los Angeles Basin (Riedel et al., 2012; Mielke et al., 2013). The mixing ratios of N₂O₅ were typically low in most of the nights but reached maximum of 434 pptv (1-minute averaged) on the night of 23-24 August. These observations suggest the existence of active N₂O₅-ClNO₂ chemistry in the marine boundary layer atmosphere of southern China.

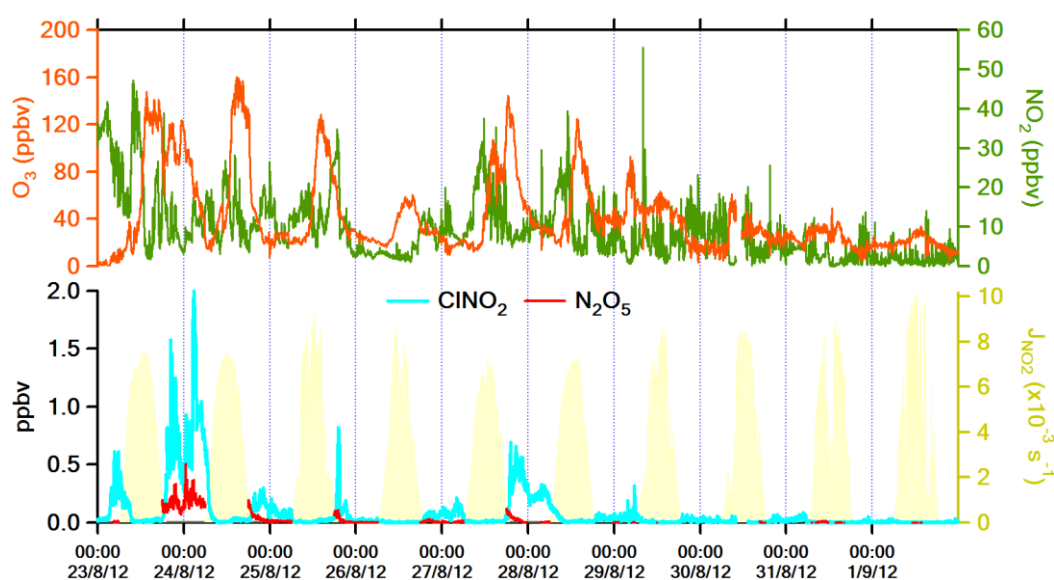


Figure 4.3. Time series of ClNO₂ and N₂O₅ together with related parameters measured at Hok Tsui from 23 August to 1 September 2012.

The day-to-day variation of ClNO₂ and N₂O₅ observed at Hok Tsui was highly related to the differences of air masses origin, as illustrated by the 24-h back trajectories calculated by the HYSPLIT model (Draxler et al., 2014). The air masses during the measurements at Hok Tsui were divided into three clusters, namely the urban/continental, near coastal and marine air masses (see Figure 4.4). During 23-26 August when high night-time ClNO₂ and N₂O₅ were measured, the site was significantly influenced by polluted plumes from the urban areas of Hong Kong and the inland of PRD region. These plumes contained abundant ozone and moderate levels of NO₂, favoring the production of N₂O₅. This condition, in turn, facilitated the formation of ClNO₂ given the fact that the chloride aerosol is always adequate this coastal site (Cheng et al., 2000). For example, on the night of 23-24 August, approximately 90 ppbv of ozone together with 10 ppbv of NO₂ were observed along with ClNO₂ exceeding 1.9 ppbv and N₂O₅ >200 pptv. On 27-29 August, the air masses were from the coastal line of PRD which probably have mixed influences of urban and marine air, with a mean NO₂ of 9 ppbv, O₃ of 20 ppbv, ClNO₂ of 135 pptv and N₂O₅ of 25 pptv (Table 4.2). In contrast, relatively low mixing ratios of ClNO₂ of 15 pptv and N₂O₅ of 5 pptv were detected from 30 August to 1 September when the air masses were dominated by the maritime air with low ozone and NO₂. Obviously, the availability of N₂O₅ precursors (i.e., O₃ and NO₂) is the limiting factor of the N₂O₅ and ClNO₂ production at this site.

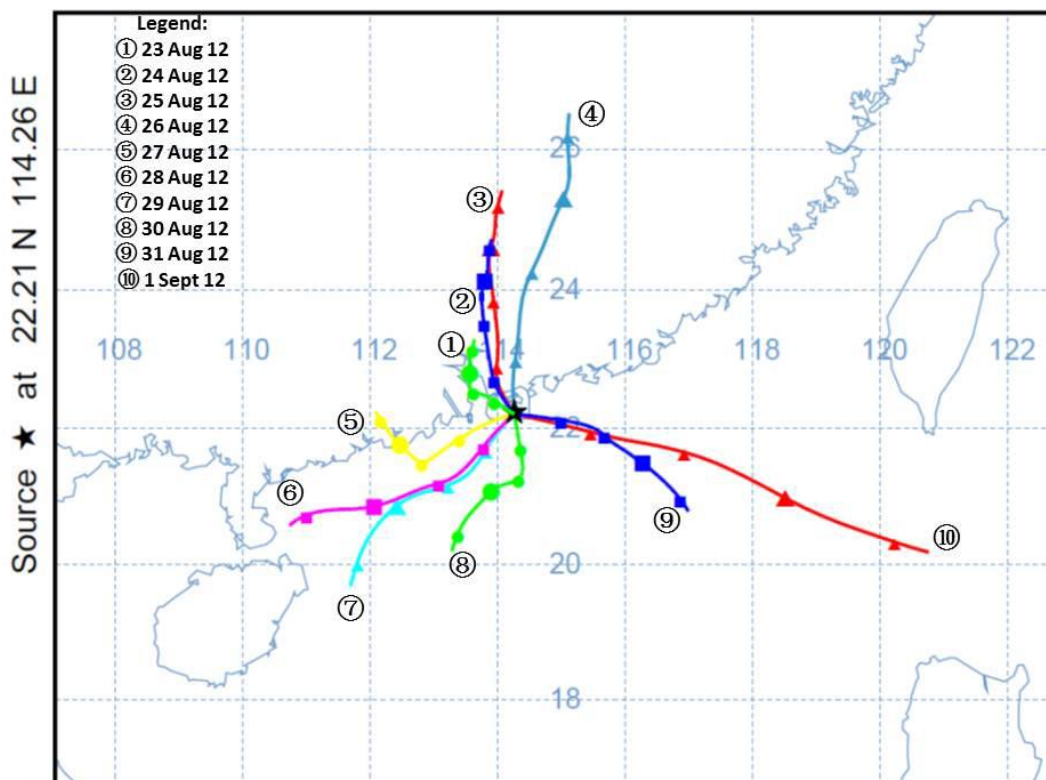


Figure 4.4. Twenty-four hour back trajectories from HYSPLIT covering the period of 23 August 2012 to 1 September 2012.

Table 4.2. Mean mixing ratio of nighttime NO_2 , O_3 , N_2O_5 , and ClNO_2 in three different types of air masses categories.

Air mass	NO_2 (ppbv)	O_3 (ppbv)	N_2O_5 (pptv)	ClNO_2 (pptv)
Continental/Urban	10	90	180	256
Near coastal	9	20	25	135
Marine	5	17	5	15

4.5 Potential impacts of ClNO_2

ClNO_2 can be an important radical source in the daytime (Young et al., 2012) and may affect the ozone formations in polluted regions (Osthoff et al., 2008, Simon et al., 2010; Sarwar et al., 2014). In order to assess the potential impact of ClNO_2 , the

production rate of Cl atom (P(Cl)) through ClNO₂ photolysis was calculated with equation (4.1).

$$P(\text{Cl}) = j_{\text{ClNO}_2}[\text{ClNO}_2] \quad (4.1)$$

Tung Chung:

As shown in Figure 4.5, photolysis of ClNO₂ in the four different seasons contributed to significant Cl atom production in the morning. The P(Cl) reached a maximum 3 hours after the sunrise (~08:00) and decreased gradually towards to noon. Production of Cl atom was the highest during the spring with a maximal rate of 0.02 pptv/s, corresponding to the high ClNO₂ concentrations and moderate sunlight intensity. Smallest P(Cl) of 0.005 pptv/s was predicted during the winter due to the relatively less intense sunlight which will reduce the efficiency of ClNO₂ photolysis. These results indicate that the contribution of ClNO₂ to the oxidative chemistry may vary between seasons.

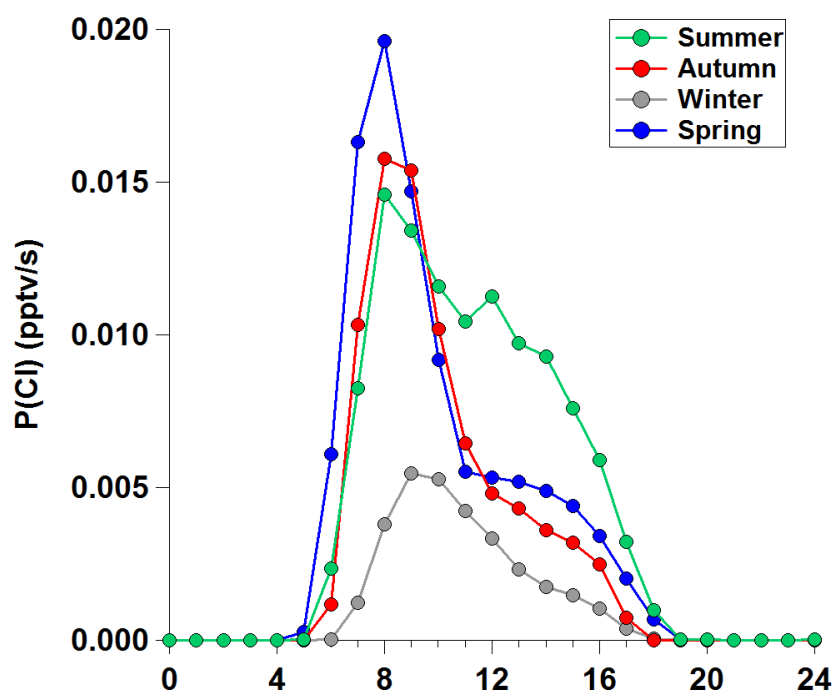


Figure 4.5. Cl atom production rate in four different seasons at Tung Chung.

Hok Tsui:

The Cl atom production rate at Hok Tsui was calculated and compared with the production rate of OH ($P(\text{OH})$) via ozone photolysis (equation 4.2), which is the dominant radical source in the atmosphere.

$$P(\text{OH}) = 2j_{\text{O}_1\text{D}}[\text{O}_3]k_{\text{H}_2\text{O}}[\text{H}_2\text{O}]/(k_{\text{H}_2\text{O}}[\text{H}_2\text{O}] + k_{\text{N}_2}[\text{N}_2] + k_{\text{O}_2}[\text{O}_2]) \quad (4.2)$$

Figure 4.6 depicts an example of the production rate of Cl atom and the ratio of Cl atom production to OH production on 24 August 2012. After sunrise (i.e., 06:00-07:00, local time), fast photolysis of ClNO_2 led to the high production of Cl atom (maximum rate = 0.012 pptv/s) that exceeded the OH production from ozone photolysis by a factor of 3. Consequently, ClNO_2 photolysis should be an important radical source in the early morning period, although the ozone photolysis became more and more important later. Cl atom is an important oxidant toward VOCs especially

alkanes, with the reaction rates of several orders of magnitude faster than OH (Atkinson et al., 1999; Tanaka et al., 2003). Therefore, the production of ClNO₂ over the night may play a significant role in initiating the next day's photochemistry.

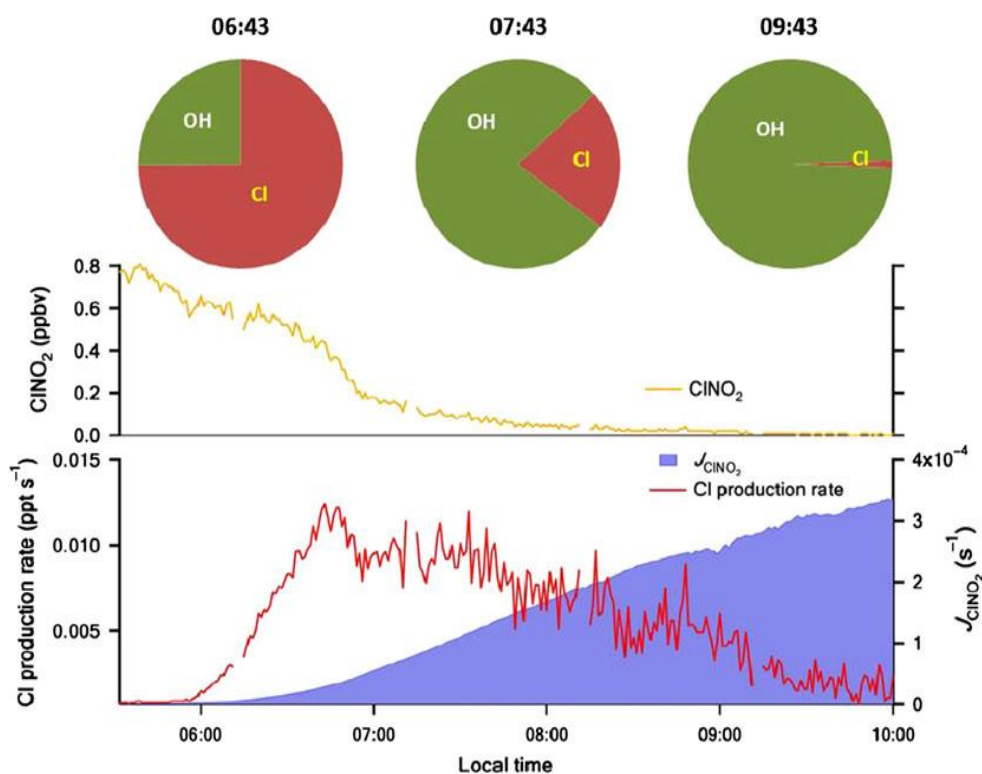


Figure 4.6. The Cl production rate on 24 August 2012. Pie charts represent the ratio of Cl production from ClNO₂ and OH production via photolysis of ozone.

A colleague (Likun Xue) later constrained the measured ClNO₂ into a chemical box model (MCM) with updated Cl chemistry module to investigate the impact of ClNO₂ on the ozone production. They found that the ClNO₂ caused up to 10.3% increase in the daily average ozone production at this site (refer to the publication of Xue et al. (2015) for more information).

4.6 Summary

Extrapolation of the findings from these two initial studies provides the baseline in understanding of the presence of ClNO₂ in Asian coastal regions. A clear diurnal pattern of ClNO₂ was observed at Tung Chung, where ClNO₂ primarily accumulates at night and reach lowest concentrations in the noon-time. Highest ClNO₂ was found during the autumn season followed by spring, winter and summer season. The abundant of ClNO₂ in the four seasons indicate that the production of ClNO₂ is a year-round phenomenon. Data collected at another coastal site, Hok Tsui, also revealed high levels of ClNO₂ of up to 2 ppbv in the continental/urban air masses of Hong Kong and PRD region. Photolysis of ClNO₂ was shown to produce a significant amount of Cl atom with production rate up to 0.02 pptv/s in the early morning. The Cl atom production rates can exceed the P(OH) via O₃ photolysis by several factors. These results suggest that the ClNO₂ plays a major role in jump-starting the atmospheric photochemistry in the polluted marine boundary layer of southern China.

Chapter 5 Optimization of CIMS for N₂O₅ and ClNO₂ measurement in polluted China environment

Measurements of ClNO₂ and N₂O₅ with a TD-CIMS were shown to subject to high interference in Hong Kong. Therefore, we reconfigured the TD-CIMS to an unheated version of CIMS that detects N₂O₅ and ClNO₂ as ion clusters. The heater was removed, and the electric field of the collisional dissociation chamber was reduced to allow more production of I(N₂O₅)⁻ and I(ClNO₂)⁻ cluster ions, which were used to quantify the N₂O₅ and ClNO₂ concentrations. This method had been extensively applied in North America and was believed to be free of interferences (e.g. Kercher et al., 2009). However, its applicability is yet to be tested and verified in the polluted environment of China. A series of development and testing were conducted in the laboratory of The Hong Kong Polytechnic University to improve the quality of the measurements. This chapter first presents results from the calibrations and internal background zeroing of the CIMS. Testing on the inlet transmission efficiency was performed and the ambient N₂O₅ measurement of CIMS was verified by comparing with the N₂O₅ measurement made by a CRDS. The potential application of a corona discharge ion source for ambient measurement of N₂O₅ and ClNO₂ was also assessed.

5.1 Instrument sensitivity towards N_2O_5 and ClNO_2

5.1.1 Calibration

Calibration is an important step to capture the changes in instrument sensitivity due to internal or external factors. A calibration system was developed to calibrate the CIMS. Figure 5.1 shows the setup of the off-line calibration system. It includes a calibrator and two flow controllers used to generate a 5 SLPM stream of humidified zero air. One stream of zero air was controlled by a flow controller (range: 0-5 LPM, Key Instruments) and passed through a water bubbler (filled with ~ 250 ml of ultrapure deionized water). The effluent of the bubbler was then mixed with the other stream of dry zero air which was controlled by another flow controller (range: 0-10 LPM, Key Instruments). The humidity in the zero air stream was adjusted by the different flow rates of the two streams of air. The relative humidity (RH) and air temperature of the humidified zero air stream were monitored with a hygrometer probe. The N_2O_5 or ClNO_2 standard was then added into the stream of humidified zero air prior to the inlet of the CIMS. The location for adding the standard was optimized so that the CIMS could detect the highest possible signals.

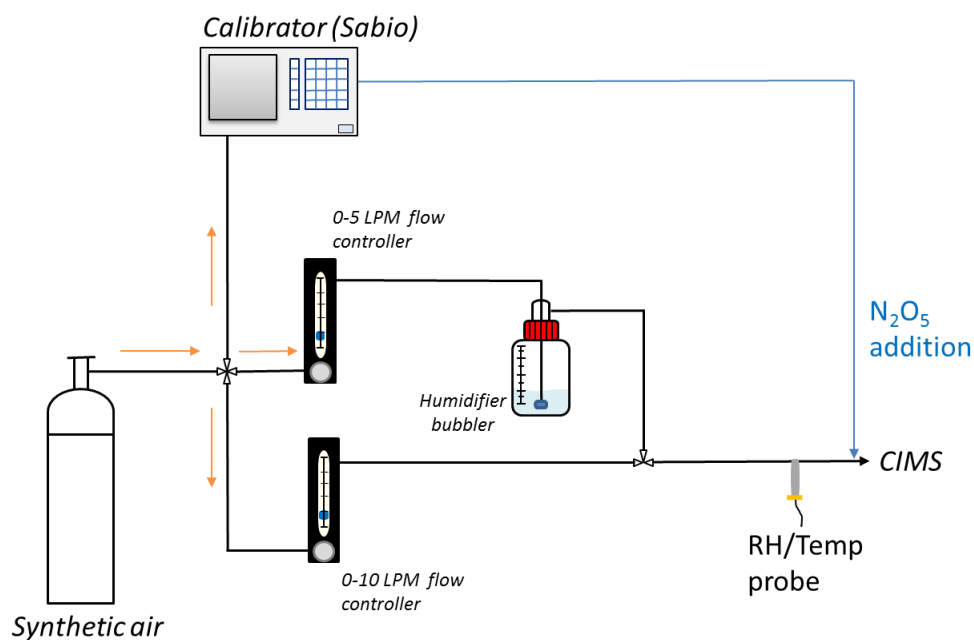


Figure 5.1. Schematic diagram of the off-line calibration system for N_2O_5 . The black line represents $\frac{1}{4}$ " O.D. PFA tubing and blue line is $\frac{1}{8}$ " O.D. PFA tubing.

An example of off-line N_2O_5 and ClNO_2 calibrations in humidify zero air (RH= ~55%) is shown in Figure 5.2. The N_2O_5 signal at 235 *a.m.u.* and ClNO_2 signal at 208 *a.m.u.* response linearly with the increase of the standard concentrations. Linear least squares fits resulted in a slope of 0.97 Hz/pptv and 1.04 Hz/pptv for N_2O_5 and ClNO_2 , respectively, with excellent correlation coefficients ($R^2 > 0.99$). The given slopes may represent the correction factors in units of hertz (Hz) per pptv of N_2O_5 or ClNO_2 .

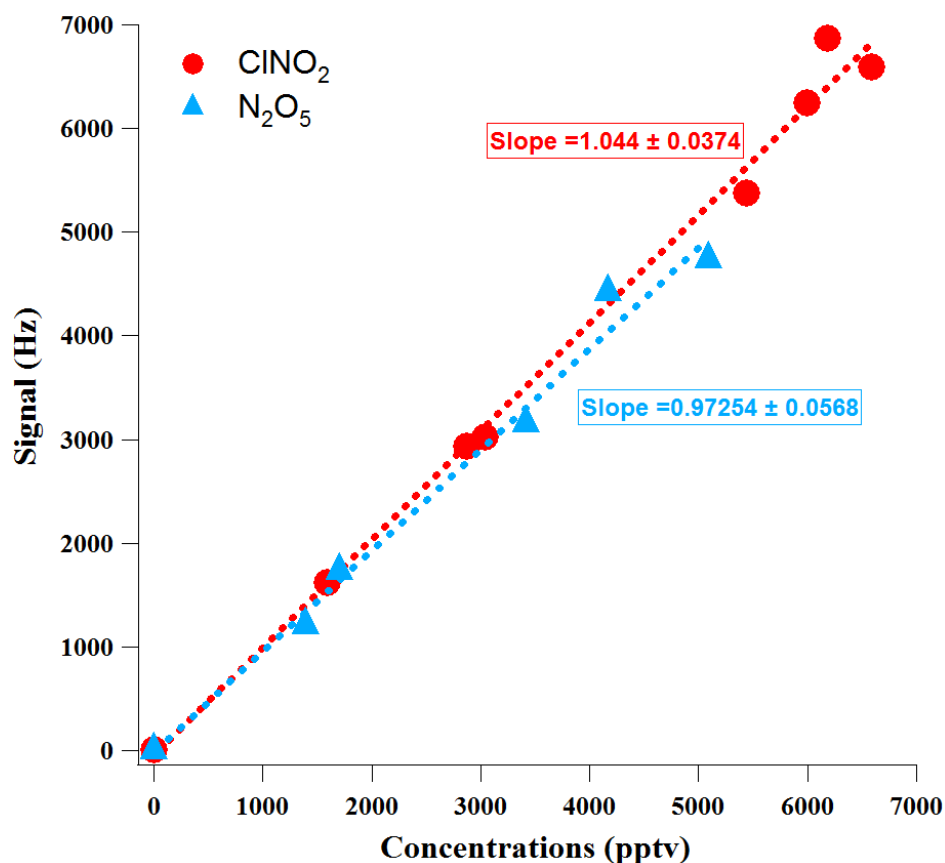


Figure 5.2. The CIMS N_2O_5 and ClNO_2 signal at $\text{I}(\text{N}_2\text{O}_5)^-$ and $\text{I}(\text{ClNO}_2)^-$ versus the concentrations of N_2O_5 and ClNO_2 . The calibrations were conducted in a humidified zero air stream maintained at $\text{RH} \sim 55\%$.

5.1.2 Effect of humidity on the sensitivities of N_2O_5 and ClNO_2

As mentioned in the CIMS ionization scheme of N_2O_5 and ClNO_2 (see Chapter 3), iodide reacts with a water molecule in the sample air to form $\text{I}(\text{H}_2\text{O})^-$ cluster which later reacts with the analytes, N_2O_5 and ClNO_2 , to produce $\text{I}(\text{N}_2\text{O}_5)^-$ and $\text{I}(\text{ClNO}_2)^-$ clusters. It means that the humidity could mediate the clusters formation and affects the sensitivities of N_2O_5 and ClNO_2 during the measurement. Figure 5.3 shows the plots of relative humidity versus the $\text{I}(\text{H}_2\text{O})^-$ and the RH dependence of N_2O_5 and ClNO_2 sensitivities. The curve fittings of the RH and sensitivities of N_2O_5 and ClNO_2 indicated a positive dependence on RH and reached the highest sensitivity at 50%-

70% of RH (shaded in yellow area of Figure 5.3). A comparison of N_2O_5 and ClNO_2 sensitivities in the optimum region (i.e., at $\text{RH} = 60\%$) with those in dry condition (i.e. $\text{RH} < 3\%$) yielded a difference of sensitivity of about 6-9 times, indicating calibrations under dry condition will lead to overestimation of N_2O_5 and ClNO_2 concentrations. As in higher RH condition (after the threshold region), the N_2O_5 sensitivities decreased with further increase in RH, but the sensitivity of ClNO_2 remained relatively constant at a higher RH. These water-dependent results are similar to those observed by other CIMS setups (Kercher et al., 2009; Mielke et al. 2011).

The behaviors of humidity-dependent for N_2O_5 and ClNO_2 sensitivities at low humidity condition can be explained as follows. The addition of H_2O molecules may chemically function as a third body to stabilize the iodide-analyte clusters by distributing the excess energy over a greater number of vibrational modes and carrying away excess energy from the ion-molecule collision, which can lead to the increase of sensitivity (Lee et al., 2014). However, at higher RH, the kinetic enhancement is not enough to compensate for the loss of N_2O_5 to the water (hydrolysis), and therefore the $\text{I}(\text{N}_2\text{O}_5)^-$ formation may decrease with further increase of humidity. By contrast, the ClNO_2 does not exhibit similar behavior at high humidity because it has low water solubility.

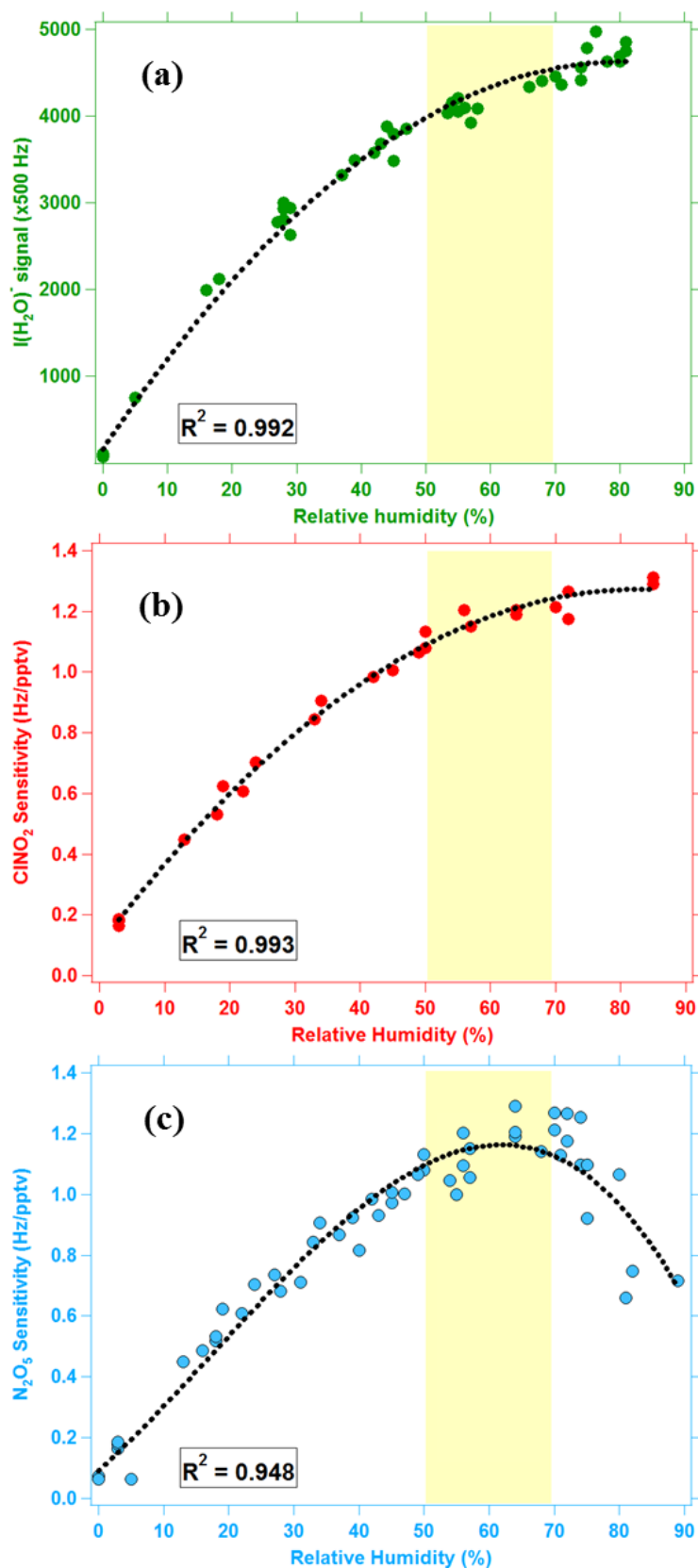


Figure 5.3. The CIMS a) $I(\text{H}_2\text{O}^+)$ ion signal; b) sensitivity of ClNO_2 ; and c) sensitivity of N_2O_5 versus humidity (RH) in the range of 0-90% at room temperature. The color circle dots represent the experiment data and the break-line is the trend-line of curve fittings.

5.2 Determinations of instrument zero and detection limits

In order to account for the CIMS signal of $I(N_2O_5)^-$ and $I(ClNO_2)^-$ that are not due to N_2O_5 or $ClNO_2$, a background zeroing system was developed (see section 3.4) and tested in the field. The N_2O_5 and $ClNO_2$ were scrubbed from ambient air by the zeroing system, and the remaining signal was recorded as background signal which includes the internal electronic noise and interferences (ions that have the same *a.m.u.* with the N_2O_5 and $ClNO_2$ iodide clusters). Figure 5.4 displays a typical time series of ambient and background signals for N_2O_5 (235 *a.m.u.*) and $ClNO_2$ (208 *a.m.u.*). The N_2O_5 showed ambient signals in the range of 20-100 Hz and had background signals of ~10 Hz when background zeroing was performed. Whereas, the ambient signal for $ClNO_2$ ranged from 40-260 Hz and the background signals were about 10 Hz. By using the example sensitivity of N_2O_5 and $ClNO_2$ shown in Figure 5.2, the background concentrations of N_2O_5 (10 Hz/0.97 pptv/Hz) and $ClNO_2$ (10 Hz/1.04 pptv/Hz) were ~10 pptv. Testing with others background zeroing method such as by-passing the sample air through a fully-packed activated carbon tube or purging the instrument with zero gas showed similar background signals with those determined by the hot tube zeroing system ($p < 0.01$).

The minimum concentration that can be detected by the instrument is termed as the detection limit. It can be statistically differentiated from the instrumental signal to noise (S/N) ratio, and the equation used for the determination of detection limits of the CIMS is the following:

$$S_m = S_{bkg} + k\sigma_{bkg} \quad (5.1)$$

$$\text{Detection limit} = \frac{S_m - S_{\text{bkg}}}{\text{Sensitivity}} \quad (5.2)$$

Here, S_m is the minimum distinguishable signal (determined from equation 5.1), S_{bkg} is the mean background signals (when N_2O_5 and ClNO_2 are not present in the system) correspond to the time intervals of ion measurement, k is the confidence level to be used in the calculation, ranging from 1 to 3, and σ_{bkg} is the standard error of the background signals. Based on the 1 min averaged background signal of N_2O_5 and ClNO_2 and the sensitivities determined in Figure 5.2, the detection limit (3σ) of the CIMS was 5 pptv for both N_2O_5 and ClNO_2 .

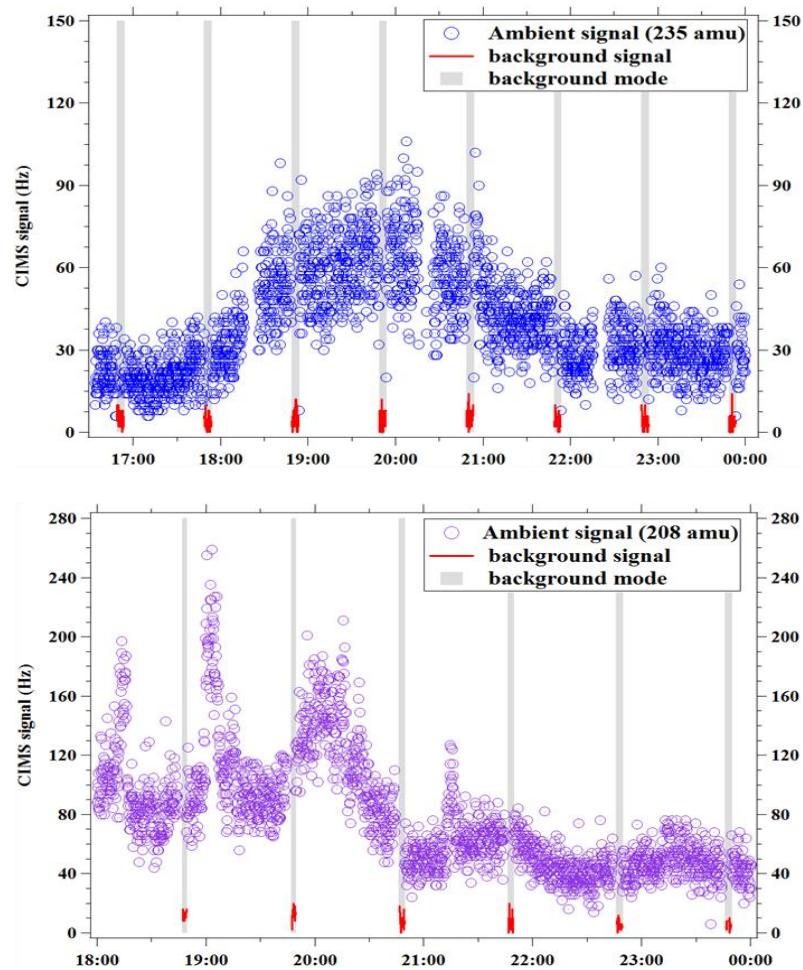


Figure 5.4. An example of raw background signal versus ambient signal for N_2O_5 (upper panel) and ClNO_2 (lower panel) taken at 8-s time resolution. During ambient measurement, background measurements were performed for a duration of 3 min in every hour.

5.3 Inlet transmission efficiency

The measurement can be affected by the aerosol deposition on the sampling inlet of the instrument. If chloride aerosol deposited on the surfaces of the inlet, ClNO₂ can arise from the N₂O₅. A series of testing was performed to monitor the potential conversion of N₂O₅ and ClNO₂ in inlet used for ambient sampling and to evaluate the potential application of a Teflon filter in the sampling inlet to reduce inlet artifact.

5.3.1 Conversion of N₂O₅ to ClNO₂ on the inlet

An entirely new 2-m long PFA tubing with an addition port (a PFA union tee) fixed at the front (at the beginning of the tubing) and rear (~10 cm before the CIMS inlet) was used to investigate the inlet chemistry. A known concentration of N₂O₅ (4.1 ppbv) was alternately added through the two addition port into a stream of 6 SLPM humidified zero gas with RH controlled at ~60% (for optimum instrument responses, see Figure 5.3) to detect the changes of N₂O₅ and ClNO₂ signals between the two locations. Figure 5.5 illustrates the percentage of the N₂O₅ signal loss and increase of ClNO₂ in relative to the added N₂O₅ for different 'age' of inlet conditions. The new sampling inlet gave an average N₂O₅ signal loss (at 235 *a.m.u.*) of 10% but did not show any statistical difference in the ClNO₂ signal (at 208 *a.m.u.*). This N₂O₅ signal loss is likely attributed to the first-order loss process through the wall of the inlet instead of the effect of aerosol depositions. Then, the new inlet was allowed to sample the ambient air for 24 hours (1 day) and again tested with the additions of N₂O₅ in humidified zero air as mentioned above. About 22% of N₂O₅ signal loss was observed

in the '1 day' old inlet. The ClNO₂ signal also increased from <1% to 3% of the added N₂O₅ signal. Continuously sampling with the same inlet for a total of 7 days led to 41% loss of N₂O₅ and 7% of the added N₂O₅ signal was converted to ClNO₂. This enhancement suggests that the inlet is significantly affected by the ambient aerosol in particularly the chloride aerosol over the time. Previous studies at this location showed elevated PM₁₀, PM_{2.5}, and fine chloride aerosol with an average concentration of 84 μg/m³, 51 μg/m³ and 0.3 μg/m³, respectively (e.g. Ho et al., 2003). All of these testings were repeated for at least three times, and the standard deviation was shown by the error bars in Figure 5.5. Therefore, we suggest that daily replacement of the sampling line with a new set of inlet would be highly desirable for quality measurement of N₂O₅ and ClNO₂ in high aerosol loading environment of China.

However, the practice of frequent replacement of the sampling line will increase the operation cost. Considering the balance between quality measurement and the operation cost, we attempted to wash the sampling line (tubing and fittings) with phosphate/chlorine-free detergent solution (Decon90), ethanol (Sigma-Aldrich, 99.99%) and ultra-pure deionized water under ultrasonic bath (50°C). The fittings and tubing were later dried in an oven (at 110°C) for overnight before usage. As expected, the "new" sampling line showed a significant reduction of N₂O₅ loss to 14%, which was comparable to the brand new sampling inlet. Furthermore, the ClNO₂ signal did not show sign of increase (<1%) in the washed inlet. On-site tests in the later field measurements also indicated that the washing practice limited the loss of N₂O₅ on the inlet to about 10%.

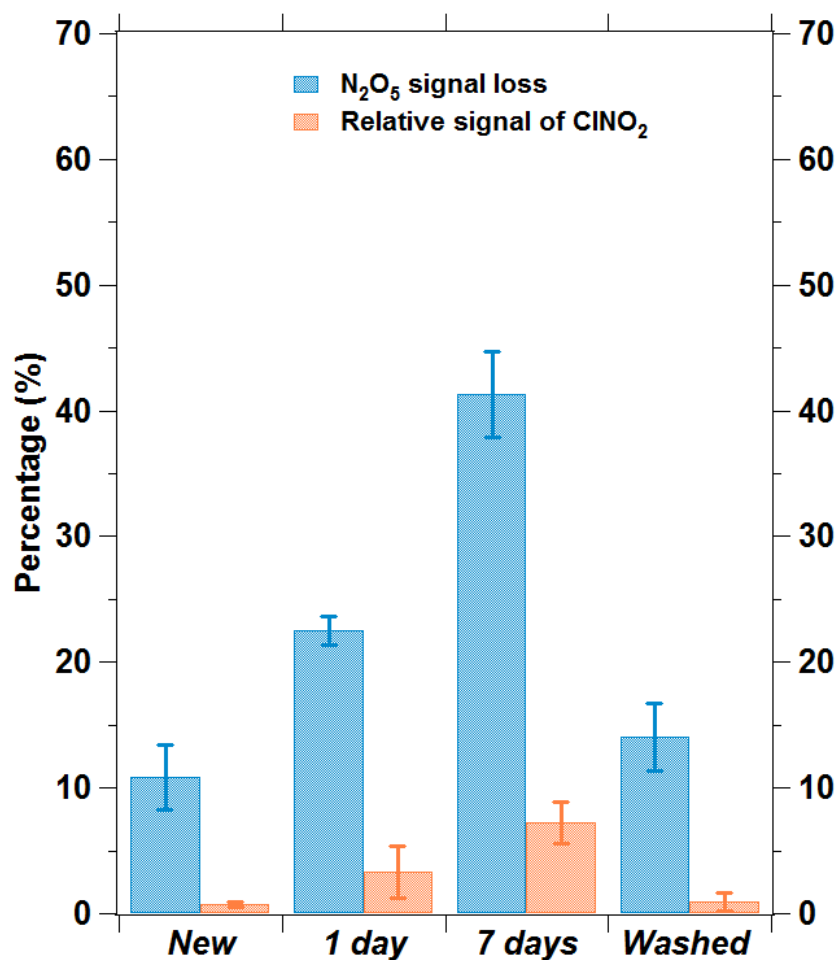


Figure 5.5. Percentage of the N₂O₅ signal loss and relatively increase in ClNO₂ signal in different types of inlet condition. The testing was performed by adding 4.1 ppbv of N₂O₅ into a stream of humidified zero air (RH=60%) at room temperature. Error bars represent the standard deviation of the tests ($n=3$).

5.3.2 Conversion of N₂O₅ to ClNO₂ on Teflon filter

As the N₂O₅ and ClNO₂ measurement are susceptible to potential inlet losses and interference due to particle deposition on the sampling line, addition of a Teflon filter before the inlet can be a good solution to prevent the aerosol from contaminating the sampling line. Indeed, this method has been applied in previous field studies in the U.S. (e.g. Dubé et al., 2006; Mielke et al., 2013). The question arises here is whether

the addition of Teflon filter is applicable in a polluted environment like Hong Kong or China.

To investigate its applicability, a filter holder (47 mm diameter) with Teflon filter (2 μm pore size, Pall Corp.) was attached at the front of the inlet and was allowed to sample ambient air for an interval of 2 hours. In between the interval, the passing efficiency of N_2O_5 through the Teflon filter was assessed by adding 4.1 ppbv of N_2O_5 into 6.0 S.LPM of ambient air. Figure 5.6a shows the evolution of percentage of N_2O_5 loss and the conversion to ClNO_2 in the interval of 2 h of ambient sampling. There was no significant difference in the N_2O_5 and ClNO_2 signals ($\leq 3\%$) for the control (without the Teflon filter inside the filter housing), sampling time (t) at zero (completely clean filter) and t at 30 min. The N_2O_5 loss rate on the filter surface was subtle at these stages ($< 0.01\%$ /min). However, the total percentage of N_2O_5 loss increased by a factor of 2, up to 7.2% after an hour of sampling and the estimated N_2O_5 loss rate was 0.14 %/min in between t = 30-60 min. The slower N_2O_5 loss rate of 0.06 %/min was observed in the final 1 hour (t = 60-20 min) and the total N_2O_5 loss reached up to ~11% at the end of the sampling.

The non-linear increment of N_2O_5 loss is unlikely to be due to the changes of other ambient factors like NO and RH as the measurement showed that NO and RH remained at around 2 ppbv and 45%, respectively, during the testing period. Instead, the testing results indicate that the filter aging which depends on the aerosol mass loading decreases the transmission efficiency of N_2O_5 through the filter. The aerosol accumulated on the surface of the Teflon filter provides abundant surface area for the heterogeneous uptake of N_2O_5 . It can be further supported by the increasing trend of

the percentage of 208 *a.m.u.* signals relative to the added N₂O₅ during the sampling duration.

Immediately after 2 hours of sampling, the aged-Teflon filter was tested with different RH to determine the combined effect of aerosols and water vapor on the N₂O₅ transmission efficiency. The percentage of N₂O₅ loss and increase of ClNO₂ relative to N₂O₅ versus the relative humidity was shown in Figure 5.6b. The percentage of N₂O₅ signal loss fall in the range of 6-12 % at lower RH regime (RH≤54%). A dramatic increase of N₂O₅ loss up to 40% was observed at 75% of relative humidity, and similar trend was observed in the ClNO₂ signal. The calculated N₂O₅ loss rate of 20% h⁻¹ was akin to the range of laboratory results from Fuch et al., (2008), where N₂O₅ loss rates of 2.4-30 % h⁻¹ were found on the Teflon filter with aerosol mass loading of 70-360 μg/m³ at RH of 78%. We, therefore, can conclude that the increase of RH together with aerosols on the Teflon filter synergize the N₂O₅ loss and enhance ClNO₂ production in the sampling line system.

Although we do not have direct aerosol measurements to quantify the exact particle loadings on the filter, the testing suggests that replacement of filter within the interval of 30 min of sampling is required to avoid a significant N₂O₅ loss on the filter. This duration is shorter than the recommendations of Dubé et al., (2006) and Fuch et al. (2008) because the ambient mass loading of aerosol in China is much higher than those found in the US and Europe (e.g. Querol et al., 2004; Tie et al., 2006; Lai et al., 2007). Combining with the high RH condition in Hong Kong, larger N₂O₅ loss and ClNO₂ artifact on the filter surfaces are expected, and more frequent replacement of

filter is required to assure good quality measurements. With this, the maintenance and operating cost will be increased and is inconvenient for long term field measurements.

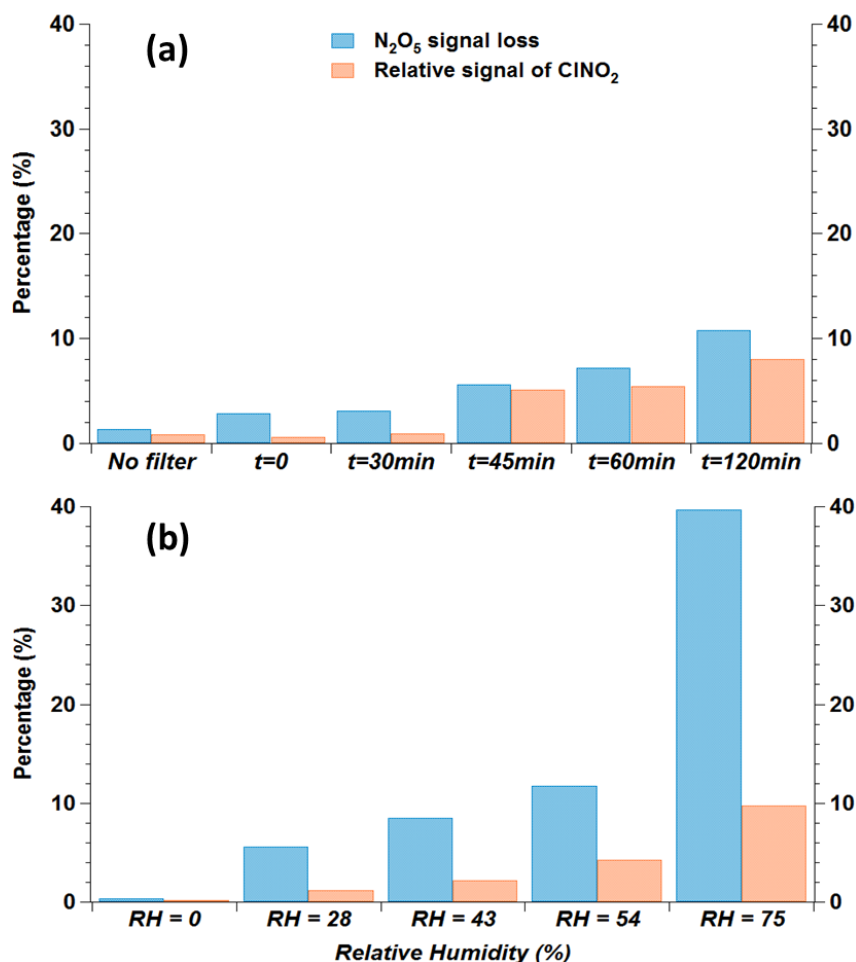


Figure 5.6. Percentage of N₂O₅ loss and relative ClNO₂ signal on Teflon filter for a) empty filter housing and intervals between 2 hours of ambient sampling b) the aged-filter (2-hour ambient sampling) in different RH conditions.

5.4 Ambient trial run

After the optimization of the CIMS, an ambient trial run was conducted in the laboratory located on the 8th floor of a building on the main campus of Hong Kong Polytechnic University to assess the performance and reliability of the optimized CIMS in measuring ambient ClNO₂ and N₂O₅. During the measurement, the inlet was

wrapped with tube insulator and heated at $\sim 30^{\circ}\text{C}$ to prevent drastic changes of RH in the sample due to the temperature difference between the outdoor and indoor air. Background zeroing was determined every hour. A known concentration of N_2O_5 (1.2 ppbv) was automatically added into the sample flow every hour to monitor the inlet chemistry as well as the changes in the instrument sensitivity due to RH. Figure 5.7 shows an example of hourly N_2O_5 addition signals for a night. The sensitivity determined from the hourly additions of N_2O_5 did not show a significant difference between day and night, indicating that the sensitivity of the CIMS was stable throughout the day. The hourly sensitivity was then interpolated into the measurement time base and was used for correcting the ambient data. The accuracy of the optimized CIMS was determined to be 25% with a precision of 3%.

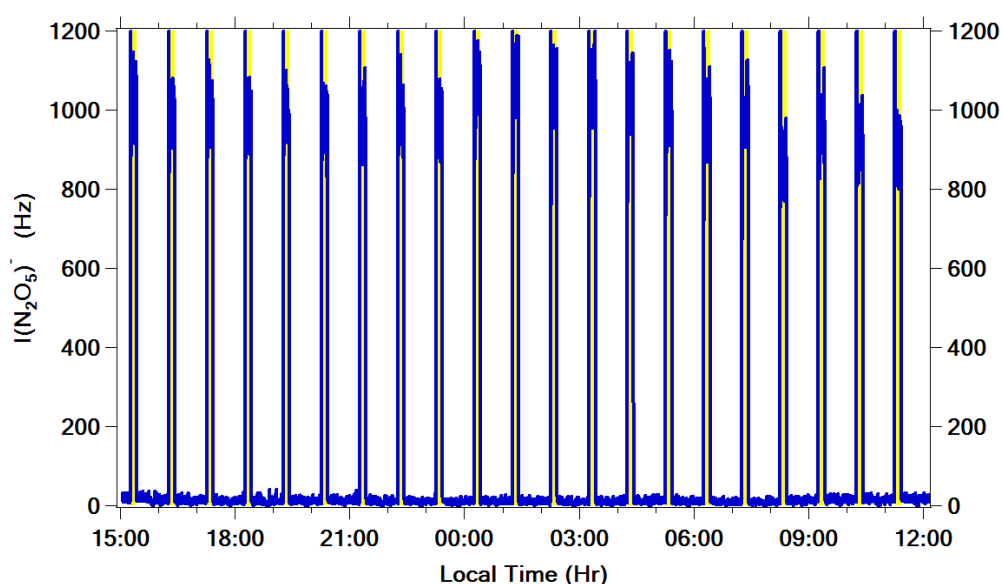


Figure 5.7. An example of the $I(\text{N}_2\text{O}_5)^-$ signal in standard addition of N_2O_5 (yellow zone) during ambient measurement.

Figure 5.8 illustrates the mixing ratios of N_2O_5 and ClNO_2 , together with NO_x and O_3 for 3 days of measurement. N_2O_5 and ClNO_2 were only observed during night,

increasing at sunset with maximum concentrations of 351 and 375 pptv for N_2O_5 and $ClNO_2$, respectively. Both N_2O_5 and $ClNO_2$ started to decline at sunrise due to the fast photolysis of NO_3 and $ClNO_2$ and achieved the lowest concentration at noon-time. The observation was in contrast to the previous N_2O_5 measurement with TD-CIMS at the same location which showed huge noon-time peak of the N_2O_5 signal at 62 *a.m.u.* (see X.Wang et al., 2014). This observation suggests that the $I(N_2O_5)^-$ (at 235 *a.m.u.*) was not subject to interference from PAN+ NO_2 as shown in the 62 *a.m.u.* signal.

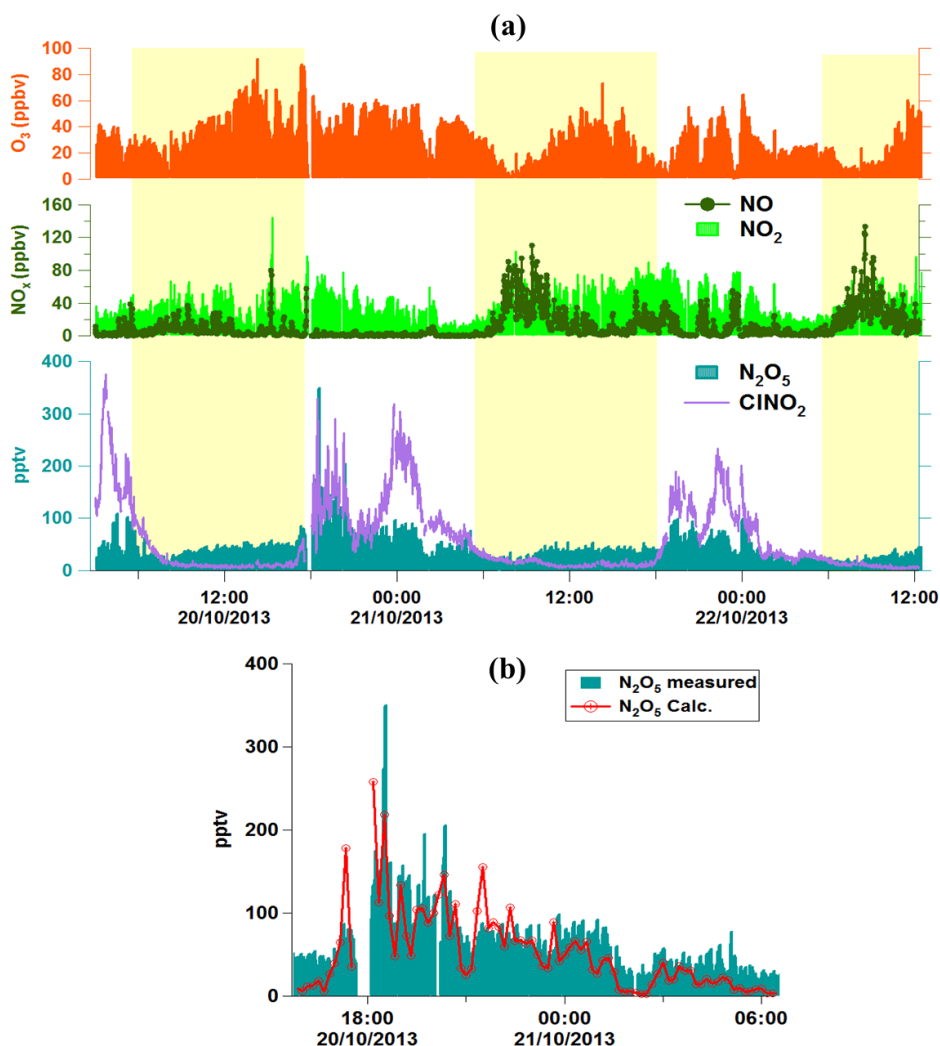


Figure 5.8. a) The concentration of N_2O_5 and $ClNO_2$ measured at Hong Kong Polytechnic University for 3 continuous nights. The yellow-shaded zone represents the daytime. b) A subset of measured N_2O_5 versus steady-state calculated N_2O_5 on the night on 20-21 October 2013.

It was reasonable that the N_2O_5 was low in concentration for the majority of the night-time because the site was highly influenced by the high NO from the nearby traffic (about 300 m away to the highway connecting to the Cross-Harbour Tunnel). The emitted NO will efficiently titrate the NO_3 and caused N_2O_5 dissociation to NO_3 . Steady state calculations of the N_2O_5 concentrations with the assumption that the N_2O_5 is only loss through $\text{NO}+\text{NO}_3$ pathway agreed with the measured N_2O_5 over the night, as shown in Figure 5.8b. The results assured that the measured signal at 235 *a.m.u.* was N_2O_5 .

5.5 Verification of ambient measurement

Further verification of the ambient measurements of N_2O_5 by the CIMS was performed in a later field study at TMS by comparing the results with those obtained from the CRDS of the NOAA (National Oceanic and Atmospheric Administration, US). The NOAA-CRDS has been previously used as the benchmark for N_2O_5 measurements in chamber studies with different types of instruments (Fuch et al., 2012). Figure 5.9 presents the scatterplot of the data from the two instruments based on the 1 min data collected in 12 days which CIMS measurements were available. The overall results showed an excellent agreement between the data set, with a correlation coefficient (R^2) of 0.93, a slope of 0.99 and intercept of 30, based on a reduced major axis (RMA) regression analysis. An example of the time series of the N_2O_5 mixing ratios from CIMS and CRDS on 1-2 December 2013 showed that the N_2O_5 correlates well in both night-time and daytime measurement. This excellent correlation indicates that our optimized CIMS is capable of measuring N_2O_5 in polluted China environment.

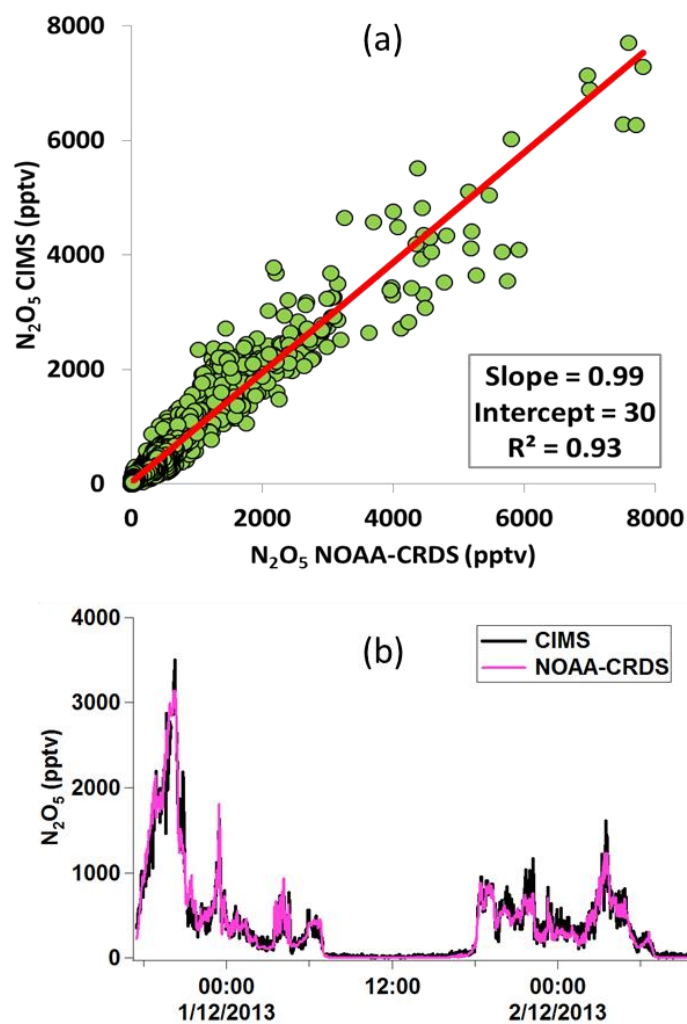


Figure 5.9. Scatterplot between 1 min averaged N_2O_5 mixing ratios from the NOAA-CRDS (x-axis) and from the CIMS (y-axis) for 12 days ($N = 9148$). a) Solid line (red) represents an RMA linear fit and b) an example of N_2O_5 mixing ratios from CIMS and CRDS during night-time and daytime.

To make sure that the measured signal at 208 *a.m.u.* was $CINO_2$ or to exclude the potential interferences from other ions which happened to have a similar atomic mass of 208 *a.m.u.* (e.g. $I^{81}Br^-$ ions from bromide containing species), the raw signal obtained at $I^{35}CINO_2^-$ (208 *a.m.u.*) was plotted against the signal of its chlorine isotope, $I^{37}CINO_2^-$ measured at 210 *a.m.u.*. Figure 5.10 displays the scatter plots of 208 *a.m.u.* versus 210 *a.m.u.* signals obtained from field measurements conducted in Hong Kong

Polytechnic University, TMS, and Wangdu. Linear fits of the signals yielded slopes between 0.31-0.33, which were $\pm 3\%$ to that theoretical chlorine isotopes ratio of 0.32, with correlation coefficients (R^2) larger than 0.96. These observations further assured that the measured signals were of a chlorine-containing species.

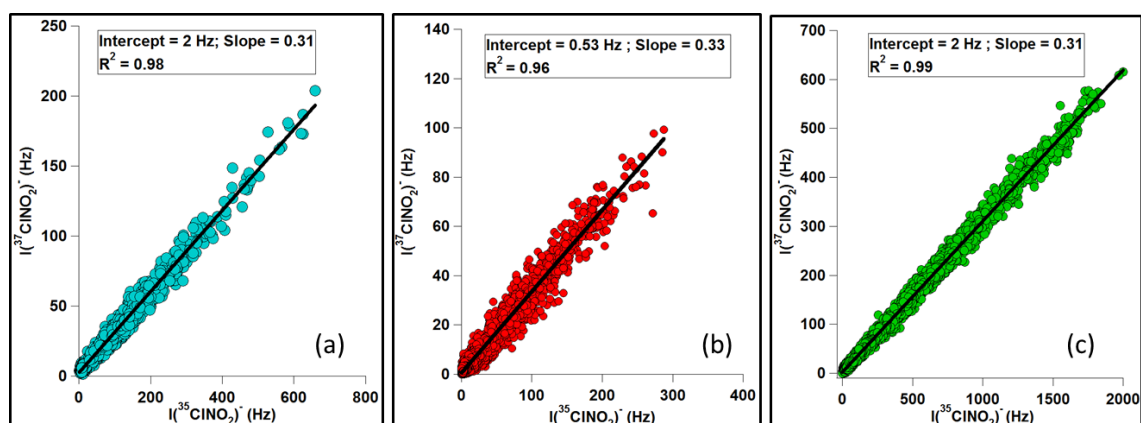


Figure 5.10. Scatter plots of 1 min averaged raw ambient signal of 208 *a.m.u.* with 210 *a.m.u.* measured at a) Hong Kong Polytechnic University b) TMS and c) Wangdu.

5.6 Testing on corona discharge as ionization source

Considering the strict government safety regulations, potential health risk to the user and the higher operating costs of using a radioactive (^{210}Po) ion source, testing on a corona discharge ion source as an alternative to the original ^{210}Po radioactive ion source was conducted for measurement of N_2O_5 and ClNO_2 . This testing was performed at a laboratory in Shandong University, Jinan and also during the field campaign in Wangdu, China.

5.6.1 Setup of corona discharges ion source

The corona discharge device was built and supplied by THS Instruments (Atlanta, USA). This corona-discharge device is only a prototype, but the similar principle and design have been applied by Kürten et al., (2011) for sulfuric acid measurement. Figure 5.11 shows the simplified schematic of the corona discharge ion source. The outer case which houses the ion source is made of a stainless steel cylinder and is attached to the customized flow tube (3.4 cm internal diameter (I.D.) and 13 cm length). The length of the outer cylinder corona ion source is 9 cm with a diameter of 1.7 cm. Inside the cylinder of corona ion source is lined with polyamide sheet (Kapton®, DuPont, USA) as an insulator. To create the corona discharge, a sharp end needle of 3 cm length was held in the middle of a brass connector attached to a custom-made SHV connector which was connected to a negative high voltage supply. The type of needle used in this setup is a gold-coated acupuncture needle with an outer diameter of 0.4 mm (Cloud & Dragon Medical Device, China) since the gold-plated needle has been demonstrated to be durable and generate relatively low NO_x and O₃ (Asbach et al., 2005). A mixture of CH₃I in N₂ was introduced into the corona device to generate reagent ion (I⁻) which then entered the reaction chamber (flow-tube) via an orifice with a diameter of 1 mm.

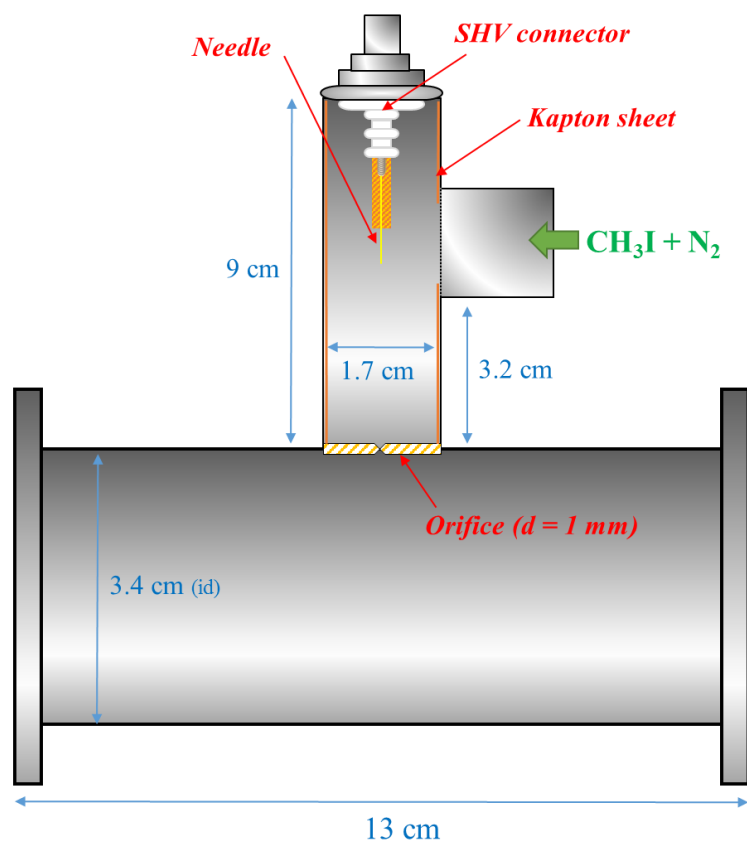


Figure 5.11. Schematic drawing of corona discharge ion source built by THS Instrument.

5.6.2 Sensitivity

After the setup of the corona discharge ion source, N_2O_5 and ClNO_2 calibrations were performed with the same method as discussed in section 5.1 with variable RH. As can be seen in Figure 5.12, the sensitivity of N_2O_5 and ClNO_2 are very low (~ 0.2 Hz/pptv) when the RH is smaller than 5%. The sensitivities of N_2O_5 and ClNO_2 reached up to 1.3 Hz/pptv and 1.1 Hz/pptv, respectively, in the optimal RH range (50%-70%). Although not directly comparable with the sensitivities from the radioactive ion source due to the different of retention time in the IMR (larger flow-tube volume for the corona setup), the trend of the curve fits for both N_2O_5 and ClNO_2

sensitivities have almost similar responses as displayed by the ^{210}Po radioactive source (comparing with Figure 5.3).

Theoretically, higher sensitivity is expected from the corona source setup because the retention time in the flow-tube will be longer for reactions of iodide and analytes to occur. However, the ratios of the N_2O_5 and ClNO_2 sensitivity from corona and radioactive were about equal to each other at different RH (see Figure 5.12), indicating a “suppression” of sensitivity in the corona discharge setup. This could be due to smaller amount of total I^- produced from the corona discharge source relative to the radioactive source. The difference, in fact, can be seen in the counts of I^- at 127 *a.m.u.* (data not shown here). The reduction in the reagent ions production may be due to: 1) human error during installing the needle (i.e. length and position) in aligning with the pinhole (between the corona and IMR), possibly creating an asymmetry ion distribution and may cause iodide ion loss or not homogenously distributed in the flow tube (Kürten et al., 2011); 2) Iodide was generated in the corona only by a point source (corona needle) rather than over a complete circular cross section like in the radioactive source. Thus, the ionization efficiency may be lower compared to the radioactive source.

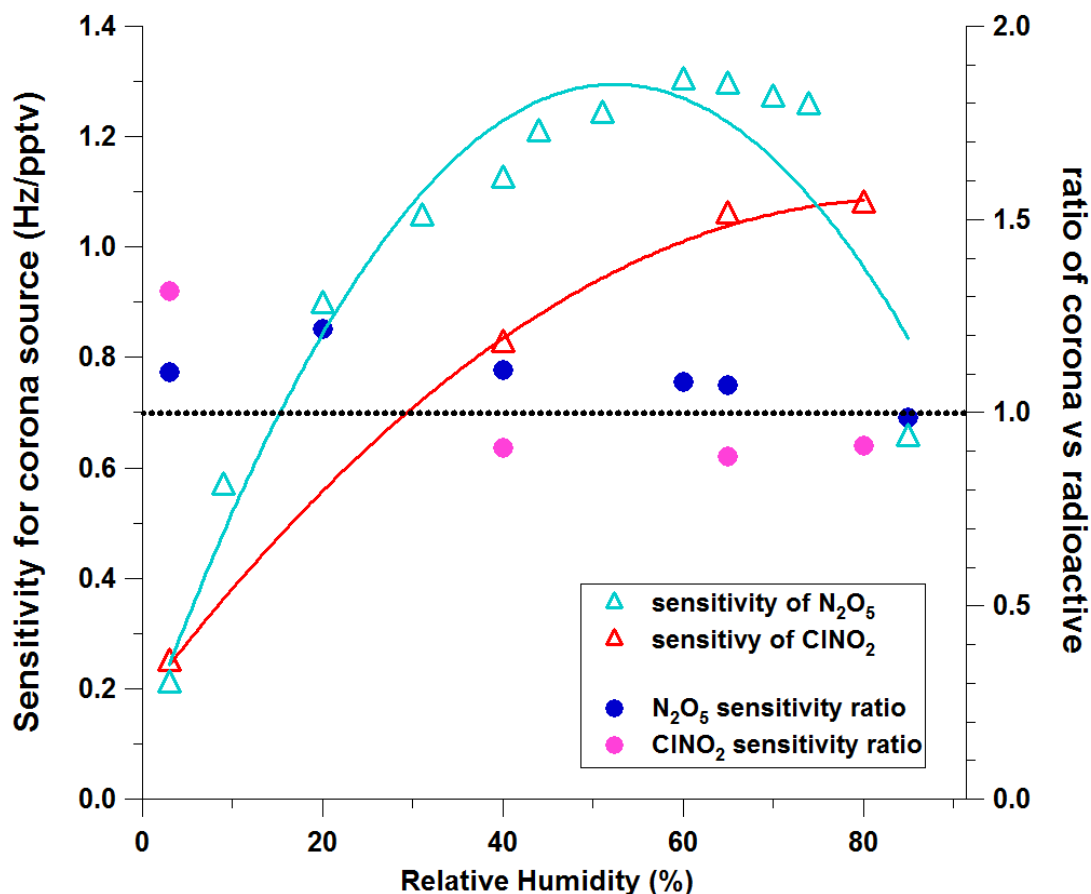


Figure 5.12. Sensitivity of N_2O_5 and $ClNO_2$ as a function of relative humidity. The blue and red solid lines are the curve fits for the data. Ratio of the sensitivity from corona to radioactive source is shown on the right y-axis.

5.6.3 Mass spectra of $I(N_2O_5)^-$ and $I(ClNO_2)^-$

Mass scans from 20 *a.m.u.* to 250 *a.m.u.* were performed in separated conditions: 1) ambient measurement by using a corona source; 2) ambient measurement by using radioactive source; and 3) calibrations, to obtain the mass spectra for $I(N_2O_5)^-$ and $I(ClNO_2)^-$. Figure 5.13 illustrates the expanded view of mass spectra for $I(N_2O_5)^-$ and $I(ClNO_2)^-$ under the different conditions. For the measurement with corona source, the $I(ClNO_2)^-$ showed two clear peaks at 208 *a.m.u.* and its isotopic chlorine at 210 *a.m.u.*, while the $I(N_2O_5)^-$ displayed a distinct peak at 235 *a.m.u.*. The results are identical to those observed with a radioactive source. A comparison with

the benchmark peaks of $\text{I}(\text{N}_2\text{O}_5)^-$ and $\text{I}(\text{ClNO}_2)^-$ scanned during the calibration with a radioactive source setup, did not vary significantly with the ambient scans.

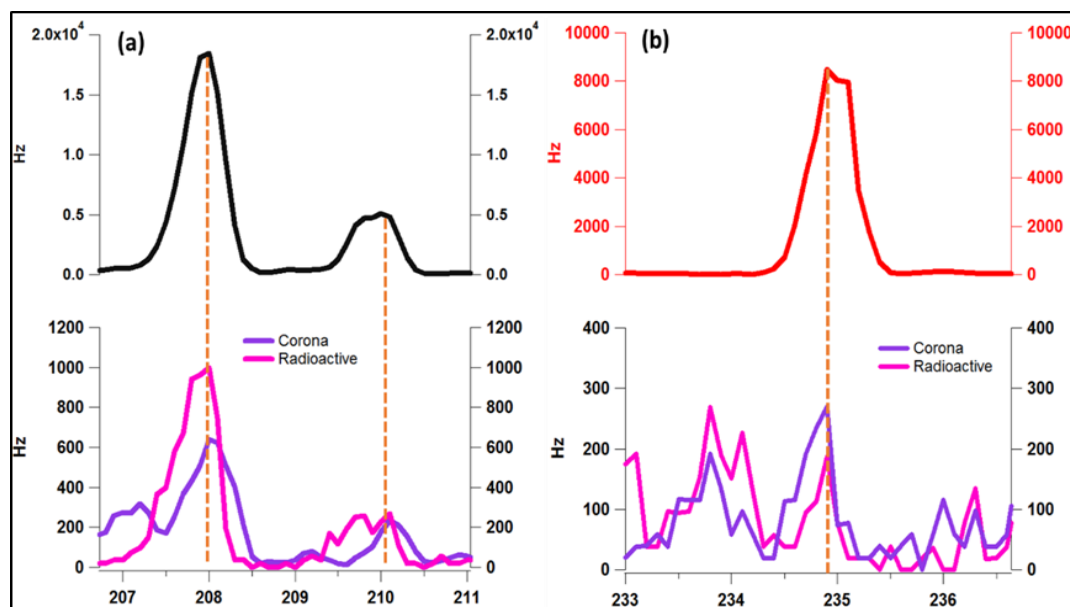


Figure 5.13. Examples of mass spectrum for a) $\text{I}(\text{ClNO}_2)^-$ (208 *a.m.u.*) and b) N_2O_5 (235 *a.m.u.*) measured with corona discharge and radioactive ion source. The upper panel shows the mass scans of $\text{I}(\text{N}_2\text{O}_5)^-$ and $\text{I}(\text{ClNO}_2)^-$ during calibration with a radioactive ion source.

5.6.4 Background and detection limits

The background signal for N_2O_5 and ClNO_2 measured with corona discharge ion source was determined with the zeroing system (same as that described in section 5.2). Figure 5.14 shows the distribution of N_2O_5 and ClNO_2 background signals from corona and radioactive source. A Gaussian function fitted to the distribution of background signal from a corona source centered at 40 Hz for both N_2O_5 and ClNO_2 . In comparison, the fit of background signals given by a radioactive source setup centered at 10 Hz or below for N_2O_5 or ClNO_2 . The higher background noise in the corona source is probably due to the additional oxidation of chemical compounds in

the sampled air by radical produced during the corona discharge processes (Jost et al., 2003; Kukui et al., 2008). With the 1 min averaged data background signals and the optimum calibration factors determined in Figure 5.12, the detection limit of CIMS with corona ion source was calculated to be 16 pptv for N_2O_5 and 14 pptv for ClNO_2 (3σ). The detection limits were about 3 times larger than those determined from CIMS operated with a radioactive source.

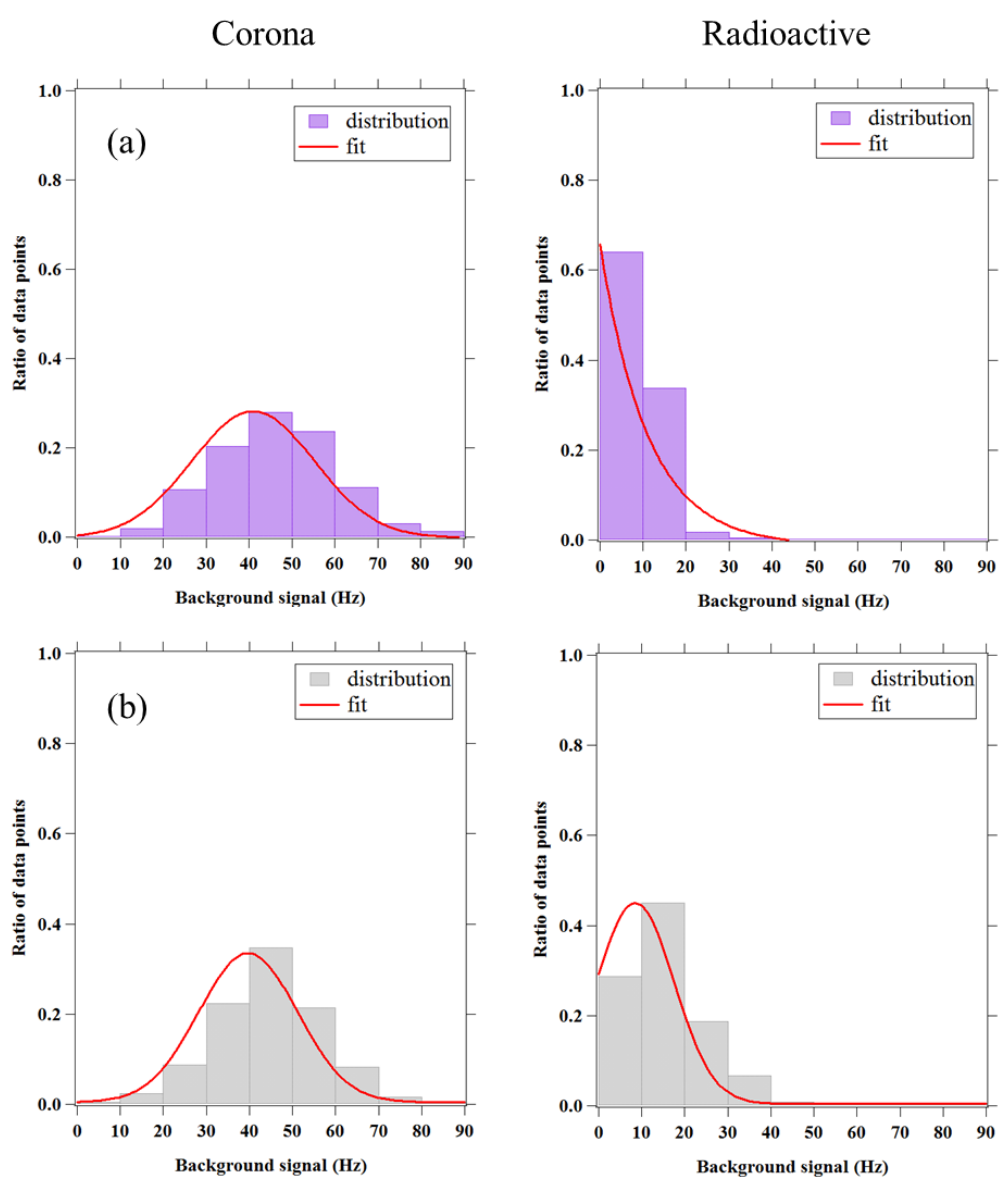


Figure 5.14. Distributions of ambient background signals for (a) ClNO_2 (in purple) and (b) N_2O_5 (in gray) from CIMS operated with corona discharge source and ^{210}Po radioactive source ($N = 902$).

5.6.5 Ambient performance and signal stability

The stability and performance of the corona discharge ion source can be affected by the variation of ambient conditions or over the time duration. Therefore, the performance of the corona discharge ion source was evaluated in continuous ambient measurements. The stability of ambient signal of the iodide-water clusters, N_2O_5 and ClNO_2 , were monitored for the whole night. Figure 5.15 depicts an example of time series of the ambient $\text{I}(\text{H}_2\text{O})^-$, $\text{I}(\text{N}_2\text{O}_5)^-$ and $\text{I}(\text{ClNO}_2)^-$ over the night. It can be seen that the signal of $\text{I}(\text{H}_2\text{O})^-$ did not drift over the night. Further checking upon the ratios of the $\text{I}(\text{H}_2\text{O})^-$ to I^- signal by occasional mass scanning also found that the ratio remained at ~ 0.25 (data not shown) throughout the night. These suggest that the corona ion source produced a stable flow of reagent ions (I^-).

The plot also illustrates that the $\text{I}(\text{N}_2\text{O}_5)^-$ and $\text{I}(\text{ClNO}_2)^-$ signals began to increase as soon as the sun set. The $\text{I}(\text{N}_2\text{O}_5)^-$ signal showed a significant peak between 19:00 to 21:00, while the $\text{I}(\text{ClNO}_2)^-$ signal kept increasing toward the midnight. On three occasions, the background zeroing of N_2O_5 and ClNO_2 were determined, and the signals immediately decreased from hundreds of counts to about 50 Hz. Then a stable N_2O_5 concentration of 1.5 ppbv was added into the sampling line at 20:37 (local time) for ~ 5 min. The N_2O_5 signal increased drastically within seconds and became stable at ~ 900 Hz (1 min average), before decreasing rapidly back to ambient level. There were no significant changes in the $\text{I}(\text{ClNO}_2)^-$ signals during the period of N_2O_5 addition, indicating no production of ClNO_2 within the CIMS system. These results suggest that the N_2O_5 and ClNO_2 are responding well to the changes of concentrations during the ambient measurement with a corona source.

Although the testing results may indicate that the corona discharge ion source was working well in the ambient measurement, over a longer time scale (~36 hours), a sudden drop in the $I(\text{H}_2\text{O})^-$ signal was observed while other signals became unstable. Such sudden changes are not common in the radioactive ion source. Upon closer inspection of the corona discharge ion source, we found that the gold-coated needle used in the corona was corroded, and the tip was darkened (see Figure 5.16). Replacing a new needle returned the signals to a normal level. These results may suggest that the needle used in the current corona source setup needs replacement within 36 hours of operation.

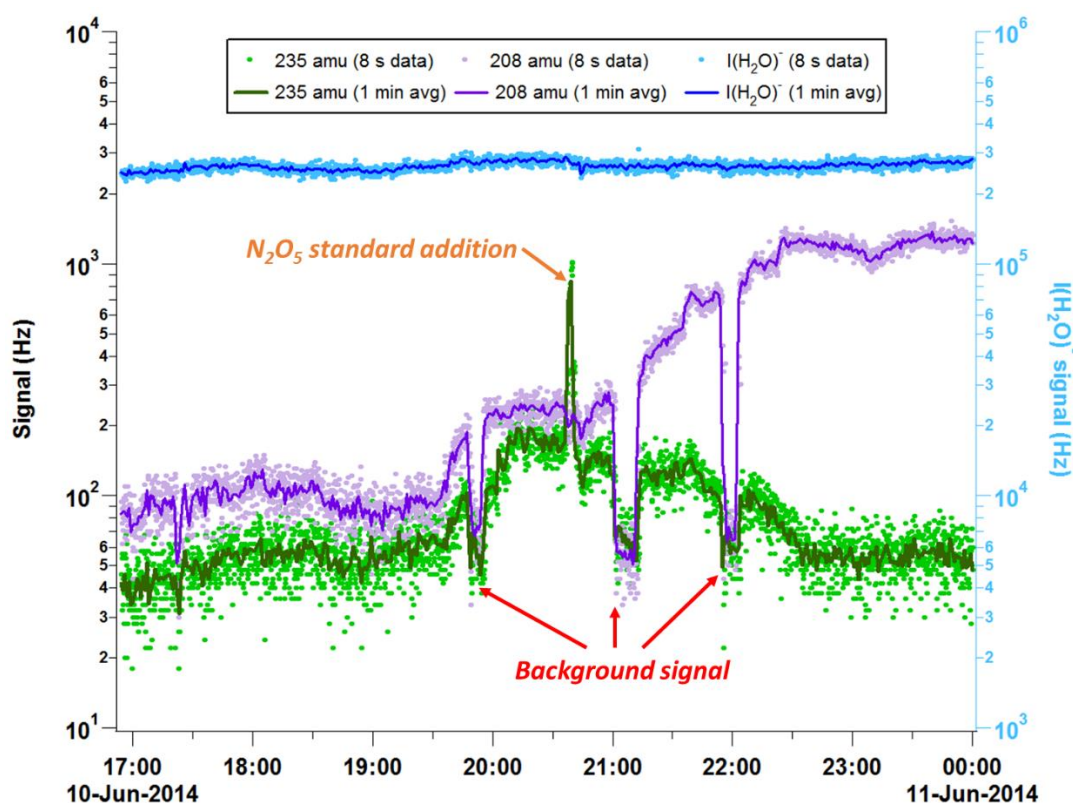


Figure 5.15. Time series of the raw ambient signal measured CIMS operated with a corona ion source. Dots represent the 8-s signal data and the solid lines are the 1-min average signal data.

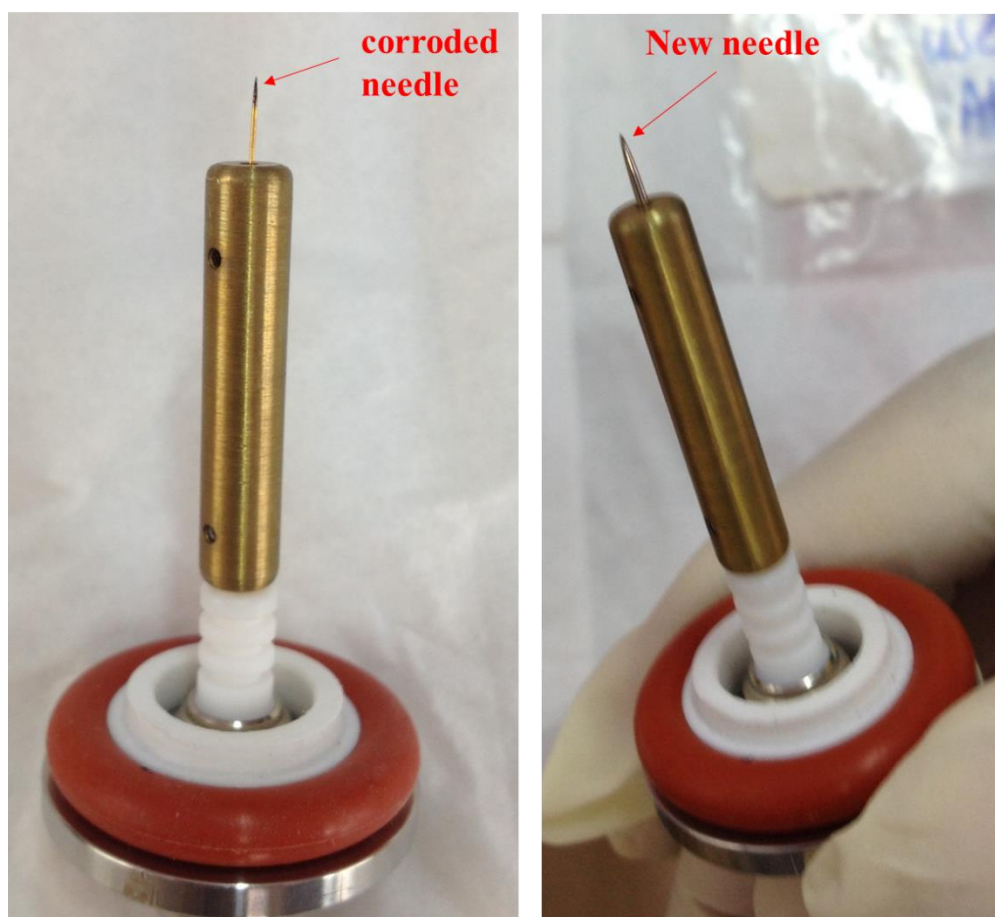


Figure 5.16. Comparison of a new gold-coated needle (right) with a corroded or ‘darkened’ one (left) after more than 36 hours of sampling.

5.7 Summary

The CIMS has been successfully modified into an unheated setup for measuring N_2O_5 and ClNO_2 . Calibrations of the instrument gave a sensitivity of 0.97 Hz/pptv and 1.04 Hz/pptv for N_2O_5 and ClNO_2 , respectively. The sensitivity was demonstrated to be humidity dependent, with optimum range between 50-70% of RH. Background noise was determined to be smaller than 10 Hz, and the detection limit of the CIMS was 5 pptv for both N_2O_5 and ClNO_2 .

Testing on the completely new inlet showed less than 10% loss of N_2O_5 and no significant ClNO_2 production in the inlet. However, after 7 days of continuous ambient sampling, the N_2O_5 loss reached 41% and 7% of the added N_2O_5 signal was converted to ClNO_2 via the surface of the inlet. Such results indicated that the inlet chemistry is critical during the measurement in China environment. Adding a Teflon filter in the sampling line was demonstrated to be impractical for reducing aerosol in the inlet for long-term measurement. Daily washing of the sampling line was shown to reduce the loss of N_2O_5 to less than 14% with negligible production of ClNO_2 on the inlet. Thus, daily changing and washing of inlet are recommended to be practiced in field measurements in China to reduce the effect of aerosol deposition on the inlet.

The CIMS was then demonstrated to perform well in the ambient trial run. The hourly standard addition of N_2O_5 was able to account for the sensitivity changes due to the ambient conditions. The measurement of N_2O_5 did not show interference (e.g. daytime peak) as was observed by a TD-CIMS previously. Verification on the N_2O_5 measurements of CIMS with those from a CRDS exhibited an excellent correlation coefficient (R^2) of 0.93, a slope of 0.99 and intercept of 30, based on an RMA regression analysis. Linear fits of the ambient ClNO_2 signal at 208 *a.m.u.* and its chlorine isotopic signals at 210 *a.m.u.* yielded slopes between 0.31-0.33 which were close to the theoretical chlorine isotope ratio of 0.32. This study points out that the optimized-CIMS method is capable of measuring N_2O_5 and ClNO_2 accurately under high humidity and high particulate loading environment of China.

Testing on a corona ion source was performed. It was found that the corona ion source was sufficiently good for measuring ambient N_2O_5 and ClNO_2 . However,

the testing suggests that it is more convenient to use a ^{210}Po radioactive as the ion source for long term field measurements since the corona ion source gives high detection limits and requires frequent replacement of the needle in the source. It is evident that more modification and optimization are needed in future to improve the current corona discharge ion source. For example, optimizing the space charge effects or trying a different needle design (e.g. material and needle tip) are highly desirable to increase the sensitivity and reduce the background signal of the instrument.

Chapter 6 Observation of ClNO₂ at a high altitude site in southern China

Majority of the previous ClNO₂ field measurements were conducted at the surface sites (Osthoff et al., 2008; Mielke et al., 2011; Riedel et al., 2012; Mielke et al., 2013; Bannan et al., 2015a; Faxon et al., 2015), which only determined the characteristics of either a NBL, with a depth of approximately 100 m, or a surface layer that may be tens of meters above the ground (Stull, 1988). Observations at the surface sites cannot distinguish the composition or chemistry within the residual layer at higher altitudes, where the largest mass of the preceding day's emission resides. To date, the study of ClNO₂ in the residual layer has remained sparse. Strategies for studying the ClNO₂ chemistry in the residual layer include measurements from aircraft (Young et al., 2012), tall towers (Riedel et al., 2013), or mountaintop sites that lie within the residual layer (Phillips et al., 2012).

After the optimization of CIMS, it was deployed to the peak of Tai Mo San (957 m a.s.l.) in the late autumn of 2013 to characterize the ClNO₂ and N₂O₅ in the PBL of Hong Kong. Other supporting measurements conducted in the Tai Mo Shan campaign included NO_x, NO_y, O₃, HONO, VOCs, particle size distributions, and aerosol ionic composition. This chapter presents the first observations of ClNO₂ and N₂O₅ within the residual layer of southern China. Comprehensive analysis of nighttime ClNO₂ formation and its impact on the next day oxidative chemistry were conducted. The implications of the daytime ClNO₂ and N₂O₅ were also discussed.

6.1 Meteorological overview at TMS

As shown by the wind rose in Figure 6.1a, the local wind at TMS was strongly influenced by the winter monsoon with prevailing wind from the east and northeast. The winds were consistently stronger at night-time and early morning, with a mean wind speed of 7.8 m/s. The wind began to slacken from late morning and reached about 2 m/s by 15:00 local time. It was accompanied by a slight rotation of the wind direction toward the northeast. These wind results indicate that in a majority of the measurement time, the site received air masses from the eastern side (South China Sea) and occasionally had some impacts of local pollution sources from the heavily urbanized/industrialized region of PRD in the northern direction (i.e. in the evening).

As the site was located at a high altitude (957 m a.s.l.), relatively colder air masses were sampled during the study with the lowest average temperature of 11°C during the night-time and up to 15.5°C in the daytime. The humidity at the site was highly variable with average RH values in the range of 56 to 75%. There were some occasions (several nights) when the sampling site was totally immersed in fog/cloud with the RH of 100%.

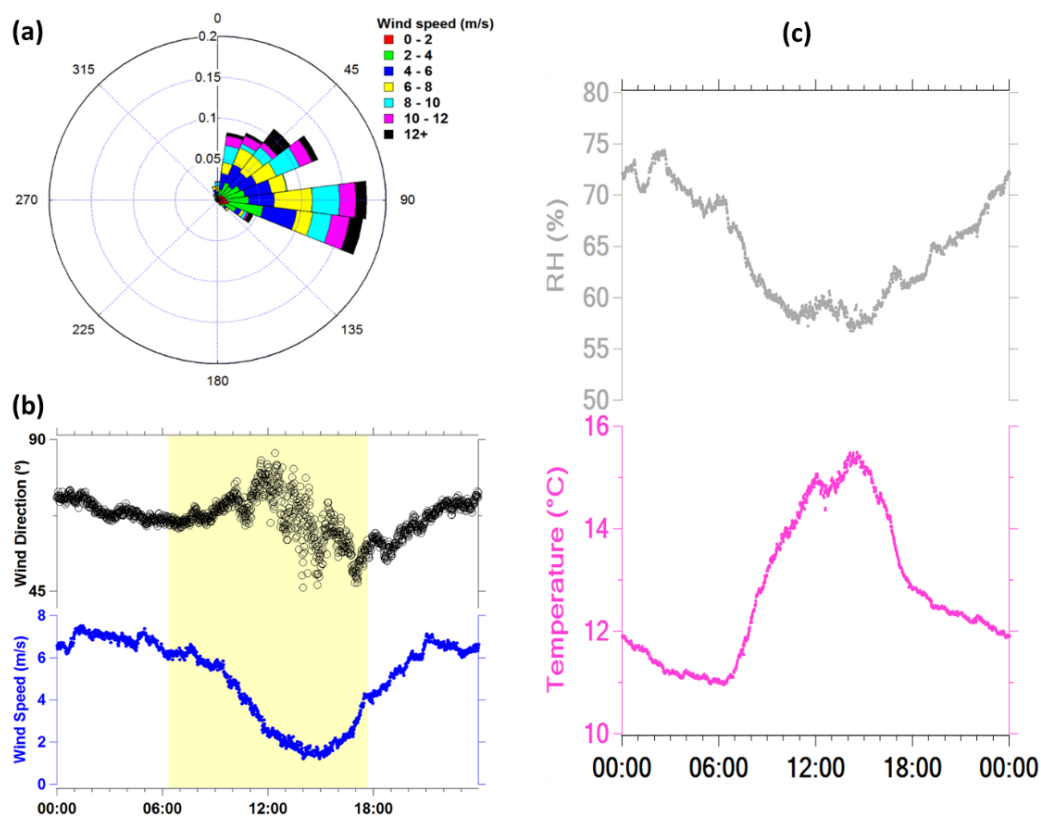


Figure 6.1. a) Wind rose plot, b) diurnal average of wind and c) diurnal average of temperature and humidity at the TMS site.

6.2 General observations at TMS

Figure 6.2 shows the time series of ClNO_2 , N_2O_5 , related chemical and meteorological parameters on 15-17 November, 23-29 November and 30 November-6 December of 2013. The CIMS only had continuous data on 12 days during the field campaign due to technical problems, and the data were mostly in the night-time as the CIMS instrument was under calibration, testing, or maintenance in most of the daytime (except for Sundays). Significant levels of pollutants like NO_y , NO_x , O_3 , and S_a were measured at TMS, indicating the influence of polluted air from the urban area of Hong Kong and the PRD region. The NO_y and NO_x were observed in the range of 2-55 ppbv and 1-50 ppbv, respectively, with a wide range of NO_x/NO_y ratios (0.1-0.95). O_3

showed characteristic of afternoon photochemical peaks, with average mixing ratios of 60 ppbv and a maximum of 107 ppbv. The aerosol loading as indicated by the S_a was significant with average value of $580 \mu\text{m}^2/\text{cm}^3$ and maximum value reaching $3700 \mu\text{m}^2/\text{cm}^3$.

The site intercepted air masses containing significant levels of ClNO_2 (>400 pptv) and N_2O_5 (>1000 pptv) during the night of 15, 16, 31 November, 1, 2, 3, 5 and 6 December, indicating the rapid night-time chemistry involving the NO_x and O_3 in this region. The highest ClNO_2 and N_2O_5 were observed on the night of 3-4 December, with mixing ratios up to 4.7 ppbv and 7.7 ppbv, respectively (1 min average). The ClNO_2 and N_2O_5 were low on the night of 25 and 29 November when the site received relatively clean air masses (with ClNO_2 <100 pptv, N_2O_5 <500 pptv, RH ~40–60% and low to moderate levels of ozone, NO_x and S_a). When the site was immersed in fog/cloud (RH = 100%) on 23 to 28 November, the ClNO_2 mixing ratio was less than 200 pptv, while very low N_2O_5 was observed (mixing ratios near the detection limit of the CIMS).

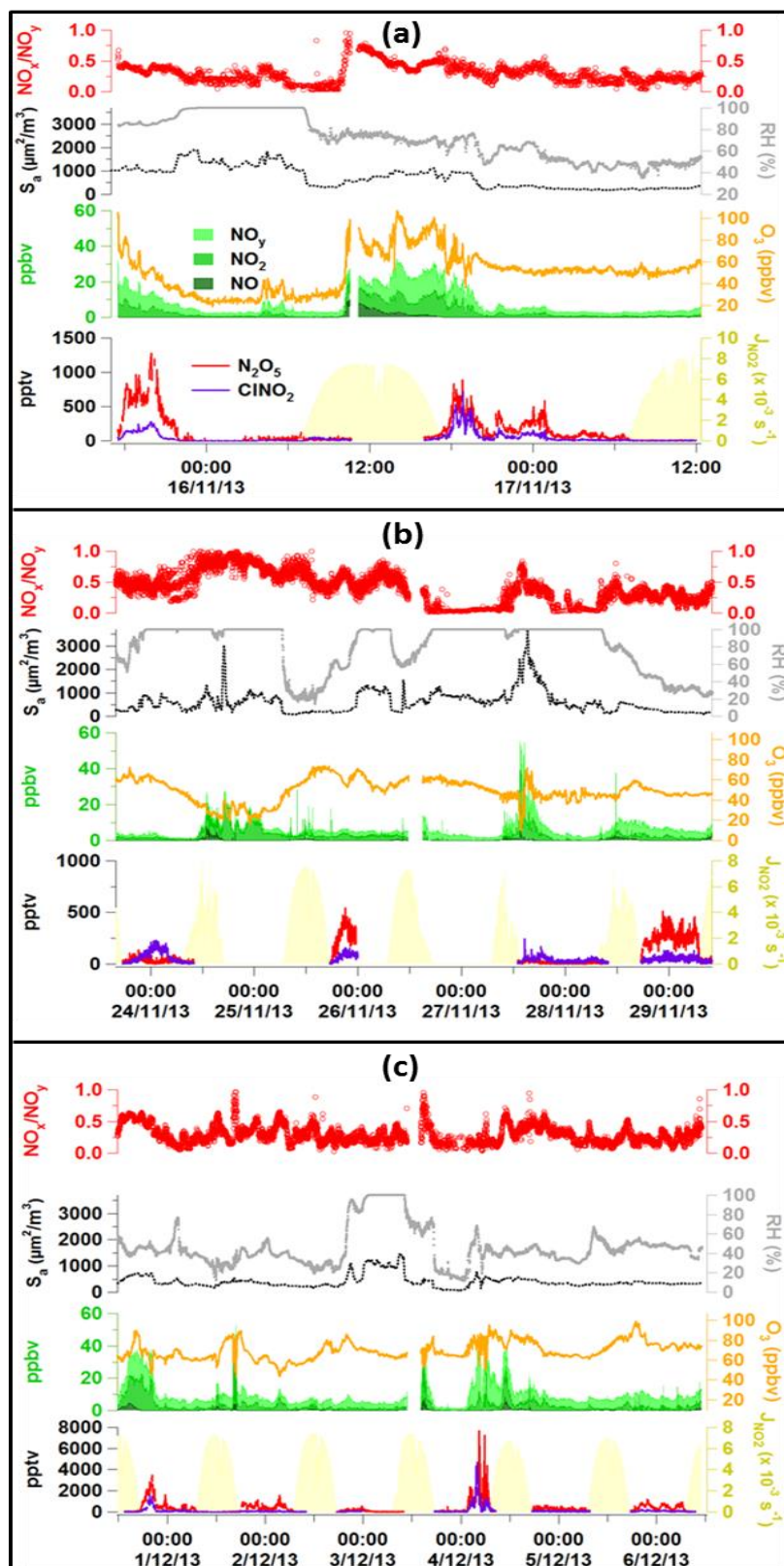


Figure 6.2. Time series of ClONO_2 , N_2O_5 and related chemical and meteorological parameters for period of a) 15-17 November 2013, b) 23-29 November 2013, c) 30 November – 6 December 2013. The data gap is due to calibrations, inlet maintenance, and instrument problems.

6.3 Variations of ClNO₂

6.3.1 Diurnal average

Figure 6.3 shows the diurnal average of ClNO₂ and N₂O₅ for the campaign. Significant levels of ClNO₂ and N₂O₅ were observed at night with concentrations up to 677 pptv and 999 pptv, respectively. On most of the nights, ClNO₂ and N₂O₅ began to increase at 17:00 (1 h before sunset) and reached a peak at about 20:00. They started to decrease after this period and remained at low levels throughout the night. There was one night (3-4 December) when extremely high ClNO₂ and N₂O₅ mixing ratios were observed in the early morning (~04:00-05:00). This case resulted in a significant peak at the early morning of the diurnal average for ClNO₂ and N₂O₅. The different ClNO₂ and N₂O₅ characteristics of these two peaks are further discussed with two examples in the sub-sections below.

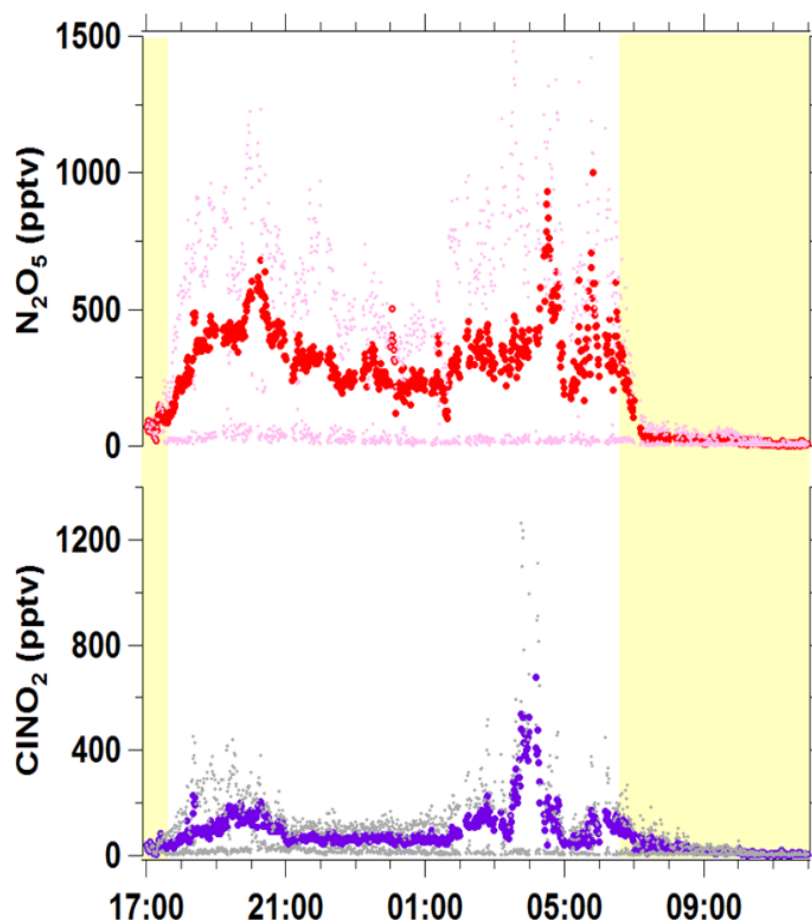


Figure 6.3. The diurnal average of N_2O_5 (red) and ClNO_2 (purple) for the campaign. Dots represent the 10th and 90th percentile of the N_2O_5 (pink) and ClNO_2 (grey) data set.

6.3.2 Night of 30 November-1 December: Early ClNO_2 peak

On the night of 30 November to 1 December, the site intercepted a plume with high levels of ClNO_2 (maximum of 1.6 ppbv) and N_2O_5 (maximum of 3.5 ppbv) for about three hours after sunset (Figure 6.4). This ClNO_2 -laden plume was in accordance with the observation of high concentrations of NO_y (> 30 ppbv), NO_x (> 10 ppbv), O_3 (>50 ppbv) and S_a (> 400 $\mu\text{m}^2/\text{cm}^3$). The ClNO_2 constituted 5.4% of NO_y and 11.5% of NO_z (= $\text{NO}_y - \text{NO}_x$); the sum of ClNO_2 and N_2O_5 accounted for 54% of the NO_z (see Figure 6.5a). The ClNO_2 to N_2O_5 ratios in the plume ranged from 0.2 to 0.6.

Moderate NO_x to NO_y ratios (~ 0.4 - 0.7) were observed in the plume (see Figure 6.5b), suggesting ‘young’ (i.e. less photochemically aged) air masses being sampled.

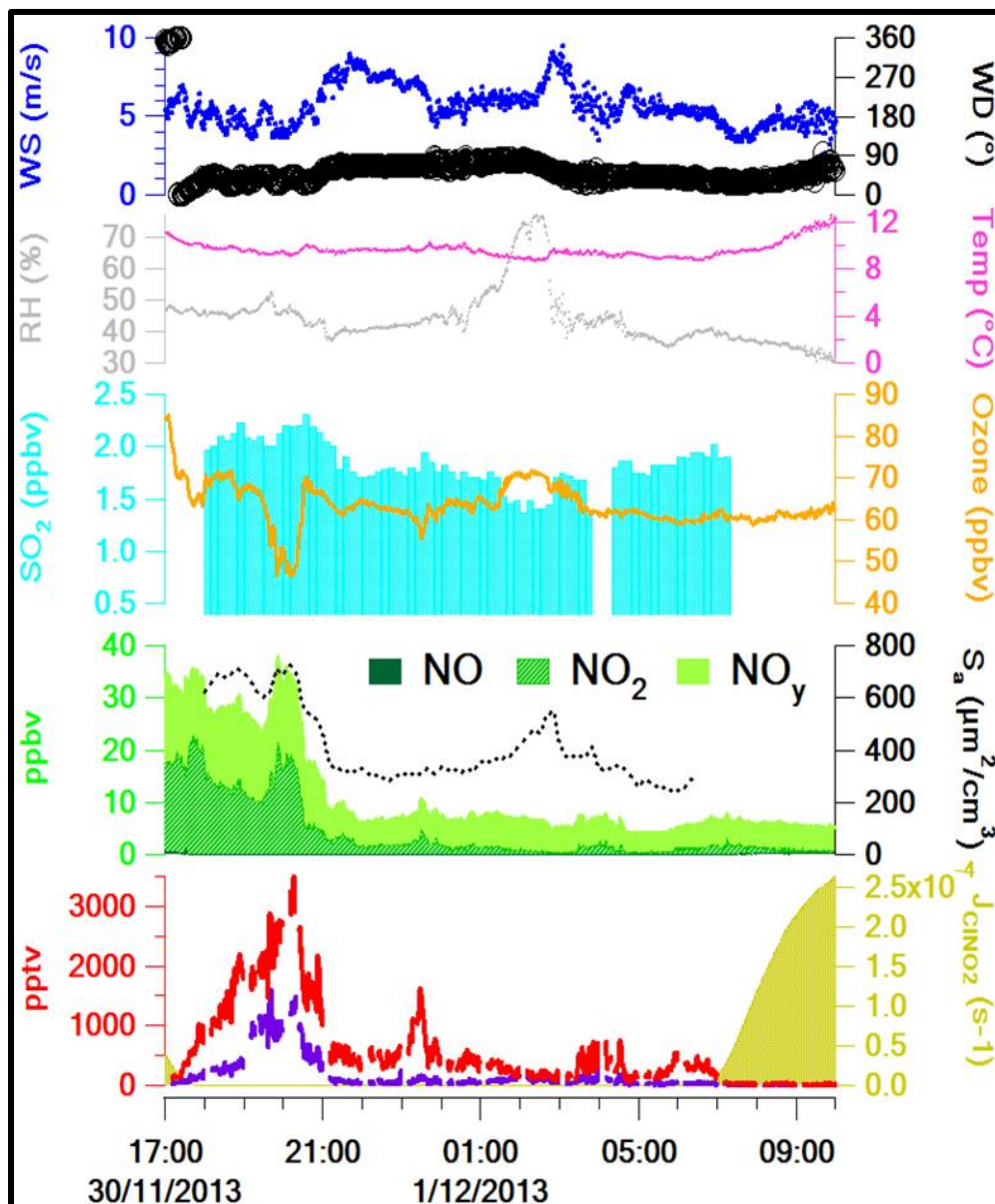


Figure 6.4. An expanded view of ClNO_2 and related chemical and meteorological parameters for 30 November-1 December 2013, as the example of the typical diurnal pattern at TMS.

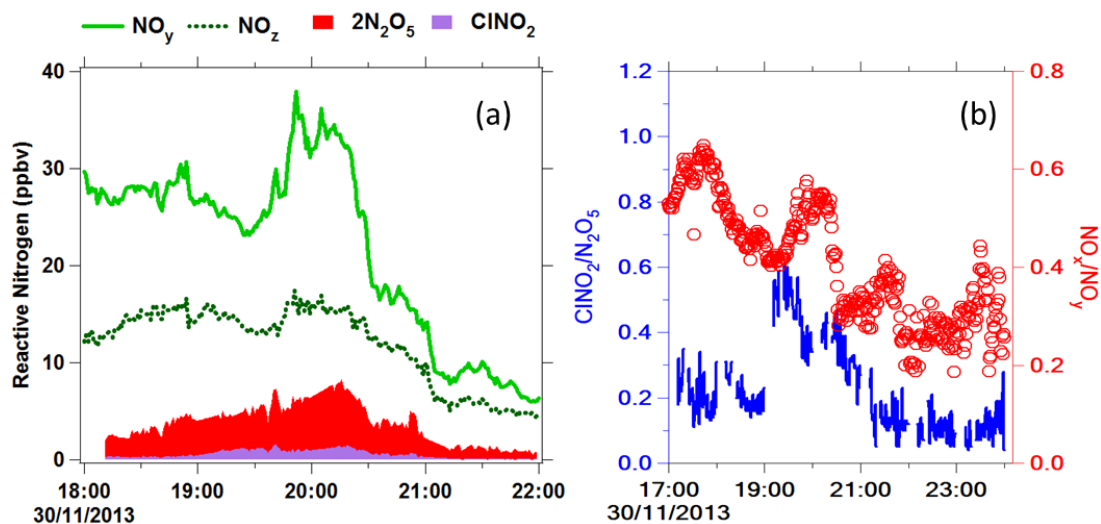


Figure 6.5. a) The concentration of N_2O_5 and ClNO_2 in relation to the NO_z and NO_y . N_2O_5 has been multiplied by two-fold (as it contains two nitrogen atoms) and is stacked on the ClNO_2 . b) The ratio of NO_x/NO_y in relation to $\text{ClNO}_2/\text{N}_2\text{O}_5$ ratios on the night of 30 November 2013.

A 12-hour backward particle dispersion was simulated by the HYbrid Single-Particle Lagrangian Integrated Trajectory (HYSPLIT) model (Draxler et al., 2014) with the output from Weather Research and Forecasting (WRF) model to obtain the air masses history on this night. This analysis was conducted by a colleague, Qinyi Li and the detail has been described in Wang et al., (2016). Figure 6.6 illustrates that the air mass arriving at TMS at 17:00 and 20:00 originated from a large area covering the Hong Kong urban area, coastal region and inland of PRD in the north. This result suggests that the mixtures of marine air (a source of chloride) and pollutants (i.e. O_3 and NO_2) emitted from the surrounding urban areas contributed to significant ClNO_2 production in the region. The history of air mass arriving at 03:00 originated from the coastline of the north-eastern sector which is the less densely-populated region. This result is consistent with the observation of a drastic decrease in the mixing ratios of ClNO_2 , N_2O_5 , and other pollutants after the change of wind direction from north to east/northeast at around 21:00 (see Figure 6.4).

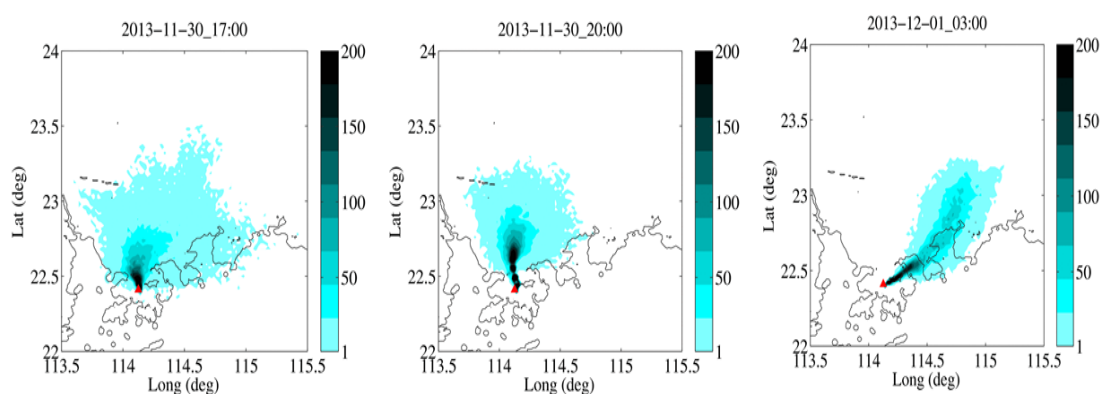


Figure 6.6. Twelve-hour backward particle dispersion for 17:00, 20:00 on 30 November and 03:00 of 1 December. Contours represent the number of particles in each 0.02 degree latitude \times 0.02 degree longitude grid.

The overall chemical and meteorological results of this night suggest that the high ClNO_2 and N_2O_5 plume in the early evening are likely contributed by ‘young’ air masses containing emissions from the marine and the nearby urban areas of Hong Kong (e.g. Tsuen Wan & Yuen Long) and PRD (e.g. Shenzhen). Other examples of similar conditions were shown on the nights of 15-16 November and 16-17 November which had similar diurnal patterns with significant concentrations of ClNO_2 and N_2O_5 observed at 20:00-21:00 and air masses originated from the northern sector.

6.3.3 Night of 3-4 December: Extremely high ClNO_2 and N_2O_5 plume

Figure 6.7 depicts the detailed variations of ClNO_2 , N_2O_5 , related chemical and meteorological parameters on the night of 3-4 December. The ClNO_2 and N_2O_5 in this night were unique and different from the typical conditions at TMS. The polluted air mass arrived at the site in a much later period of the night (at approximately 02:00). Extremely high mixing ratios of ClNO_2 and N_2O_5 of up to 4.7 ppbv and 7.7 ppbv (1

min-average), respectively, were observed between 03:30 and 05:00. To our knowledge, these concentrations are currently the highest value ever reported in the literature. Different relationships of ClNO_2 and N_2O_5 were observed in three periods of this event (which are labeled as I, II, and III in Figure 6.7).

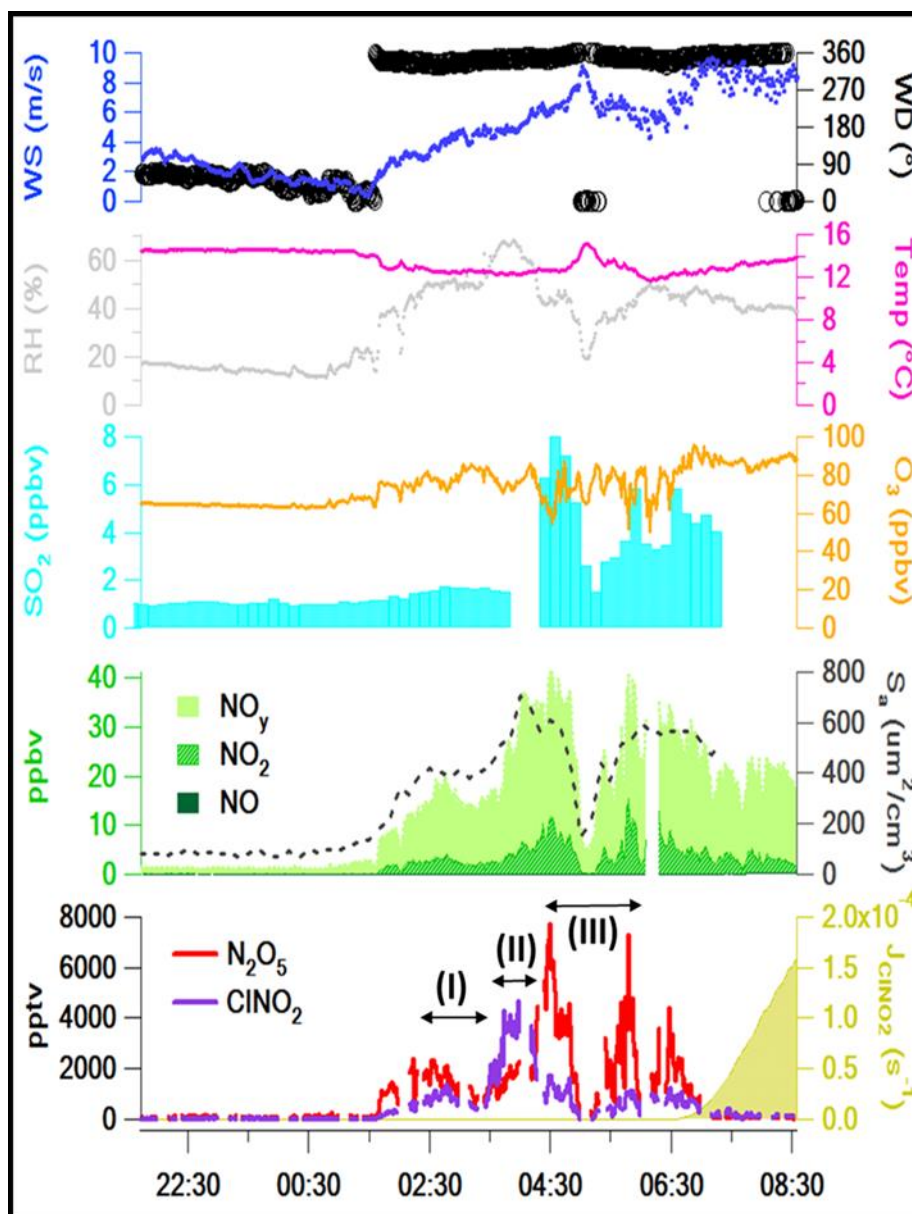


Figure 6.7. Expanded time series of ClNO_2 , N_2O_5 and related chemical and meteorological parameters for 3-4 December 2013. The arrows indicate Plumes I, II, and III (as identified in the text).

As shown in Figure 6.8a, the fractions of ClNO_2 in NO_y and NO_z were between 4-20% and 9-23%, respectively. The results are comparable to those observed in other polluted places like Los Angeles and Houston, with the percentage of up to 15-20% (Osthoff et al., 2008; Mielke et al., 2013). However, the sum of ClNO_2 and N_2O_5 accounted for about half of the NO_z , with a maximum of 61% at TMS. These fractions are a strong indicator of significant ClNO_2 and N_2O_5 production in the planetary boundary layer of Hong Kong, implying their importance as the NO_x reservoir which may affect the atmospheric chemistry in the region.

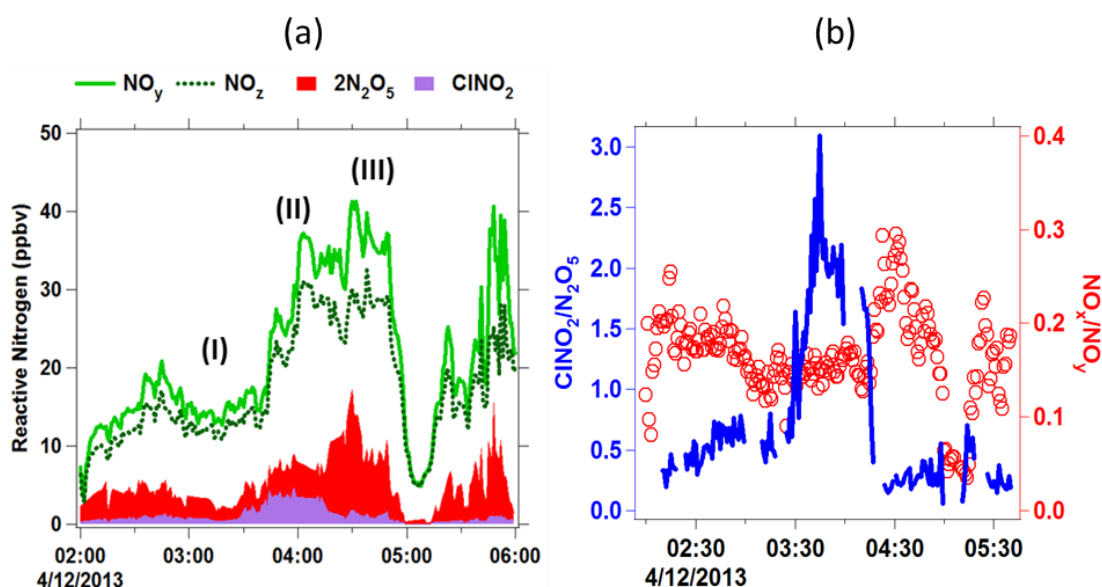


Figure 6.8. a) The concentration of N_2O_5 and ClNO_2 in relation to the NO_z and NO_y in the three different plumes (I, II, and III) on the night of 4 December 2013. N_2O_5 has been multiplied by two-fold and is stacked on the ClNO_2 . b) The ratios of NO_x/NO_y in relation to $\text{ClNO}_2/\text{N}_2\text{O}_5$ ratios.

Variation of ClNO_2 to N_2O_5 ratios was observed from 02:00 to 06:00. In Plume I (02:30-03:30), ClNO_2 and N_2O_5 rose almost simultaneously with an average $\text{ClNO}_2/\text{N}_2\text{O}_5$ ratio of 0.44 (see Figure 6.8b). Then, Plume II saw a sharp rise in ClNO_2 and a slow increase in N_2O_5 between 03:30-04:30, indicating more efficient ClNO_2

production via N_2O_5 heterogeneous reaction as given by the larger mean $\text{ClNO}_2/\text{N}_2\text{O}_5$ ratios of 1.98. An opposite pattern of Plume III with high N_2O_5 and low ClNO_2 mixing ratios (mean $\text{ClNO}_2/\text{N}_2\text{O}_5$ ratios of 0.24) was measured at 04:30-06:00, indicative of less efficient N_2O_5 heterogeneous uptake.

An examination on the ionic compositions of the $\text{PM}_{2.5}$ sample at this night (18:00–06:00) revealed a higher level of chloride (see Table 6.1). The mass ratio of $[\text{Cl}^-]$ to $[\text{Na}^+]$ was significantly larger than that collected during the following daytime of 4 December (2.48 versus 0.91) and was larger than the mean ratio in sea water (1.8) (Seinfeld and Pandis, 2006). This observation indicates the presence of significant amount of non-oceanic Cl^- in the air masses sampled at the night of 4 December. As shown in the following paragraph (refer to Figure 6.9), a back trajectory calculation showed that the air mass at the night of 3–4 December originated from inland areas of the PRD, suggesting the existence of anthropogenic chloride in the PRD region, possibly from coal-burning sources (e.g. coal-fired power plants) given the concurrent increase in SO_2 concentrations (see Figure 6.7). Such inference is supported by previous $\text{PM}_{2.5}$ aerosol observations in the region, indicative of elevated chloride levels relative to sodium (mass ratio of 2.80) compared to those from ocean sprays (e.g., Tan et al., 2009).

Table 6.1. Particulate chloride and sodium for night of 3-4 December and daytime of 4 December 2013.

Time	$\text{Cl}^-(\mu\text{g}/\text{m}^3)$	$\text{Na}^+(\mu\text{g}/\text{m}^3)$	$[\text{Cl}^-]/[\text{Na}^+]$
3-4 Dec 2013 (18:00 – 06:00)	0.57	0.23	2.48
4 Dec 2013 (10:00 – 22:00)	0.21	0.23	0.91

Figure 6.9 shows the 12-h backward air mass trajectories simulated for this night. Before the arrival of the ClNO₂ and N₂O₅ plume at midnight (00:00), the air traveled from the coastal and offshore areas in the east. However, in the middle of the polluted air (at 04:00), one branch of the air originated from the north and from low altitudes, which would transport pollutants from urban areas in Shenzhen and inland areas of the PRD. The increase of RH and pollutants like SO₂ and NO_y at 04:00 (refer to Figure 6.7) are consistent with the meteorological indication of surface air masses. These air masses were well processed chemically as indicated by the average NO_x/NO_y ratios of 0.17, 0.15 and 0.23 in Plume I, II and III, respectively (see Figure 6.8b).

Based on the above chemical and meteorological analysis, the highest ClNO₂ and N₂O₅ case observed on the night of 3-4 December represents air masses from the polluted PRD region with prolonged night-time processing. The site intercepted this aged plume as a consequence of different atmospheric dynamics on that night, for instance, the changing of wind direction at a later part of the night (refer to Figure 6.7). Further analysis of a night-time chemical clock for this night based on the odd oxygen budget also showed an extended overnight processing for plumes between 02:00-06:00 with estimated processing time between 5.4–7.4 h. (see Brown et al., 2016).

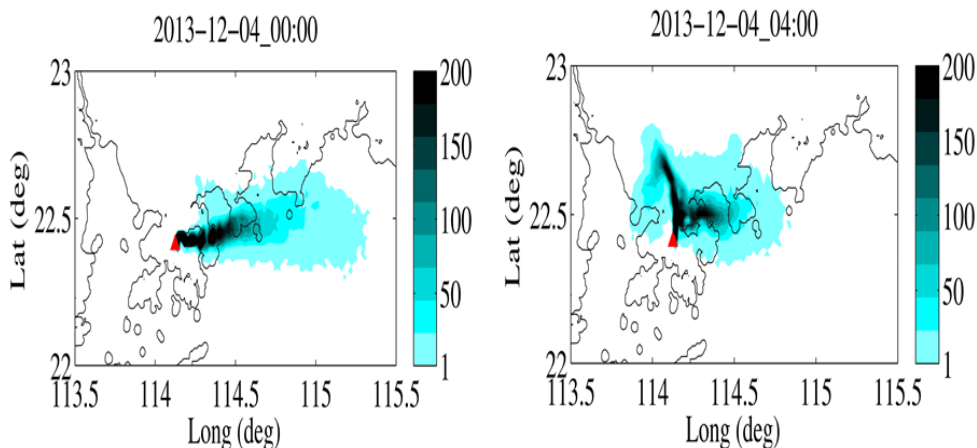


Figure 6.9. Examples of 12-h backward particle dispersion for 00:00 and 04:00 on 4 December. Contours represent the number of particles in each 0.02 degree latitude \times 0.02 degree longitude grid.

6.4 N₂O₅ heterogeneous uptake and production of ClNO₂

The ratios of ClNO₂ to N₂O₅ were shown above to vary among nights or change drastically within a short period, indicating the variations in N₂O₅ reactivity and efficiency in the production of ClNO₂. This section examines night-time production rate of NO₃ (P(NO₃)), N₂O₅ heterogeneous uptake, and ClNO₂ yields that contributed to the observation of high ClNO₂ and N₂O₅ at TMS. The above two cases of high ClNO₂ were chosen for this analysis. The case on 30 November - 1 December represents the ‘young’ ClNO₂-laden plumes, while the three different plumes (Plume I, II and III) in the extreme case on the night of 3-4 December 2013 represent the ‘aged’ ClNO₂ plumes.

Table 6.2 summarizes the key ClNO₂ production parameters for the selected cases. The P(NO₃) is a metric of N₂O₅ and was calculated from the reaction of NO₂ with O₃ (see R1.1) according to equation (6.1) (Wayne et al., 1991).

$$P(\text{NO}_3) = k_{1.1}[\text{NO}_2][\text{O}_3] \quad (6.1)$$

The average $P(\text{NO}_3)$ determined in the ‘young’ ClNO_2 peak on 30 November and Plume I to III on 4 December were 1.4 and 0.5-1.3 ppbv/hr, respectively. The rates are considered to be large compared to the rates derived from suburban of Boulder (Brown et al., 2007) and at a rural mountaintop in Germany (Crowley et al., 2010), but are comparable to the high end of $P(\text{NO}_3)$ observed in other urban areas (e.g., Brown et al., 2011). The large production rate of NO_3 at this site is due to the presence of higher levels of NO_2 and O_3 (see Figure 6.4 and 6.7).

Table 6.2. ClNO_2 production parameters in the ‘young’ ClNO_2 -laden plume and ‘aged’ ClNO_2 plumes (three plumes).

	P_{NO_3} (ppbv/hr) ^a	$k(\text{N}_2\text{O}_5)_{\text{het}}$ (s ⁻¹)	$\gamma_{\text{N}_2\text{O}_5}$	S_a ($\mu\text{m}^2/\text{cm}^3$) ^a	ϕ
30 Nov	1.4	2.09×10^{-4}	0.0050	703	0.33
4 Dec					
Plume I	0.5	1.03×10^{-4}	0.0043	402	0.30
Plume II	0.9	1.83×10^{-4}	0.0047	651	0.46
Plume III	1.3	1.28×10^{-4}	0.0036	589	0.19

^a mean value

An iterative box model (Wagner et al., 2013), which comprises of five reactions related to NO_3 and N_2O_5 production and loss, was used to predict the N_2O_5 loss rate coefficient ($k(\text{N}_2\text{O}_5)_{\text{het}}$) with constraints of the measured O_3 , NO_2 , N_2O_5 , and temperature. Several assumptions were made in this analysis: 1) the N_2O_5 loss was only through heterogeneous reactions of N_2O_5 ; 2) the reaction duration (zero time) was set at the time of sunset (17:52 LT, for these cases); 3) there were no nocturnal fresh emissions in the plume; 4) it was assumed that the NO_2 only involved in the production of $\text{NO}_3/\text{N}_2\text{O}_5$. As shown in Table 6.2, the N_2O_5 loss rate coefficient for

these cases varied from $2.09 \times 10^{-4} \text{ s}^{-1}$ in the ‘young’ ClNO₂-laden plume to 1.03×10^{-4} , 1.83×10^{-4} and $1.28 \times 10^{-4} \text{ s}^{-1}$, respectively, in the aged ClNO₂ plumes (Plume I, II and III). By applying the predicted $k(\text{N}_2\text{O}_5)_{\text{het}}$, $C_{\text{N}_2\text{O}_5}$ of 240 m/s, and particle surface area into equation (2.3), the N₂O₅ uptake coefficient was estimated to be 0.0050, 0.0043, 0.0047, and 0.0036 for the ‘young’ ClNO₂-laden plume, Plume I, II, and III, respectively. These values are similar to those reported in the residual boundary layer and in the free troposphere (Brown et al., 2009; Brown et al., 2013; Wagner et al., 2013) where lower water content may be the limiting factor for N₂O₅ uptake. High N₂O₅ uptake in Plume II can be justified by the largest aerosol surface area and the highest relative humidity in this plume. The $\gamma(\text{N}_2\text{O}_5)$ are also comparable with those estimated by a steady state approach (see Brown et al., 2016).

The yield of ClNO₂ was derived from the slope (m) of the plot between ClNO₂ and total nitrate (aerosol NO₃⁻ + HNO₃ gas) as described in Riedel et al., (2013).

$$\phi(\text{ClNO}_2) = \frac{2m}{1+m} \quad (6.2)$$

In this study, the total nitrate was calculated as NO_y - NO_x - HONO - PAN- 2N₂O₅ - NO₃ - ClNO₂. All, except PAN, were concurrently measured in the field campaign. Since PAN and ozone are the products of photochemical reaction and they normally show good correlation, the PAN concentration was estimated from the ozone measurement at TMS by using the mean PAN/O₃ ratio of 0.013 (ppbv/ppbv) observed at a coastal site in Hong Kong (Xu et al., 2015a). As this method does not account for nitrate produced photochemically, it thus provides a lower estimate of the ClNO₂ yield. The estimated ϕ was the highest in Plume II (0.46), consistent with the observation of the high ClNO₂. The determined ϕ values are within the range of ϕ reported in Houston and Los Angeles (Osthoff et al., 2008; Mielke et al., 2013).

It can be concluded that the very high concentration of ClNO₂ in the ‘aged’ Plume II was initiated by the large NO₃ production and moderate $\gamma(\text{N}_2\text{O}_5)$ and ClNO₂ yield.

6.5 Impact of the ClNO₂ on the production rate of Cl atom and O₃

Since the maximum concentration of ClNO₂ observed in Plume II and III were about 1-3 hours before sunrise, they can be used as the initial concentration of ClNO₂, [ClNO₂]₀, to estimate the evolution of the Cl atom production rate via photolysis of ClNO₂ in the plume after sunrise. It was assumed that no additional ClNO₂ production between the period of observation and sunrise and the ClNO₂ only undergoes first-order decay (via photolysis). Dilution or mixing was not considered in this calculation. The concentration of ClNO₂ as a function of time was calculated with equation (6.3) and the P(Cl) was determined from equation (4.1).

$$[\text{ClNO}_2] = [\text{ClNO}_2]_0 e^{-j\text{ClNO}_2 t} \quad (6.3)$$

The ClNO₂ peak in Plume II (4.7 ppbv) represents the high ClNO₂ yield case while the moderate ClNO₂ peak in Plume III (1.1 ppbv) represents lower ClNO₂ yield case. Figure 6.10 shows the Cl atom production rates from different initial ClNO₂ concentrations against the time. The Cl production rate via photolysis of ClNO₂ in Plume II achieved a maximum rate of 0.59 pptv/s at about 09:00 and remained prominent throughout the morning hours. The ClNO₂ in Plume III resulted in Cl production rate of 0.14 pptv/s. These production rates are larger than the highest Cl production rate in Los Angeles which reported 0.13 pptv/s (Riedel et al., 2014) and the differences might suggest the variable role of ClNO₂ in different polluted

environments. The large Cl production from ClNO₂ would then oxidize the VOCs, resulting in the increase of O₃ production. By adding the ClNO₂ from Plume II and III into an explicit chemical box model, the O₃ increased by 5-16% at the ozone peak or 11–41% daytime ozone production in the following day. As this modeling work was contributed by a colleague (Likun Xue), the reader is referred to Wang et al., (2016) for more details of the modeling results and discussion.

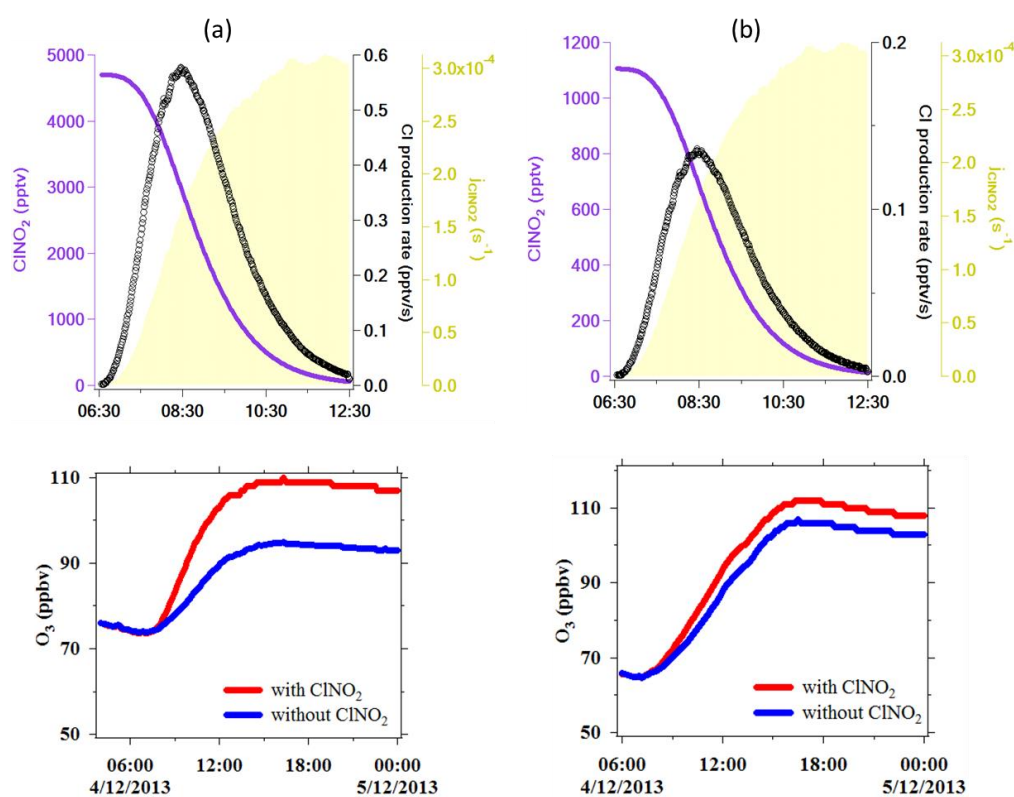


Figure 6.10. Cl production rate (black circle) from photolysis of ClNO₂ in Plume II and III of the extreme case. The lower panel shows the O₃ increases caused by constraining the ClNO₂ in Plume II and III into an MCM box model (The MCM result was provided by L. Xue, refer to Wang et al., 2016 for more details).

6.6 Presence of daytime N₂O₅ and ClNO₂ at TMS

6.6.1 Daytime N₂O₅ chemistry

At TMS, the highest NO_x and O₃ were usually observed during the late afternoon and early evening (see Figure 6.2). The abundant of NO_x and O₃ may potentially lead to active NO₃ and N₂O₅ chemistry during this period. Figure 6.11 shows the daytime mixing ratios of N₂O₅ and ClNO₂ plotted on a logarithmic scale of two individual examples on 27 November and 30 November 2013. From 13:30 to 17:30, N₂O₅ mixing ratios increased continuously throughout the day to a maximum of ~45 pptv on 27 November and ~357 pptv on 30 November. Also shown in Figure 6.11 is the predicted daytime N₂O₅ from a steady state assumption between production through R1.1& R1.2 and loss via photolysis of NO₃ (j_{NO_3}) and NO₃+NO. If other losses of NO₃ and N₂O₅ are small relative to the j_{NO_3} and NO₃+NO, the daytime steady state in N₂O₅ can be predicted by equation (6.4) (Brown et al., 2005).

$$\text{N}_2\text{O}_5 (\text{daytime}) = K_{\text{eq}}[\text{NO}_2] \frac{\text{P}(\text{NO}_3)}{k_{2.1}[\text{NO}] + j_{\text{NO}_3}} \quad (6.4)$$

The P(NO₃) on 30 November was at 1-3 ppbv/h, while the 27 November case had P(NO₃) of 0.5-1.0 ppbv/h with a sharp peak of 3 ppbv/h observed at ~14:30. During the late afternoon of 30 November, the observed and calculated N₂O₅ were in good agreement, where the observations were about 80% of the calculation between 13:30 and sunset. By contrast, the N₂O₅ concentrations on 27 November were much smaller, accounting for about 10% of the calculations during the same period of the day. It suggests that 90% of NO₃ and N₂O₅ losses were not from the photolysis of NO₃ and reaction of NO₃+NO. The relative humidity was 100% during the whole afternoon

of 27 November, indicating that the sampling site was directly impacted by fog/cloud event and that heterogeneous uptake of N_2O_5 to fog/cloud droplets can be the major candidate for the inconsistency (Lelieveld and Crutzen, 1990). To assess such contribution, heterogeneous loss rate coefficient of N_2O_5 was added into equation (6.4) to give a new equation (6.5) (Osthoff et al., 2006).

$$\text{N}_2\text{O}_5 \text{ (daytime)} = K_{\text{eq}}[\text{NO}_2] \frac{P(\text{NO}_3)}{k_{2.1}[\text{NO}] + j_{\text{NO}_3} + k(\text{N}_2\text{O}_5)_{\text{het}}K_{\text{eq}}[\text{NO}_2]} \quad (6.5)$$

The $k(\text{N}_2\text{O}_5)_{\text{het}}$ was adjusted to match the measured mixing ratios of N_2O_5 and the calculation showed that a $k(\text{N}_2\text{O}_5)_{\text{het}}$ of $4.24 \times 10^{-3} \text{ s}^{-1}$ was needed to rationalize the observation with calculation values (>85%). This analysis indicates that heterogeneous uptake of N_2O_5 is likely significant and fast in fog/cloud event.

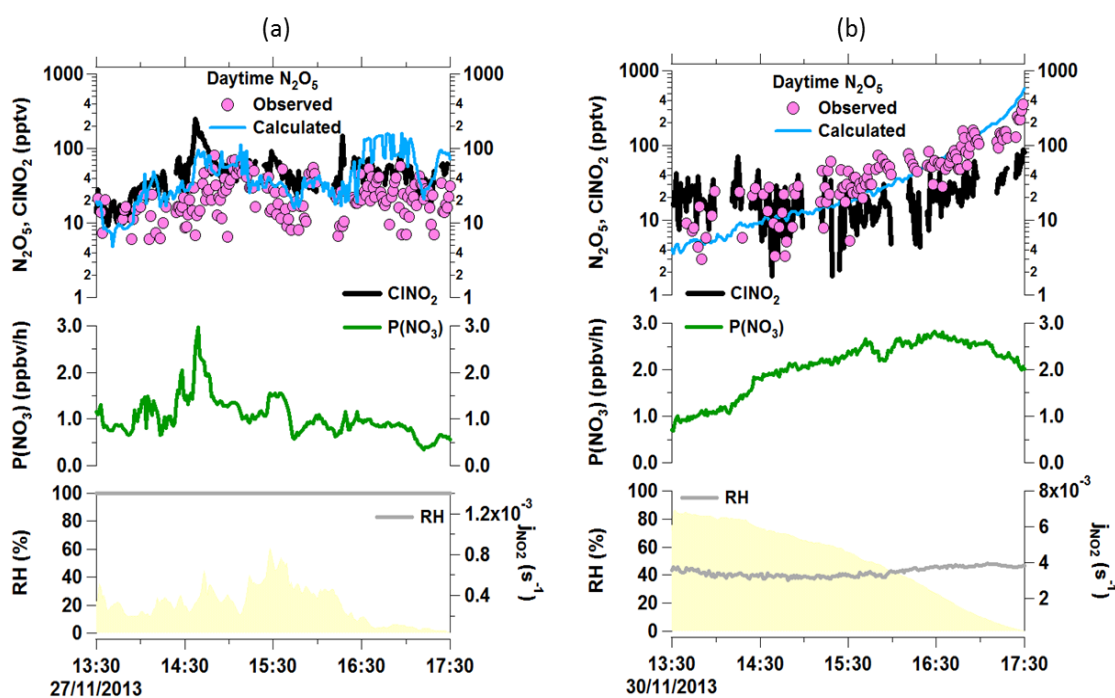


Figure 6.11. Observed and calculated daytime N_2O_5 (from equation 6.4) and observed ClONO_2 (for the period when these data were available), production rate of the nitrate radical, and relative humidity for (a) 27 November and (b) 30 November 2013.

Figure 6.11 also illustrates the observation of the product of N_2O_5 heterogeneous uptake, $ClNO_2$, during daylight hours for both days. On foggy/cloudy (high-RH) day, the average $ClNO_2$ mixing ratio in the afternoon was 50 pptv, with a maximum of 245 pptv. Observation of such small $ClNO_2$ mixing ratios in plumes which have large $P(NO_3)$ and $k(N_2O_5)_{het}$ indicate that the $ClNO_2$ yield was low. The observations of low $ClNO_2$ in fog/cloud droplets which mainly contain water is consistent with the reduction of $ClNO_2$ yield with increase of aerosol water content (Bertram and Thornton, 2009; Roberts et al., 2009). On the clear (low-RH) day, $ClNO_2$ was present at a concentration similar to or smaller than that of daytime N_2O_5 (about 20 pptv), likely as a result of less rapid N_2O_5 heterogeneous uptake, but potentially higher $ClNO_2$ yield. The production of $ClNO_2$ during the daytime under both wet and dry conditions can be a source of photolabile chlorine atom in the afternoon and may affect the oxidative capacity of the downwind area.

6.6.2 Daytime N_2O_5 chemistry as an HNO_3 source

If the main daytime N_2O_5 loss processes during the late afternoon of 27 November was through heterogeneous reaction and the $ClNO_2$ yield was low, the resulting conversion of NO_x to soluble nitric acids (HNO_3) would proceed at twice the rate of $P(NO_3)$. The production rate of HNO_3 via N_2O_5 heterogeneous uptake ($P(HNO_3)_{het}$) can be given by equation (6.6) and (6.7) below, where \mathcal{E} is the fraction of NO_3 production via **loss** through N_2O_5 relative to the total lost through NO_3 and N_2O_5 (Brown et al., 2004, Wagner et al., 2012).

$$P(HNO_3)_{het} = 2 \times \mathcal{E} \times P(NO_3) \quad (6.6)$$

$$\mathcal{E} = \frac{1}{1 + \frac{k(NO_3)}{k(N_2O_5)_{het}} \frac{1}{K_{eq}[NO_2]}} \quad (6.7)$$

The calculated upper limit of $P(\text{HNO}_3)_{\text{het}}$ for the afternoon of 27 November was 1.6 ppbv/h. The major daytime production of HNO_3 via reaction of OH with NO_2 ($k_{\text{OH}+\text{NO}_2}[\text{OH}][\text{NO}_2]$) at this period was estimated to proceed at approximately 1 ppbv/h, assuming a low OH concentration of 2×10^6 molecules/cm³ in late afternoon of fog/cloud event (Ervens et al., 2003; Lu et al., 2012). Hence, the daytime production of HNO_3 via N_2O_5 heterogeneous reactions can be essentially faster than the photochemical conversion through OH+ NO_2 in this polluted fog/cloud event.

6.6.3 Daytime N_2O_5 chemistry as an NO_3 source and impact on VOC oxidation

Other than the active N_2O_5 heterogeneous uptake reaction to produce $\text{HNO}_3/\text{NO}_3^-$ and ClNO_2 , the presence of daytime N_2O_5 also implies the presence of NO_3 which could play a significant role in the oxidation of daytime VOCs (Geyer et al., 2003). Under equilibrium condition of N_2O_5 and NO_3 , the NO_3 concentration on 27 November reached a maximum of 3 pptv at ~15:00 and was up to 4 pptv on 30 November in the evening (~16:30). The oxidation rate of NO_3 +VOC can be calculated through equation (6.8), where $\sum_i k_i$ is the sum of the reaction coefficients of NO_3 with VOCs (Atkinson and Arey, 2003; Brown et al., 2011).

$$\text{VOC oxidation rate} (\text{NO}_3) = \sum_i k_i [\text{NO}_3][\text{VOC}_i] \quad (6.8)$$

As VOC measurements are not always available during this campaign, the VOC composition measured on 12:22 of 27 November 2013 (see Table 6.3) was used for this calculation and was assumed to be similar in both the foggy/cloudy and clear day.

Table 6.3. The VOCs mixing ratios sampled at 12:22 (LT) on 27th November 2013

<i>VOCs</i>	<i>Mixing ratios (pptv)</i>
<i>Methane</i>	1926 (ppbv)
<i>Alkanes</i>	
Ethane	2668
Propane	1583
i-Butane	509
n-Butane	739
i-Pentane	497
n-Pentane	687
n-Hexane	68
n-Nonane	30
n-Heptane	49
<i>Alkenes</i>	
Ethene	407
Propene	64
1-Pentene	3
1-Butene	14
i-Butene	29
trans-2-Butene	1
cis-2-Butene	1
<i>Aromatic</i>	
Benzene	384
Toluene	698
Ethylbenzene	143
m/p-Xylene	122
o-Xylene	55
<i>Biogenic</i>	
DMS	48
Isoprene	166
alpha-Pinene	24
beta-Pinene	7

Figure 6.12 shows the oxidation rate of VOCs by daytime NO₃ and OH radical, sorted by alkanes, alkenes, aromatic and biogenic. The daytime NO₃ mixing ratios initiated significant oxidation of VOCs at TMS, with the sum VOCs oxidation rates

of 0.09 ppbv/h on 27 November and 0.12 ppbv/h on 30 November. A comparison of the VOCs oxidation by daytime NO_3 of the two cases with those driven by OH radical (calculated with $[\text{OH}] = 2 \times 10^6 \text{ molecule/cm}^3$) indicated that the NO_3 oxidations of alkenes and biogenic were comparable to the OH-driven oxidations. In contrast, NO_3 only has minor contribution to the oxidations of alkanes and aromatics. Therefore, it is likely that the active daytime N_2O_5 chemistry occurred during the fog/cloud event or early hours of the evening is important for the oxidation of alkenes and biogenic VOCs which may contribute to the formation of secondary organic aerosols (Rollins et al., 2012) in the region.

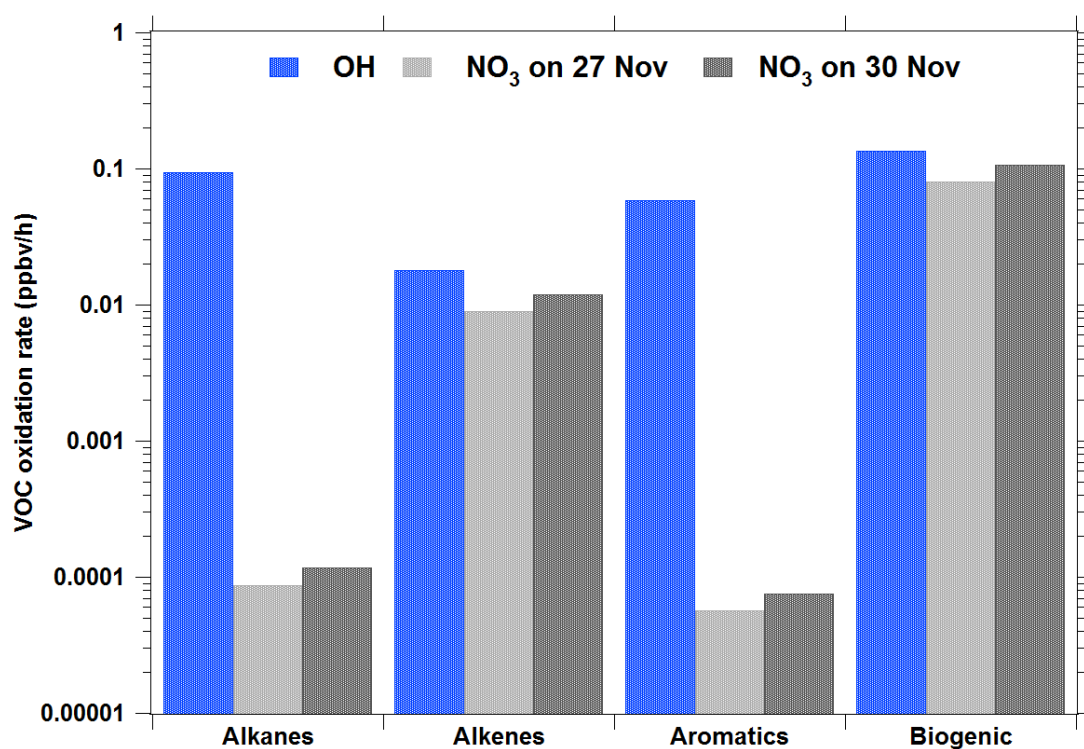


Figure 6.12. The VOC oxidation rate by NO_3 in the daytime of 27 and 30 November 2013 in comparison with the VOC oxidation rate by OH (assumed at a mixing ratio of $2 \times 10^6 \text{ molecule/cm}^3$).

6.7 Summary

This campaign reports the first observation of ClNO₂ in the upper part of the planetary boundary layer of southern China. Measurements took place at Tai Mo Shan, a mountaintop observatory (957 m a.s.l.) in Hong Kong and within the polluted region of PRD. ClNO₂ and N₂O₅ were frequently measured in early periods of the night at this high altitude site, with maximum mixing ratios ranging from 50 to 1500 pptv for ClNO₂ and 200 to 3500 pptv for N₂O₅. The highest ever reported ClNO₂ of 4.7 ppbv and N₂O₅ of 7.7 ppbv (1 min average) were observed during the early morning of 4 December 2013 in extensively processed air from major industrial/urban areas of the PRD. Calculations demonstrate that fast P(NO₃) together with moderate N₂O₅ heterogeneous uptake and ClNO₂ yield initiated the large ClNO₂ event. Photolysis of the nightly produced ClNO₂ in the daytime produces Cl atom with a rate of up to 0.59 pptv/s. Although the high ClNO₂ was only observed in one case, we believe that such concentrations may occur in other locations downwind of the PRD pollution sources and in other polluted regions like the North China Plain (Beijing), which have strong emissions of NO_x and Cl⁻ aerosol.

Small mixing ratios of N₂O₅ (up to 200 pptv) and ClNO₂ (up to 245 pptv) were observed during the late afternoons, indicative of active N₂O₅ chemistry in the region. Observations of the daytime N₂O₅ concentrations were consistent with the value predicted by photochemical steady state on a clear day but showed a large discrepancy between observed and calculated N₂O₅ in the polluted foggy/cloudy day. Heterogeneous uptake of N₂O₅ was shown to be critical in fog/cloud event and was the dominant source of soluble nitrate during the daytime. The presence of daytime

N_2O_5 at late afternoon also significantly contributes to the oxidation of alkenes and biogenic VOCs, with rates comparable to those oxidation driven by OH radical. These observations may suggest that the N_2O_5 chemistry plays important roles in the aerosol formation and oxidation of VOCs in the polluted region influenced by fog and/or cloud. More studies are needed to confirm this effect.

Chapter 7 Observation of ClNO₂ and its impact on VOC oxidation in polluted environment of northern China

The North China Plain covers an area of 409,500 km² and is home to several megacities like Beijing, Tianjin, and Shijiazhuang. This region has been long suffering from severe photochemical and haze pollutions (e.g. Zhang et al., 2014; Zhang et al., 2015) and it is one of the most polluted regions in China according to the Ministry of Environmental Protection (MEP China, 2015). Despite the severe pollution and readily available of the ClNO₂ precursors (i.e. NO_x and Cl⁻ aerosol) in the region, heterogeneous production of ClNO₂ and its impact are unknown in NCP due to lack of direct field measurement.

To fill in this knowledge gap, the CIMS was deployed to a semi-rural site, Wangdu, in Hebei province during the summer of 2014. This study was a part of an international collaborative field campaign, the Campaigns of Air Quality Research in Beijing and Surrounding Regions (CARE-Beijing) 2014 with the main focus to understand the full picture of oxidative processes in the region. The current chapter presents an overview measurement of ClNO₂, N₂O₅ and related parameters at Wangdu. The heterogeneous chemistry of ClNO₂ was examined and discussed. Investigation on the cause of sustained morning ClNO₂ peaks and the potential sources of aerosol chloride that drive the ClNO₂ productions were conducted. Impacts of the ClNO₂ on the primary radical productions and VOCs oxidations rates were also assessed in this study.

7.1 Overview results

The CIMS measurements took place from 20 June to 9 July 2014. Figure 7.1 illustrates the temporal variations of ClNO₂, N₂O₅, related trace gasses, PM_{2.5} and selected meteorological parameters. The data gaps were caused by the technical problems and calibrations or maintenance of the instruments which usually conducted in the afternoon of each day. Elevated concentrations of ClNO₂ were observed in all of the 13 nights with full CIMS measurements with typical night-time mixing ratios >350 pptv. The highest ClNO₂ was measured on 20-21 June with concentration up to 2070 pptv (1 min average). There were several nights when the ClNO₂ mixing ratios were less than 200 pptv, for example on the night of 24, 29 June, and 9 July 2014. These levels of ClNO₂ are comparable with the previous observations in both marine/coastal (Osthoff et al., 2008; Riedel et al., 2012; Mielke et al., 2013) and continental sites (Thornton et al., 2010; Phillips et al., 2012; Riedel et al., 2013). In contrast, low concentrations of N₂O₅ (smaller than 200 pptv) were observed in every night, suggesting a fast loss of N₂O₅, except on the night of 28-29 June 2014 when concentration up to 430 pptv (1 min average) of N₂O₅ was observed in the air masses which had low NO (<2 ppbv) and humidity (RH = <40%).

Observation of the elevated ClNO₂ was in agreement with the expectation of abundant of ClNO₂ precursors such as NO_x, O₃, and aerosols in the NCP environment. As depicted in Figure 7.1, the afternoon concentrations of O₃ exceeded 90 ppbv on majority of days with a maximum value of 146 ppbv, suggestive of intense photochemical reactions during this period. NO_x mixing ratios were in the range of 10-80 ppbv, reflecting strong emissions of NO_x in the region. Similarly, aerosol

loading was considerably high, with $\text{PM}_{2.5}$ mass concentration exceeding $60 \mu\text{g}/\text{m}^3$ on most of the days and reached the highest value of $220 \mu\text{g}/\text{m}^3$.

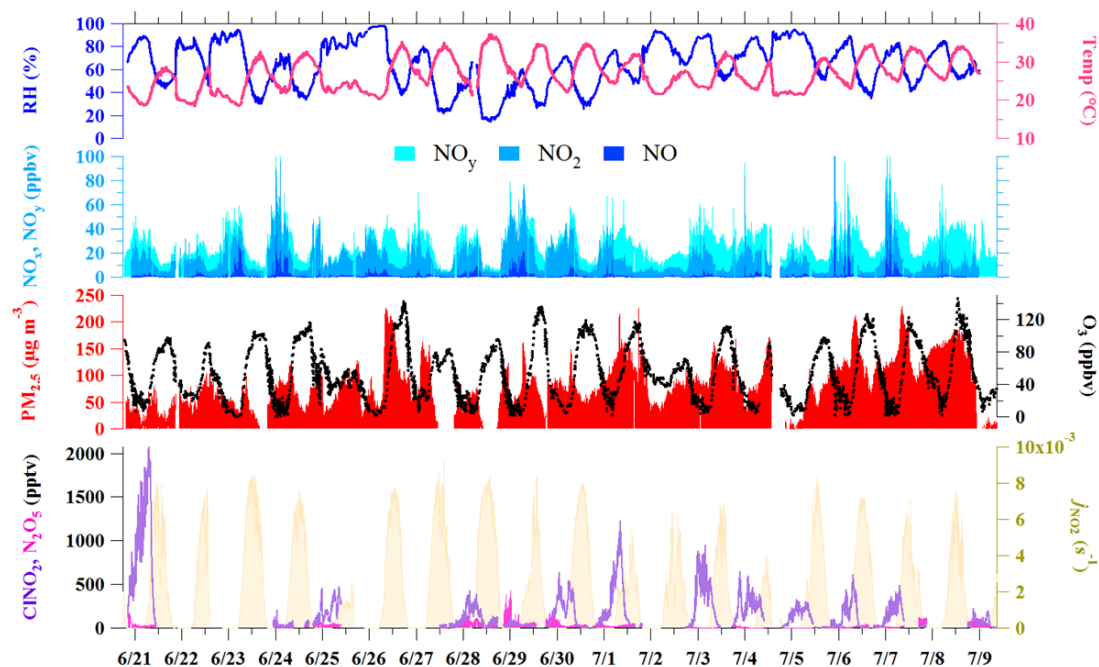


Figure 7.1. Time series of ClNO_2 , N_2O_5 , related species and meteorological parameters observed at Wangdu. Data are at 1 min time resolution, except for the NO_x data (5 min average).

Figure 7.2 shows the 12-h backward particle dispersion trajectories with 08:00 as the starting time, covering the period from 21 June – 9 July 2014. There were no significant changes in the origins of the air masses arriving at 00:00 and 14:00 (data not shown). These results were simulated from WRF-HYSPLIT and were conducted by a colleague (Qinyi Li). Overall, the study period can be meteorologically separated into three parts. The first part, 21-23 June 2014, indicates air masses from megacities of Tianjin and Beijing (passing over Baoding). The highest ClNO_2 level was observed during this period. The second part begins on 24 June 2014 and ends 7 July 2014 with the majority of air masses originating from the southern sector and passing over a portion of urban areas of Shijiazhuang. The ClNO_2 concentrations were in the range

of tens of pptv to 1.2 ppbv. The final part is for 8-9 July 2014 with air masses mostly from the less developed mountainous areas in the northwest sector, and the CINO₂ concentrations were low (<200 pptv). The entire field campaign was dominated by the air masses from southern regions, which is the common summertime condition in NCP.

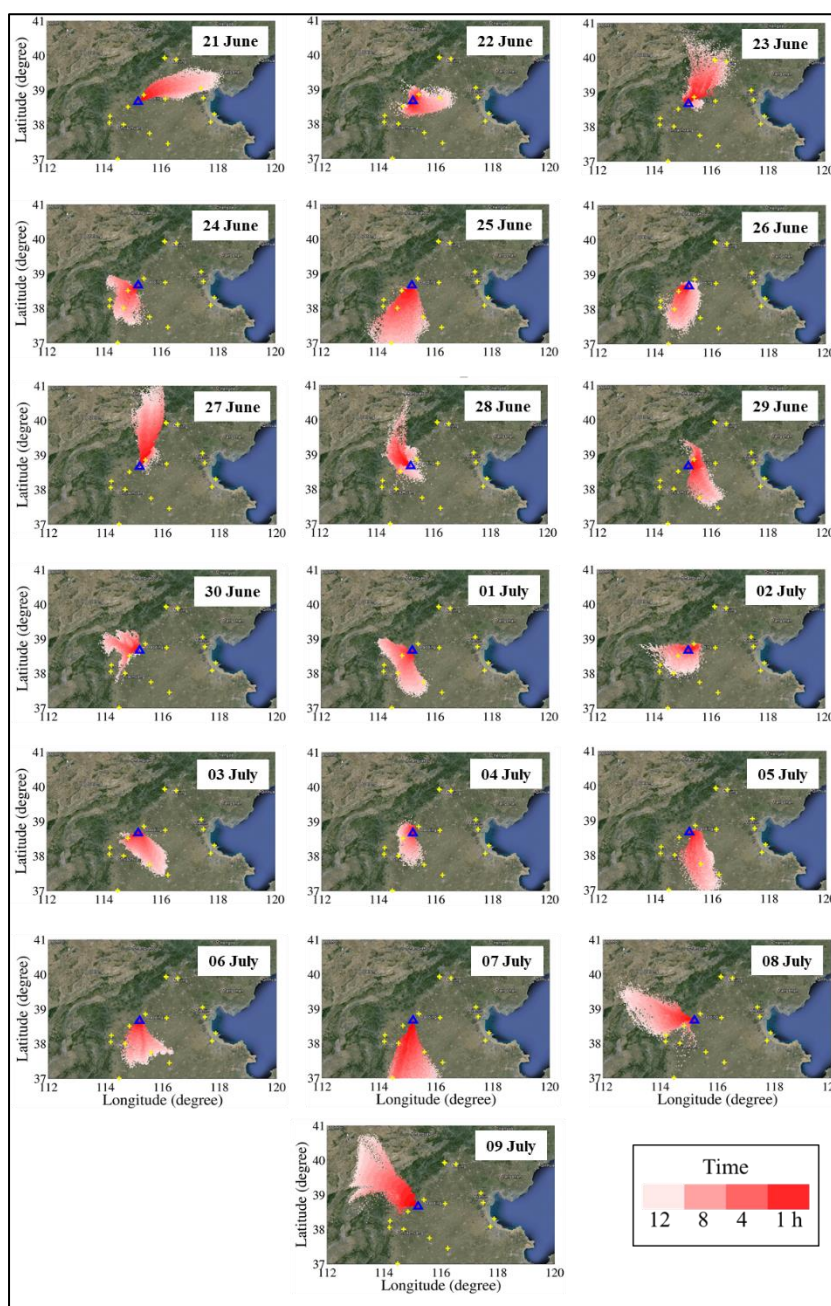


Figure 7.2. History of air masses arriving at the measurement site at 08:00 (12 h backward). Yellow cross represents the major coal-fired power plant in the region.

7.2 Diurnal variations

Figure 7.3 illustrates the diurnal variation of ClNO₂ and relevant chemical data during the campaign average, the highest ClNO₂ case and highest N₂O₅ case. ClNO₂ exhibited a clear diurnal cycle with accumulation of ClNO₂ after sunset (~20:00) and reached a peak at ~08:00 in the morning. It then declined gradually to concentrations near the detection limit at noon. The diurnal average mixing ratios of ClNO₂ in this study were 15-550 pptv. Its precursors, N₂O₅, only showed a small peak right after sunset with a maximum average mixing ratio of 90 pptv, and remained at levels near the detection limit of the CIMS for the rest of the night. The average nighttime (20:00 – 04:30) ClNO₂:N₂O₅ ratio was 9. The NO_y, NO_x, and S_a also showed a similar pattern with ClNO₂. They increased at sunset with average nighttime concentration of 29 ppbv, 21 ppbv and 1880 μm²/cm³, respectively, and were at lowest levels in mid-day. The average nighttime NO_x to NO_y ratio was 0.72. Diurnal variation of O₃ was anti-correlated with that for NO_x, with the former concentration rapidly decreasing at nightfall. The average nighttime O₃ concentration was 33 ppbv.

The highest mixing ratio of ClNO₂ was observed on 20-21 June in the outflow of Tianjin megacity. The ClNO₂ mixing ratios in the megacity case were in the range of 110 to 2070 pptv, while N₂O₅ peaked at 169 pptv (Figure 7.3b). The ClNO₂:N₂O₅ ratio was large on this night with average nighttime ratio of 38. NO_y, O₃, and S_a were generally at similar levels with the average condition, but the NO_x was less abundant at this night compared to the campaign average, with a mean value of 16 ppbv. Smaller NO_x/NO_y ratio of ~0.55 was found on this night, indicating more aged air masses being sampled.

As mentioned above, the largest N_2O_5 concentration of 430 pptv was observed on 28-29 June, in air masses from the north of the site. On this night, the ClNO_2 was low with maximum level reaching 100 pptv, leading to much smaller average $\text{ClNO}_2/\text{N}_2\text{O}_5$ ratio of 0.6. The smaller average $\text{ClNO}_2/\text{N}_2\text{O}_5$ ratio is consistent with the lower S_a of $840 \mu\text{m}^2/\text{cm}^3$. The measured nighttime average NO_y , NO_x , and O_3 were 34 ppbv, 32 ppbv, and 22 ppbv, respectively, and the average NO_x/NO_y ratio was 0.9, suggesting that the sampled air masses were extremely fresh.

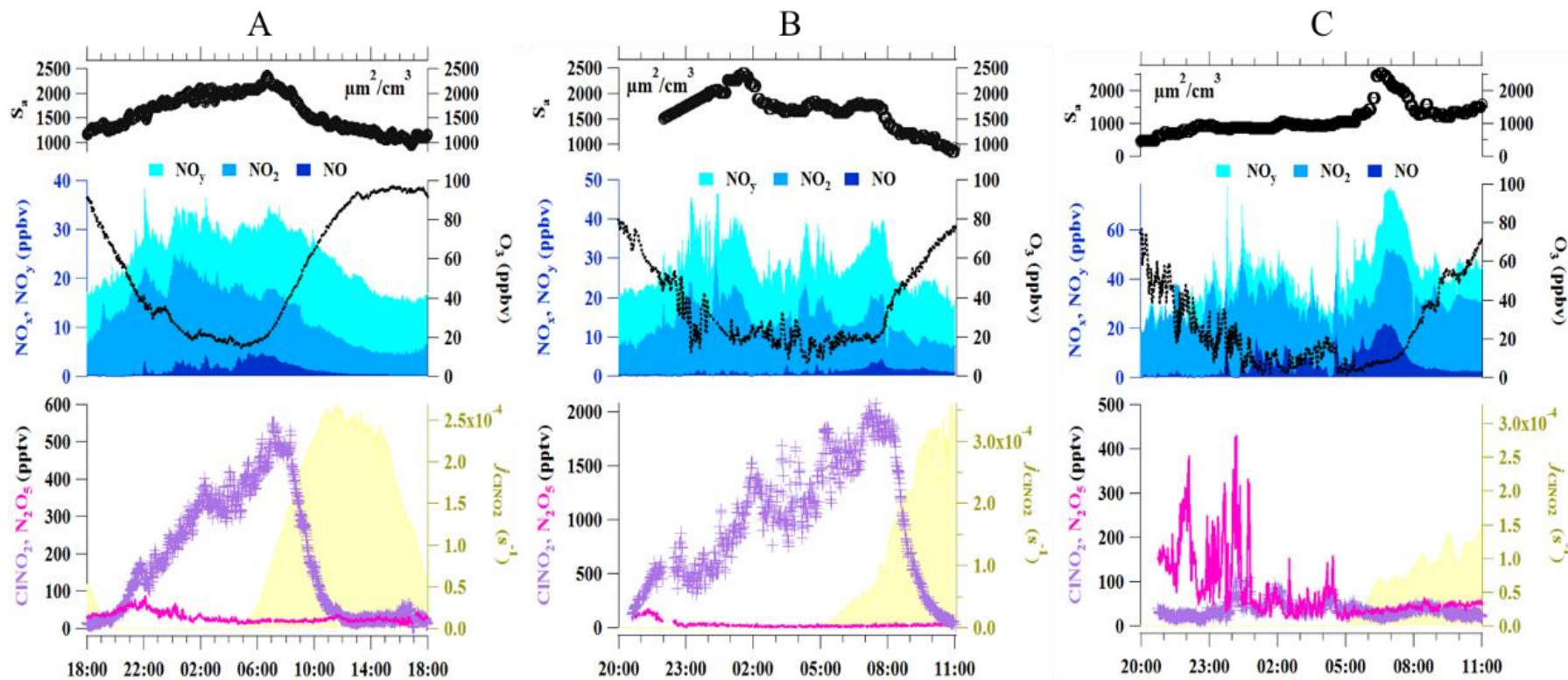


Figure 7.3. Diurnal variation of ClNO_2 , N_2O_5 , NO_x , NO_y , O_3 and particle surface area for a) campaign average (from 20 June to 9 July 2014 when ClNO_2 data is available); b) 20-21 June; c) 28-29 June.

7.3 Factors affecting the variation of ClNO₂/N₂O₅ ratios

To gain insight into the reasons for variation of ClNO₂/N₂O₅ of the campaign average, 20-21 June (highest ClNO₂/N₂O₅) and 28-29 June (lowest ClNO₂/N₂O₅) cases, the production rate of NO₃, N₂O₅ reactivity (i.e. N₂O₅ heterogeneous uptake and dissociation to NO₃), ClNO₂ yield and ClNO₂ formation rate were examined.

7.3.1 Production rate of NO₃

P(NO₃) indicates the upper limit to the possible production of N₂O₅ which is an important metric for ClNO₂ formation (Mielke et al., 2013). The P(NO₃) can be calculated with the observed NO₂ and O₃ concentration through equation (6.1) as mentioned in Chapter 6. Figure 7.4 shows the nighttime P(NO₃) for the campaign average, the night of 20-21 June and 28-29 June at Wangdu. A mean nighttime P(NO₃) of 1.7 ± 0.6 ppbv/h was found in the campaign average. The P(NO₃) of campaign average did not show much difference from other days. For example, on the 20-21 June, the average P(NO₃) was estimated to be 1.3 ± 0.5 ppbv/h. Slightly higher P(NO₃) was found on 28-29 June with an average value of 2.0 ± 1.4 ppbv/h, corresponding to the higher NO_x concentrations on this night. The production rates of NO₃ were comparable in these cases but the ClNO₂ concentrations were different, indicating that the NO_x and O₃ are not the limiting factors for ClNO₂ production in this region.

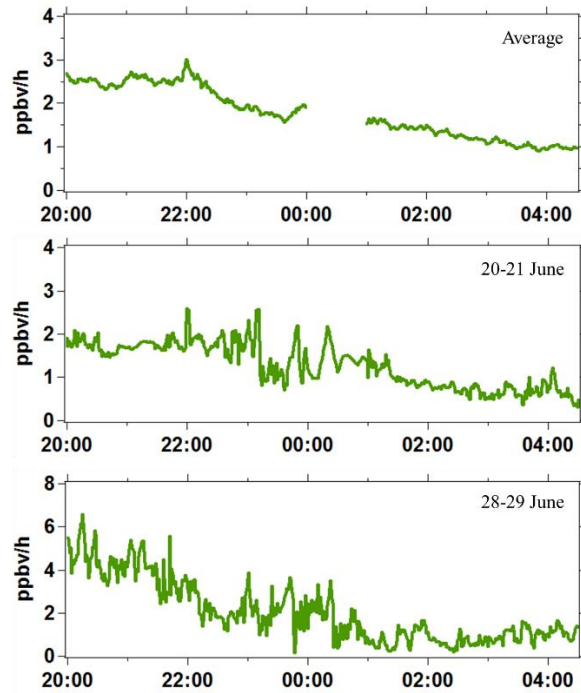


Figure 7.4. The production rate of NO_3 for the nighttime of campaign average, 20-21 June, and 28-29 June.

7.3.2 N_2O_5 reactivity

The reactivity of N_2O_5 was assessed with the inverse N_2O_5 steady state lifetime analysis via equation (7.1) and (7.2) as shown below (e.g. Platt et al., 1984; Brown et al., 2003, 2006, 2009, 2016).

$$\tau(\text{N}_2\text{O}_5)^{-1} = \frac{P(\text{NO}_3)}{[\text{N}_2\text{O}_5]} = \frac{k(\text{NO}_3)}{K_{\text{eq}}[\text{NO}_2]} + k(\text{N}_2\text{O}_5)_{\text{het}} \quad (7.1)$$

$$k(\text{NO}_3) = k_{2,1}[\text{NO}] + \sum_i k_i [\text{VOC}_i] \quad (7.2)$$

The steady state inverse lifetime of N_2O_5 , $\tau(\text{N}_2\text{O}_5)^{-1}$, is the sum of the N_2O_5 loss rate coefficient via dissociation to NO_3 (i.e. $k(\text{NO}_3)/K_{\text{eq}}[\text{NO}_2]$) and N_2O_5 heterogeneous loss rate coefficient ($k(\text{N}_2\text{O}_5)_{\text{het}}$) (refer to equation 7.1). The total N_2O_5 reactivity can be obtained by dividing the $P(\text{NO}_3)$ with the observed N_2O_5 mixing ratios (Brown et al., 2009). The $k(\text{NO}_3)$ represents the loss rate coefficient of NO_3 reactions with NO and VOCs (see equation 7.2). Thus, $k(\text{N}_2\text{O}_5)_{\text{het}}$ can be obtained by subtracting $k(\text{NO}_3)/K_{\text{eq}}[\text{NO}_2]$ from the determined total N_2O_5 reactivity. This analysis was only

conducted for the period between ~20:30 (0.5 h after sunset) until ~23:30 when there were no significant or transient NO plumes (refer to Figure 7.3), because sudden interception of fresh emissions could lead to the failure of the N₂O₅ steady-state approximation in the air mass (e.g. Brown et al. 2003, 2011, 2016).

Figure 7.5 depicts the averaged total N₂O₅ reactivity and fractions of N₂O₅ loss through NO₃ and heterogeneous loss of N₂O₅ for the campaign average and two different ClNO₂/N₂O₅ ratios cases on 20-21 June and 28-29 June. The determined $\tau(\text{N}_2\text{O}_5)^{-1}$ was $1.3 \times 10^{-2} \text{ s}^{-1}$ for campaign average, $5.8 \times 10^{-3} \text{ s}^{-1}$ for the night of 20-21 June and $6.3 \times 10^{-3} \text{ s}^{-1}$ was found on 28-29 June, suggesting that the average total loss rate coefficient of N₂O₅ is about twice of that cases on 20-21 June and 28-29 June. However, the fractions of N₂O₅ reactivity were different in these three examples. N₂O₅ reactivity of the average condition was mainly dominated by loss via NO₃+NO (80%), followed by loss via NO₃+VOC (9%) and N₂O₅ heterogeneous loss (11%), which are in-line with its relatively higher NO background. For the 20-21 June case, although it had lower $\tau(\text{N}_2\text{O}_5)^{-1}$, the N₂O₅ heterogeneous loss had about equal contribution with the loss via NO₃ (NO₃+NO and NO₃+VOC), and was a factor of 2 faster than the campaign average. The 28-29 June case had much smaller $k(\text{N}_2\text{O}_5)_{\text{het}}$, accounting for only 7% of total N₂O₅ reactivity. Half of the N₂O₅ reactivity of this case was due to the reactions of NO₃ with the VOC, which was probably contributed by the biomass burning events occurred around the region during this period (see Figure 7.12 in section 7.5).

The $k(\text{N}_2\text{O}_5)_{\text{het}}$ was later used to predict the $\gamma(\text{N}_2\text{O}_5)$ through equation (2.3). The N₂O₅ uptake coefficient was 0.014 for the average condition. Much larger $\gamma(\text{N}_2\text{O}_5)$

of 0.030 was derived for the case of 20-21 June. In comparison, the night of 28-29 June showed a smaller $\gamma(\text{N}_2\text{O}_5)$ of 0.009. This lower $\gamma(\text{N}_2\text{O}_5)$ was most likely due to the lower RH, leading to a low aerosol liquid water content on this night and could reduce the uptake efficiency of N_2O_5 onto the aerosol (Hu and Abbatt, 1997; Bertram and Thornton, 2009). The $\gamma(\text{N}_2\text{O}_5)$ derived at Wangdu lie within the range of previous field studies conducted in other polluted regions, which reported $\gamma(\text{N}_2\text{O}_5)$ of <0.001 to 0.03 (e.g. Brown et al., 2006; Bertram et al. 2009; Morgan et al., 2015).

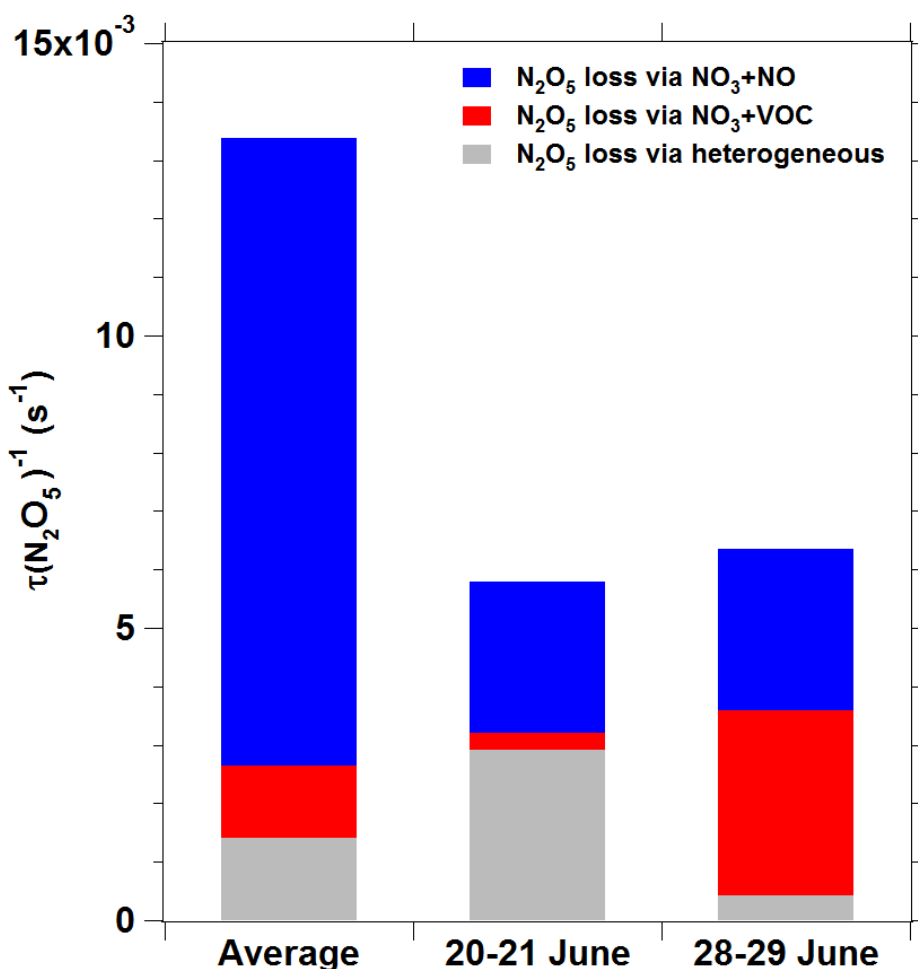


Figure 7.5. The fractions of N_2O_5 loss rate coefficient through NO_3+NO , NO_3+VOC , and heterogeneous reaction for campaign average, 20-21 June, and 28-29 June.

7.3.3 Yield of ClNO₂

Since the ClNO₂ does not involve in night-time reactions, it builds up throughout the night. Therefore, the ClNO₂ yield (ϕ_{obs}) can be obtained by dividing the ClNO₂ concentration over the integrated amount of N₂O₅ uptake loss, as shown in equation (7.3).

$$\phi_{\text{obs}} = \frac{[\text{ClNO}_2]}{\int k(\text{N}_2\text{O}_5)_{\text{het}}[\text{N}_2\text{O}_5] dt} \quad (7.3)$$

The integration was performed with the $k(\text{N}_2\text{O}_5)_{\text{het}}$ as predicted above over the duration from 08:30 to 23:30. As illustrated in Figure 7.6, the average ϕ_{obs} for the campaign average was 0.29, and a comparable ϕ_{obs} of 0.35 was found on the night of 20-21 June. For the night of 28-29 June, much lower average ϕ_{obs} of 0.09 was determined.

Figure 7.6 also shows a comparison of ϕ_{obs} with the ϕ_{calc} calculated from the laboratory-parameterization (see equation (2.4) in Chapter 2) with measured concentrations of aerosol chloride and water content (Roberts et al., 2009; Bertram and Thornton, 2009). The estimated mean ϕ_{calc} was 0.77, 0.78 and 0.93 for the average condition, 20-21 June, and 28-29 June, respectively. These values were much higher than those determined with the field measured ClNO₂ and N₂O₅ concentrations above. The inconsistency of these results may suggest that one or more variables are missed out or are not adequately represented by the laboratory derived parameterization. Riedel et al. (2013) have reported that the Cl⁻ particle phase or partitioning states of Cl⁻ across the aerosol population can cause the overestimation of ϕ_{calc} relative to the

field derived yield. Another reason for the overestimation of the ϕ_{calc} is the possible effects of molecules which can compete to react with NO_2^+ (e.g. Mielke et al., 2013). The presence of phenols or bromides in the aerosols have been shown to reduce the ClNO_2 production efficiency in laboratory studies (Schweitzer et al., 1998; Heal et al., 2007; Ryder et al., 2015). During the study period, biomass burning activities were active in the region (refer to section 3.1.4). The burning activities may release a significant amount of phenolic and bromides compounds (Manö and Andreae, 1994; Chan et al., 2006; Zhang et al., 2007; Akagi et al., 2011), which could reduce the ClNO_2 formation efficiency. Obviously, more studies are needed to confirm the above effects in order to refine the parameterization of ClNO_2 production on ambient aerosol in this region.

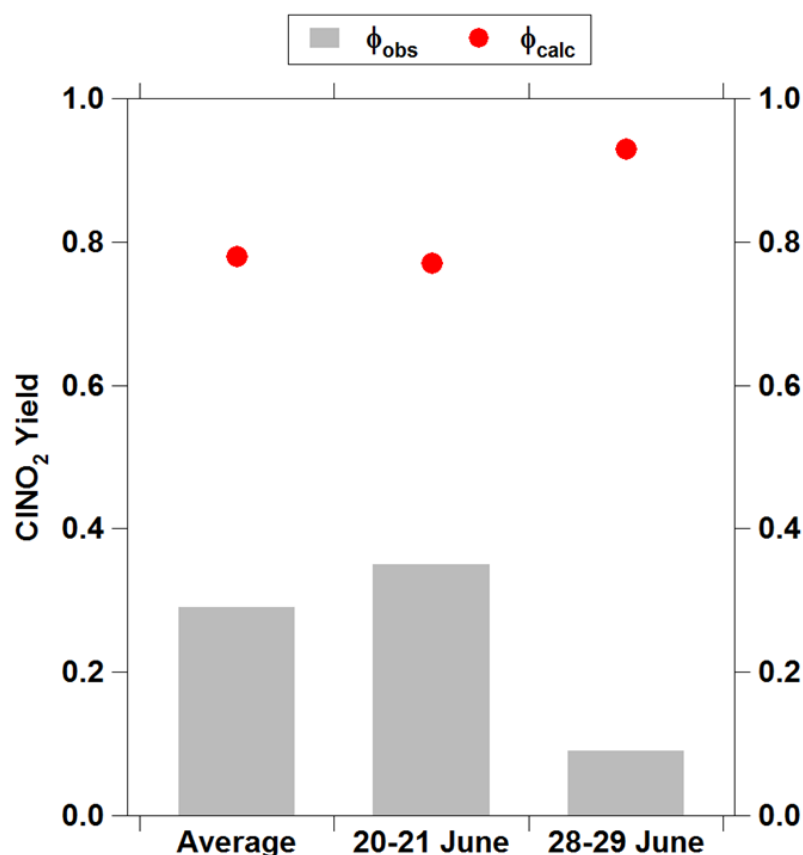


Figure 7.6. Comparison of ClNO_2 yield determined in the observation with the calculated ClNO_2 yield from the laboratory derived parameterization.

7.3.4 ClNO₂ production rate

Figure 7.7 shows the ClNO₂ production rates of the three cases, calculated by applying the above $k(\text{N}_2\text{O}_5)_{\text{het}}$ and ϕ_{obs} into equation (2.1). It is noted that P(ClNO₂) of 20-21 June was about a factor of 4 larger than the campaign average and was ~16 times of the P(ClNO₂) on the night of 28-29 June. The relatively larger ClNO₂ production rate can be justified by the two-times higher $k(\text{N}_2\text{O}_5)_{\text{het}} \times \phi_{\text{obs}}$ and more abundant N₂O₅ (c.a. 2 times larger than average condition) in the 20-21 June case which was due to the less N₂O₅ loss through conversion to NO₃ (as shown above). This result is consistent with the observed four-times higher ClNO₂/N₂O₅ ratios in the 20-21 June case compared to the campaign average (c.f. Figure 7.3). These results demonstrate that the faster heterogeneous N₂O₅ loss, moderate ClNO₂ yield and smaller loss via NO₃ are the major reasons for the high ClNO₂ concentrations at Wangdu.

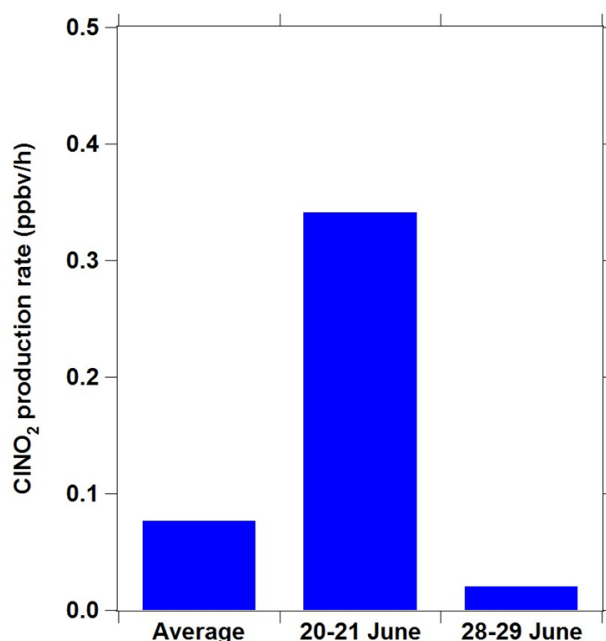


Figure 7.7. The production rates of ClNO₂ for 20-21 June, 28-29 June, and campaign average.

7.4 Sustained ClNO₂ morning peak

A salient feature of this study is the observation of sustained morning ClNO₂ peaks. Figure 7.8 illustrates the examples of sustained ClNO₂ morning peaks and related chemical characteristics for the campaign average and the highest ClNO₂/N₂O₅ ratio case on 21 June case and lowest ClNO₂/N₂O₅ case (29 June) as mentioned in the previous section. ClNO₂ concentration continued to increase after sunrise (at ~04:40) and persisted for about 4 hours from sunrise for almost every day (12 out of 13 days with full CIMS measurements). The average mixing ratio of the morning ClNO₂ peak was 550 pptv and the highest ClNO₂ case on 21 June reaching ppbv level, while very small ClNO₂ peak was observed in the case of 29 June. These results are discrepant from the typical diurnal patterns of ClNO₂ observed at other places (e.g. Osthoff et al., 2008; Thornton et al., 2010; Riedel et al., 2012; Mielke et al., 2013) including our studies in Hong Kong (refer to Chapter 4 and 6), which showed a decline of ClNO₂ levels at sunrise. Only two recent studies in London and Texas have reported the observations of morning ClNO₂ peaks (Bannan et al., 2015a; Faxon et al., 2015), but their concentrations were much smaller than the values observed here.

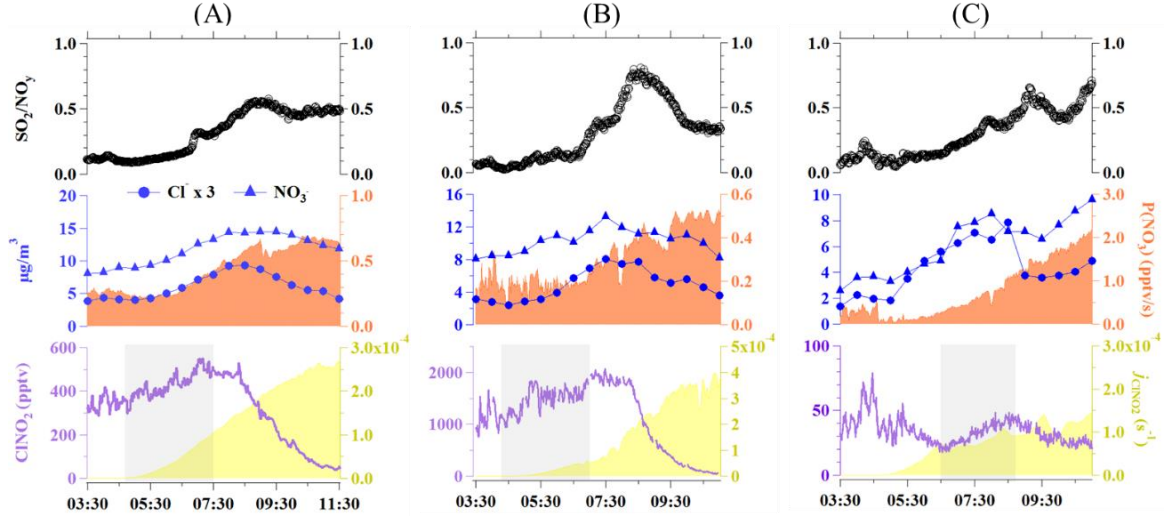


Figure 7.8. An expanded view of the sustained morning CINO₂ peaks together with some relevant chemical information including SO₂/NO_y, Cl⁻ (×3), NO₃⁻, and P(NO₃) for a) campaign average; b) 21 June; and c) 29 June.

7.4.1 Factors contributing to the sustained CINO₂ morning peak

The CINO₂ enhancement (Δ CINO₂) in the morning could be caused by in-situ CINO₂ productions and/or the vertical mixing (i.e. downward mixing) of the produced CINO₂ from aloft. The in-situ production of CINO₂ was calculated for the area shaded in light grey as shown in the Figure 7.8, by constraining the measured N₂O₅ and j_{CINO_2} into equation 7.4, which is similar to equation (2.1) but with additional consideration of photolysis loss of CINO₂ (Wagner et al., 2013; Mielke et al., 2013).

$$\frac{d[\text{CINO}_2]}{dt} = \phi k(\text{N}_2\text{O}_5)_{\text{het}}[\text{N}_2\text{O}_5] - j_{\text{CINO}_2}[\text{CINO}_2] \quad (7.4)$$

As the $k(\text{N}_2\text{O}_5)_{\text{het}}$ and ϕ determined at the night-time (in section 7.3) are irrelevant to be applied during the daytime, the $k(\text{N}_2\text{O}_5)_{\text{het}}$ here was predicted from equation (2.3). The $\gamma(\text{N}_2\text{O}_5)$ of 0.03 and unity CINO₂ yield (1.0) were used in the calculations. These numbers were adopted from the upper-end values determined in previous field studies (Brown et al., 2006; Bertram et al., 2009; Riedel et al., 2013). Therefore, the calculated

values represent the upper limits of ClNO₂ production. As shown in Figure 7.9, the predicted ΔClNO_2 with $\gamma(\text{N}_2\text{O}_5) \times \phi = 0.03$ did not agree well with the observations of the three cases. The sensitivity tests on the range of $\gamma(\text{N}_2\text{O}_5) \times \phi$ found that larger $\gamma(\text{N}_2\text{O}_5) \times \phi$ of 0.06 - 0.09 were required, in order to reproduce the measured ΔClNO_2 in the average condition and case of 21 June. However, such large $\gamma(\text{N}_2\text{O}_5) \times \phi$ are not supported by the currently understanding of ambient N₂O₅ uptake and ClNO₂ yield in the literature. In contrast, the $\gamma(\text{N}_2\text{O}_5) \times \phi = 0.03$ give extremely larger production of ClNO₂ than the observed ΔClNO_2 on the day of 29 June. These results suggest that in-situ ClNO₂ production is unlikely the major cause in driving the ClNO₂ morning increase.

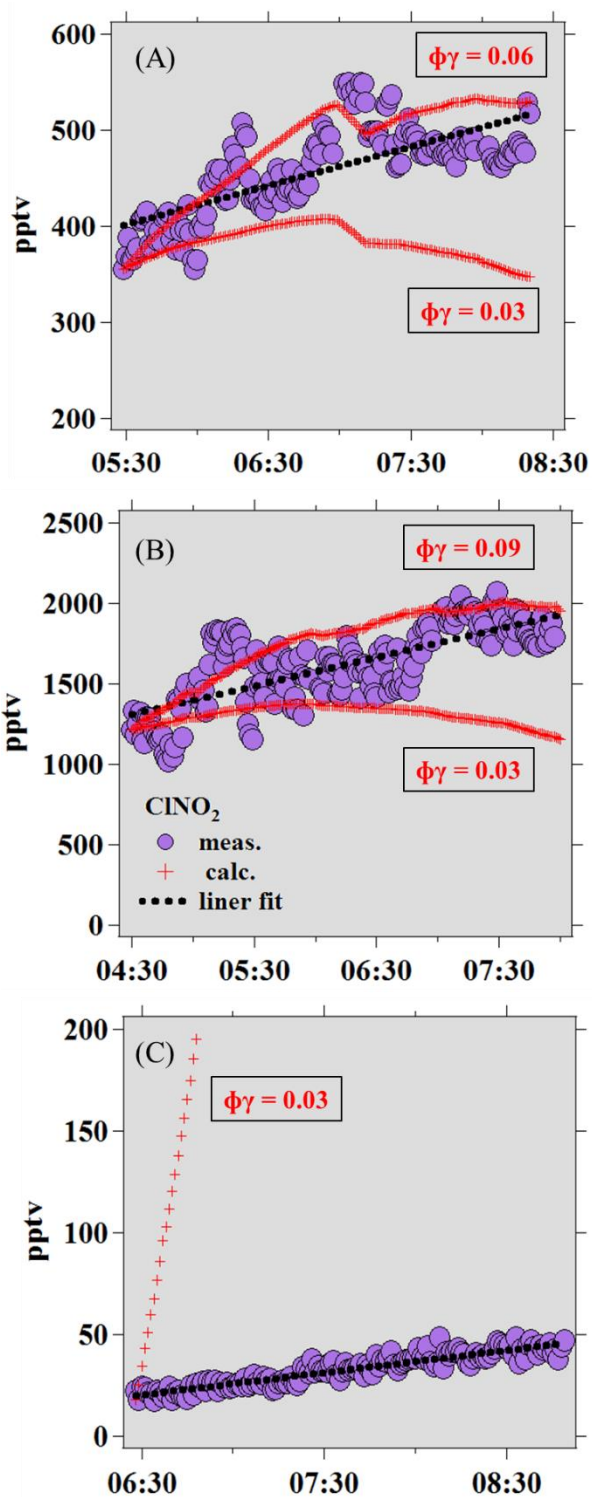


Figure 7.9. The observed enhancement of CINO₂ and the calculated in-situ production of CINO₂ for a) campaign average; b) 21 June case; and c) 29 June case.

Meteorological and chemical data showed evidence that the downward mixing of CINO₂-rich air aloft after sunrise are the cause of the CINO₂ morning peaks observed at Wangdu. Figure 7.10 depicts the proportions of air arriving at the

measurements site from various heights at different time derived from the simulations of WRF-HYSPLIT (data were provided by Qinyi Li). Prior to sunrise (at 04:00), more than 95% of the air masses that arrived at the sampling site were mostly confined to the ground level (< 200 m above ground level, a.g.l.). Shortly after sunrise (at 05:00), the contribution of higher altitudes air masses (> 200m a.g.l.) increased considerably after the break-up of NBL. As time advanced, more fraction of higher-altitude air masses impacted the ground site. For example, more than half of the air masses at 08:00 were from the altitude higher than 200 m (Figure 7.10a and 7.10b), indicating strong downward mixing processes. However, less contribution of higher level air masses (< 30% are from altitude >200 m a.g.l.) was observed on the morning of 29 June (Figure 7.10c). These different levels of entrainment are consistent with the observation of the various concentrations of ClNO₂ morning peaks.

The chemical data is consistent with the meteorological analysis above. As illustrated in Figure 7.8, the SO₂/NO_y ratios in the three examples increased significantly from ~0.1 to a ~0.8 right after sunrise, indicative of the influence of plumes from coal-fired power plants. The pollutant emitted from the power-plants' elevated stacks normally reside above the NBL due to poor vertical mixing at night-time. In addition to SO₂ emissions, coal-fired power plants also emit considerable amount of NO_x and Cl⁻ particles (McCulloch et al., 1999; Zhao et al., 2008). Hence, it can be interpreted that the addition of NO_x and Cl⁻ particles together with high aerosol loading and O₃ formed in the preceding daytime led to significant production of ClNO₂ above the NBL, which indeed have been observed in other field observations (Wagner et al., 2012; Young et al., 2012; Riedel et al., 2013). The precursors of ClNO₂ such as

Cl⁻ particle and P(NO₃) and a co-product of chlorine activation, nitrate (NO₃⁻) particle, also showed notable enhancements in the morning hours (refer to Figure 7.8).

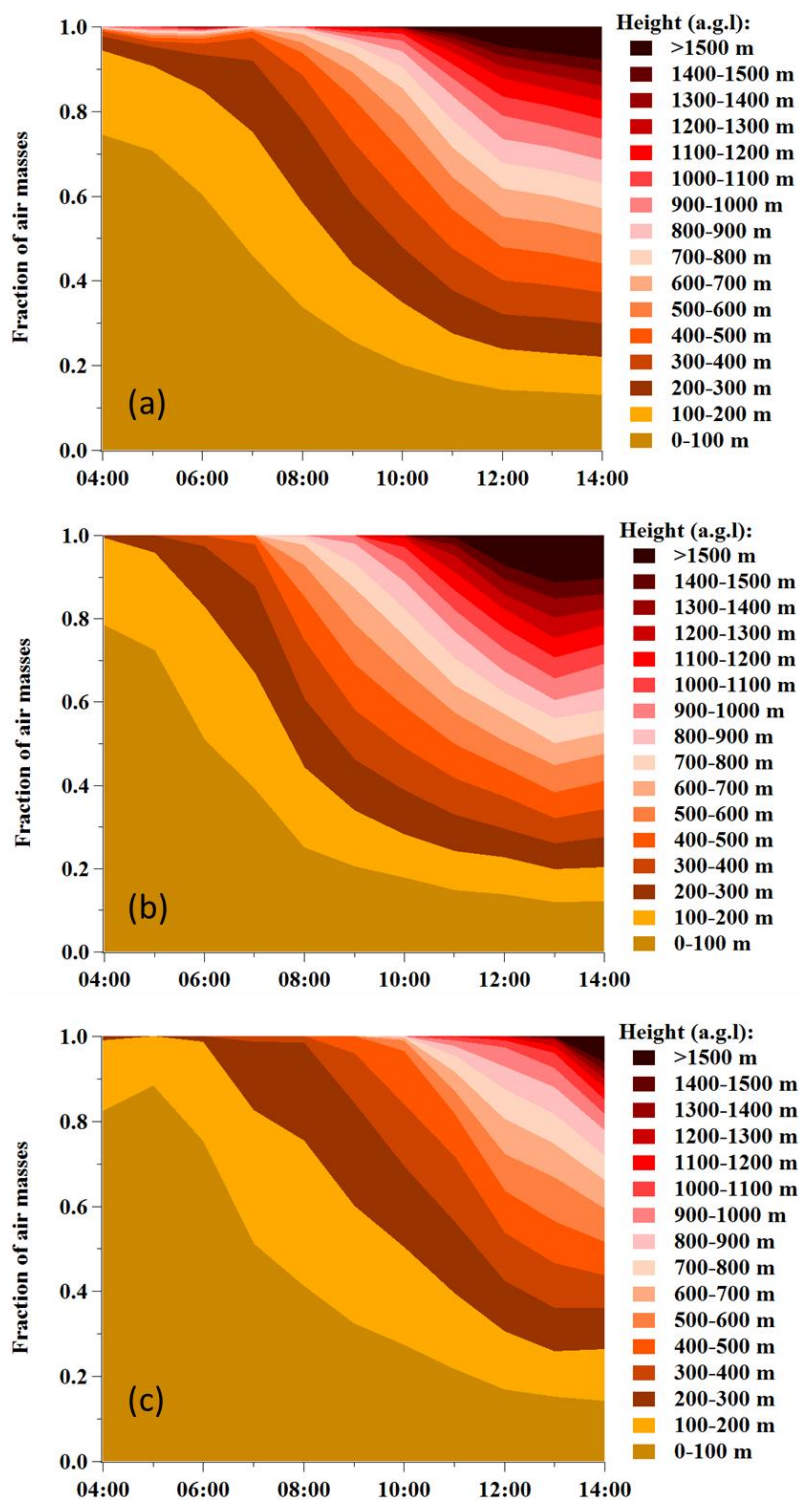


Figure 7.10. Fractions of air masses arriving at the Wangdu site at different time of the day (average condition). These fractions are derived from the simulation results of 1 h backward-in-time HYSPLIT.

7.4.2 Prediction of the ClNO₂ concentrations in the residual layer

As established above, the sustained morning peak was due to the entrainment process which brought concentrated ClNO₂ in the RL to ground surface after sunrise. In order to have an overview of the ClNO₂ presented in the RL, a simplified one-dimensional (1D) model was used to demonstrate the entrainment. This model consists of two layers of air before sunrise; NBL and RL, with ClNO₂ mixing ratios of C_n and C_r, respectively (see Figure 7.11a). It was assumed that no mixing of air masses (and ClNO₂) between the two layers. The two layers are efficiently mixed after sunrise, giving a constant mixing ratio of ClNO₂ (C_p). The height of the daytime planetary boundary layer (H_p) and NBL (H_n) was calculated by the WRF model (data provided by Qinyi Li). As it 's hard to determine the effective mixing height of ClNO₂ in the RL, the depth of the RL (H_r) was treated as the difference between H_p and H_n in this calculation. Previous studies of ClNO₂ vertical distribution showed that the most concentrated ClNO₂ layer typically fall within several hundreds of meter above the ground (Young et al., 2012; Riedel et al., 2013; Wagner et al., 2012; Brown et al., 2013), suggesting the H_r adopted here is reasonable to account for the ClNO₂ in RL. C_n and C_p are the observed ClNO₂ concentration before (at 05:00) and after (at 08:00) sunrise, respectively. The ClNO₂ mixing ratio in RL layer before sunrise can be estimated by the mass balance approach with consideration of ClNO₂ loss via photolysis between 05:00 and 08:00 as in equation (7.5).

$$C_p \times H_p = (C_n \exp(-j_{\text{ClNO}_2} t) \times H_n) + (C_r \exp(-j_{\text{ClNO}_2} t) \times H_r) \quad (7.5)$$

Here, j_{ClNO_2} is the photolysis rate of ClNO₂ and t is time in second.

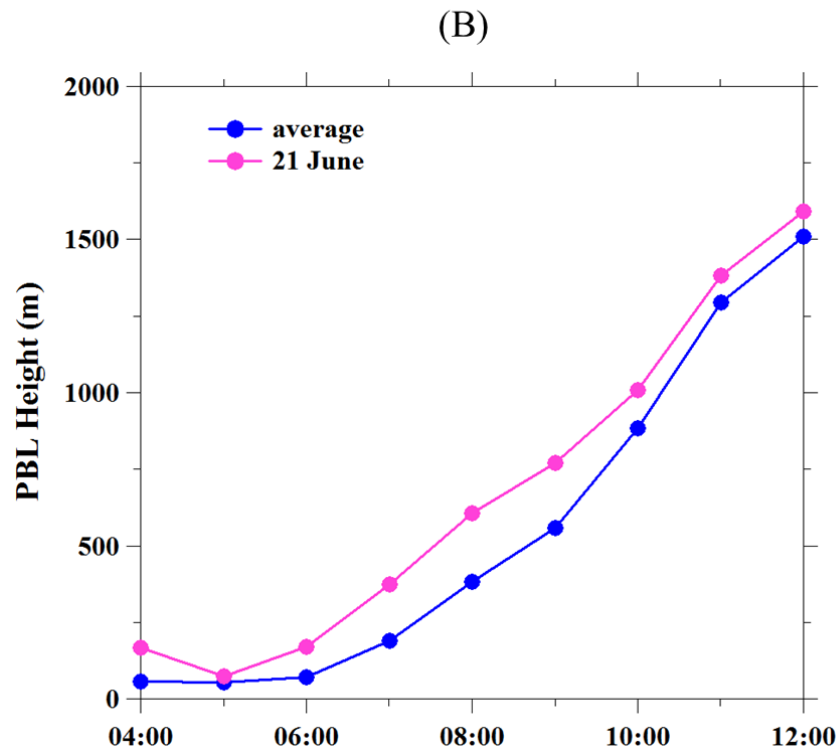
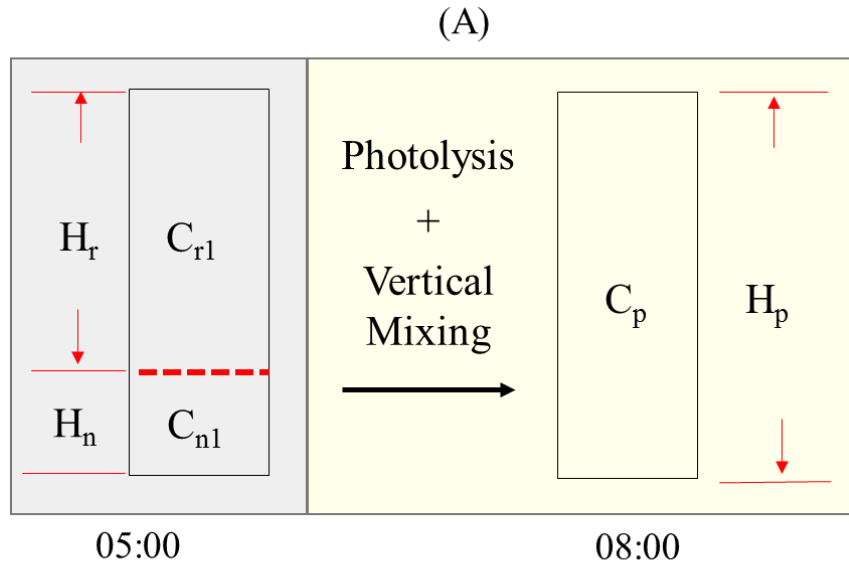


Figure 7.11. a) Conceptual diagram of the simplified 1D model used to demonstrate the entrainment; b) the WRF-simulated boundary layer heights (above ground level) for the average condition and 21 June case.

For the campaign average, WRF simulated boundary layer height is 30 m and 325 m (a.g.l.) at 5:00 and 8:00, respectively (refer to Figure 7.11b), yielding a concentration of ClNO_2 in RL of 1.7 ppbv. As for the 21 June case with boundary

layer height of 72 m at 05:00 and 610 m at 08:00, the ClNO_2 in RL by sunrise would be 4.0 ppbv. These concentrations fall within the range of aircraft and tower measurements in RL of US (Wagner et al., 2012; Young et al., 2012; Riedel et al., 2013) and are comparable to the highest ClNO_2 observed at a mountain site in southern China (refer to Chapter 6). These values also indicate that heterogeneous productions of ClNO_2 are important and elevated mixing ratios of ClNO_2 may frequently present in the residual layer of northern China.

7.5 Chloride availability and its potential sources

The observations of elevated ClNO_2 at Wangdu require sufficient amount of chloride aerosols to support its productions throughout the night. Substantial levels of fine Cl^- aerosols were frequently observed during the night-time (20:00-09:30) with mean concentrations of $1.6 \mu\text{g}/\text{m}^3$ and maximum up to $6.8 \mu\text{g}/\text{m}^3$ (Figure 7.12). The Cl^- observations were similar to the level of Cl^- commonly found in NCP that has an average range of $1\text{-}6 \mu\text{g}/\text{m}^3$ (He et al., 2001; Sun et al., 2012; Huang et al., 2014; Sun et al., 2015), suggesting the presence of significant chloride sources in the region. Meteorological analysis as shown by the air mass back-trajectories at Wangdu revealed that most of the air masses that arrived at the site are of continental origins, and there were limited of direct influences from marine (refer to Figure 7.2). Furthermore, the fine aerosol compositions of $[\text{Cl}^-]/[\text{Na}^+]$ mass ratios showed in the Figure 7.12 appear to be larger (maximum up to 2.9) than the theoretical sea-water ratio of 1.8 (Seinfeld and Pandis, 2006) for most of the time. These indicate that the Cl^- were not solely from the marine aerosols but were also influenced by non-marine chloride emitting sources.

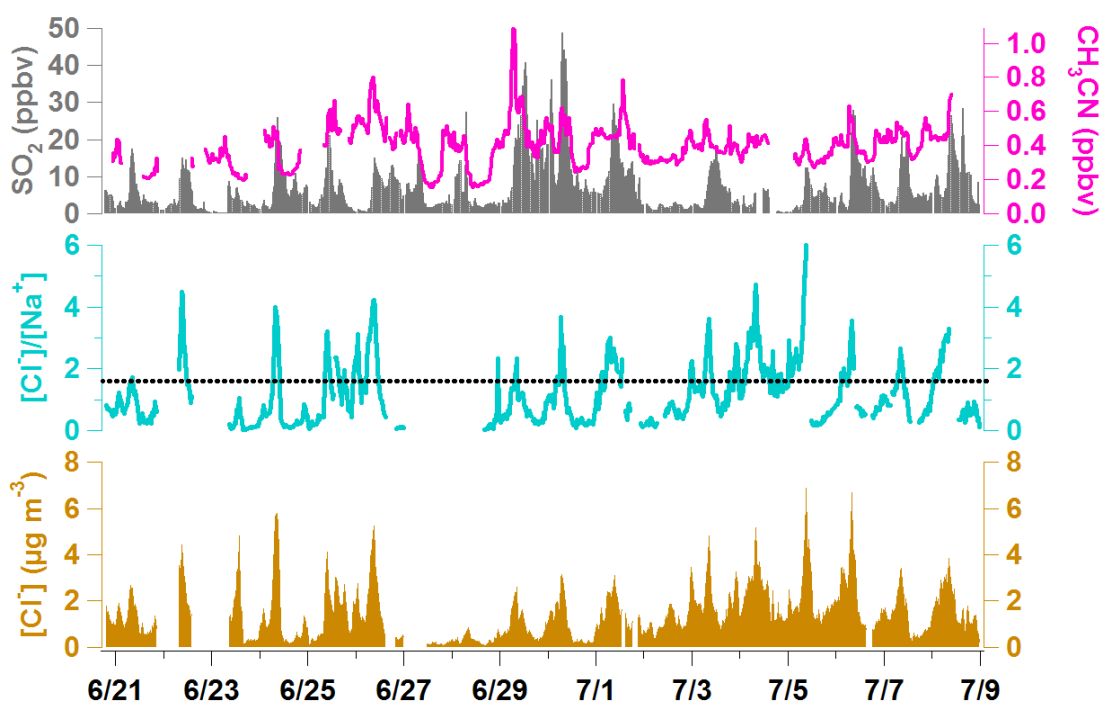


Figure 7.12. Concentrations of fine Cl^- , SO_2 (a coal-fired power plant indicator) and CH_3CN (a biomass burning indicator) from 20 June to 9 July 2014. The black dash line represents the mass ratio of $[\text{Cl}^-]$ to $[\text{Na}^+]$ in seawater (1.8).

The influence of regional anthropogenic activities on the chloride measurement at Wangdu was investigated. Table 7.1 shows the correlations of Cl^- aerosol concentrations with the mixing ratios of SO_2 and acetonitrile (CH_3CN) for each night (20:00 – 09:30). SO_2 was chosen as the tracer that associated with the emissions of coal-fired power plant (e.g. Zhao et al., 2013), while CH_3CN is an important indicator for biomass burning (e.g. de Gouw et al., 2003). SO_2 and Cl^- were correlated in majority of the nights, with 11 out of the 16 nights have correlations (r) > 0.75 and slopes varied between 0.083 - 0.365. The results are within the expectation because there are many coal-fired power plants located in the vicinity of the sampling site, and the back-trajectories were shown to intercept these power plants before reaching the sampling site (see Figure 7.2). Rich chlorine content (average of 260 mg/kg) has been found in the coal used in China (Zhang et al., 2012). Combustion of

coals under high temperature and oxygen-free environment can release up to 97% of the chlorine in the coal as HCl gas (Gibb, 1983) which can then be transformed into aerosol phase (Cl⁻ aerosol) through neutralization processes in the ambient air.

Table 7.1. Correlations and slopes of chloride with power plant (SO₂) and biomass burning (CH₃CN) indicators from 20:00-09:30.

Time (20:00 to 09:30)	[Cl ⁻]		With SO ₂		With CH ₃ CN		
	Mean (µg/m ³)	Mean [SO ₂] (ppbv)	Slope	Correlation (<i>r</i>)	Mean [CH ₃ CN] (ppbv)	Slope	Correlation (<i>r</i>)
20-21 June	1.450	5.74	0.092	0.858	0.35	2.20	0.330
21-22 June	2.792	3.87	0.267	0.963	<i>n/a</i>	<i>n/a</i>	<i>n/a</i>
23-24 June	1.729	5.65	0.234	0.946	0.43	0.10	0.003
24-25 June	0.760	4.88	0.235	0.852	0.39	36.96	0.547
25-26 June	1.988	2.79	0.281	0.833	0.56	11.27	0.893
27-28 June	0.335	6.67	0.008	0.213	0.39	-1.33	0.577
28-29 June	0.915	7.44	0.083	0.831	0.55	2.77	0.830
29-30 June	1.429	22.67	0.048	0.719	0.48	4.96	0.442
30 June – 1 July	1.283	10.43	0.094	0.781	0.45	6.01	0.268
01-02 July	0.762	2.53	0.089	0.630	0.32	4.76	0.448
02-03 July	2.187	3.84	0.195	0.762	0.43	10.68	0.548
03-04 July	2.636	3.69	0.314	0.613	0.39	12.76	0.566
04-05 July	2.158	2.55	0.365	0.922	0.35	30.09	0.924
05-06 July	2.857	7.29	0.112	0.776	0.44	12.86	0.763
06-07 July	1.720	6.04	0.113	0.853	0.46	9.84	0.502
07-08 July	1.939	8.70	0.084	0.607	0.49	2.14	0.157

For most of the nights, the Cl^- did not show correlation with the CH_3CN , except in 4 nights (25-26 June, 28-29 June, 4-5 July, and 5-6 July) where the r is larger than 0.75. Figure 7.13 depicts an example of biomass burning events mostly in the south of Wangdu on 27-29 June. Open burning of the agricultural residues was shown to contribute massive of Cl^- aerosol, accounting for 40% of the soluble inorganic or 4.5% of the $\text{PM}_{2.5}$ concentrations (Mcmeeking et al., 2009). Li et al., (2007) determined that burning the wheat straw and maize stover harvested in China give Cl^- emission factors of 0.83 and 2.7 g/kg, respectively. A previous study reported that the direct sampling of biomass burning plumes during the harvesting season in China caused a remarkable increment in Cl^- concentration ($>20 \mu\text{g}/\text{m}^3$) (Li et al., 2014).

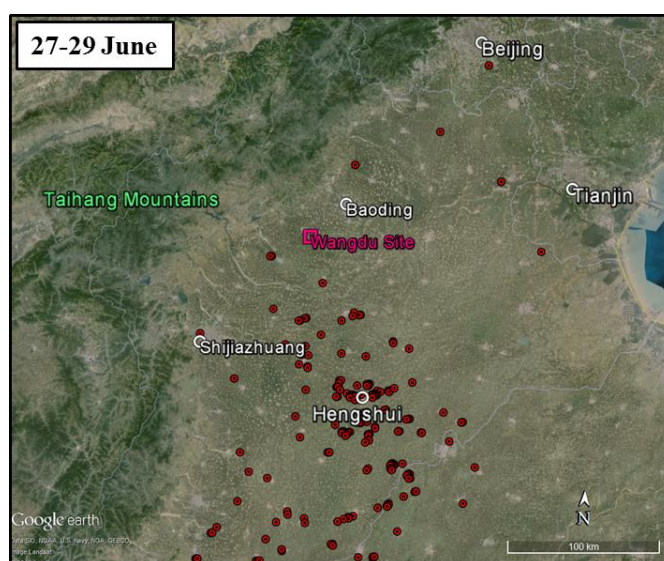


Figure 7.13. An example of biomass burning event from the active fire hotspots data (red dots) on 27-29 June.

The current analysis infers that the coal-fired power plants have major contributions to the availability of chloride at Wangdu, while biomass burning is an occasional source of chloride or particularly important during the harvesting seasons. Nevertheless, there are several nights where the Cl^- had weak correlations with both

SO₂ and CH₃CN. These observations may imply the existence of other chloride sources which required more investigations.

7.6 Impacts of ClNO₂ on the oxidative chemistry

This section examines the contributions of ClNO₂ to the primary radical production and the oxidation of VOCs at Wangdu. The analysis only focuses on the campaign average condition and the 21 June case to represent the average and maximum effects.

7.6.1 Primary radical production

Photolysis of ClNO₂ and reaction of HCl with OH are the two most prominent Cl atom sources in polluted environments (Riedel et al., 2012; 2014). The production rate of Cl atom (P(Cl)) via photolysis of ClNO₂ can be predicted by $j_{\text{ClNO}_2}[\text{ClNO}_2]$ while P(Cl) from the latter source is given by $k_{\text{OH+Cl}}[\text{HCl}][\text{OH}]$. Figure 7.14 illustrates the P(Cl) derived from the photolysis of ClNO₂ and HCl+OH during the daytime. It shows that photolysis of ClNO₂ was the prime source of Cl atom in Wangdu (contribute >85% of the Cl atom production). The P(Cl) via ClNO₂ was efficient from sunrise to ~11:00 and reached maximum at ~08:00, corresponding to the peak concentration of ClNO₂, while the reaction of HCl+OH only become important during the afternoon. The sum of the Cl production rates from the two sources reached 2.6×10^6 molecules/cm³/s for the average condition, and up to 8.3×10^6 molecules/cm³/s for the 21 June case.

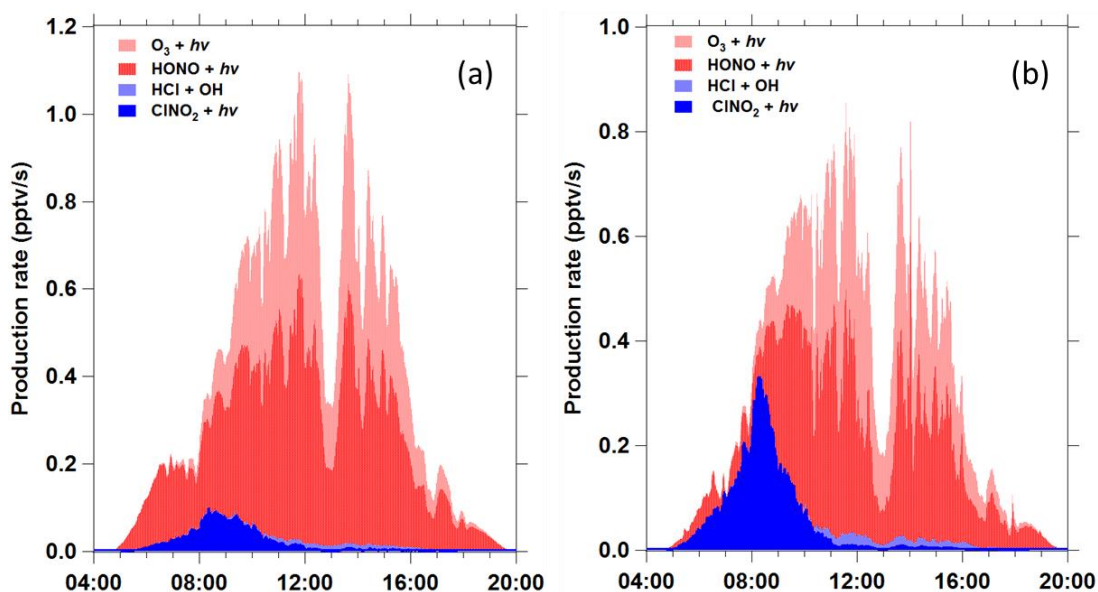


Figure 7.14. The relative importance of production rate of Cl atom from photolysis of ClNO_2 and reaction of $\text{OH}+\text{HCl}$ for a) the campaign average and b) the 21 June case, in comparison with the production rates of primary OH radical ($\text{P}(\text{OH})$). The $\text{P}(\text{OH})$ from photolysis of O_3 is stacked on the $\text{P}(\text{OH})$ from HONO.

To elucidate the significant productions of Cl radical, the total $\text{P}(\text{Cl})$ was compared with the production rates of OH radical. The OH radical production rate was calculated from two important primary sources of OH radical including the photolysis of ozone and HONO (Liu et al., 2012; Lu et al., 2013) and the sum of OH radical production rate ($\text{P}(\text{OH})$) is given by equation (7.6).

$$\text{P}(\text{OH}) = \frac{2j_{\text{O}_3}[\text{O}_3]k_{\text{H}_2\text{O}}[\text{H}_2\text{O}]}{k_{\text{H}_2\text{O}}[\text{H}_2\text{O}] + k_{\text{N}_2}[\text{N}_2] + k_{\text{O}_2}[\text{O}_2]} + j_{\text{HONO}}[\text{HONO}] \quad (7.6)$$

As illustrated in Figure 7.14, the $\text{P}(\text{Cl})$ was as important as $\text{P}(\text{OH})$ during the morning hours, where $\text{P}(\text{Cl})/\text{P}(\text{OH})$ ratio accounted for up to 0.28 and 0.96 for the campaign average and 21 June, respectively. Integrated production of Cl atoms over the entire morning (04:40-11:00) for the campaign average attributed to 11% of primary radical productions from the mentioned sources. The integrated $\text{P}(\text{Cl})$ in the morning of 21 June contributed to 25% of the summed primary radical productions. A complete analysis of the impact of ClNO_2 on daily primary radical budget had been conducted

with an explicit chemical box model (MCM; simulation was performed by another colleague, Hui Yun). The model results demonstrate that photolysis of ClNO₂ contributed to 10% of the daily RO_x (OH, HO₂, and RO₂) production rate on the average condition and with a much larger contribution of 30% in the case of 21 June (refer to our publication of Tham et al., 2016). All of these results underline the importance of ClNO₂ as a crucial source of primary radical in this region.

7.6.2 VOCs oxidation

In what follows, the effect of Cl atom on VOC oxidation at Wangdu was assessed. The oxidation rate of VOCs is given by the following equation:

$$-\frac{d[\text{VOC}]}{dt} = [\text{radical}] \sum_i k_i [\text{VOC},i] \quad (7.7)$$

Where [radical] is the concentration of measured OH or Cl atoms calculated using a time-dependent chlorine chemistry box model (see section 3.7) and [VOC,*i*], represents the corresponding measured concentration of each species of alkane, alkene, alkyne, aromatic and oxygenated VOC (OVOC). The *k_i* is the bimolecular rate coefficient for the reaction of radical with each VOC species at the measured pressure and temperature (IUPAC Kinetic database; Orlando et al., 2003; Atkinson et al., 2007; Riedel et al., 2014; Young et al., 2014). The mean concentrations of trace gasses, VOCs and other parameters that serve as inputs of the chlorine chemistry model and VOC oxidation rate calculations are summarized in Table 7.2.

Table 7.2. Mean concentrations and standard deviations (σ) of each species and meteorological conditions used as input in the box model simulations. Concentrations are in ppbv unless mentioned.

Species	Average		21 June	
	Mean	σ	Mean	σ
ClNO ₂	0.186	0.162	0.521	0.648
NO	1.32	1.30	0.65	0.76
NO ₂	13.11	5.96	10.37	5.28
O ₃	54.3	30.2	54.6	29.1
OH (pptv)	0.100	0.115	0.124	0.120
HO ₂ (pptv)	13.21	12.07	10.49	8.97
HCl	1.15	0.40	1.26	0.93
methane	2361	362	2090	233
methanol	24.707	5.673	15.698	4.805
acetaldehyde	1.887	0.357	1.349	0.383
acetic acid	5.013	0.897	2.437	0.610
acetone	4.796	0.583	3.345	0.353
formaldehyde	7.247	1.394	3.475	0.545
methylethylketone	2.004	0.106	3.401	0.562
ethane	2.950	0.454	2.465	0.717
ethene	1.813	0.860	1.034	0.721
propane	1.171	0.304	1.186	0.456
propene	0.310	0.170	0.221	0.161
i-butane	0.413	0.130	0.359	0.159
n-butane	0.701	0.249	0.591	0.292
ethyne	1.490	0.282	0.835	0.267
trans-2-butene	0.177	0.027	0.062	0.023
cis-2-butene	0.015	0.006	0.011	0.011
i-pentane	0.411	0.141	0.310	0.181
n-pentane	0.322	0.124	0.204	0.129
isoprene	0.664	0.473	0.249	0.237
n-hexane	0.148	0.064	0.120	0.085
benzene	1.007	0.265	0.592	0.229
n-heptane	0.080	0.025	0.061	0.037

toluene	0.786	0.273	0.566	0.291
ethylbenzene	0.198	0.066	0.160	0.089
o-xylene	0.097	0.036	0.069	0.034
Acetonitrile	0.497	0.144	0.302	0.050
Aerosol surface area ($\mu\text{m}^2/\text{m}^3$)	1.60×10^{-3}	3.72×10^{-4}	1.24×10^{-3}	4.92×10^{-4}
Temperature (K)	300.00	3.12	296.49	3.56
Relative Humidity (%)	64	12	67	17
j_{NO_2} (s^{-1}) ^a	3.16×10^{-3}	2.01×10^{-3}	3.33×10^{-3}	2.52×10^{-3}
j_{Cl_2} (s^{-1}) ^a	7.18×10^{-4}	4.74×10^{-4}	7.62×10^{-4}	5.87×10^{-4}
j_{HOCl} (s^{-1}) ^a	8.02×10^{-5}	5.29×10^{-5}	8.49×10^{-5}	7.08×10^{-5}
j_{ClNO_2} (s^{-1}) ^a	1.27×10^{-4}	8.06×10^{-5}	1.53×10^{-4}	1.26×10^{-4}
j_{ClO} (s^{-1}) ^a	1.16×10^{-5}	7.67×10^{-6}	1.45×10^{-5}	1.47×10^{-5}

*derived from TUV model and scaled with j_{NO_2}

^a average from sunrise to sunset

Table 7.3 summarizes the integrated oxidation rate of the alkane, alkyne, alkene aromatic and OVOC by Cl atom over the entire morning (from sunrise to 11:00) for average condition and 21 June. Although OH is the much more dominant radical in the daytime, Cl atom induced a rapid oxidation of VOCs with integrated VOCs oxidation of 0.467 ppbv on average and 1.691 ppbv on 21 June, representing 3% and 16% of the summed morning oxidation by OH and Cl atom. As in the average condition, 11%, 9%, 2%, 1% and 2% of the morning alkane, alkyne, alkene, aromatic and OVOC, respectively, were oxidized by Cl atom. While the Cl atom on 21 June contributed to 46% of oxidation of alkane, 37% of alkyne, 10% of alkene, 7% of aromatic and 13% of OVOC throughout the morning. The results suggested that Cl atom was an important oxidant for the predominated group of VOCs, alkanes, and also played a significant role in the oxidation of alkyne, alkene and OVOCs at Wangdu.

Table 7.3. The relative importance of Cl on oxidation rates of different VOCs groups for average condition and the 21 June case.

VOC group	Average			21 June		
	Σ oxidation ^{*a}	Cl + VOC ^a		Σ oxidation ^{*a}	Cl + VOC ^a	
	ppbv	ppbv	%	ppbv	ppbv	%
Alkane	0.961	0.108	11	1.134	0.525	46
Alkyne	0.114	0.014	9	0.093	0.035	37
Alkene	3.485	0.054	2	1.989	0.200	10
Aromatics	1.195	0.015	1	1.034	0.071	7
OVOCs	11.421	0.281	2	6.446	0.860	13

^a integrated from sunrise to 11:00

*Sum of VOC oxidation rates by OH radical and Cl atom

The increase of VOCs oxidation by Cl atom would produce additional RO₂ radical, and together with highly abundant NO_x in the region, production of ozone will be significantly enhanced, especially during the early morning hours when the reactivity of OH is relatively slower. With the increase of O₃, the reaction of Cl atom with O₃ (see R2.12) would increase too, leading to enhancement of ClO which would be effectively recycled back to Cl atom and enhance the formation of secondary HO_x (OH and HO₂) (see R2.13 to 2.14 in Chapter 2). The perturbation of the complex chlorine and HO_x chemistry may further affect the oxidative capacity throughout the day and may have implications on the production rate of secondary organic aerosol as well.

7.7 Summary

The study unveiled the first field observation of ClNO₂ in northern China and documented the presence of elevated ClNO₂ during the summertime in this highly

polluted region. Mixing ratios of ClNO₂ were typically larger than 350 pptv during the campaign. Highest ClNO₂ mixing ratio of 2070 pptv (1 min average) was measured on 20-21 June, which was characterized to have 2 times faster N₂O₅ heterogeneous uptake rate and four-fold larger ClNO₂ production rate than those for the campaign average condition. Much smaller ClNO₂/N₂O₅ ratio was observed on 28-29 June and was justified by the relatively lower N₂O₅ uptake and ClNO₂ yield. ClNO₂ often increased even after sunrise and peaked 4 hours later. Downward mixing of concentrated ClNO₂-air in the residual layer is believed to be the major cause of these observations, and the strength of the entrainment was consistent with the different levels of ClNO₂ morning peaks. The concentrations of ClNO₂ in the RL were estimated in the range of 1.7-4.0 ppbv, which are supported by our previous Hong Kong mountain-top observation of ClNO₂ of up to 4.7 ppbv in well-processed plumes. Though the sustained morning ClNO₂ has yet to be widely observed in other places of NCP, the Wangdu result implies strong formation of ClNO₂ in the residual layers over the polluted regions of northern China. This study also provides evidence for the existence of non-oceanic sources of fine chloride aerosol from coal-fired power plants and open burning of crop residues. Calculations suggest that photolysis of ClNO₂ was a prominent source of Cl atoms and oxidized up to 46% of alkane, 37% of alkyne, 10% of alkene, 7% of aromatic and 13% of OVOC throughout the morning. These additional oxidative processes are expected to have important impacts on the air quality in the region by enhancing formation of ozone and secondary aerosols.

Chapter 8 Conclusions

8.1 Key findings and conclusions

This thesis reports the first detailed field investigation of ClNO₂ chemistry in China with a chemical ionization mass spectrometry. The study advances our understanding of the concentrations of ClNO₂, the conditions and factors leading to ClNO₂ formation, and the impacts of ClNO₂ on the oxidative chemistry in the polluted environment.

Preliminary field measurements with a TD-CIMS at two coastal sites in Hong Kong revealed significant concentrations of ClNO₂ during night-time, similar to those observed in other polluted coastal regions. They provided an initial insight into active N₂O₅-ClNO₂ chemistry in the region. Heterogeneous formation of ClNO₂ was found to be a year-round phenomenon in Hong Kong and was impacted by the emissions from the urban cores in Hong Kong and Pearl River Delta region.

This study optimized the CIMS to simultaneously measure ClNO₂ and N₂O₅ with high sensitivity (~1 Hz/pptv) and low detection limit (5 pptv). A number of tests were conducted. An excellent agreement between the ambient N₂O₅ measurements of CIMS and a CRDS (slope = 0.99, R²= 0.93) and the similarity of the measured isotopic ratios of ClNO₂ further verified the capability of the optimized CIMS for measuring ClNO₂ and N₂O₅ under high humidity and

particulate conditions.

Field measurement with the optimized CIMS reported the presence of high concentrations of ClNO₂ and N₂O₅ in the upper planetary boundary layer of Hong Kong obtained at a mountain-top site in Hong Kong (957 m a.s.l.) during the late autumn of 2013. The highest ever reported ClNO₂ (4.7 ppbv, 1 min average) and N₂O₅ (7.7 ppbv) were observed in one early morning in extensively processed air transported from the major industrial/urban areas of the PRD. The highly accumulated ClNO₂ was initiated by the fast production of NO₃, and moderate N₂O₅ uptake and ClNO₂ production yield. High levels ClNO₂ had a large impact on the production rate of Cl atom (up to 0.59 pptv/s) in the next morning. Despite the low observation frequency of such high ClNO₂ event at TMS, it is believed that high ClNO₂ may frequently occur and impact the oxidative capacity in other locations downwind of pollution sources of the PRD. Another key result of the TMS campaign was the observation of significant concentrations of N₂O₅ and ClNO₂ in the late afternoon of a polluted foggy/cloudy day. The large discrepancy between the observed and calculated N₂O₅ in a polluted foggy/cloudy day suggests that the heterogeneous uptake of N₂O₅ on fog/cloud droplets may be an important source of soluble nitrates and additional source of oxidants during the daytime.

The first ClNO₂ measurement in the highly polluted region of northern China unambiguously documented elevated ClNO₂ with the highest concentration reached 2070 pptv. An interesting finding of this campaign is that the peak concentration of ClNO₂ often occurred 4 hours after sunrise, which is discrepant from the previously reported typical ClNO₂ diurnal pattern in other places.

Entrainment of ClNO₂-rich air in the residual layer is believed to be the dominant cause of these morning peaks. The concentrations of ClNO₂ in RL are estimated in the range of 1.7-4.0 ppbv, suggesting strong formations of ClNO₂ in the residual layers over the polluted regions of northern China. The production of ClNO₂ at Wangdu was supported by the existence of non-marine sources of fine chloride aerosol from coal-fired power plants and open burning of crop residues. Photolysis of the ClNO₂ was a primary source of Cl atom and significantly increased the morning-time oxidation of VOCs that could ultimately enhance the ozone production in the region.

Overall, the results of this thesis unveil the presence of abundant ClNO₂ that jump-starting the daytime oxidation chemistry in polluted regions of southern and northern China. In view of the potentially significant impact of ClNO₂ production on the oxidative capacity, it is important to consider the ClNO₂ and N₂O₅ chemistry when assessing tropospheric ozone, secondary aerosol, as well as the fate of greenhouse gasses in China.

8.2 Future work

In order to obtain a full picture of the importance of ClNO₂ heterogeneous production in China, the following areas are suggested for future research:

- More ground measurements of ClNO₂ and N₂O₅ are suggested in other regions with strong emissions of NO_x and Cl⁻ aerosol, such as the inland areas of the PRD, the North China Plain, the Yangtze River Delta region

(Shanghai) and the Sichuan basin (Chengdu). Vertical measurements are recommended to obtain information on the variation of ClNO_2 and related parameters with altitudes.

- Further research is needed to refine the parameterizations for the N_2O_5 heterogeneous uptake coefficient and ClNO_2 yield for application to China's environment.
- More investigations are needed on the impact of N_2O_5 heterogeneous uptake processes on the aerosol formation (i.e. nitrate aerosol) in China to better understand the role of N_2O_5 chemistry in regional haze pollution.
- Improvement of the current measurement technique or application of new methods for concurrent measurement of ClNO_2 , Cl_2 , HOCl and ClO is suggested. The information on the additional chlorine compounds helps to verify the current knowledge on the sources of Cl atom and to improve the understanding of the budget and impact of Cl atoms in China.

References

- Akagi, S., Yokelson, R.J., Wiedinmyer, C., Alvarado, M., Reid, J., Karl, T., Crouse, J., Wennberg, P., 2011. Emission factors for open and domestic biomass burning for use in atmospheric models. *Atmospheric Chemistry and Physics* 11, 4039-4072.
- Aldener, M., Brown, S.S., Stark, H., Williams, E.J., Lerner, B.M., Kuster, W.C., Goldan, P.D., Quinn, P.K., Bates, T.S., Fehsenfeld, F.C., Ravishankara, A.R., 2006. Reactivity and loss mechanisms of NO₃ and N₂O₅ in a polluted marine environment: Results from in situ measurements during New England Air Quality Study 2002. *Journal of Geophysical Research: Atmospheres* 111, D23S73.
- Asbach, C., Kuhlbusch, T.A., Fissan, H., 2005. Effect of corona discharge on the gas composition of the sample flow in a Gas Particle Partitioner. *Journal of Environmental Monitoring* 7, 877-882.
- Atkinson, R., Arey, J., 2003. Gas-phase tropospheric chemistry of biogenic volatile organic compounds: a review. *Atmospheric Environment* 37, Supplement 2, 197-219.
- Atkinson, R., Baulch, D., Cox, R., Hampson Jr, R., Kerr, J., Rossi, M., Troe, J., 1999. Evaluated kinetic and photochemical data for atmospheric chemistry, organic species: Supplement VII. *Journal of Physical and chemical reference Data* 28, 191-393.
- Atkinson, R., Baulch, D.L., Cox, R.A., Crowley, J.N., Hampson, R.F., Hynes, R.G., Jenkin, M.E., Rossi, M.J., Troe, J., 2007. Evaluated kinetic and photochemical data for atmospheric chemistry: Volume III - gas phase reactions of inorganic halogens. *Atmospheric Chemistry and Physics*. 7, 981-1191.
- Aufmhoff, H., Schäuble, D., Roiger, A., Arnold, F., Jurkat, T., Voigt, C., Schlager, H., 2012. Chemical Ionization Mass Spectrometric Measurements of Atmospheric Trace Gases, in: Schumann, U. (Ed.), *Atmospheric Physics: Background – Methods – Trends*. Springer Berlin Heidelberg, Berlin, Heidelberg, pp. 277-296.
- Bannan, T.J., 2015. Measurements of trace gases that may indicate or influence the tropospheric oxidising capacity using a chemical ionisation mass spectrometer (CIMS). Thesis, University of Manchester.
- Bannan, T.J., Booth, A.M., Bacak, A., Muller, J.B.A., Leather, K.E., Le Breton, M., Jones, B., Young, D., Coe, H., Allan, J., Visser, S., Slowik, J.G., Furger, M., Prévôt, A.S.H., Lee, J., Dunmore, R.E., Hopkins, J.R., Hamilton, J.F., Lewis, A.C., Whalley, L.K., Sharp, T., Stone, D., Heard, D.E., Fleming, Z.L., Leigh, R., Shallcross, D.E., Percival, C.J., 2015a. The first UK measurements of nitryl chloride using a chemical ionization mass spectrometer in central London in the summer of 2012, and an investigation of the role of Cl atom oxidation. *Journal of Geophysical Research: Atmospheres* 120, 5638-5657.
- Behnke, W., George, C., Scheer, V., Zetzsch, C., 1997. Production and decay of ClNO₂ from the reaction of gaseous N₂O₅ with NaCl solution: Bulk and aerosol experiments. *Journal of Geophysical Research: Atmospheres* 102, 3795-3804.
- Bertram, T.H., Thornton, J.A., 2009. Toward a general parameterization of N₂O₅ reactivity on aqueous particles: the competing effects of particle liquid water, nitrate and chloride. *Atmospheric Chemistry and Physics* 9, 8351-8363.

- Bertram, T.H., Thornton, J.A., Riedel, T.P., Middlebrook, A.M., Bahreini, R., Bates, T.S., Quinn, P.K., Coffman, D.J., 2009. Direct observations of N₂O₅ reactivity on ambient aerosol particles. *Geophysical Research Letters* 36, L19803.
- Birmili, W., Stratmann, F., Wiedensohler, A., 1999. Design of a DMA-based size spectrometer for a large particle size range and stable operation. *Journal of Aerosol Science* 30, 549-553.
- Blake, D.R., Smith, T.W., Chen, T.Y., Whipple, W.J., Rowland, F.S., 1994. Effects of biomass burning on summertime nonmethane hydrocarbon concentrations in the Canadian Wetlands. *Journal of Geophysical Research: Atmospheres* 99, 1699-1719.
- Bohn, B., Corlett, G.K., Gillmann, M., Sanghavi, S., Stange, G., Tensing, E., Vrekoussis, M., Bloss, W.J., Clapp, L.J., Kortner, M., Dorn, H.P., Monks, P.S., Platt, U., Plass-Dulmer, C., Mihalopoulos, N., Heard, D.E., Clemitshaw, K.C., Meixner, F.X., Prevot, A.S.H., Schmitt, R., 2008. Photolysis frequency measurement techniques: results of a comparison within the ACCENT project. *Atmospheric Chemistry and Physics* 8, 5373-5391.
- Brown, S.S., Dibb, J.E., Stark, H., Aldener, M., Vozella, M., Whitlow, S., Williams, E.J., Lerner, B.M., Jakoubek, R., Middlebrook, A.M., DeGouw, J.A., Warneke, C., Goldan, P.D., Kuster, W.C., Angevine, W.M., Sueper, D.T., Quinn, P.K., Bates, T.S., Meagher, J.F., Fehsenfeld, F.C., Ravishankara, A.R., 2004. Nighttime removal of NO_x in the summer marine boundary layer. *Geophysical Research Letters* 31, L07108.
- Brown, S.S., Dube, W.P., Fuchs, H., Ryerson, T.B., Wollny, A.G., Brock, C.A., Bahreini, R., Middlebrook, A.M., Neuman, J.A., Atlas, E., Roberts, J.M., Osthoff, H.D., Trainer, M., Fehsenfeld, F.C., Ravishankara, A.R., 2009. Reactive uptake coefficients for N₂O₅ determined from aircraft measurements during the Second Texas Air Quality Study: Comparison to current model parameterizations. *Journal of Geophysical Research: Atmospheres* 114, D00F10.
- Brown, S.S., Dubé, W.P., Karamchandani, P., Yarwood, G., Peischl, J., Ryerson, T.B., Neuman, J.A., Nowak, J.B., Holloway, J.S., Washenfelder, R.A., Brock, C.A., Frost, G.J., Trainer, M., Parrish, D.D., Fehsenfeld, F.C., Ravishankara, A.R., 2012. Effects of NO_x control and plume mixing on nighttime chemical processing of plumes from coal-fired power plants. *Journal of Geophysical Research: Atmospheres* 117, D07304.
- Brown, S.S., Dube, W.P., Osthoff, H.D., Wolfe, D.E., Angevine, W.M., Ravishankara, A.R., 2007. High resolution vertical distributions of NO₃ and N₂O₅ through the nocturnal boundary layer. *Atmospheric Chemistry and Physics* 7, 139-149.
- Brown, S.S., Dubé, W.P., Peischl, J., Ryerson, T.B., Atlas, E., Warneke, C., de Gouw, J.A., te Lintel Hekkert, S., Brock, C.A., Flocke, F., Trainer, M., Parrish, D.D., Fehsenfeld, F.C., Ravishankara, A.R., 2011. Budgets for nocturnal VOC oxidation by nitrate radicals aloft during the 2006 Texas Air Quality Study. *Journal of Geophysical Research: Atmospheres* 116, D24305.
- Brown, S.S., Dube, W.P., Tham, Y.J., Zha, Q.Z., Xue, L.K., Poon, S., Wang, Z., Blake, D.R., Tsui, W., Parrish, D.D., Wang, T., 2016. Nighttime chemistry at a high altitude site above Hong Kong. *Journal of Geophysical Research: Atmospheres* 121, 2457-2475.

- Brown, S.S., Osthoff, H.D., Stark, H., Dubé, W.P., Ryerson, T.B., Warneke, C., de Gouw, J.A., Wollny, A.G., Parrish, D.D., Fehsenfeld, F.C., Ravishankara, A.R., 2005. Aircraft observations of daytime NO_3 and N_2O_5 and their implications for tropospheric chemistry. *Journal of Photochemistry and Photobiology A: Chemistry* 176, 270-278.
- Brown, S.S., Ryerson, T.B., Wollny, A.G., Brock, C.A., Peltier, R., Sullivan, A.P., Weber, R.J., Dubé, W.P., Trainer, M., Meagher, J.F., Fehsenfeld, F.C., Ravishankara, A.R., 2006. Variability in nocturnal nitrogen oxide processing and its role in regional air quality. *Science* 311, 67-70.
- Brown, S.S., Stark, H., Ciciora, S.J., Ravishankara, A., 2001. In-situ measurement of atmospheric NO_3 and N_2O_5 via cavity ring-down spectroscopy. *Geophysical research letters* 28, 3227-3230.
- Brown, S.S., Stark, H., Ravishankara, A., 2003. Applicability of the steady state approximation to the interpretation of atmospheric observations of NO_3 and N_2O_5 . *Journal of Geophysical Research: Atmospheres* 108, 4539.
- Brown, S.S., Stutz, J., 2012. Night time radical observations and chemistry. *Chemical Society Reviews* 41, 6405-6447.
- Brown, S.S., Thornton, J.A., Keene, W.C., Pszenny, A.A.P., Sive, B.C., Dubé, W.P., Wagner, N.L., Young, C.J., Riedel, T.P., Roberts, J.M., VandenBoer, T.C., Bahreini, R., Öztürk, F., Middlebrook, A.M., Kim, S., Hübler, G., Wolfe, D.E., 2013. Nitrogen, Aerosol Composition, and Halogens on a Tall Tower (NACHTT): Overview of a wintertime air chemistry field study in the Front Range urban corridor of Colorado. *Journal of Geophysical Research: Atmospheres* 118, 8067-8085.
- Cai, X.Y., Ziemba, L.D., Griffin, R.J., 2008. Secondary aerosol formation from the oxidation of toluene by chlorine atoms. *Atmospheric Environment* 42, 7348-7359.
- Chan, C., Tang, J., Li, Y., Chan, L., 2006. Mixing ratios and sources of halocarbons in urban, semi-urban and rural sites of the Pearl River Delta, South China. *Atmospheric Environment* 40, 7331-7345.
- Chang, W.L., Bhave, P.V., Brown, S.S., Riemer, N., Stutz, J., Dabdub, D., 2011. Heterogeneous Atmospheric Chemistry, Ambient Measurements, and Model Calculations of N_2O_5 : A Review. *Aerosol Science and Technology* 45, 665-695.
- Cheng, Z., Lam, K., Chan, L., Wang, T., Cheng, K., 2000. Chemical characteristics of aerosols at coastal station in Hong Kong. I. Seasonal variation of major ions, halogens and mineral dusts between 1995 and 1996. *Atmospheric Environment* 34, 2771-2783.
- Crowley, J.N., Schuster, G., Pouvesle, N., Parchatka, U., Fischer, H., Bonn, B., Bingemer, H., Lelieveld, J., 2010. Nocturnal nitrogen oxides at a rural mountain-site in south-western Germany. *Atmospheric Chemistry and Physics* 10, 2795-2812.
- Crowley, J.N., Thieser, J., Tang, M.J., Schuster, G., Bozem, H., Beygi, Z.H., Fischer, H., Diesch, J.M., Drewnick, F., Borrmann, S., Song, W., Yassaa, N., Williams, J., Pöhler, D., Platt, U., Lelieveld, J., 2011. Variable lifetimes and loss mechanisms for NO_3 and N_2O_5 during the DOMINO campaign: contrasts between marine, urban and continental air. *Atmospheric Chemistry and Physics* 11, 10853-10870.

- Curtis, A., Sweetenham, W., 1987. FACSIMILE, AERE Harwell publication R 12805. Computer Science and Systems Division, Harwell Laboratory, Oxfordshire, UK.
- Daescu, D.N., Sandu, A., Carmichael, G.R., 2003. Direct and adjoint sensitivity analysis of chemical kinetic systems with KPP: II—Numerical validation and applications. *Atmospheric Environment* 37, 5097-5114.
- de Gouw, J., Warneke, C., Parrish, D., Holloway, J., Trainer, M., Fehsenfeld, F., 2003. Emission sources and ocean uptake of acetonitrile (CH₃CN) in the atmosphere. *Journal of Geophysical Research: Atmospheres* 108, 4329.
- Dentener, F.J., Crutzen, P.J., 1993. Reaction of N₂O₅ on tropospheric aerosols: Impact on the global distributions of NO_x, O₃, and OH. *Journal of Geophysical Research: Atmospheres* 98, 7149-7163.
- Ding, A.J., Wang, T., Thouret, V., Cammas, J.P., Nédélec, P., 2008. Tropospheric ozone climatology over Beijing: analysis of aircraft data from the MOZAIC program. *Atmospheric Chemistry and Physics* 8, 1-13.
- Dong, H.B., Zeng, L.M., Hu, M., Wu, Y.S., Zhang, Y.H., Slanina, J., Zheng, M., Wang, Z.F., Jansen, R., 2012. Technical Note: The application of an improved gas and aerosol collector for ambient air pollutants in China. *Atmospheric Chemistry and Physics* 12, 10519-10533.
- Draxler, R., Stunder, B., Rolph, G., Stein, A., Taylor, A., 2014: HYSPLIT_4 User's Guide, NOAA Air Resources Laboratory, Silver Spring, Md..
- Dubé, W.P., Brown, S.S., Osthoff, H.D., Nunley, M.R., Ciciora, S.J., Paris, M.W., McLaughlin, R.J., Ravishankara, A.R., 2006. Aircraft instrument for simultaneous, in situ measurement of NO₃ and N₂O₅ via pulsed cavity ring-down spectroscopy. *Review of Scientific Instruments* 77, 034101.
- Duncan, B.N., Lamsal, L.N., Thompson, A.M., Yoshida, Y., Lu, Z., Streets, D.G., Hurwitz, M.M., Pickering, K.E., 2016. A space-based, high-resolution view of notable changes in urban NO_x pollution around the world (2005–2014). *Journal of Geophysical Research: Atmospheres* 121, 976–996.
- Edwards, P.M., Brown, S.S., Roberts, J.M., Ahmadov, R., Banta, R.M., deGouw, J.A., Dube, W.P., Field, R.A., Flynn, J.H., Gilman, J.B., Graus, M., Helmig, D., Koss, A., Langford, A.O., Lefer, B.L., Lerner, B.M., Li, R., Li, S.-M., McKeen, S.A., Murphy, S.M., Parrish, D.D., Senff, C.J., Soltis, J., Stutz, J., Sweeney, C., Thompson, C.R., Trainer, M.K., Tsai, C., Veres, P.R., Washenfelder, R.A., Warneke, C., Wild, R.J., Young, C.J., Yuan, B., Zamora, R., 2014. High winter ozone pollution from carbonyl photolysis in an oil and gas basin. *Nature* 514, 351-354.
- Edwards, P.M., Young, C.J., Aikin, K., deGouw, J., Dubé, W.P., Geiger, F., Gilman, J., Helmig, D., Holloway, J.S., Kercher, J., Lerner, B., Martin, R., McLaren, R., Parrish, D.D., Peischl, J., Roberts, J.M., Ryerson, T.B., Thornton, J., Warneke, C., Williams, E.J., Brown, S.S., 2013. Ozone photochemistry in an oil and natural gas extraction region during winter: simulations of a snow-free season in the Uintah Basin, Utah. *Atmospheric Chemistry and Physics* 13, 8955-8971.
- Ervens, B., George, C., Williams, J.E., Buxton, G.V., Salmon, G.A., Bydder, M., Wilkinson, F., Dentener, F., Mirabel, P., Wolke, R., Herrmann, H., 2003. CAPRAM 2.4 (MODAC

- mechanism): An extended and condensed tropospheric aqueous phase mechanism and its application. *Journal of Geophysical Research: Atmospheres* 108, 4426.
- Faxon, C., Bean, J., Ruiz, L., 2015. Inland Concentrations of Cl₂ and ClNO₂ in southeast Texas suggest chlorine chemistry significantly contributes to atmospheric reactivity. *Atmosphere* 6, 1487.
- Finlayson-Pitts, B.J., Ezell, M.J., Pitts, J.N., 1989. Formation of chemically active chlorine compounds by reactions of atmospheric NaCl particles with gaseous N₂O₅ and ClONO₂. *Nature* 337, 241-244.
- Folkers, M., Mentel, T.F., Wahner, A., 2003. Influence of an organic coating on the reactivity of aqueous aerosols probed by the heterogeneous hydrolysis of N₂O₅. *Geophysical Research Letters* 30, 1644.
- Frenzel, A., Scheer, V., Sikorski, R., George, C., Behnke, W., Zetzsch, C., 1998. Heterogeneous Interconversion Reactions of BrNO₂, ClNO₂, Br₂, and Cl₂. *The Journal of Physical Chemistry A* 102, 1329-1337.
- Fuchs, H., Simpson, W., Apodaca, R., Brauers, T., Cohen, R., Crowley, J., Dorn, H.-P., Dubé, W., Fry, J., Häsel, R., 2012. Comparison of N₂O₅ mixing ratios during NO₃Comp 2007 in SAPHIR. *Atmospheric Measurement Techniques* 5, 2763-2777.
- Ganske, J.A., Ezell, M.J., Berko, H.N., Finlayson-Pitts, B.J., 1991. The reaction of OH with ClNO₂ at 298 K: kinetics and mechanisms. *Chemical Physics Letters* 179, 204-210.
- Gao, X., Xue, L., Wang, X., Wang, T., Yuan, C., Gao, R., Zhou, Y., Nie, W., Zhang, Q., Wang, W., 2012. Aerosol ionic components at Mt. Heng in central southern China: abundances, size distribution, and impacts of long-range transport. *Science of the Total Environment* 433, 498-506.
- Gaston, C.J., Thornton, J.A., 2016. Reacto-diffusive Length of N₂O₅ in aqueous sulfate- and chloride-containing aerosol particles. *The Journal of Physical Chemistry A* 120, 1039-1045.
- Gaston, C.J., Thornton, J.A., Ng, N.L., 2014. Reactive uptake of N₂O₅ to internally mixed inorganic and organic particles: the role of organic carbon oxidation state and inferred organic phase separations. *Atmospheric Chemistry and Physics* 14, 5693-5707.
- George, C., Ponche, J.L., Mirabel, P., Behnke, W., Scheer, V., Zetzsch, C., 1994. Study of the Uptake of N₂O₅ by Water and NaCl Solutions. *The Journal of Physical Chemistry* 98, 8780-8784.
- Geyer, A., Alicke, B., Ackermann, R., Martinez, M., Harder, H., Brune, W., di Carlo, P., Williams, E., Jobson, T., Hall, S., Shetter, R., Stutz, J., 2003. Direct observations of daytime NO₃: Implications for urban boundary layer chemistry. *Journal of Geophysical Research: Atmospheres* 108(D12), 4368.
- Ghosh, B., Papanastasiou, D.K., Talukdar, R.K., Roberts, J.M., Burkholder, J.B., 2012. Nitryl chloride (ClNO₂): UV/Vis absorption spectrum between 210 and 296 K and O(³P) quantum yield at 193 and 248 nm. *The Journal of Physical Chemistry A* 116, 5796-5805.

- Gibb W.H., 1983. Corrosion resistant materials for coal conversion systems, ed. Meadowcroft, D.B. and Manning, M.I., Applied Science, London, p. 25.
- Graedel, T.E., Keene, W., 1996. The budget and cycle of Earth's natural chlorine. *Pure and Applied Chemistry* 68, 1689-1697.
- Griffiths, P.T., Badger, C.L., Cox, R.A., Folkers, M., Henk, H.H., Mentel, T.F., 2009. Reactive uptake of N_2O_5 by aerosols containing dicarboxylic acids: Effect of particle phase, composition, and nitrate content. *The Journal of Physical Chemistry A* 113, 5082-5090.
- Guo, H., Jiang, F., Cheng, H., Simpson, I., Wang, X., Ding, A., Wang, T., Saunders, S., Wang, T., Lam, S., 2009. Concurrent observations of air pollutants at two sites in the Pearl River Delta and the implication of regional transport. *Atmospheric Chemistry and Physics* 9, 7343-7360.
- Guo, J., Tilgner, A., Yeung, C., Wang, Z., Louie, P.K.K., Luk, C.W.Y., Xu, Z., Yuan, C., Gao, Y., Poon, S., Herrmann, H., Lee, S., Lam, K.S., Wang, T., 2014. Atmospheric Peroxides in a polluted subtropical environment: Seasonal variation, sources and sinks, and importance of heterogeneous processes. *Environmental Science & Technology* 48, 1443-1450.
- He, K., Yang, F., Ma, Y., Zhang, Q., Yao, X., Chan, C.K., Cadle, S., Chan, T., Mulawa, P., 2001. The characteristics of $\text{PM}_{2.5}$ in Beijing, China. *Atmospheric Environment* 35, 4959-4970.
- Heal, M.R., Harrison, M.A., Cape, J.N., 2007. Aqueous-phase nitration of phenol by N_2O_5 and ClNO_2 . *Atmospheric environment* 41, 3515-3520.
- Hennig, T., Massling, A., Brechtel, F., Wiedensohler, A., 2005. A tandem DMA for highly temperature-stabilized hygroscopic particle growth measurements between 90% and 98% relative humidity. *Journal of Aerosol Science* 36, 1210-1223.
- Hilboll, A., Richter, A., Burrows, J.P., 2013. Long-term changes of tropospheric NO_2 over megacities derived from multiple satellite instruments. *Atmospheric Chemistry and Physics* 13, 4145-4169.
- Ho, K.F., Lee, S.C., Chan, C.K., Yu, J.C., Chow, J.C., Yao, X.H., 2003. Characterization of chemical species in $\text{PM}_{2.5}$ and PM_{10} aerosols in Hong Kong. *Atmospheric Environment* 37, 31-39.
- Hoffman, R.C., Gebel, M.E., Fox, B.S., Finlayson-Pitts, B.J., 2003. Knudsen cell studies of the reactions of N_2O_5 and ClONO_2 with NaCl: development and application of a model for estimating available surface areas and corrected uptake coefficients. *Physical Chemistry Chemical Physics* 5, 1780-1789.
- Hofzumahaus, A., Rohrer, F., Lu, K., Bohn, B., Brauers, T., Chang, C.C., Fuchs, H., Holland, F., Kita, K., Kondo, Y., Li, X., Lou, S., Shao, M., Zeng, L., Wahner, A., Zhang, Y., 2009. Amplified trace gas removal in the troposphere. *Science* 324, 1702-1704.
- Hu, J.H., Abbatt, J.P.D., 1997. Reaction probabilities for N_2O_5 hydrolysis on sulfuric acid and ammonium sulfate aerosols at room temperature. *The Journal of Physical Chemistry A* 101, 871-878.

- Huang, R.J., Zhang, Y., Bozzetti, C., Ho, K.F., Cao, J.-J., Han, Y., Daellenbach, K.R., Slowik, J.G., Platt, S.M., Canonaco, F., Zotter, P., Wolf, R., Pieber, S.M., Bruns, E.A., Crippa, M., Ciarelli, G., Piazzalunga, A., Schwikowski, M., Abbaszade, G., Schnelle-Kreis, J., Zimmermann, R., An, Z., Szidat, S., Baltensperger, U., Haddad, I.E., Prevot, A.S.H., 2014. High secondary aerosol contribution to particulate pollution during haze events in China. *Nature* 514, 218-222.
- Huey, L.G., 2007. Measurement of trace atmospheric species by chemical ionization mass spectrometry: Speciation of reactive nitrogen and future directions. *Mass Spectrometry Reviews* 26, 166-184.
- Huey, L.G., Hanson, D.R., Howard, C.J., 1995. Reactions of SF_6^- and I^- with atmospheric trace gases. *The Journal of Physical Chemistry* 99, 5001-5008.
- Jimenez, J.L., Canagaratna, M.R., Donahue, N.M., Prevot, A.S.H., Zhang, Q., Kroll, J.H., DeCarlo, P.F., Allan, J.D., Coe, H., Ng, N.L., Aiken, A.C., Docherty, K.S., Ulbrich, I.M., Grieshop, A.P., Robinson, A.L., Duplissy, J., Smith, J.D., Wilson, K.R., Lanz, V.A., Hueglin, C., Sun, Y.L., Tian, J., Laaksonen, A., Raatikainen, T., Rautiainen, J., Vaattovaara, P., Ehn, M., Kulmala, M., Tomlinson, J.M., Collins, D.R., Cubison, M.J., Dunlea, J., Huffman, J.A., Onasch, T.B., Alfarra, M.R., Williams, P.I., Bower, K., Kondo, Y., Schneider, J., Drewnick, F., Borrmann, S., Weimer, S., Demerjian, K., Salcedo, D., Cottrell, L., Griffin, R., Takami, A., Miyoshi, T., Hatakeyama, S., Shimono, A., Sun, J.Y., Zhang, Y.M., Dzepina, K., Kimmel, J.R., Sueper, D., Jayne, J.T., Herndon, S.C., Trimborn, A.M., Williams, L.R., Wood, E.C., Middlebrook, A.M., Kolb, C.E., Baltensperger, U., Worsnop, D.R., 2009. Evolution of Organic Aerosols in the Atmosphere. *Science* 326, 1525-1529.
- Jost, C., Sprung, D., Kenntner, T., Reiner, T., 2003. Atmospheric pressure chemical ionization mass spectrometry for the detection of tropospheric trace gases: the influence of clustering on sensitivity and precision. *International Journal of Mass Spectrometry* 223, 771-782.
- Keene, W.C., Khalil, M.A.K., Erickson, D.J., McCulloch, A., Graedel, T.E., Lobert, J.M., Aucott, M.L., Gong, S.L., Harper, D.B., Kleiman, G., Midgley, P., Moore, R.M., Seuzaret, C., Sturges, W.T., Benkovitz, C.M., Koropalov, V., Barrie, L.A., Li, Y.F., 1999. Composite global emissions of reactive chlorine from anthropogenic and natural sources: Reactive Chlorine Emissions Inventory. *Journal of Geophysical Research: Atmospheres* 104, 8429-8440.
- Kennedy, O.J., Ouyang, B., Langridge, J.M., Daniels, M.J.S., Bauguitte, S., Freshwater, R., McLeod, M.W., Ironmonger, C., Sendall, J., Norris, O., Nightingale, R., Ball, S.M., Jones, R.L., 2011. An aircraft based three channel broadband cavity enhanced absorption spectrometer for simultaneous measurements of NO_3 , N_2O_5 and NO_2 . *Atmospheric Measurement Techniques* 4, 1759-1776.
- Kercher, J.P., Riedel, T.P., Thornton, J.A., 2009. Chlorine activation by N_2O_5 : simultaneous, in situ detection of $ClNO_2$ and N_2O_5 by chemical ionization mass spectrometry. *Atmospheric Measurement Techniques* 2, 193-204.
- Kim, M.J., Farmer, D.K., Bertram, T.H., 2014. A controlling role for the air-sea interface in the chemical processing of reactive nitrogen in the coastal marine boundary layer. *Proceedings of the National Academy of Sciences* 111, 3943-3948.

- Kukui, A., Ancellet, G., Le Bras, G., 2008. Chemical ionisation mass spectrometer for measurements of OH and Peroxy radical concentrations in moderately polluted atmospheres. *Journal of atmospheric chemistry* 61, 133-154.
- Kürten, A., Rondo, L., Ehrhart, S., Curtius, J., 2011. Performance of a corona ion source for measurement of sulfuric acid by chemical ionization mass spectrometry. *Atmospheric Measurement Techniques* 4, 437-443.
- Lai, S.C., Zou, S.C., Cao, J.J., Lee, S.C., Ho, K.F., 2007. Characterizing ionic species in PM_{2.5} and PM₁₀ in four Pearl River Delta cities, South China. *Journal of Environmental Sciences* 19, 939-947.
- Langridge, J.M., Ball, S.M., Shillings, A.J.L., Jones, R.L., 2008. A broadband absorption spectrometer using light emitting diodes for ultrasensitive, in situ trace gas detection. *Review of Scientific Instruments* 79, 123110.
- Lee, B.H., Lopez-Hilfiker, F.D., Mohr, C., Kurtén, T., Worsnop, D.R., Thornton, J.A., 2014. An iodide-adduct high-resolution time-of-flight chemical-ionization mass spectrometer: Application to atmospheric inorganic and organic compounds. *Environmental Science & Technology* 48, 6309-6317.
- Lelieveld, J., Crutzen, P., 1990. Influences of cloud photochemical processes on tropospheric ozone. *Nature* 343, 227-233.
- Li, J., Song, Y., Mao, Y., Mao, Z., Wu, Y., Li, M., Huang, X., He, Q., Hu, M., 2014. Chemical characteristics and source apportionment of PM_{2.5} during the harvest season in eastern China's agricultural regions. *Atmospheric Environment* 92, 442-448.
- Li, X., Rohrer, F., Hofzumahaus, A., Brauers, T., Haseler, R., Bohn, B., Broch, S., Fuchs, H., Gomm, S., Holland, F., Jäger, J., Kaiser, J., Keutsch, F.N., Lohse, I., Lu, K., Tillmann, R., Wegener, R., Wolfe, G.M., Mentel, T.F., Kiendler-Scharr, A., Wahner, A., 2014. Missing gas-phase source of HONO inferred from Zeppelin measurements in the troposphere. *Science* 344, 292-296.
- Li, X., Wang, S., Duan, L., Hao, J., Li, C., Chen, Y., Yang, L., 2007. Particulate and trace gas emissions from open burning of wheat straw and corn stover in China. *Environmental Science & Technology* 41, 6052-6058.
- Liao, J., Huey, L.G., Liu, Z., Tanner, D.J., Cantrell, C.A., Orlando, J.J., Flocke, F.M., Shepson, P.B., Weinheimer, A.J., Hall, S.R., Ullmann, K., Beine, H.J., Wang, Y.H., Ingall, E.D., Stephens, C.R., Hornbrook, R.S., Apel, E.C., Riemer, D., Fried, A., Mauldin, R.L., Smith, J.N., Staebler, R.M., Neuman, J.A., Nowak, J.B., 2014. High levels of molecular chlorine in the Arctic atmosphere. *Nature Geoscience* 7, 91-94.
- Liu, H., Zhao, C., Nekat, B., Ma, N., Wiedensohler, A., van Pinxteren, D., Spindler, G., Müller, K., Herrmann, H., 2014. Aerosol hygroscopicity derived from size-segregated chemical composition and its parameterization in the North China Plain. *Atmospheric Chemistry and Physics* 14, 2525-2539.
- Liu, Y., Lu, K., Dong, H., Li, X., Cheng, P., Zou, Q., Wu, Y., Liu, X., Zhang, Y., 2016. In situ monitoring of atmospheric nitrous acid based on multi-pumping flow system and liquid waveguide capillary cell. *Journal of Environmental Sciences* 43, 273-284.

- Liu, Z., Wang, Y., Gu, D., Zhao, C., Huey, L., Stickel, R., Liao, J., Shao, M., Zhu, T., Zeng, L., 2012. Summertime photochemistry during CAREBeijing-2007: RO_x budgets and O₃ formation. *Atmospheric Chemistry and Physics* 12, 7737-7752.
- Lu, K., Rohrer, F., Holland, F., Fuchs, H., Bohn, B., Brauers, T., Chang, C., Häseler, R., Hu, M., Kita, K., 2012. Observation and modelling of OH and HO₂ concentrations in the Pearl River Delta 2006: A missing OH source in a VOC rich atmosphere. *Atmospheric chemistry and physics* 12, 1541-1569.
- Lu, K.D., Hofzumahaus, A., Holland, F., Bohn, B., Brauers, T., Fuchs, H., Hu, M., Häseler, R., Kita, K., Kondo, Y., Li, X., Lou, S.R., Oebel, A., Shao, M., Zeng, L.M., Wahner, A., Zhu, T., Zhang, Y.H., Rohrer, F., 2013. Missing OH source in a suburban environment near Beijing: observed and modelled OH and HO₂ concentrations in summer 2006. *Atmospheric Chemistry and Physics* 13, 1057-1080.
- Manö, S., Andreae, M.O., 1994. Emission of methyl bromide from biomass burning. *Science*, 1255-1255.
- Matsumoto, J., Kosugi, N., Imai, H., Kajii, Y., 2005. Development of a measurement system for nitrate radical and dinitrogen pentoxide using a thermal conversion/laser-induced fluorescence technique. *Review of Scientific Instruments* 76, 064101.
- McCulloch, A., Aucott, M.L., Benkovitz, C.M., Graedel, T.E., Kleiman, G., Midgley, P.M., Li, Y.F., 1999. Global emissions of hydrogen chloride and chloromethane from coal combustion, incineration and industrial activities: Reactive Chlorine Emissions Inventory. *Journal of Geophysical Research: Atmospheres* 104, 8391-8403.
- McLaren, R., Wojtal, P., Majonis, D., McCourt, J., Halla, J.D., Brook, J., 2010. NO₃ radical measurements in a polluted marine environment: links to ozone formation. *Atmospheric Chemistry and Physics* 10, 4187-4206.
- McMeeking, G.R., Kreidenweis, S.M., Baker, S., Carrico, C.M., Chow, J.C., Collett, J.L., Hao, W.M., Holden, A.S., Kirchstetter, T.W., Malm, W.C., Moosmuller, H., Sullivan, A.P., Wold, C.E., 2009. Emissions of trace gases and aerosols during the open combustion of biomass in the laboratory. *Journal of Geophysical Research: Atmospheres* 114, D19210.
- Mentel, T.F., Sohn, M., Wahner, A., 1999. Nitrate effect in the heterogeneous hydrolysis of dinitrogen pentoxide on aqueous aerosols. *Physical Chemistry Chemical Physics* 1, 5451-5457.
- Mielke, L.H., Furgeson, A., Odame-Ankrah, C.A., Osthoff, H.D., 2015. Ubiquity of ClNO₂ in the urban boundary layer of Calgary, Alberta, Canada. *Canadian Journal of Chemistry* 94, 414-423.
- Mielke, L.H., Furgeson, A., Osthoff, H.D., 2011. Observation of ClNO₂ in a mid-continental urban environment. *Environmental Science & Technology* 45, 8889-8896.
- Mielke, L.H., Stutz, J., Tsai, C., Hurlock, S.C., Roberts, J.M., Veres, P.R., Froyd, K.D., Hayes, P.L., Cubison, M.J., Jimenez, J.L., Washenfelder, R.A., Young, C.J., Gilman, J.B., de Gouw, J.A., Flynn, J.H., Grossberg, N., Lefer, B.L., Liu, J., Weber, R.J., Osthoff, H.D., 2013. Heterogeneous formation of nitryl chloride and its role as a nocturnal NO_x reservoir species during CalNex-LA 2010. *Journal of Geophysical Research: Atmospheres* 118, 638-610,652.

- Mijling, B., van der A, R.J., Zhang, Q., 2013. Regional nitrogen oxides emission trends in East Asia observed from space. *Atmospheric Chemistry and Physics* 13, 12003-12012.
- Ministry of Environmental Protection (MEP) China, (2015). Heavy air pollution lingers in some cities in Beijing-Tianjin-Hebei region and surrounding area, http://english.mep.gov.cn/News_service/infocus/201512/t20151203_318373.htm.
- Morgan, W.T., Ouyang, B., Allan, J.D., Aruffo, E., Di Carlo, P., Kennedy, O.J., Lowe, D., Flynn, M.J., Rosenberg, P.D., Williams, P.I., Jones, R., McFiggans, G.B., Coe, H., 2015. Influence of aerosol chemical composition on N₂O₅ uptake: airborne regional measurements in northwestern Europe. *Atmospheric Chemistry and Physics* 15, 973-990.
- Morris, E.D., Niki, H., 1973. Reaction of dinitrogen pentoxide with water. *The Journal of Physical Chemistry* 77, 1929-1932.
- Mozurkewich, M., Calvert, J.G., 1988. Reaction probability of N₂O₅ on aqueous aerosols. *Journal of Geophysical Research: Atmospheres* 93, 15889-15896.
- O'Keefe, A., Deacon, D.A., 1988. Cavity ring-down optical spectrometer for absorption measurements using pulsed laser sources. *Review of Scientific Instruments* 59, 2544-2551.
- Orlando, J.J., Tyndall, G.S., Apel, E.C., Riemer, D.D., Paulson, S.E., 2003. Rate coefficients and mechanisms of the reaction of Cl-atoms with a series of unsaturated hydrocarbons under atmospheric conditions. *International Journal of Chemical Kinetics* 35, 334-353.
- Osthoff, H.D., Roberts, J.M., Ravishankara, A.R., Williams, E.J., Lerner, B.M., Sommariva, R., Bates, T.S., Coffman, D., Quinn, P.K., Dibb, J.E., Stark, H., Burkholder, J.B., Talukdar, R.K., Meagher, J., Fehsenfeld, F.C., Brown, S.S., 2008. High levels of nitryl chloride in the polluted subtropical marine boundary layer. *Nature Geoscience* 1, 324-328.
- Osthoff, H.D., Sommariva, R., Baynard, T., Pettersson, A., Williams, E.J., Lerner, B.M., Roberts, J.M., Stark, H., Goldan, P.D., Kuster, W.C., Bates, T.S., Coffman, D., Ravishankara, A.R., Brown, S.S., 2006. Observation of daytime N₂O₅ in the marine boundary layer during New England Air Quality Study–Intercontinental Transport and Chemical Transformation 2004. *Journal of Geophysical Research: Atmospheres* 111, D23S14.
- Parrish, D.D., Buhr, M.P., Trainer, M., Norton, R.B., Shimshock, J.P., Fehsenfeld, F.C., Anlauf, K.G., Bottenheim, J.W., Tang, Y.Z., Wiebe, H.A., Roberts, J.M., Tanner, R.L., Newman, L., Bowersox, V.C., Olszyna, K.J., Bailey, E.M., Rodgers, M.O., Wang, T., Berresheim, H., Roychowdhury, U.K., Demerjian, K.L., 1993. The total reactive oxidized nitrogen levels and the partitioning between the individual species at six rural sites in eastern North America. *Journal of Geophysical Research: Atmospheres* 98, 2927-2939.
- Pfeifer, S., Birmili, W., Schladitz, A., Muller, T., Nowak, A., Wiedensohler, A., 2014. A fast and easy-to-implement inversion algorithm for mobility particle size spectrometers considering particle number size distribution information outside of the detection range. *Atmospheric Measurement Techniques* 7, 95-105.
- Pfeifer, S., Muller, T., Weinhold, K., Zikova, N., dos Santos, S.M., Marinoni, A., Bischof, O.F., Kyal, C., Ries, L., Meinhardt, F., Aalto, P., Mihalopoulos, N., Wiedensohler, A., 2016. Intercomparison of 15 aerodynamic particle size spectrometers (APS 3321):

- uncertainties in particle sizing and number size distribution. *Atmospheric Measurement Techniques* 9, 1545-1551.
- Phillips, G.J., Tang, M.J., Thieser, J., Brickwedde, B., Schuster, G., Bohn, B., Lelieveld, J., Crowley, J.N., 2012. Significant concentrations of nitryl chloride observed in rural continental Europe associated with the influence of sea salt chloride and anthropogenic emissions. *Geophysical Research Letters* 39, L10811.
- Platt, U., Meinen, J., Pöhler, D., Leisner, T., 2009. Broadband Cavity Enhanced Differential Optical Absorption Spectroscopy (CE-DOAS) - applicability and corrections. *Atmospheric Measurement Techniques* 2, 713-723.
- Plenge, J., Flesch, R., Schürmann, M.C., Rühl, E., 2001. Photofragmentation of nitryl chloride in the ultraviolet regime and vacuum ultraviolet regime. *The Journal of Physical Chemistry A* 105, 4844-4850.
- Ramanathan, V., Crutzen, P.J., Kiehl, J.T., Rosenfeld, D., 2001. Aerosols, Climate, and the Hydrological Cycle. *Science* 294, 2119-2124.
- Riedel, T.P., Bertram, T.H., Crisp, T.A., Williams, E.J., Lerner, B.M., Vlasenko, A., Li, S.-M., Gilman, J., de Gouw, J., Bon, D.M., Wagner, N.L., Brown, S.S., Thornton, J.A., 2012. Nitryl chloride and molecular chlorine in the coastal marine boundary layer. *Environmental Science & Technology* 46, 10463-10470.
- Riedel, T.P., Bertram, T.H., Ryder, O.S., Liu, S., Day, D.A., Russell, L.M., Gaston, C.J., Prather, K.A., Thornton, J.A., 2012a. Direct N₂O₅ reactivity measurements at a polluted coastal site. *Atmospheric Chemistry and Physics* 12, 2959-2968.
- Riedel, T.P., Lin, Y.H., Budisulistiorini, H., Gaston, C.J., Thornton, J.A., Zhang, Z.F., Vizuete, W., Gold, A., Surratt, J.D., 2015. Heterogeneous reactions of isoprene-derived epoxides: Reaction probabilities and molar secondary organic aerosol yield estimates. *Environmental Science & Technology Letters* 2, 38-42.
- Riedel, T.P., Wagner, N.L., Dubé, W.P., Middlebrook, A.M., Young, C.J., Öztürk, F., Bahreini, R., VandenBoer, T.C., Wolfe, D.E., Williams, E.J., Roberts, J.M., Brown, S.S., Thornton, J.A., 2013. Chlorine activation within urban or power plant plumes: Vertically resolved ClNO₂ and Cl₂ measurements from a tall tower in a polluted continental setting. *Journal of Geophysical Research: Atmospheres* 118, 8702-8715.
- Riedel, T.P., Wolfe, G.M., Danas, K.T., Gilman, J.B., Kuster, W.C., Bon, D.M., Vlasenko, A., Li, S.M., Williams, E.J., Lerner, B.M., Veres, P.R., Roberts, J.M., Holloway, J.S., Lefer, B., Brown, S.S., Thornton, J.A., 2014. An MCM modeling study of nitryl chloride (ClNO₂) impacts on oxidation, ozone production and nitrogen oxide partitioning in polluted continental outflow. *Atmospheric Chemistry and Physics* 14, 3789-3800.
- Roberts, J.M., Osthoff, H.D., Brown, S.S., Ravishankara, A.R., 2008. N₂O₅ oxidizes chloride to Cl₂ in acidic atmospheric aerosol. *Science* 321, 1059-1059.
- Roberts, J.M., Osthoff, H.D., Brown, S.S., Ravishankara, A.R., Coffman, D., Quinn, P., Bates, T., 2009. Laboratory studies of products of N₂O₅ uptake on Cl⁻ containing substrates. *Geophysical Research Letters* 36, L20808.

- Rohrer, F., Lu, K., Hofzumahaus, A., Bohn, B., Brauers, T., Chang, C.-C., Fuchs, H., Haseler, R., Holland, F., Hu, M., Kita, K., Kondo, Y., Li, X., Lou, S., Oebel, A., Shao, M., Zeng, L., Zhu, T., Zhang, Y., Wahner, A., 2014. Maximum efficiency in the hydroxyl-radical-based self-cleansing of the troposphere. *Nature Geoscience* 7, 559-563.
- Rollins, A.W., Browne, E.C., Min, K.E., Pusede, S.E., Wooldridge, P.J., Gentner, D.R., Goldstein, A.H., Liu, S., Day, D.A., Russell, L.M., Cohen, R.C., 2012. Evidence for NO_x control over nighttime SOA formation. *Science* 337, 1210-1212.
- Rossi, M.J., 2003. Heterogeneous reactions on salts. *Chemical reviews* 103, 4823-4882.
- Russell, A.R., Valin, L.C., Cohen, R.C., 2012. Trends in OMI NO₂ observations over the United States: effects of emission control technology and the economic recession. *Atmospheric Chemistry and Physics* 12, 12197-12209.
- Ryder, O.S., Ault, A.P., Cahill, J.F., Guasco, T.L., Riedel, T.P., Cuadra-Rodriguez, L.A., Gaston, C.J., Fitzgerald, E., Lee, C., Prather, K.A., Bertram, T.H., 2014. On the role of particle inorganic mixing state in the reactive uptake of N₂O₅ to ambient aerosol particles. *Environmental Science & Technology* 48, 1618-1627.
- Ryder, O.S., Campbell, N.R., Shalowski, M., Al-Mashat, H., Nathanson, G.M., Bertram, T.H., 2015. Role of organics in regulating ClNO₂ production at the air-sea interface. *The Journal of Physical Chemistry A* 119, 8519-8526.
- Sander, R., Baumgaertner, A., Gromov, S., Harder, H., Jockel, P., Kerkweg, A., Kubistin, D., Regelin, E., Riede, H., Sandu, A., Taraborrelli, D., Tost, H., Xie, Z.Q., 2011. The atmospheric chemistry box model CAABA/MECCA-3.0. *Geoscientific Model Development* 4, 373-380.
- Sandu, A., Daescu, D.N., Carmichael, G.R., 2003. Direct and adjoint sensitivity analysis of chemical kinetic systems with KPP: Part I—theory and software tools. *Atmospheric Environment* 37, 5083-5096.
- Sandu, A., Sander, R., 2006. Technical note: Simulating chemical systems in Fortran90 and Matlab with the Kinetic PreProcessor KPP-2.1. *Atmos Chem Phys* 6, 187-195.
- Sarwar, G., Simon, H., Bhave, P., Yarwood, G., 2012. Examining the impact of heterogeneous nitryl chloride production on air quality across the United States. *Atmospheric Chemistry and Physics* 12, 6455-6473.
- Sarwar, G., Simon, H., Xing, J., Mathur, R., 2014. Importance of tropospheric ClNO₂ chemistry across the Northern Hemisphere. *Geophysical Research Letters* 41, 4050-4058.
- Schweitzer, F., Mirabel, P., George, C., 1998. Multiphase Chemistry of N₂O₅, ClNO₂, and BrNO₂. *The Journal of Physical Chemistry A* 102, 3942-3952.
- Seinfeld, J.H., Pandis, S.N., 2006. *Atmospheric Chemistry and Physics: From Air Pollution to Climate Change*. Wiley.
- Simon, H., Kimura, Y., McGaughey, G., Allen, D.T., Brown, S.S., Coffman, D., Dibb, J., Osthoff, H.D., Quinn, P., Roberts, J.M., Yarwood, G., Kemball-Cook, S., Byun, D., Lee, D., 2010. Modeling heterogeneous ClNO₂ formation, chloride availability, and chlorine cycling in Southeast Texas. *Atmospheric Environment* 44, 5476-5488.

- Simon, H., Kimura, Y., McGaughey, G., Allen, D.T., Brown, S.S., Osthoff, H.D., Roberts, J.M., Byun, D., Lee, D., 2009. Modeling the impact of ClNO₂ on ozone formation in the Houston area. *Journal of Geophysical Research: Atmospheres* 114, D00F03.
- Simpson, I.J., Blake, N.J., Barletta, B., Diskin, G.S., Fuelberg, H.E., Gorham, K., Huey, L.G., Meinardi, S., Rowland, F.S., Vay, S.A., Weinheimer, A.J., Yang, M., Blake, D.R., 2010. Characterization of trace gases measured over Alberta oil sands mining operations: 76 speciated C₂–C₁₀ volatile organic compounds (VOCs), CO₂, CH₄, CO, NO, NO₂, NO_y, O₃ and SO₂. *Atmospheric Chemistry and Physics* 10, 11931-11954.
- Simpson, W.R., Brown, S.S., Saiz-Lopez, A., Thornton, J.A., Glasow, R.V., 2015. Tropospheric Halogen Chemistry: Sources, Cycling, and Impacts. *Chemical Reviews* 115, 4035-4062.
- Slusher, D.L., Huey, L.G., Tanner, D.J., Flocke, F.M., Roberts, J.M., 2004. A thermal dissociation-chemical ionization mass spectrometry (TD-CIMS) technique for the simultaneous measurement of peroxyacyl nitrates and dinitrogen pentoxide. *Journal of Geophysical Research: Atmospheres* 109, D19315.
- Stull, R. B., 1988. *An Introduction to Boundary Layer Meteorology*, Kluwer Academic, Dordrecht, Netherlands.
- Stutz, J., Alicke, B., Ackermann, R., Geyer, A., White, A., Williams, E., 2004. Vertical profiles of NO₃, N₂O₅, O₃, and NO_x in the nocturnal boundary layer: 1. Observations during the Texas Air Quality Study 2000. *Journal of Geophysical Research: Atmospheres* 109, D12306.
- Sun, H.Y., Zhang, X.Y., Chen, S.Y., Pei, D., Liu, C.M., 2007. Effects of harvest and sowing time on the performance of the rotation of winter wheat-summer maize in the North China Plain. *Industrial Crops and Products* 25, 239-247.
- Sun, Y., Wang, Z., Dong, H., Yang, T., Li, J., Pan, X., Chen, P., Jayne, J.T., 2012. Characterization of summer organic and inorganic aerosols in Beijing, China with an Aerosol Chemical Speciation Monitor. *Atmospheric environment* 51, 250-259.
- Sun, Y.L., Wang, Z.F., Du, W., Zhang, Q., Wang, Q.Q., Fu, P.Q., Pan, X.L., Li, J., Jayne, J., Worsnop, D.R., 2015. Long-term real-time measurements of aerosol particle composition in Beijing, China: seasonal variations, meteorological effects, and source analysis. *Atmospheric Chemistry and Physics* 15, 10149-10165.
- Tan, J.H., Duan, J.C., Chen, D.H., Wang, X.H., Guo, S.J., Bi, X.H., Sheng, G.Y., He, K.B., Fu, J.M., 2009. Chemical characteristics of haze during summer and winter in Guangzhou. *Atmospheric Research* 94, 238-245.
- Tan, Z., Fuchs, H., Lu, K., Bohn, B., Broch, S., Dong, H., Gomm, S., Haeseler, R., He, L., Hofzumahaus, A., Holland, F., Li, X., Liu, Y., Lu, S., Rohrer, F., Shao, M., Wang, B., Wang, M., Wu, Y., Zeng, L., Zhang, Y., Wahner, A., Zhang, Y., 2016. Radical chemistry at a rural site (Wangdu) in the North China Plain: Observation and model calculations of OH, HO₂ and RO₂ radicals. *Atmospheric Chemistry and Physics Discussions* 2016, 1-48.
- Tanaka, P.L., Riemer, D.D., Chang, S., Yarwood, G., McDonald-Buller, E.C., Apel, E.C., Orlando, J.J., Silva, P.J., Jimenez, J.L., Canagaratna, M.R., 2003. Direct evidence for

- chlorine-enhanced urban ozone formation in Houston, Texas. *Atmospheric Environment* 37, 1393-1400.
- Tang, M.J., Thieser, J., Schuster, G., Crowley, J.N., 2010. Uptake of NO_3 and N_2O_5 to Saharan dust, ambient urban aerosol and soot: a relative rate study. *Atmospheric Chemistry and Physics* 10, 2965-2974.
- Tang, M.J., Thieser, J., Schuster, G., Crowley, J.N., 2012. Kinetics and mechanism of the heterogeneous reaction of N_2O_5 with mineral dust particles. *Physical Chemistry Chemical Physics* 14, 8551-8561.
- Thaler, R.D., Mielke, L.H., Osthoff, H.D., 2011. Quantification of nitryl chloride at part per trillion mixing ratios by thermal dissociation cavity ring-down spectroscopy. *Analytical Chemistry* 83, 2761-2766.
- Tham, Y.J., Wang, Z., Li, Q., Yun, H., Wang, W., Wang, X., Xue, L., Lu, K., Ma, N., Bohn, B., Li, X., Kecorius, S., Größ, J., Shao, M., Wiedensohler, A., Zhang, Y., Wang, T., 2016. Significant concentrations of nitryl chloride sustained in the morning: Investigations of the causes and impacts on ozone production in a polluted region of northern China. *Atmospheric Chemistry and Physics Discussion* 2016, 1-34.
- Tham, Y.J., Yan, C., Xue, L., Zha, Q., Wang, X., Wang, T., 2014. Presence of high nitryl chloride in Asian coastal environment and its impact on atmospheric photochemistry. *Chinese Science Bulletin* 59, 356-359.
- Thornton, J.A., Abbatt, J.P.D., 2005. N_2O_5 Reaction on Submicron Sea Salt Aerosol: Kinetics, Products, and the Effect of Surface Active Organics. *The Journal of Physical Chemistry A* 109, 10004-10012.
- Thornton, J.A., Braban, C.F., Abbatt, J.P.D., 2003. N_2O_5 hydrolysis on sub-micron organic aerosols: the effect of relative humidity, particle phase, and particle size. *Physical Chemistry Chemical Physics* 5, 4593-4603.
- Thornton, J.A., Kercher, J.P., Riedel, T.P., Wagner, N.L., Cozic, J., Holloway, J.S., Dubé, W.P., Wolfe, G.M., Quinn, P.K., Middlebrook, A.M., Alexander, B., Brown, S.S., 2010. A large atomic chlorine source inferred from mid-continental reactive nitrogen chemistry. *Nature* 464, 271-274.
- Tie, X., Brasseur, G.P., Zhao, C., Granier, C., Massie, S., Qin, Y., Wang, P., Wang, G., Yang, P., Richter, A., 2006. Chemical characterization of air pollution in Eastern China and the Eastern United States. *Atmospheric Environment* 40, 2607-2625.
- Tsai, C., Wong, C., Hurlock, S., Pikelnaya, O., Mielke, L.H., Osthoff, H.D., Flynn, J.H., Haman, C., Lefer, B., Gilman, J., de Gouw, J., Stutz, J., 2014. Nocturnal loss of NO_x during the 2010 CalNex-LA study in the Los Angeles Basin. *Journal of Geophysical Research: Atmospheres* 119, 13,004-013,025.
- Wagner, N.L., Riedel, T.P., Roberts, J.M., Thornton, J.A., Angevine, W.M., Williams, E.J., Lerner, B.M., Vlasenko, A., Li, S.M., Dubé, W.P., Coffman, D.J., Bon, D.M., de Gouw, J.A., Kuster, W.C., Gilman, J.B., Brown, S.S., 2012. The sea breeze/land breeze circulation in Los Angeles and its influence on nitryl chloride production in this region. *Journal of Geophysical Research: Atmospheres* 117, D00V24.

- Wagner, N.L., Riedel, T.P., Young, C.J., Bahreini, R., Brock, C.A., Dubé, W.P., Kim, S., Middlebrook, A.M., Öztürk, F., Roberts, J.M., Russo, R., Sive, B., Swarthout, R., Thornton, J.A., VandenBoer, T.C., Zhou, Y., Brown, S.S., 2013. N₂O₅ uptake coefficients and nocturnal NO₂ removal rates determined from ambient wintertime measurements. *Journal of Geophysical Research: Atmospheres* 118, 9331-9350.
- Wang, M., Zeng, L., Lu, S., Shao, M., Liu, X., Yu, X., Chen, W., Yuan, B., Zhang, Q., Hu, M., Zhang, Z., 2014. Development and validation of a cryogen-free automatic gas chromatograph system (GC-MS/FID) for online measurements of volatile organic compounds. *Analytical Methods* 6, 9424-9434.
- Wang, S., Shi, C., Zhou, B., Zhao, H., Wang, Z., Yang, S., Chen, L., 2013. Observation of NO₃ radicals over Shanghai, China. *Atmospheric Environment* 70, 401-409.
- Wang, T., Ding, A., Gao, J., Wu, W.S., 2006. Strong ozone production in urban plumes from Beijing, China. *Geophysical Research Letters* 33, L21806.
- Wang, T., Ding, A.J., Blake, D.R., Zahorowski, W., Poon, C.N., Li, Y.S., 2003. Chemical characterization of the boundary layer outflow of air pollution to Hong Kong during February–April 2001. *Journal of Geophysical Research: Atmospheres* 108(D20), 8787.
- Wang, T., Tham, Y.J., Xue, L., Li, Q., Zha, Q., Wang, Z., Poon, S.C.N., Dubé, W.P., Blake, D.R., Louie, P.K.K., Luk, C.W.Y., Tsui, W., Brown, S.S., 2016. Observations of nitryl chloride and modeling its source and effect on ozone in the planetary boundary layer of southern China. *Journal of Geophysical Research: Atmospheres* 121, 2476-2489.
- Wang, T., Wei, X.L., Ding, A.J., Poon, C.N., Lam, K.S., Li, Y.S., Chan, L.Y., Anson, M., 2009. Increasing surface ozone concentrations in the background atmosphere of Southern China, 1994–2007. *Atmospheric Chemistry and Physics* 9, 6217-6227.
- Wang, X., Wang, T., Yan, C., Tham, Y.J., Xue, L., Xu, Z., Zha, Q., 2014. Large daytime signals of N₂O₅ and NO₃ inferred at 62 amu in a TD-CIMS: chemical interference or a real atmospheric phenomenon? *Atmospheric Measurement Techniques* 7, 1-12.
- Wayne, R.P., Barnes, I., Biggs, P., Burrows, J.P., Canosa-Mas, C.E., Hjorth, J., Le Bras, G., Moortgat, G.K., Perner, D., Poulet, G., Restelli, G., Sidebottom, H., 1991. The nitrate radical: Physics, Chemistry, and the Atmosphere The nitrate radical: Physics, chemistry, and the atmosphere. *Atmospheric Environment. Part A. General Topics* 25, 1-203.
- Wiedensohler, A., Birmili, W., Nowak, A., Sonntag, A., Weinhold, K., Merkel, M., Wehner, B., Tuch, T., Pfeifer, S., Fiebig, M., Fjåraa, A.M., Asmi, E., Sellegri, K., Depuy, R., Venzac, H., Villani, P., Laj, P., Aalto, P., Ogren, J.A., Swietlicki, E., Williams, P., Roldin, P., Quincey, P., Hüglin, C., Fierz-Schmidhauser, R., Gysel, M., Weingartner, E., Riccobono, F., Santos, S., Gruning, C., Faloon, K., Beddows, D., Harrison, R., Monahan, C., Jennings, S.G., O'Dowd, C.D., Marinoni, A., Horn, H.-G., Keck, L., Jiang, J., Scheckman, J., McMurry, P.H., Deng, Z., Zhao, C.S., Moerman, M., Henzing, B., De Leeuw, G., Löschau, G., Bastian, S., 2012. Mobility particle size spectrometers: harmonization of technical standards and data structure to facilitate high quality long-term observations of atmospheric particle number size distributions. *Atmospheric Measurement Techniques* 5, 657- 685.

- Wilkins Jr, R., Dodge, M., Hisatsune, I., 1974. Kinetics of nitric oxide catalyzed decomposition of nitryl chloride and its related nitrogen isotope exchange reactions. *The Journal of Physical Chemistry* 78, 2073-2076.
- Wood, E.C., Wooldridge, P.J., Freese, J.H., Albrecht, T., Cohen, R.C., 2003. Prototype for in situ detection of atmospheric NO₃ and N₂O₅ via Laser-Induced Fluorescence. *Environmental Science & Technology* 37, 5732-5738.
- Xu, Z., Wang, T., Wu, J., Xue, L., Chan, J., Zha, Q., Zhou, S., Louie, P.K.K., Luk, C.W.Y., 2015. Nitrous acid (HONO) in a polluted subtropical atmosphere: Seasonal variability, direct vehicle emissions and heterogeneous production at ground surface. *Atmospheric Environment* 106, 100-109.
- Xu, Z., Wang, T., Xue, L.K., Louie, P.K.K., Luk, C.W.Y., Gao, J., Wang, S.L., Chai, F.H., Wang, W.X., 2013. Evaluating the uncertainties of thermal catalytic conversion in measuring atmospheric nitrogen dioxide at four differently polluted sites in China. *Atmospheric Environment* 76, 221-226.
- Xu, Z., Xue, L., Wang, T., Xia, T., Gao, Y., Louie, P.K., Luk, C.W., 2015a. Measurements of peroxyacetyl nitrate at a background site in the Pearl River Delta Region: Production efficiency and regional transport. *Aerosol and Air Quality Research* 15, 833-841.
- Xue, L., Wang, T., Louie, P.K.K., Luk, C.W.Y., Blake, D.R., Xu, Z., 2014. Increasing external effects negate local efforts to control ozone air pollution: A case study of Hong Kong and implications for other Chinese cities. *Environmental Science & Technology* 48, 10769-10775.
- Xue, L.K., Saunders, S.M., Wang, T., Gao, R., Wang, X.F., Zhang, Q.Z., Wang, W.X., 2015. Development of a chlorine chemistry module for the Master Chemical Mechanism. *Geoscientific Model Development* 8, 4823-4849.
- Yang, D., Li, C., Lau, A.K.-H., Li, Y., 2013. Long-term measurement of daytime atmospheric mixing layer height over Hong Kong. *Journal of Geophysical Research: Atmospheres* 118, 2422-2433.
- Yeung, M.C., Lee, B.P., Li, Y.J., Chan, C.K., 2014. Simultaneous HTDMA and HR-ToF-AMS measurements at the HKUST Supersite in Hong Kong in 2011. *Journal of Geophysical Research: Atmospheres* 119, 9864-9883.
- Young, C.J., Washenfelder, R.A., Edwards, P.M., Parrish, D.D., Gilman, J.B., Kuster, W.C., Mielke, L.H., Osthoff, H.D., Tsai, C., Pikel'naya, O., Stutz, J., Veres, P.R., Roberts, J.M., Griffith, S., Dusanter, S., Stevens, P.S., Flynn, J., Grossberg, N., Lefer, B., Holloway, J.S., Peischl, J., Ryerson, T.B., Atlas, E.L., Blake, D.R., Brown, S.S., 2014. Chlorine as a primary radical: evaluation of methods to understand its role in initiation of oxidative cycles. *Atmospheric Chemistry and Physics* 14, 3427-3440.
- Young, C.J., Washenfelder, R.A., Roberts, J.M., Mielke, L.H., Osthoff, H.D., Tsai, C., Pikel'naya, O., Stutz, J., Veres, P.R., Cochran, A.K., VandenBoer, T.C., Flynn, J., Grossberg, N., Haman, C.L., Lefer, B., Stark, H., Graus, M., de Gouw, J., Gilman, J.B., Kuster, W.C., Brown, S.S., 2012. Vertically resolved measurements of nighttime radical reservoirs; in Los Angeles and their contribution to the urban radical budget. *Environmental Science & Technology* 46, 10965-10973.

- Yuan, B., Chen, W., Shao, M., Wang, M., Lu, S., Wang, B., Liu, Y., Chang, C.C., Wang, B., 2012. Measurements of ambient hydrocarbons and carbonyls in the Pearl River Delta (PRD), China. *Atmospheric Research* 116, 93-104.
- Zhang, L., Wang, S., Meng, Y., Hao, J., 2012. Influence of mercury and chlorine content of coal on mercury emissions from coal-fired power plants in China. *Environmental Science & Technology* 46, 6385-6392.
- Zhang, L., Wang, T., Lv, M., Zhang, Q., 2015. On the severe haze in Beijing during January 2013: Unraveling the effects of meteorological anomalies with WRF-Chem. *Atmospheric Environment* 104, 11-21.
- Zhang, Q., Streets, D.G., He, K., Wang, Y., Richter, A., Burrows, J.P., Uno, I., Jang, C.J., Chen, D., Yao, Z., 2007. NO_x emission trends for China, 1995–2004: The view from the ground and the view from space. *Journal of Geophysical Research: Atmospheres* 112.
- Zhang, Q., Yuan, B., Shao, M., Wang, X., Lu, S., Lu, K., Wang, M., Chen, L., Chang, C.-C., Liu, S., 2014. Variations of ground-level O₃ and its precursors in Beijing in summertime between 2005 and 2011. *Atmospheric Chemistry and Physics* 14, 6089-6101.
- Zhang, Y., Min, S., Zhang, Y., Zeng, L., He, L., Bin, Z., Wei, Y., Zhu, X., 2007. Source profiles of particulate organic matters emitted from cereal straw burnings. *Journal of Environmental Sciences* 19, 167-175.
- Zhao, B., Wang, S., Liu, H., Xu, J., Fu, K., Klimont, Z., Hao, J., He, K., Cofala, J., Amann, M., 2013. NO_x emissions in China: historical trends and future perspectives. *Atmospheric Chemistry and Physics* 13, 9869-9897.
- Zhao, Y., Wang, S.X., Duan, L., Lei, Y., Cao, P.F., Hao, J.M., 2008. Primary air pollutant emissions of coal-fired power plants in China: Current status and future prediction. *Atmospheric Environment* 42, 8442-8452.
- Zipprich, J.L., Harris, S.A., Fox, J.C., Borzelleca, J.F., 2002. An analysis of factors that influence personal exposure to nitrogen oxides in residents of Richmond, Virginia. *Journal of Exposure Analysis and Environmental Epidemiology* 12, 273-285.